AD-A146 210 DIELECTRIC AND OPTICAL PROPERTIES OF SPUTTERED THIN FILMS(U) UNIVERSITY OF SOUTHERN CALIFORNIA LOS ANGELES OPTICAL MATERIA... A R TANGUAY JUL 84 USC/OMDL-1101 1/2

UNCLASSIFIED ARO-16291.3-PH DAAG29-79-C-0175 F/G 20/6 NL

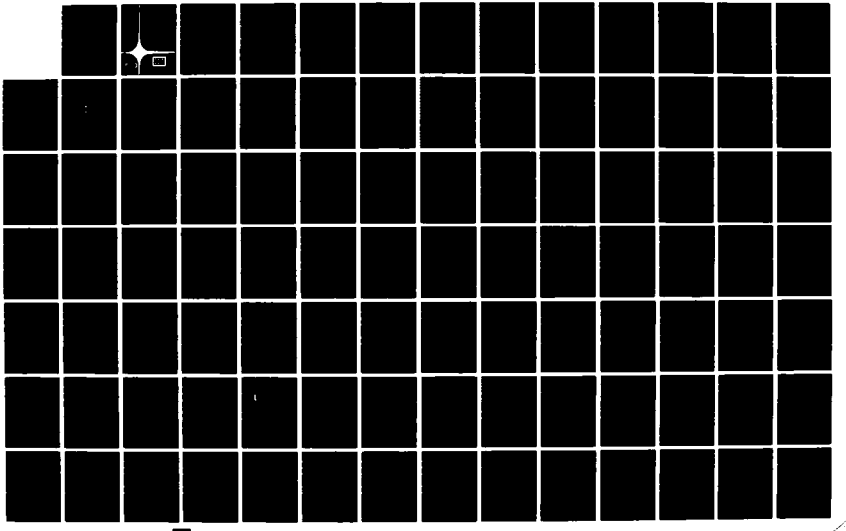

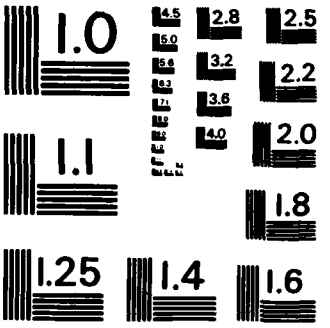


MICROCOPY RESOLUTION TEST CHART
NATIONAL BUREAU OF STANDARDS - 1963 - A

ENGINEERING

AD-A146 210

ARO 16291.3-PH

(2)

UNIVERSITY OF SOUTHERN CALIFORNIA

# DIELECTRIC AND OPTICAL PROPERTIES OF SPUTTERED THIN FILMS

GRANT DAAG-29-79-C-0175,
15 September, 1979 - 14 September, 1983

FINAL TECHNICAL REPORT

Submitted To:

U. S. Army Research Office
P. O. Box 12211
Research Triangle Park, NC 27709

Submitted By:

Armand R. Tanguay, Jr.
Optical Materials and Devices Laboratory
University of Southern California

July, 1984



IPI

IMAGE PROCESSING INSTITUTE

UNCLASSIFIED

SECURITY CLASSIFICATION OF THIS PAGE

## REPORT DOCUMENTATION PAGE

| | |
|---|---|
| 1a. REPORT SECURITY CLASSIFICATION<br>UNCLASSIFIED | 1b. RESTRICTIVE MARKINGS |
| 2a. SECURITY CLASSIFICATION AUTHORITY | 3. DISTRIBUTION/AVAILABILITY OF REPORT<br>APPROVED FOR PUBLIC RELEASE:<br>DISTRIBUTION UNLIMITED |
| 2b. DECLASSIFICATION/DOWNGRADING SCHEDULE | |
| 4. PERFORMING ORGANIZATION REPORT NUMBER(S)<br>USC OMDL-1101 | 5. MONITORING ORGANIZATION REPORT NUMBER(S) |
| 6a. NAME OF PERFORMING ORGANIZATION<br>UNIVERSITY OF SOUTHERN CALIFORNIA<br>6b. OFFICE SYMBOL (If applicable) | 7a. NAME OF MONITORING ORGANIZATION<br>U. S. ARMY RESEARCH OFFICE |
| 6c. ADDRESS (City, State and ZIP Code)<br>OPTICAL MATERIALS AND DEVICES LABORATORY<br>UNIVERISTY PARK MC-0483<br>LOS ANGELES, CALIFORNIA 90089-0483 | 7b. ADDRESS (City, State and ZIP Code)<br>P. O. BOX 12211<br>RESEARCH TRIANGLE PARK, NC 27709 |
| 8a. NAME OF FUNDING/SPONSORING ORGANIZATION<br>8b. OFFICE SYMBOL (If applicable) | 9. PROCUREMENT INSTRUMENT IDENTIFICATION NUMBER<br>DAAG29-79-C-0175 |
| 8c. ADDRESS (City, State and ZIP Code) | 10. SOURCE OF FUNDING NOS.<br>PROGRAM ELEMENT NO. / PROJECT NO. / TASK NO. / WORK UNIT NO. |
| 11. TITLE (Include Security Classification) DIELECTRIC AND OPTICAL PROPERTIES OF SPUTTERED THIN FILMS | |
| 12. PERSONAL AUTHOR(S)<br>DR. ARMAND R. TANGUAY, JR. | |
| 13a. TYPE OF REPORT<br>FINAL REPORT<br>13b. TIME COVERED FROM 9/15/79 TO 9/14/83 | 14. DATE OF REPORT (Yr., Mo., Day)<br>1984, JULY<br>15. PAGE COUNT<br>135 |
| 16. SUPPLEMENTARY NOTATION The views, opinions, and/or findings contained in this report are those of the author and should not be construed as an official Department of the Army position, policy, or decision, unless so designated by other documentation. | |

| 17. COSATI CODES | | |
|---|---|---|
| FIELD | GROUP | SUB. GR. |
| | | |
| | | |

18. SUBJECT TERMS (Continue on reverse if necessary and identify by block number)
SPATIAL LIGHT MODULATORS, PROM, PRIZ, POCKELS READOUT OPTICAL MODULATOR, ELECTROOPTIC SPATIAL LIGHT MODULATORS, DIELECTRIC THIN FILMS, RF SPUTTERING, SPECTROSCOPIC ELLIPSOMETRY, (over)

19. ABSTRACT (Continue on reverse if necessary and identify by block number)


The primary focus of this research program concerned the optimization of the resolution of Electrooptic Spatial Light Modulators such as the Pockels Readout Optical Modulator (PROM), for applications in optical processing and computing.

The initial approach derived from the realization that the resolution and sensitivity of Electrooptic Spatial Light Modualtors depend strongly on the parameters describing the thin film dielectric layers utilized in the device. In particular, the resolution of a multi-layer Electrooptic Spatial Light Modulator was shown to increase dramatically with increasing layer dielectric constant and with decreasing layer thickness. Thus, RF magnetron sputtering was investigated as a means of depositing novel thin film overcoatings with enhanced dielectric constants (of order 50) while maintaining extremely high values of the dielectric breakdown strength and volume resistivity. A thin film deposition facility was designed, constructed, and evaluated that has provision for two cylindrical magnetron sputterguns, a DC plasma/RF triode sputtergun, in situ mass spectrometric residual gas


| | |
|---|---|
| 20. DISTRIBUTION/AVAILABILITY OF ABSTRACT<br>UNCLASSIFIED/UNLIMITED ☒ SAME AS RPT. ☐ DTIC USERS ☐ | 21. ABSTRACT SECURITY CLASSIFICATION<br>UNCLASSIFIED |
| 22a. NAME OF RESPONSIBLE INDIVIDUAL | 22b. TELEPHONE NUMBER (Include Area Code)<br>22c. OFFICE SYMBOL |

DD FORM 1473, 83 APR EDITION OF 1 JAN 73 IS OBSOLETE.

UNCLASSIFIED

SECURITY CLASSIFICATION OF THIS PAGE

18. SUBJECT TERMS (continued)

OPTICAL INFORMATION PROCESSING

19. ABSTRACT (continued)

diagnostics, and an optically shaft-encoded, digitally controlled planetary system. In addition, a scanning spectroscopic ellipsometer was constructed for analysis of a broad range of thin film parameters.

The focus of the research evolved early on in the program to incorporate an extensive theoretical and experimental study of the charge carrier dynamics in the active electrooptic/photoconductive device layer, and to determine the impact of such exposure-induced charge distributions on the sensitivity and resolution of the devices. The electric field distribution for the full three layer dielectric problem was solved analytically for the first time, incorporating layer thickness, layer dielectric constants, and point charge location in the resultant expression. A longitudinal charge transport model was developed to determine the effects of device constitutive, material, and exposure parameters on the resultant longitudinal charge distribution. These results allowed for the calculation of the resultant sensitivity and resolution by means of a Greens function method. Most importantly, it was demonstrated that very large improvements in both sensitivity and resolution can be achieved through optimized device design and operational mode. Experimental results on devices constructed during the course of the research program conclusively supported the theoretical predictions.

A novel spatial light modulator concept (the Photorefractive Incoherent-to-Coherent Optical Converter) was discovered during the course of the program that operates on the principle of selective spatial erasure of a holographically written diffraction grating. This device offers surprisingly good performance at a very low fabrication cost compared to all other currently available devices.

# DIELECTRIC AND OPTICAL PROPERTIES OF SPUTTERED THIN FILMS

## TABLE OF CONTENTS

DIELECTRIC AND OPTICAL PROPERTIES OF SPUTTERED THIN FILMS

## LIST OF FIGURES

DIELECTRIC AND OPTICAL PROPERTIES OF SPUTTERED THIN FILMS

LIST OF APPENDICES

## 1. INTRODUCTION

Of critical importance to the eventual performance of numerous coherent optical image processors and highly parallel computers is the development of a high speed, recyclable, linear, high resolution, selectively erasable image storage transducer operable in nearly real time. Applications for such a transducer abound, including incoherent-to-coherent conversion, pattern recognition and image feature extraction, level slicing, edge enhancement, low light level image integration, scratch pad memory, and page composition for data entry in holographic memory systems. In response to this need, a wide variety of candidate devices have been proposed in the past ten years, based on photochromic, liquid crystal, photorefractive, magnetooptic, electrooptic, deformable membrane, thermoplastic, photodichroic, and ambidextrous effects in numerous configurations. (see, for example, [1] and [2]). The device category comprised of Electrooptic Spatial Light Modulators contains a number of leading candidates, due to a combination of wide dynamic range, high sensitivity, intermediate storage time, relative simplicity of construction and operation, and long term durability. This category includes the Pockels Readout Optical Modulator or PROM [3, 4], a Soviet modification of the PROM called the PRIZ [5, 6], the Microchannel Spatial Light Modulator (MSLM) [7, 8], the TITUS ($e^-$-beam DKDP) [9, 10] and photo-TITUS (Se-DKDP) [10], and the Photorefractive Incoherent-to-Coherent Optical Converter [11, 12, 13].

The PROM is a two-dimensional spatial light modulator and image storage device comprised of a thin electrooptic crystal sandwiched between transparent insulating layers and transparent conducting electrodes. In operation, an input-image intensity distribution creates electron-hole pairs near one electrooptic crystal insulating layer interface which separate under the influence of an applied field. This charge separation results in a redistribution of voltage between the electrooptic crystal and insulating layers. A two-dimensional electric field replica of the input intensity distribution is thus created which can be read out utilizing polarized light (of wavelength beyond the photoconductivity edge for nondestructive readout) via the linear electrooptic effect. Both transmissive and reflective readout schemes are possible, as are both amplitude and phase modulation.

The PROM relies for its successful operation on the rather unique combination of properties required of the active electrooptic material. These properties include photoconductivity with high quantum efficiency, optical transparency in the visible spectrum, a large dielectric constant, very high resistivity, and a sizeable electrooptic

effect. In addition, the usual materials constraints must be satisfied, including ease of growth, control of crystal perfection, and reproducibility of critical characteristics. At the present time, bismuth silicon oxide ($Bi_{12}SiO_{20}$) is the material of choice for the PROM on the basis of the above requirements.

Bismuth silicon oxide (BSO) is a cubic (space group I23), photoconductive, electrooptic, semi-insulating material that has found applications in a number of technologically important devices. In addition to its unique qualifications for use in the Pockels Readout Optical Modulator and the PRIZ (a Soviet version of the PROM utilizing crystallographic orientations of BSO other than <001>), BSO has been reported as having among the highest known photorefractive sensitivities for read-write volume holographic storage with associated high-quality image reconstruction [14, 15]. Real time double exposure interferometry with BSO crystals utilized in a transverse electrooptic configuration has been achieved, offering new flexibility to nondestructive test procedures [16]. Furthermore, $Bi_{12}SiO_{20}$ belongs to a family of isomorphic compounds that may find wide application in integrated optics [17]. The importance of bismuth silicon oxide to these optical device applications is supplemented by equally intriguing acoustic propagation characteristics, which have guaranteed its usefulness in various surface acoustic wave (SAW) device configurations [18].

Major features of the operational physics of the PROM that determine its suitability for specific applications in optical processing include resolution, sensitivity, charge transport, and operational modes (including prime, superprime, and erasure). All four of these important characteristics can be shown to be fundamentally interrelated and dependent on the device material and constitutive properties (including, for example, the thickness and dielectric constants of the dielectric blocking layers), as well as on the charge dynamics of the bismuth silicon oxide layer during exposure to writing illumination. Previous treatments of electrooptic spatial light modulator resolution (through calculations of the ideal electrostatic modulation transfer function) [19, 20] neglected important space charge redistribution effects, and hence could not be compared directly with experiment. The one dimensional charge transfer model of Sprague [21] was advanced to predict the wavelength dependence of the exposure sensitivity, but has been shown to contain several errors. Under the ARO-funded research program, a comprehensive model of the sensitivity and resolution of electrooptic spatial light modulators has been developed which resolves many of these previous

shortcomings, as described in detail in Section 3. In particular, the model allows examination of the mechanism involved in the resolution-enhancing "superprime" mode of operation [22].

A novel electrooptic configuration has been proposed for PROM-like devices that utilizes only transverse electric field components instead of the usual use of longitudinal field components in the traditional PROM structure [5, 6]. Such "PRIZ" (a Soviet acronym for "image transducer") structures were reported to exhibit enhanced resolution and sensitivity, as well as orientational selectivity, dc suppression, and (in a modified PRIZ device) dynamic change detection (sensitivity only to the component in the image that changes with time at greater than a threshold rate) [23, 24, 25, 26]. The sensitivity and resolution characteristics of the PRIZ-type devices have been modeled, and compared with corresponding PROM characteristics [27, 28, 29, 30, 31, 32]. This comparison revealed a strong dependence on device operating mode, input wavelength, applied bias, and integrity of the dielectric blocking layers [31, 32]. Further, significant signal-dependent phase modulation was discovered for the PRIZ geometries that does not occur in the PROM [28]. These considerations led to the discovery of a modified PRIZ configuration that promises to circumvent a number of PROM and PRIZ shortcomings [33]. Details of this new device are provided in Section 3.

The Microchannel Spatial Light Modulator [7, 8] has been developed by Prof. Cardinal Warde at the Massachusetts Institute of Technology. Fundamentally, it is an image-intensified version of the TITUS [9, 10] device, in which an electron beam is utilized to deposit spatially-modulated charge on the surface of an electrooptic crystal. The charge pattern is sensed by means of the longitudinal or transverse electrooptic effect, in direct analogy to the readout method employed for the PROM and PRIZ. In the MSLM configuration, gain is provided by a microchannel plate, which both accelerates and multiplies electrons emitted from a photocathode to result in enhanced charge deposition per incident photon. Adjustment of the gap potential between the microchannel plate and the crystal surface allows for both positive and negative writing modes, and for numerous optical processing and optical logic functions [34]. Results of a collaborative effort to further understand and improve MSLM device performance are described in the Research Program Summary.

Another exceedingly interesting electrooptic spatial light modulator is the Photorefractive Incoherent-to-Coherent Optical Converter [10, 11, 12]. This novel device

is based on volume holographic storage in photorefractive materials such as bismuth silicon oxide. In operation, an incoherently-illuminated image plane is used to selectively erase a uniform volume phase grating in the BSO crystal, resulting in a two-dimensional incoherent-to-coherent conversion. Although the write, read, and erase functions are conceptually distinct from those characterizing the PROM, many similarities in device physics exist such that contributions to understanding in one case lead naturally to useful implications in the other.

Prospective Department of Defense applications for this array of real time image storage devices are numerous. The PROM, PRIZ, MSLM, and/or the PICOC devices are expected to be particularly useful in pattern recognition (friend/foe identification, smart tracking systems, geodetic and terrestrial agricultural surveys, celestial navigation systems), feature enhancement and feature extraction, data compression prior to bandwidth-limited transmission, and optical computing (high speed algorithms for two-dimensional calculations). In addition, the real time formation of synthetic aperture radar images has recently been demonstrated utilizing an electrooptic spatial light modulator [35], which provides exceptional weight, power, size, and cost advantages over competitive all-electronic approaches. Photorefractive devices exhibit tremendous promise for real time holographic nondestructive testing [36], and for the implementation of certain classes of nonlinear functions [37] on two-dimensional images for use in feature identification and topographic analysis. Furthermore, they are envisioned as potential solutions to the problem of dynamically programmable optical interconnections for VLSI and wafer-scale integrated circuits [38, 39].

## 2. STATEMENT OF TECHNICAL OBJECTIVES

The primary objective of this research program was to develop methods of enhancing the sensitivity and resolution of Electrooptic Spatial Light Modulators such as the Pockels Readout Optical Modulator (PROM) [3, 4] and the PRIZ [5, 6]. The initial approach was to explore the utilization of sputter-deposited inorganic refractory oxide coatings of high dielectric constant, high dielectric breakdown strength, and high resistivity as dielectric blocking layers in the various devices. The potential advantage of such coatings is significantly enhanced device resolution as the dielectric constant is increased toward that of the active electrooptic crystal layer ($\epsilon$(BSO) = 56 $\epsilon_0$), and as the layer thickness is reduced (while maintaining high voltage standoff capability).

In parallel with the approach focused on dielectric blocking layer modification, a theoretical and experimental effort to determine the contribution of volume space charge redistribution effects to the sensitivity and resolution of Electrooptic Spatial Light Modulators was undertaken. It was discovered early on that the effects of charge redistribution were quite striking, and the research program was subsequently reoriented to focus primarily on device physical understanding that could be utilized to optimize the design and operation of available devices.

The principal results of these investigations are summarized in the following Section.

## 3. SUMMARY OF RESEARCH PROGRAM

As described in Section 2 (above), the completed research program was characterized by two principal efforts undertaken in order to improve the resolution and sensitivity of Electrooptic Spatial Light Modulators. The principal results are summarized in separate sections below, comprising Section 3.1, "Dielectric and Optical Properties of Sputtered Thin Films" and Section 3.2, "Fundamental Properties of Electrooptic Spatial Light Modulators".

### 3.1 DIELECTRIC AND OPTICAL PROPERTIES OF SPUTTERED THIN FILMS

The initial approach to the objective of improving the resolution and/or sensitivity of Electrooptic Spatial Light Modulators involved replacing the traditional dielectric blocking layers of the PROM (vapor deposited parylene, poly-chloro-para-xylylene) with inorganic sputter-deposited layers. The goal was to obtain new blocking layer coatings characterized by enhanced dielectric constants (of order 50), enhanced dielectric breakdown strength (to allow reduction in the layer thickness), and high volume resistivity. These coatings would provide several additional benefits as well. First, they would likely exhibit reduced scattering relative to parylene (with a concomitant enhancement in the Fourier plane signal-to-noise ratio). Second, they should exhibit improved resistance to humidity-induced dielectric breakdown (a notorious difficulty with organic coatings). Finally, the inorganic coatings should be stable under UV irradiation, and hence be free from the photodecomposition effects observed with parylene coatings.

This portion of the research program was undertaken in collaboration with a separately funded program at Itek Corporation, Lexington, Massachusetts (Sputter Deposition of Dielectric Thin Films, DAAG29-77-C-0027; Dr. Ralph E. Aldrich, Principal Investigator; Final Report: February, 1980). The collaboration was to consist of initial development of novel coatings at Itek, followed by extensive deposition parametrization and thin film characterization at USC. Due to the fact that the Itek effort was discontinued within a few months of the onset of the USC program, the desired substantive collaboration was not feasible. Nonetheless, members of Itek Optical Systems Division (notably the principal investigator, Dr. Ralph E. Aldrich) provided us with an excellent starting base, and continued to interact with our program in a significant way throughout the course of the research effort.

The first major effort undertaken was the choice of deposition technology, and

construction of an appropriate deposition facility. As outlined in detail in the original grant proposal, RF magnetron sputtering was initially chosen as a technique offering significant advantages for the deposition of inorganic refractory oxide coatings such as $SiO_2$, $TiO_2$, $HfO_2$, $Ta_2O_5$, $ZrO_2$, and others. These advantages include high deposition rates, separation of target from substrate, independent control of reactive ambient, and the relative elimination of fractionation characteristic of traditional electron beam and resistance heating techniques.

Although a system design was completed for an RF/DC multi-gun sputtering system in the first few months of the grant period, fabrication difficulties and parts shortages caused the contractor (Sloan Technology, Santa Barbara) to delay system delivery until the end of the second grant year. As a result, progress on this program aspect was delimited relative to the initial plan, which led to a substantial program redirection (as described more fully in Section 3.2 below).

The assembled system is shown schematically in Fig. 1. An all-cryogenic vacuum station was assembled to allow for the maintenance of high vacuum conditions in an organic-free environment. This consisted of a three stage cryosorb forepump manifold and a CTI-Cryogenics CTI-8 Cryopump. A UTI Mass Spectrometer with differential turbomolecular pump is used with variable orifices to allow precise determination of constituent ambient gases during pumpdown and also during deposition. An argon/oxygen ratiometer/controller is being added to allow accurate control of the reactive gas mixture during the deposition process. The sputter-deposition sources include two Sloan S-310 Sputterguns (cylindrical magnetrons that employ 3" diameter hot-pressed targets) and an L.M. Simard PLASMAX Triode Sputtergun (a planar triode for 1" diameter single crystal targets). A 3 kW RF supply and a 2 kW DC supply provide either RF (for dielectrics) or DC (for metals) power to the plasma of the S-310 guns through integrated matching network. A 500 W RF supply and matching network supplies power to the substrate planetary fixture to allow for pre-deposition substrate cleaning and bias sputtering with independent plasma control during deposition. Control electronics and an RF matching network for the PLASMAX sputtergun allow independent control of the DC plasma current drawn between an anode and cathode, and of the fraction impinging on the target.

Initial system calibration runs were performed with Al targets in the S-310 guns, resulting in extremely durable and adherent coatings that could be used for determination

# USC SPUTTER DEPOSITION/ION MILL FACILITY

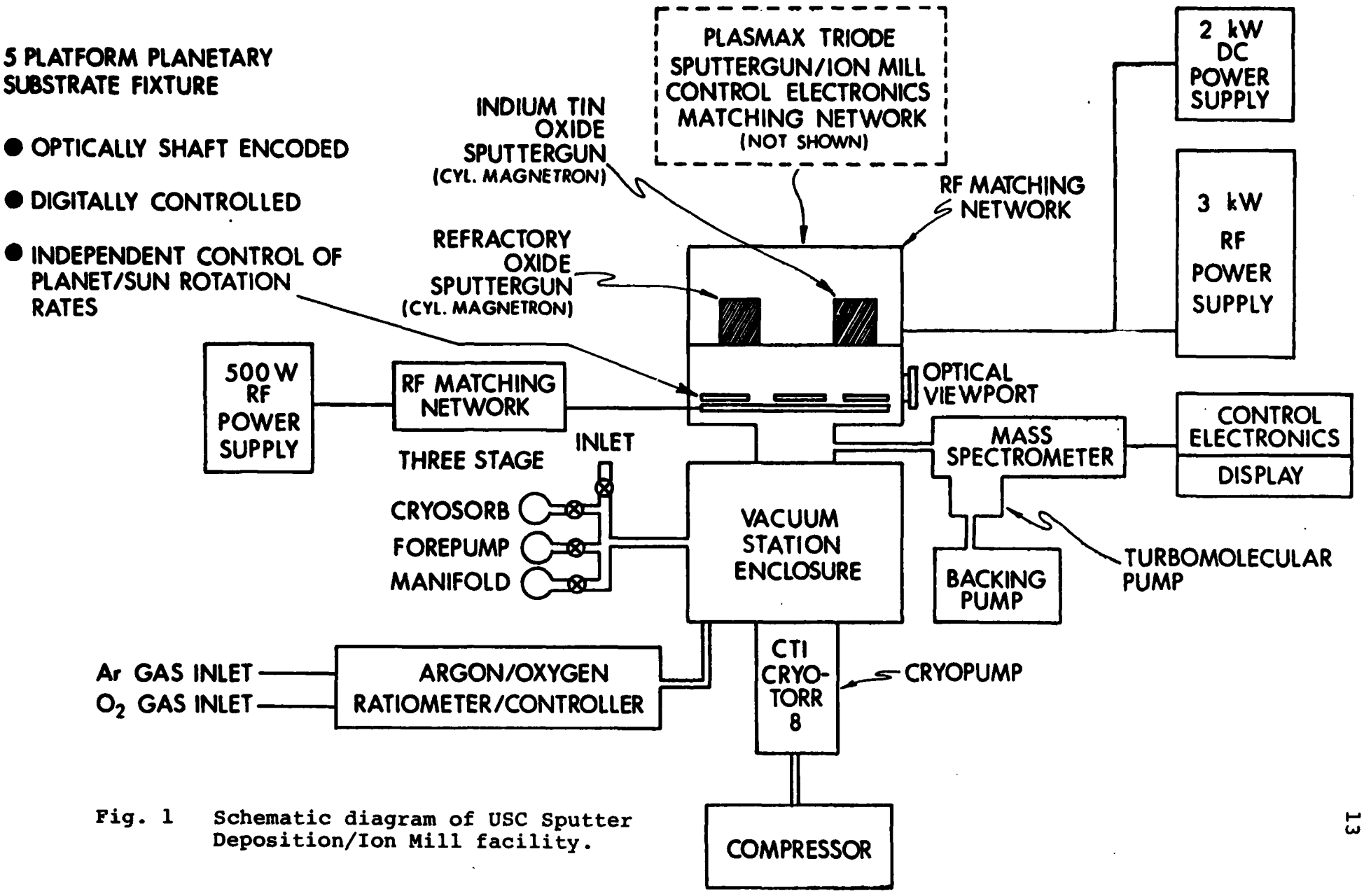


Fig. 1 Schematic diagram of USC Sputter Deposition/Ion Mill facility.

of the dependence of film thickness on source-substrate separation, and radial profiles (both stationary and under full planetary motion). It should be noted that the planetary system is unique in its capability for digital control (using an optical shaft encoder) of independent planet/sun rotation rates, fixed planetary positions, and shutter position. This allows for substantial flexibility in deposition mode selection, allowing for multilayer sequential thin film depositions on a single planet, or highly uniform deposition on a large number of substrates under full planetary motion.

Subsequent to the calibration runs, film coatings of both indium tin oxide (for transparent conductive coatings) and silicon dioxide (for transparent dielectric blocking layers) were deposited from the cylindrical magnetrons. The ITO coatings were of very high quality, provided $O_2$ was bled into the system at base pressures of approximately $10^{-4}$ - $10^{-3}$ Torr to mix with the Ar ambient. These films were utilized as transparent counterelectrodes on a wide range of PROM and PRIZ devices. The silicon dioxide coatings obtained from hot-pressed cylindrical targets (supplied by Sloan Technology) were of disappointing quality, exhibiting significant current leakage and field-bias effects (likely due to incorporated Na ions). However, silicon dioxide coatings deposited from ultra high purity quartz (semiconductor-grade furnace tubing) were of considerable interest, particularly when deposited under conditions of reverse bias sputtering. Under such conditions, significant improvements in both film resistivity and film density (as determined ellipsometrically in comparison of the index of refraction with bulk values) were observed. These results are preliminary in nature, and are under continuing investigation with support from other sources.

Characterization of as-deposited thin films is complicated and, at times, frustrating. In order to gain maximum information from each sputtered coating, we designed and constructed a computer-controlled spectroscopic ellipsometer in collaboration with Prof. Anupam Madhukar (USC Department of Materials Science), as described in detail in succeeding paragraphs. Wavelength-dispersive ellipsometry is capable of providing macroscopic (index dispersion, absorption coefficient dispersion, film thickness, real and imaginary dielectric functions, etc.) as well as microscopic (grain-size, thickness inhomogeneity, etc.) information about deposited optical coatings. Such information is vital to the development of optimized coating procedures for multi-parameter deposition techniques.

The spectroscopic ellipsometer facility comprises a laboratory containing an optical

table; the ellipsometer optics and electronics; an array-processor based computer for real time on-line data analysis, reduction, and interpretation; several terminals with associated high resolution monitors for data entry, experimental control and theoretical modeling studies; and a sample preparation area. The ellipsometer has been designed initially with several goals in mind, following the pioneering and detailed investigations of Aspnes [50]: broad wavelength region of data collection capability, high speed data collection and essentially real time data reduction and analysis, and associated interactive theoretical modeling and fitting. To this end, the initial design parameters for the ellipsometric system have included: a wavelength range of 8000 to 2000 A (1.6 eV to 6.2 eV) in a maximum of 600 steps of 2 A each, automatic integration of ellipsometric amplitude and phase measurement cycles for improved signal to noise ratio, real time Fast Fourier Transforms of the measured ac signal for rapid data accumulation and manipulation, and optimized overall accuracy in measurement of the dielectric function to 1 part in $10^3$ with a relative precision of 1 part in $10^5$.

The optical design is best described with reference to Fig. 2. A Xenon arc lamp (150 W with F/1 UV grade collimating optics) acts as the light source, and is incident on the mounted sample at an incidence angle of 70° after passage through appropriate filters (to eliminate unwanted infrared irradiation on the polarizer and sample) and a synchronously rotating Rochon prism polarizer. An aperture is employed to separate the ordinary ray from the unwanted extraordinary ray. The reflected beam is passed through a programmable angle Rochon prism analyzer, and is subsequently focused onto the entrance slit of a double pass monochromator with holographically ruled gratings. The signal beam emergent from the monochromator is detected with a high quantum efficiency photomultiplier, the output of which is current-to-voltage converted, digitized, and entered in the computer. The PMT power supply has provision for digital input so that the gain can be controlled to keep the PMT in its most linear regime regardless of the wavelength variation in light intensity from the source and variations in sample reflectance/absorbance. The rotating polarizer is optically shaft encoded to allow digitization of its rotation angle (in 256 increments) and consequent absolute phasing. A programmable shutter has been incorporated to provide automatic baseline compensation (dark current normalization) at each wavelength step, if desired. The sample is mounted on a flexible six degree of freedom sample holder that allows high orientational precision in alignment of the optical train.

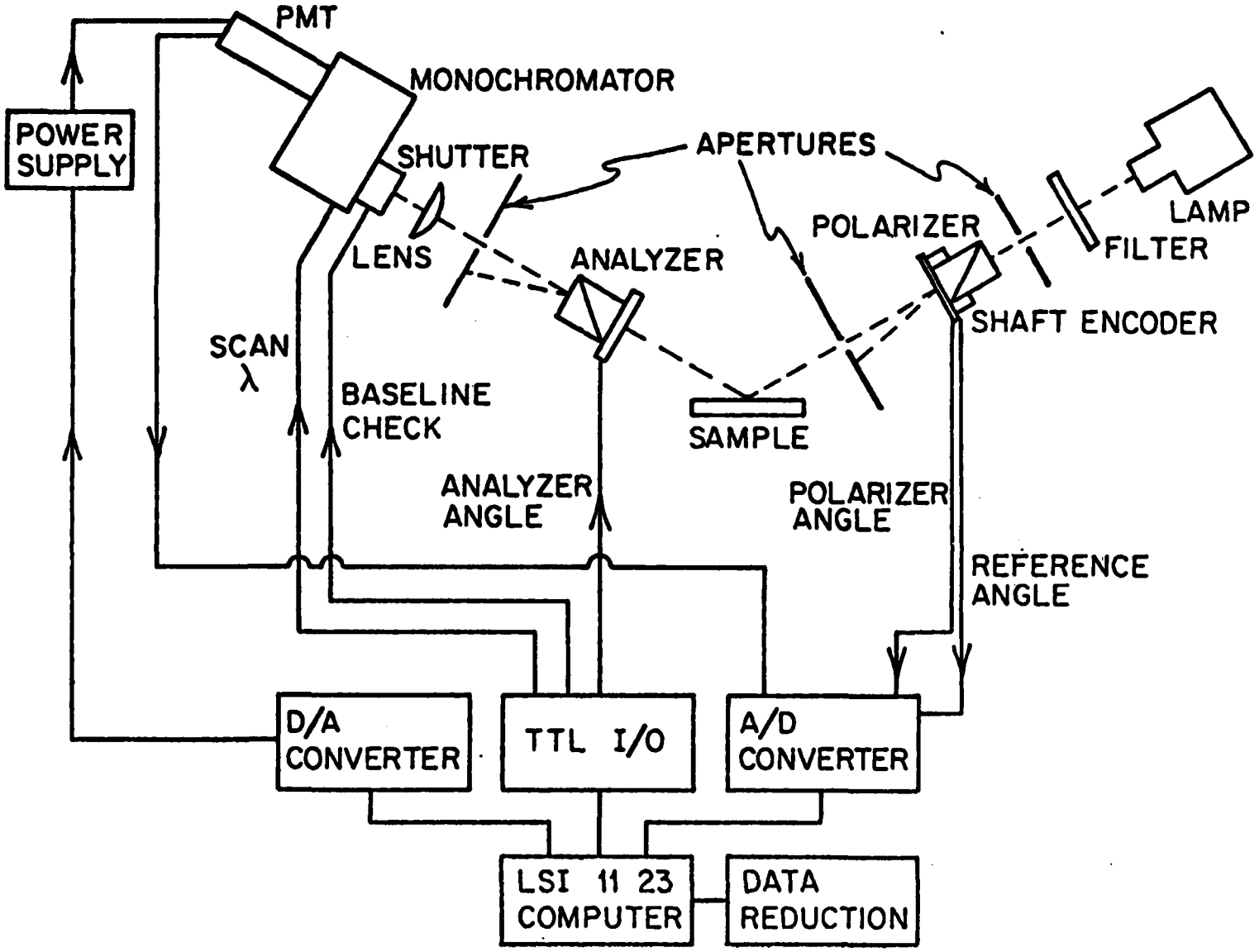


Fig. 2 Schematic diagram of USC computer-controlled spectroscopic ellipsometer facility.

Control of the apparatus, data collection, data reduction and error analysis, and theoretical modeling are implemented by means of an LSI 11/23 mainframe with associated array processor, disk drive, input/output terminals, high resolution plotter/monitors, and a line printer/point plotter. The array processor allows a 256 point discrete Fourier transform to be performed in 50 msec., following data collection and signal averaging at each wavelength.

Primary system extensions planned for the near future include capability for dry box (inert gas) sample handling and continuous inert gas overflow during measurement, an ultra-high vacuum system for research requiring atomically clean surfaces (in materials systems where adatom reactions are likely to distort the measurements), associated mass spectrometric residual gas analysis capability, provision for glow discharge cleaning of surfaces in situ prior to measurement, and extension of the wavelength region of system capability to the near infrared (1.6 eV to 0.5 eV).

At the present time, the ellipsometer is fully operational, and calibration runs are in progress. The potent combination of sputter deposition facilities and a wavelength-dispersive ellipsometer developed under this research program will provide extensive thin film deposition and analysis capabilities for a wide range of applications in optical devices. Research in these areas is continuing under separate funding.

## 3.2 FUNDAMENTAL PROPERTIES OF ELECTROOPTIC SPATIAL LIGHT MODULATORS

During the course of the research effort on sputter-deposited coatings, it was discovered that volume space charge effects within the active electrooptic crystal layer of ESLMs such as the PROM could have a demonstrably large impact on the resultant resolution and sensitivity of the devices. With the encouragement of our ARO technical monitor, Dr. Issai Lefkowitz, we redirected a substantial portion of the research effort toward the investigation of this dependence. This redirection resulted in a wide range of theoretical and experimental discoveries, as described in succeeding paragraphs.

The theoretical and experimental investigation of the factors affecting resolution and charge transfer dynamics in electrooptic spatial light modulators such as the Pockels Readout Optical Modulator (PROM) [3, 4], the PRIZ [5, 6], the Microchannel Spatial Light Modulator (MSLM) [7, 8], and the photo-DKDP [10] and electron-beam-DKDP [9, 10] image storage devices is now nearly complete. The theoretical approach to the resolution problem initially involved deriving the electrostatic field distribution from a fixed

distribution of point charges located at the interface between two dissimilar dielectrics bounded by ground planes. The electric field modulation resulting from a longitudinal distribution of charges of given transverse spatial frequency can be directly related to the exposure-dependent modulation transfer function of the device. We have obtained an analytic expression for the Fourier transform of the voltage distribution from a single point charge (which is also directly related to the modulation transfer function) for the full three layer dielectric problem, and have extended the theory to include the dependence of the voltage distribution on the point charge location within the electrooptic crystal. The resultant analytic expression contains the dielectric constants of the blocking layers and electrooptic crystal, and the thicknesses of the three layers, as well as the location of the point charge. This formulation allows the effects of charge trapping within the bulk of the electrooptic crystal to be modeled. In particular, the low spatial frequency response decreases linearly, and the high spatial frequency response decreases exponentially with the distance of the point charge from the electrooptic crystal/dielectric blocking layer interface. Thus the overall sensitivity and resolution are degraded strongly by charge storage in the bulk away from the interface.

Utilizing superposition, this formulation has been further extended to accommodate arbitrary charge distributions of significant physical interest. In particular, an iterative exposure-induced charge transfer and trapping model has been formulated to calculate the charge distribution throughout the electrooptic crystal layer resulting from optical exposure at various wavelengths. The charge distributions so obtained have been utilized to calculate the dependence of the device modulation transfer function on exposure level, exposure wavelength, device operational mode, mobility-lifetime product, and device configurational and constitutive parameters. The results indicate that very large variations in both sensitivity and resolution can result from differences in these parameters. For example, a substantial improvement in the resolution is achieved as the writing wavelength approaches the band gap of the electrooptic crystal. Such improvements are quite striking in experimental device resolution tests. In addition, it has been shown that in the limit of high spatial frequencies, the modulation transfer function decreases as the inverse square of the spatial frequency regardless of the particular shape of the charge distribution. The shape of the charge distribution does, however, influence both the device exposure sensitivity and the spatial frequency above which the modulation transfer function asymptotically approaches the inverse square dependence on spatial frequency.

Application of these results has been made to a wide variety of PROM device design cases (including both symmetric and asymmetric devices) and specialized exposure conditions (particularly x-ray [40] and electron-beam [41] sources), as well as to other types of electrooptic spatial light modulators such as the MSLM and photo-DKDP devices. Furthermore, the theoretical formulation allows investigation of possible voltage-modulated recording techniques for resolution enhancement (such as the "superprime mode" [3]), and of flash erasure sensitivity and completeness. These results have numerous implications with regard to improving electrooptic spatial light modulator device resolution [ARO Pubs. 1, 2, 3, 4, 5, 6, 10, 11, 12, 13, 14, 16, 17].

PROM-like structures have been investigated [5, 6; ARO Pubs. 3, 4, 5, 6, 12, 13, 14] that were reported to exhibit significantly enhanced resolution and sensitivity relative to traditional PROM structures. Such devices are fabricated from bismuth silicon oxide crystals oriented along <111> and <110> axes, as opposed to the usual <001> orientation. In these orientations, the longitudinal electrooptic effect does not contribute to the resultant image amplitude (as in the traditional <001> orientation). Instead, these novel configurations utilize the transverse electrooptic effect deriving from transverse fields within the bulk of the electrooptic crystal, induced by spatially varying components of the input image distribution. Since the electrooptic effect is antisymmetric under reversal of the electric field direction, transverse field contributions to the image are characterized by an antisymmetric point spread function. This implies that the device modulation transfer function will exhibit a bandpass character with no response at zero spatial frequency. This characteristic is useful in some optical processing applications requiring dc suppression. In addition, since field components in orthogonal transverse directions couple to different elements of the electrooptic tensor, the modulation transfer function will be sensitive in general to both the orientation of each spatial frequency component of the image (grating wavevector dependence) and to the polarization of the readout illumination. This orientation dependence is described in detail in ARO Pubs. 4, 5, and 6. Utilization of this effect allows for both one-dimensional and two-dimensional image reconstruction through appropriate choice of readout polarization.

We have modified our solution of the three layer dielectric problem to allow calculation of the integrated transverse potential drop (the integration is performed in the longitudinal or charge motion direction) for both point charge cases and continuous charge distributions. These calculations allow us to analyze potential PRIZ as well as

PROM device performance. The results include the dependence of the modulation transfer function on device constitutive parameters, crystallographic orientation, and dielectric anisotropy in the electrooptic crystal layer [ARO Pubs. 3, 4, 5, 6, 11, 12, 13, 14]. Numerous <111> and <110> oriented devices have been fabricated in our laboratory with vapor-deposited parylene blocking layers and RF magnetron sputtered indium tin oxide transparent conductive electrodes. Primary characterization measurements have included diffraction efficiency as a function of spatial frequency, which can easily be related to the modulation transfer function of the device. Experiments to date confirm all of the essential model predictions.

During the measurement program described above, we have established a number of new observations about transverse field effect PROMs. First and foremost, the operational mode (direction of externally applied field during the writing sequence) utilized is critically important to the optimization of device characteristics. In this respect, the <001> PROMs and <111> PRIZs show essentially opposite behavior due to significant differences in response to similarly placed volume charge distributions [ARO Pub. 3]. Hence the operational mode that optimizes <001> PROM performance is opposite from the operational mode that optimizes <111> PRIZ performance. Second, charge conservation within the photoconductive/electrooptic crystal layer in general enhances <001> PROM sensitivity, while diminishing <111> PRIZ sensitivity. Leaky parylene layers increase <111> PRIZ diffraction efficiency at the expense of device storage time. Numerous phase effects have been theoretically derived and experimentally demonstrated in the <111> PRIZ [ARO Pubs. 4, 6]. Although the longitudinal field does not contribute to the signal amplitude, it can be shown to induce a signal-dependent phase modulation that is present in concert with the transverse field-induced signal-dependent amplitude modulation. Such phase effects diminish the usefulness of the device for applications in which Fourier-plane processing is desired, as well as produce point-spread function anisotropies in the image plane in the presence of strain birefringence or imperfectly aligned polarizer/analyzer pairs.

In a collaborative effort with Professor Cardinal Warde at the Massachusetts Institute of Technology, these concepts have recently been applied to the Microchannel Spatial Light Modulator [ARO Pub. 16]. In this case, it has been shown that the 55° cut $LiNbO_3$ active layer (which optimizes the amplitude sensitivity) introduces phase nonuniformities similar to those observed in $Bi_{12}SiO_{20}$ [ARO Pubs. 4, 6]. Finally, utilization

of the exposure-induced charge transport model has allowed us to predict, and subsequently experimentally observe, striking nonlinearities in the transfer characteristics (output amplitude as a function of input exposure) of the <111> PRIZ. Such intriguing effects in <111> and <110> oriented PRIZ devices are under continuing investigation.

Quite recently, we fabricated a <111>-PRIZ-type device without blocking layers, which according to a Soviet research group [26] exhibited dynamic change detection, i.e., only that portion of the image that has recently changed appears in the output plane. On the contrary, using BSO crystals grown at USC, we found that excellent image storage characteristics were obtained in this device configuration. The advantages of this configuration are numerous: (1) the absence of dielectric blocking layers significantly enhances the measured (and theoretically predicted) resolution, as shown in Fig. 4 [33]; (2) the presence of parallel ground planes on opposite crystal surfaces ensures that the longitudinal voltage is space-invariant, which eliminates signal-dependent phase nonuniformities; (3) charge non-conservation is enhanced by allowing photo-induced electrons to reach the far electrode, which increases the device sensitivity; (4) high dielectric breakdown strength, high sensitivity blocking layers are no longer required, which eliminates a source of multiple reflections and significantly reduces the difficulty and expense of device fabrication; (5) the resolution, sensitivity, and linearity can be varied through proper choice of the device operating mode; and (5) monopolar (non-switching) power supplies can be used for device operation due to the constancy of the longitudinal applied voltage. A potential disadvantage is the accompanying reduction in image storage time, although the approximately fifteen second image decay time experimentally observed is more than adequate for a wide range of applications. This device clearly merits further intensive investigatory effort.

An experimental determination of the charge carrier dynamics under both uniform and nonuniform exposure in a PROM structure by means of transverse electrooptic imaging was undertaken to allow measurement of the appropriate exposure-induced electric field distribution function for refinements to the theoretical modulation transfer function calculations. Preliminary results suggested that the applied field distribution within the bulk of the electrooptic crystal prior to exposure is quite uniform longitudinally (as opposed to the distribution expected for the case of space-charge-limited current injection, for example). In addition, these measurements have been extended to the case of uniform exposure by fabrication of a PROM-structure 1.5 mm x 1.6 mm x 11 mm in

size. Application of the external applied field under conditions of no exposure showed several interesting effects, including charge injection through the (dielectrically imperfect) parylene blocking layer. Exposure in forward mode (illuminated electrode negative) showed charge distribution effects throughout the bulk of the device, while exposure in reverse mode (illuminated electrode positive) showed strong charge confinement near the electrode. This result confirms an independent experiment that indicated a much larger mobility-lifetime product for electrons than for holes [42]. It also confirms semi-quantitatively the predictions of the charge transport model advanced earlier. This effort is extremely important to the design of new devices with improved resolution, and to investigations of novel voltage modulated recording techniques for enhanced device performance. In addition, it appears likely that this technique will allow accurate measurements of mobility-lifetime products to be made in low mobility short lifetime electrooptic materials that are difficult to characterize otherwise. It is important to note here that this technique is currently the subject of intensive research in the Soviet Union [43, 44, 45, 46, 47, 48, 49], as applied to the case of BSO with no blocking layers under various types of optical exposure conditions. The shape of the exposure-induced longitudinal charge distributions is quite similar to those predicted by the charge transport model [29, 30].

Recently, we have discovered a new type of two-dimensional spatial light modulator that is capable of performing real-time incoherent-to-coherent image transductions with resolution and sensitivity comparable to those presently achieved with PROM and PRIZ devices [ARO Pubs. 7, 8, 9, 15]. This novel device, termed a Photorefractive Incoherent-to-Coherent Optical Converter (PICOC), is comprised of a single crystal of a photoconductive and electrooptic material such as bismuth silicon oxide with transversely deposited metal electrodes. The geometry is identical to that utilized in the photorefractive volume holographic storage experiments described above. The crystal is illuminated by two plane wave writing beams from an Argon ion laser that form a uniform diffraction grating in the photorefractive medium. An incoherent image is focused onto the crystal surface, which selectively erases the grating as a function of the local image intensity. Diffraction of a third (reading) beam from the grating results in creation of a coherent replica of the incoherent input image. In preliminary experiments, a resolution exceeding 15 line pairs/mm was achieved without extensive optimization. We have since shown that the resolution can be extended to beyond 100 line pairs/mm by a simple

wavevector matching geometry [ARO Pubs. 9, 15], and the device sensitivity can be improved by a factor of 20 by a Schlieren readout technique in the positive image mode [ARO Pub. 15].

Such a combination of volume holographic storage and spatial light modulator characteristics is unique, and suggests many novel optical processing configurations. In addition, such PICOC devices are easy to fabricate, durable, and inexpensive, all of which are potential advantages relative to currently available spatial light modulators.

Details of the above areas of investigation are given in the publications appended to this report, and in the Ph.D. thesis of Dr. Yuri Owechko [ARO Pub. 11].

## 4. PUBLICATIONS

### 4.1 Published Manuscripts (ARO Sponsorship)


1. Y. Owechko and A. R. Tanguay, Jr., "Effects of Charge Dynamics and Device Parameters on the Resolution of Electrooptic Spatial Light Modulators", Proceedings of the SPIE International Symposium, San Diego, August, 1979, 202, 110-121, (1979).

2. Y. Owechko and A. R. Tanguay, Jr., "Exposure-Induced Charge Distribution Effects on the Modulation Transfer Function (MTF) of Electrooptic Spatial Light Modulators", Proceedings of the SPIE International Symposium, Los Angeles, February, 1980, 218, 67-80, (1980).

3. A. R. Tanguay, Jr., "Spatial Light Modulators for Real Time Optical Processing", Proc. ARO Workshop on Future Directions for Optical Information Processing, 52-76, Texas Tech. Univ., Lubbock, Texas (1980), (Invited Review Paper).

4. Y. Owechko and A. R. Tanguay, Jr., "Effects of Operating Mode on Electrooptic Spatial Light Modulator Resolution and Sensitivity", Optics Letters, 7, 587-589, (1982).

5. Y. Owechko and A. R. Tanguay, Jr., "Effects of Crystallographic Orientation on Electrooptic Spatial Light Modulator Amplitude and Phase Responses", Optics Communications, 44, 239-242, (1983).

6. Y. Owechko and A. R. Tanguay, Jr., "Theoretical Resolution Limitations of Electrooptic Spatial Light Modulators. I. Fundamental Considerations", Journal of the Optical Society of America, A, 1, 635-643, (1984).

7. Y. Owechko and A. R. Tanguay,Jr., "Theoretical Resolution Limitations of Electrooptic Spatial Light Modulators. II. Effects of Crystallographic Orientation", Journal of the Optical Society of America, A, 1, 644-652, (1984).

8. Y. Shi, D. Psaltis, A. Marrakchi, and A. R. Tanguay, Jr., "Photorefractive Incoherent-to-Coherent Optical Converter", Applied Optics (Rapid Communications), 22 (23), 3665-3667 (1983).

9. J. Yu, D. Psaltis, A. Marrakchi, and A. R. Tanguay, Jr., "Photorefractive Incoherent-to-Coherent Optical Conversion", Proc. SPIE, 465, (in press, 1984).

10. A. Marrakchi, A. R. Tanguay, Jr., J. Yu, and D. Psaltis, "Photorefractive Incoherent-to-Coherent Optical Converter: Physical and Materials Considerations", Proc. SPIE, 465, (in press, 1984).

11. Y. Owechko, "Effects of Charge Transport and Crystallographic Orientation on Electrooptic Spatial Light Modulator Resolution and Sensitivity", Ph.D. Thesis, University of Southern California, May, 1983.

12. Y. Owechko and A. R. Tanguay, Jr., "Theoretical Resolution Limitations of Electrooptic Spatial Light Modulators. III. Effects of Continuous Charge Distributions", in preparation for Journal of the Optical Society of America.

13. Y. Owechko and A. R. Tanguay, Jr., "Theoretical Resolution Limitations of Electrooptic Spatial Light Modulators. IV. Effects of Device Operational Mode", in preparation for Journal of the Optical Society of America.

14. Y. Owechko and A. R. Tanguay, Jr., "Theoretical Resolution Limitations of Electrooptic Spatial Light Modulators. V. Effects of Dielectric Anisotropy", in preparation for Journal of the Optical Society of America.

15. A. Marrakchi, A. R. Tanguay, Jr., D. Psaltis, and J. Yu, "Photorefractive Incoherent-to-Coherent Optical Conversion", to be published in a Special Issue of Optical Engineering, January 1985, (Invited Paper).

16. Y. Owechko, A. R. Tanguay, Jr., and C.A. Warde, "Effects of Crystallographic Orientation on Microchannel Spatial Light Modulator Amplitude and Phase Response", in preparation for Optics Communications, (1984).

17. A. R. Tanguay, Jr., "Materials Considerations for Optical Processing and Computing Devices", in preparation for Optical Engineering, Special Issue on Optical Computing, January, 1985 (Invited Review Paper).

**4.2 Conference Presentations (ARO Sponsorship)**

1. Y. Owechko and A. R. Tanguay, Jr. "Effects of Charge Dynamics and Device Parameters on the Resolution of Electrooptic Spatial Light Modulators", SPIE International Symposium, San Diego, August (1979).

2. Y. Owechko and A. R. Tanguay, Jr., "Exposure-Induced Charge Distribution Effects on the Modulation Transfer Function (MTF) of Electrooptic Light Modulators", SPIE International Symposium, Los Angeles, February (1980).

3. Y. Owechko and A. R. Tanguay, Jr., "Theoretical Resolution Limitations of Electrooptic Spatial Light Modulators", 1979 Annual Meeting of the Optical Society of America, Rochester, N.Y., (1979).

4. A. R. Tanguay, Jr., "Spatial Light Modulators for Real Time Optical Processing", ARO Workshop on Future Directions for Optical Information Processing, Lubbock, Texas, May (1980) (Invited Paper).

5. A. R. Tanguay, Jr., "Progress in Pockels Readout Optical Modulators and Variable Grating Mode Liquid Crystal Devices", U.S. Army Research Office, Durham, North Carolina, May (1980).

6. Y. Owechko and A. R. Tanguay, Jr., "Modulation Transfer Function Model for Electrooptic Spatial Light Modulators", 1980 Annual Meeting of the Optical Society of America, Chicago, Illinois, (1980).

7. A. R. Tanguay, Jr., "Real-Time Spatial Light Modulators for Coherent Optical Processing Applications", Second SPSE Symposium on Optical Data Display, Processing, and Storage, Las Vegas, Nevada, (1981), (Invited Paper).

8. Y. Owechko and A. R. Tanguay, Jr., "Exposure-Induced Charge Transport Model of Electrooptic Spatial Light Modulator Sensitivity", 1981 Annual Meeting of the Optical Society of America, Orlando, Florida, (1981).

9. Y. Owechko and A. R. Tanguay, Jr., "Electrooptic Spatial Light Modulators: Effects of Operational Mode and Crystallographic Orientation", 1981 Annual Meeting of the Optical Society of America, Orlando, Florida, (1981).

10. A. R. Tanguay, Jr., "Information Processing and Holography", Invited Panel Member, 1981 Annual Meeting of the Optical Society of America, Orlando, Florida, (1981).

11. A. R. Tanguay, Jr., "Materials Considerations for Electrooptic Spatial Light Modulators", American Vacuum Society Annual Meeting, Anaheim, (March, 1982) (Invited Paper).

12. A. R. Tanguay, Jr "Recent Advances in Spatial Light Modulators for Coherent Optical Processing Applications", Conference on Lasers and Electro-Optics

(CLEO), Phoenix, Arizona, (May, 1982) (Invited Paper).

13. A. R. Tanguay, Jr., "Recent Progress in Spatial Light Modulators for Coherent Optical Processing Applications", Gordon Research Conference on Optical Information Processing and Holography, Plymouth, New Hampshire, (June, 1982) (Invited Paper).

14. A. R. Tanguay, Jr., "Polarization Properties of Birefringent Phase Gratings", Gordon Research Conference on Optical Information Processing and Holography, Plymouth, New Hampshire, (June, 1982) (Invited Paper).

15. A. R. Tanguay, Jr., "Single Crystal and Thin Film Electrooptic Materials: Characterization for Optical Device Applications", DARPA Materials Research Council Symposium, La Jolla, California, (July, 1982) (Invited Paper).

16. A. R. Tanguay, Jr. and Y. Owechko, "Materials Considerations for Electrooptic Spatial Light Modulators", 1982 Annual Meeting of the Optical Society of America, Tucson, Arizona, (1982).

17. Y. Owechko and A. R. Tanguay, Jr., "Imaging Properties of the PRIZ Electrooptic Spatial Light Modulators", 1982 Annual Meeting of the Optical Society of America, Tucson, Arizona, (1982).

18. A. R. Tanguay, Jr., "Polarization Properties of Birefringent Phase Gratings", 1982 Annual Meeting of the Optical Society of America, Tucson, Arizona, (1982).

19. Y. Owechko and A. R. Tanguay, Jr., "Fundamental and Materials Limitations of Electrooptic Spatial Light Modulators", SPIE International Symposium, Los Angeles, California, (1983), (Invited Paper).

20. D. Psaltis, A. R. Tanguay, Jr., J. Yu, and A. Marrakchi, "Photorefractive Incoherent-to-Coherent Optical Converter: A Novel Spatial Light Modulator", SPIE International Symposium, Los Angeles, California, (1984), (Invited Paper).

21. A. R. Tanguay, Jr., D. Psaltis, A. Marrakchi, and J. Yu, "Photorefractive Incoherent-to-Coherent Optical Converter: Physical and Materials Considerations", SPIE International Symposium, Los Angeles, California, (1984), (Invited Paper).

22. A. R. Tanguay, Jr., "Materials Considerations for Optical Processing and Computing Devices", SPIE International Symposium Critical Review: Optical Computing, Los Angeles, California, (1984), (Invited Paper).

23. A. R. Tanguay, Jr., "Materials Requirements for Optical Processing and Computing Devices: Electrooptics", NSF Workshop on "The Future of Lightwave Technology", Los Angeles, California, (1984), (Invited Paper).

24. A. R. Tanguay, Jr., "Electrooptic Spatial Light Modulation", Gordon Research

Conference on Optical Information Processing and Holography, Plymouth, New Hampshire, (1984), (Invited Paper).

## 5. SCIENTIFIC PERSONNEL

The following scientific personnel contributed to the research summarized in this report, and were either supported in part by the U. S. Army Research Office or were supported in part by the University of Southern California through cost-sharing.

1. Professor Armand R. Tanguay, Jr., Principal Investigator
2. Yuri Owechko, Graduate Research Assistant
3. Abdellatif Marrakchi, Graduate Research Assistant
4. Frank Lum, Senior Research Technician

During the course of the research program, the following degree was awarded:

1. Yuri Owechko, Ph.D. in Materials Science, May, 1983, Thesis: "Effects of Charge Transport and Crystallographic Orientation on Electrooptic Spatial Light Modulator Resolution and Sensitivity".

## 6. REFERENCES


1. A. R. Tanguay, Jr., "Spatial Light Modulators for Real Time Optical Processing", Proc. ARO Workshop on Future Directions for Optical Information Processing, Texas Tech University, Lubbock, Texas, (1980).

2. D. Casasent, "Spatial Light Modulators", Proc. IEEE, 65, 143-157, (1978).

3. B. A. Horwitz and F. J. Corbett, "The PROM--Theory and Applications for the Pockels Readout Optical Modulator", Opt. Eng., 17, 353-364, (1978).

4. G. J. M. Aitken and R. Balaberda, "Evaluation of PROM Characteristics", Appl. Opt., 23, 901-904, (1984).

5. M. P. Petrov, V. I. Marakhonov, M. G. Shlyagin, A. V. Khomenko, and M. V. Krasin'kova, "Use of PRIZ Spatial Modulator for Information Processing", Sov. Tech. Phys. Lett., 25, 752-753, (1980).

6. A. A. Berezhnoi, "Anisotropic Image Recording in Bismuth Silicate Crystals", Sov. Tech. Phys. Lett., 6, 494-496, (1980).

7. C. Warde, A. D. Fisher, D. M. Cocco, and M. Y. Burmawi, "Microchannel Spatial Light Modulator", Opt. Lett., 3, 196-198, (1978).

8. C. Warde, A. M. Weiss, A. D. Fisher, and J. I. Thackara, "Optical Information Processing Characteristics of the Microchannel Spatial Light Modulator", Appl. Opt., 20, 2066-2074, (1981).

9. G. Marie, J. Donjon, and J. P. Hazan, "Pockels Effect Imaging Devices and Their Applications", in Advances in Image Pickup and Display, Vol. 1, B. Kazan, Ed., Academic Press, New York, (1974), pp. 255-302.

10. D. Casasent, S. Natu, T. Luu, G. Lebreton, and E. DeBalzelaire, "New Birefringence Theory and the Uses of the Photo-DKDP Spatial Light Modulator in Optical Processing", Proc. SPIE, 202, 122-131, (1980).

11. Y. Shi, D. Psaltis, A. Marrakchi, and A. R. Tanguay, Jr., "Photorefractive Incoherent-to-Coherent Optical Converter", Appl. Opt. (Rapid Communications), 22, 3665-3667, (1983).

12. D. Psaltis, J. Yu, A. Marrakchi, and A. R. Tanguay, Jr., "Photorefractive Incoherent-to-Coherent Optical Conversion", Proc. SPIE, 465, (in press), (1984).

13. A. Marrakchi, A. R. Tanguay, Jr., J. Yu, and D. Psaltis, "Photorefractive Incoherent-to-Coherent Optical Converter: Physical and Materials Considerations", Proc. SPIE, 465, (in press), (1984).

14. J. P. Huignard and F. Micheron, "High Sensitivity Read-Write Volume

Holographic Storage in $Bi_{12}SiO_{20}$ and $Bi_{12}GeO_{20}$ Crystals", Appl. Phys. Lett., 29, 591-593, (1976).

15. G. C. Valley and M. B. Klein, "Optimal Properties of Photorefractive Materials for Optical Data Processing", Opt. Eng., 22, 704-711, (1983).

16. J. P. Huignard and J. P. Herriau, "Real-Time Double-Exposure Interferometry with $Bi_{12}SiO_{20}$ Crystals in Transverse Electrooptic Configuration", Appl. Opt., 16, 1807-1809, (1977).

17. A. A. Ballman, H. Brown, P. K. Tien, and R. J. Martin, "The Growth of Single Crystalline Waveguiding Thin Films of Piezoelectric Sillenites", J. Cryst. Growth, 20, 251-255, (1973).

18. J. C. Brice and R. G. Pratt, "Bismuth Silicon Oxide: A Useful Material for Acoustic Surface Wave Filters", IEE Colloquium on Metals for Pyroelectric Materials and Applications, London, (1975).

19. W. R. Roach, "Resolution of Electrooptic Light Valves", IEEE Trans. Elec. Dev., ED-21, 453-459, (1974).

20. J. Donjon, M. Decaesteker, B. Monod, and K. Petit, "Spatial Resolution of Optical Relays Using the Pockels' Effect", Acta Elec., 18, 187, (1975).

21. R. A. Sprague, "Effect of Bulk Carriers on PROM Sensitivity", J. Appl. Phys., 46, 1673, (1975).

22. B. Horwitz and R. Aldrich, Itek Corporation, Lexington, Massachusetts, Private Communication.

23. M. P. Petrov, A. V. Khomenko, M. V. Krasin'kova, V. I. Marakhonov, and M. G. Shlyagin, "The PRIZ Image Converter and its Use in Optical Data Processing Systems", Sov. Phys. Tech. Phys., 26, 816-821, (1981).

24. D. Casasent, F. Caimi, and A. Khomenko, "Soviet PRIZ Spatial Light Modulator", Appl. Opt., 20, 3090-3092, (1981).

25. D. Casasent, F. Caimi, M. P. Petrov, and A. V. Khomenko, "Applications of the PRIZ Light Modulator", Appl. Opt., 21, 3846-3854, (1982).

26. V. V. Bryskin, L. I. Korovin, M. P. Petrov, and A. V. Khomenko, "Theory of Dynamic Image Selection in Photorefractive Media", Sov. Phys. Sol. State, 24, 193-196, (1982).

27. Y. Owechko and A. R. Tanguay, Jr., "Theoretical Resolution Limitations of Electrooptic Spatial Light Modulators. I. Fundamental Considerations", J. Opt. Soc. Am. A, 1, 635-643, (1984).

28. Y. Owechko and A. R. Tanguay, Jr., "Theoretical Resolution Limitations of Electrooptic Spatial Light Modulators. II. Effects of Crystallographic Orientation", J. Opt. Soc. Am. A, 1, 644-652, (1984).

29. Y. Owechko and A. R. Tanguay, Jr., "Theoretical Resolution Limitations of Electrooptic Spatial Light Modulators. III. Effects of Continuous Charge Distributions", *in preparation for Journal of the Optical Society of America*, (1984).

30. Y. Owechko and A. R. Tanguay, Jr., "Theoretical Resolution Limitations of Electrooptic Spatial Light Modulators. IV. Effects of Device Operating Mode", in preparation for Journal of the Optical Society of America, (1984).

31. Y. Owechko and A. R. Tanguay, Jr., "Effects of Operating Mode on Electrooptic Spatial Light Modulator Resolution and Sensitivity", Opt. Lett., 7, 587-589, (1982).

32. Y. Owechko and A. R. Tanguay, Jr., "Effects of Crystallographic Orientation on Electrooptic Spatial Light Modulator Amplitude and Phase Responses", Opt. Comm., 44, 239-242, (1983).

33. Y. Owechko and A. R. Tanguay, Jr., "Enhanced Resolution and Sensitivity of Transverse Electrooptic Spatial Light Modulators", in preparation for Optics Letters, (1984).

34. C. Warde and J. Thackara, "Operating Modes of the Microchannel Spatial Light Modulator", Opt. Eng., 22, 695-703, (1983).

35. I. Abramov, Y. Owechko, and A. R. Tanguay, Jr., "Synthetic Aperture Radar Image Formation Utilizing an Electrooptic Spatial Light Modulator", Proc. NASA Spaceborne Imaging Radar Symposium, Jet Propulsion Laboratory, Pasadena, California, (1983).

36. J. AuYeung and A. R. Tanguay, Jr., "Photorefractive Materials for Real Time Holographic Nondestructive Testing Applications", International Conference on *the Applications of Lasers and Electro-Optics* '83 (ICALEO), Laser Institute of America, Los Angeles, California, (1983).

37. D. M. Pepper, J. AuYeung, D. Fekete, and A. Yariv, "Spatial Convolution and Correlation of Optical Fields Via Degenerate Four-Wave Mixing", Opt. Lett., 3, 7-9, (1978).

38. A. A. Sawchuk, "Digital Logic and Computing With Optics", Proc. SPIE, 456, (in press), (1984); also Proc. IEEE, July, (1984).

39. J. W. Goodman, F. J. Leonberger, S.-Y. Kung, and R. A. Athale, "Optical Interconnections for VLSI Systems", Proc. IEEE, July, (1984) (in press).

40. G. J. Berzins and M. Graser, Jr., "Response of a $Bi_{12}SiO_{20}$ Pockels Readout Optical Modulator to X-Rays", Appl. Phys. Lett., 34, 500-502, (1979).

41. J. C. H. Spence and A. Olsen, "Use of Pockels Readout Optical Modulator (PROMs) for Atomic Resolution Electron Image Processing", Proc. SPIE, 218, 154-160, (1980).

42. R. E. Aldrich, S. L. Hou, and M. L. Harvill, "Electrical and Optical Properties of $Bi_{12}SiO_{20}$", J. Appl. Phys., 42, 493, (1971).

43. V. V. Bryskin, L. I. Korovin, V. I. Marakhonov, and A. V. Khomenko, "Initial Stage in the Redistribution of Photoinduced Charges and Electric Fields in $Bi_{12}SiO_{20}$", Sov. Phys. Sol. State, 24, 1686-1689, (1982).

44. V. N. Astratov and A. V. Il'inskii, "Direct Investigation of the Electric Field Distribution in a $Bi_{12}GeO_{20}$ Crystal With the Aid of the Transverse Electrooptic Effect", Sov. Phys. Sol. State, 24, 61-64, (1982).

45. V. V. Bryskin, L. I. Korovin, and V. I. Marakhonov, "Effect of Light Absorption on the Electric Field Distribution in $Bi_{12}SiO_{20}$", Sov. Phys. Tech. Phys., 9, 686-9, (1983).

46. V. V. Bryksin and L. I. Korovin, "Dynamics of the Distribution of Optically Induced Charges and Electric Fields in Crystals", Sov. Phys. Sol. State, 24, 1159-1162, (1982).

47. I. T. Ovchinnikov and E. V. Yanshin, "Space-Charge Production During Optical Recording in a $Bi_{12}GeO_{20}$ Crystal", Sov. Tech. Phys. Lett., 8, 153-155, (1982).

48. V. V. Bryksin, L. I. Korovin, M. P. Petrov, and A. V. Khomenko, "Dynamics of Optical Image Formation in Crystals With the Aid of the Internal Transverse Pockels Effect, Sov. Phys. Sol. State, 24, 82-86, (1982).

49. M. P. Petrov, "Electrooptic Photosensitive Media for Image Recording and Processing", Current Trends in Optics, F. T. Arecchi and F. R. Aussenegg, Eds., Taylor and Francis, London, (1981).

50. D. E. Aspnes, J. Opt. Soc. Am., 70, 1275 (1980).

# APPENDIX I

## Effects of charge dynamics and device parameters on the resolution of electrooptic spatial light modulators

Y. Owechko, A. R. Tanguay, Jr.
Departments of Electrical Engineering and Materials Science
University of Southern California
University Park, Los Angeles, California 90007

### Abstract

The theoretical resolution of an electrooptic spatial light modulator [such as the Pockels Readout Optical Modulator (PROM)] is a function of the electrostatic field distribution arising from stored point charges located within the active electrooptic crystal layer. The Fourier transform of the voltage distribution (which can be directly related to the modulation transfer function) is derived as a function of the charge location within the electrooptic crystal. In addition, the resultant analytic expression contains the dielectric constants of the blocking layers and electrooptic crystal, and the thicknesses of the three layers. This formulation allows the effects of charge trapping within the bulk of the electrooptic crystal to be modeled. In particular, the low spatial frequency response decreases linearly and the high spatial frequency response decreases exponentially with the distance of the point charge from the dielectric blocking layer/electrooptic crystal interface. Thus the overall sensitivity and resolution are degraded strongly by charge storage in the bulk away from the interface. Utilizing superposition, this formulation can be readily extended to accommodate arbitrary charge distributions arising from different exposure parameters. The implications of these results for device design and operation are discussed.

### I. Introduction

Several electrooptic spatial light modulators (ESLM's) have been investigated for numerous applications in coherent optical signal processing, including the Pockels Readout Optical Modulator (PROM) (1), TITUS (2), PHOTOTITUS (3), and the Microchannel Spatial Light Modulator (MSLM) (4). Such devices record two-dimensional image information in the form of a charge pattern which modulates the voltage across an active (electrooptic) single crystal layer. The charge pattern is typically induced either by intensity modulation of light incident on a photoconductive layer, or by direct electron beam charge deposition. More recently, image storage in ESLM's has been accomplished by exposure to x-ray sources (5) and by high energy electron beam charge implantation (6). In each case, the image-wise modulated voltage is sensed using polarized light by means of the linear electrooptic effect.

One extremely important parameter in the characterization of candidate spatial light modulators is the limiting resolution attainable with each such device. In addition, the shape of the modulation transfer function (MTF) strongly influences the resultant image fidelity, and consequently limits the accuracy of subsequent optical processing algorithms. The resolution of an electrooptic spatial light modulator is in general determined by the field spreading within the electrooptic crystal layer. The electric field distribution is a function of the dielectric constants and thicknesses of the dielectric blocking layers and electrooptic crystal layer, and of the charge distribution within the electrooptic crystal.

A method for calculating the sine wave response of a multi-layered structure due to the impulse response of a point charge was developed by Krittman (7), who applied the method to electrostatic storage targets. Schaffert (8) has performed related work on electrostatic images with emphasis on applications to the xerographic developing process. Roach (9) derived an expression for the modulation transfer function of electrooptic light valves consisting of an isotropic dielectric layer and a dielectrically anisotropic electrooptic crystal sandwiched between two transparent conducting electrodes, for the case of a sinusoidal modulation in charge density introduced at the dielectric layer/electrooptic crystal interface. These previous analyses of resolution effects in multi-layered electrostatic structures share a common limitation, in that each model constrains the charge distribution to lie at the interface between a dielectric layer and the electrooptic crystal. Due to the nature of the charge pattern generating process in numerous applications of ESLM's, however (notably in the cases of the PROM and MSLM, and for the recent applications of x-ray exposure and high energy electron beam excitation), the resultant charge distribution is known to reside within the bulk of the electrooptic

crystal layer. A complete treatment of resolution in electrooptic spatial light modulators, therefore, must include the effects of exposure-induced longitudinal charge distributions in addition to the geometric and constitutive properties of the layer structure.

## II. Theoretical development

In order to simplify the theoretical treatment of resolution in electrooptic spatial light modulators, the Pockels Readout Optical Modulator (PROM) will be employed as a specific example, since the dielectric constant of the electrooptic crystal is isotropic. Extension of this analysis to other ESLM's (such as the TITUS device) with anisotropic electrooptic layers is relatively straightforward (9). A schematic diagram of a typical PROM structure is shown in Figure 1. The device is comprised of a photoconductive electrooptic crystal ($Bi_{12}SiO_{20}$) sandwiched between two thin dielectric blocking layers. The blocking layers are coated with transparent electrodes.

In the simplest mode of PROM operation, a voltage (typically 2000V) is applied to the electrodes, dividing between the three layers in inverse proportion to the capacitance of each layer. Since the electrooptic crystal is also photoconductive, illumination from the negative electrode side with image-wise modulated blue light causes electron-hole pair generation at a rate proportional to the incident intensity at each location. The generated charges then separate in the applied field (by electron drift into the bulk, since holes are relatively immobile in $Bi_{12}SiO_{20}$) giving rise to a reduction in voltage across the electrooptic crystal in illuminated regions. Since in the absence of illumination (subsequent to the writing process) the dielectric relaxation time ($\tau_{\varepsilon,0}$) of bismuth silicon oxide is unusually large (of order several thousand seconds), the electron distribution is trapped in the bulk; hence, the written charge pattern is stored. The resultant two dimensional voltage distribution induces a birefringence (through the linear longitudinal electrooptic effect) which alters the polarization of linearly polarized readout light oriented to bisect the principal birefringent axes, producing an image-wise modulated amplitude when viewed through a crossed analyzer. The readout amplitude transmitted through a PROM between ideal crossed polarizers may be expressed as

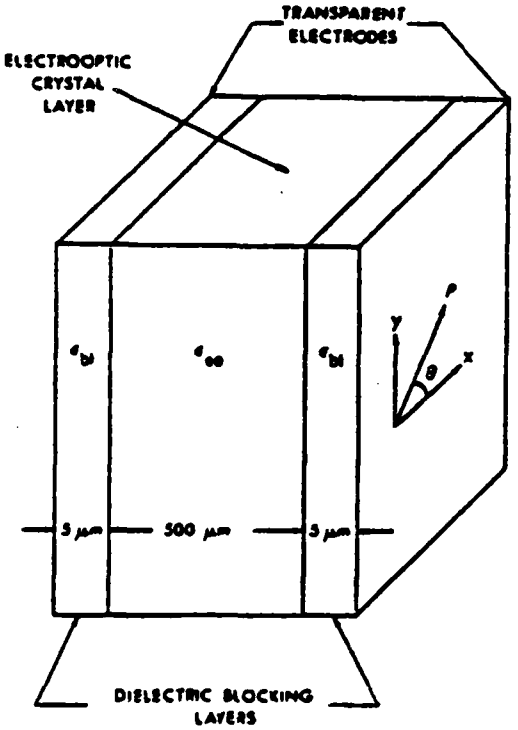


Figure 1. Structure of a typical PROM. In current PROM's, the electrooptic crystal layer is bismuth silicon oxide ($Bi_{12}SiO_{20}$, $\varepsilon_{eo} = 56\varepsilon_0$) and the dielectric blocking layers are parylene C ($\varepsilon_{bl} = 3\varepsilon_0$). The transverse coordinate system used in the derivation of V(ω) is also shown.

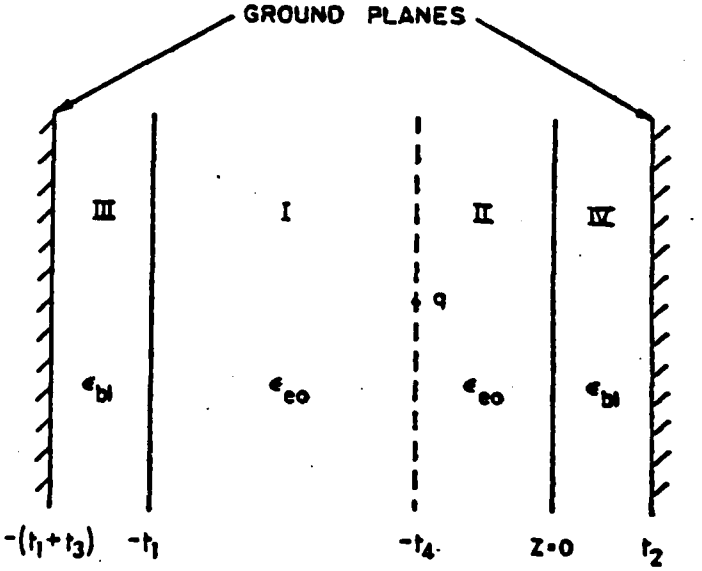


Figure 2. Longitudinal coordinate system used in the derivation of V(ω) (see Appendix I). The position of the point charge within the electrooptic crystal layer is at $z = -t_4$, while $t_1$, $t_2$, and $t_3$ are the electrooptic crystal thickness and dielectric blocking layer thicknesses, respectively.

$$A(x,y) = \frac{A_0}{\sqrt{2}} \sin\left(\frac{\pi V(x,y)}{2V_{\lambda/2}}\right) \tag{1}$$

where $A_0$ is the incident readout light amplitude, $V_{\lambda/2}$ is the half-wave voltage of the electrooptic crystal, and $V(x,y)$ is the voltage across the electrooptic crystal at image coordinates $(x,y)$. It should be noted that in the above expression it is assumed that the readout wavelength and intensity are chosen such that insignificant photoconductive charge redistribution occurs, and that the effects of natural optical activity in the bismuth silicon oxide crystal may be neglected (10,11). Thus the output amplitude is a monotonic function of the input intensity (for applied voltage less than the electrooptic half-wave voltage); such a transfer relationship is desirable for incoherent-to-coherent conversion and subsequent coherent optical signal processing operations.

From the nature of Eq. (1), it can be seen that the resolution of an electrooptic spatial light modulator depends directly on the relationship between a periodic (spatial frequency $\omega$) variation in the writing intensity, and the resultant spatial modulation of the voltage across the electrooptic crystal. The cubic symmetry (I23) of bismuth silicon oxide in conjunction with the orientation of the electrooptic crystal slice (<001>) assures that only longitudinal components of the electric field contribute to the induced birefringence through the electrooptic effect (12). Therefore, the modulation in output amplitude [see Eq. (1)] depends only on the voltage difference $V(x,y)$ between opposite sides of the electrooptic crystal at each image point $(x,y)$. In the absence of significant two-dimensional diffusion effects in comparison with the drift-aided charge separation of photogenerated electron-hole pairs (13), $V(x,y)$ will be a function of the dielectric constants and thicknesses of the electrooptic and blocking layers, the locations (in the z-direction) of the trapped hole and electron distributions resulting from the writing (image recording) process, and the spatial frequency of the charge (writing intensity) modulation in the $(x,y)$ plane. In summary, we seek to derive the dependence of each Fourier component of $V(x,y)$ (denoted $V(\omega)$) on the corresponding Fourier component of the lateral charge distribution, as a function of the device parameters and the longitudinal charge distribution.

If the longitudinal charge distribution is assumed to be such that charges are constrained to the blocking layer/electrooptic crystal interfaces, the spatial frequency dependence of the potential $V(\omega)$ may be obtained by straightforward solution (9) of the electrostatic boundary conditions with a surface charge $\sigma(x,y,z)$ given by:

$$\sigma(x,y,z) = \sigma_0[1+\cos\omega x]\delta(z). \tag{2}$$

Since the absorption coefficient of the writing light is not infinite, and since in addition the drift length of a photoexcited electron is significantly smaller than the typical electrooptic layer thickness, consideration of charge distributions within the bulk of the electrooptic crystal is necessary in order to formulate a realistic resolution model.

Consider a single point charge q located at $(x,y,z)=(0,0,-t_4)$ within the electrooptic crystal layer as shown schematically in Figure 2. Determination of the Fourier components of the potential difference $V(\omega)$ due to such a point charge is equivalent to calculation of the potential difference due to a periodic charge distribution given by

$$\sigma(x,y,z) = \sigma_0[1+\cos\omega x]\delta(z+t_4) \tag{3}$$

as a function of spatial frequency $\omega$(12). This approach has the advantage that once the solution for a single point charge has been obtained, the inherent linearity of the Fourier transform may be utilized to solve multiple charge cases by summation of single charge solutions, and continuous charge distribution cases by simple integration.

The axial symmetry of the problem can be exploited by transformation to cylindrical coordinates $(\rho,\theta,z)$ where $(\rho,\theta)$ are in the $(x,y)$ plane and z is the longitudinal coordinate, as shown in Figure 1. Since the problem is invariant with respect to the angular coordinate $\theta$, the rectilinear two-dimensional Fourier transformation becomes a Hankel transform. The voltage across the electrooptic crystal can then be written in the form:

$$V(\rho) \equiv V(\rho,-t_1)-V(\rho,0) = \frac{1}{2\pi}\int_0^\infty V(\omega)J_0(\omega\rho)\,\omega\,d\omega \tag{4}$$

where $J_0(\omega\rho)$ is the zeroth order Bessel function and $\omega$ is a radial spatial frequency (14). Expressing $V(\omega)$ as a Hankel transform leads to a striking simplification of the calculation, since the Hankel transform of the delta function charge distribution (point

charge is a constant. Hence the difficulties associated with discontinuities in the real space boundary conditions due to charge singularities are automatically removed in Fourier space.

The real space potential difference V(ρ) must satisfy Laplace's equation in all four regions depicted in Figure 2, and must also satisfy the boundary conditions at both electrodes, at both electrooptic crystal/blocking layer interfaces, and at the plane defined by the location of the point charge ($z=-t_4$). Once V(ω) is determined, V(ρ) is easily found by extracting the kernel of the Hankel transform, as shown explicitly in Appendix I, with the following result:

$$V(\rho) = \frac{q}{\varepsilon_{eo}\omega}\left\{\frac{\sinh\omega(a-t_1)}{\cosh\omega(a-t_4)\left[1-\frac{\coth\omega(b-t_4)}{\coth\omega(a-t_4)}\right]}+\frac{\sinh\omega b}{\cosh\omega(b-t_4)\left[1-\frac{\coth\omega(a-t_4)}{\coth\omega(b-t_4)}\right]}\right\} \tag{5}$$

where

$$a = t_1 + \frac{1}{\omega}\coth^{-1}\left(\frac{\varepsilon_{bl}}{\varepsilon_{eo}}\coth\omega t_3\right) \tag{6}$$

and

$$b = \frac{1}{\omega}\coth^{-1}\left(\frac{\varepsilon_{bl}}{\varepsilon_{eo}}\coth(-\omega t_2)\right) \tag{7}$$

Note that as desired, V(ω) is a function of the electrooptic crystal thickness $t_1$, the dielectric blocking layer thicknesses $t_2$ and $t_3$, the dielectric constants $\varepsilon_{ec}$ and $\varepsilon_{bl}$ of the respective layers, as well as on the location of the point charge $t_4$. In this calculation, the electrodes are both assumed to be grounded.

In the special case $t_1=t_4$, and $t_2=0$, the problem reduces to that of a charge pattern confined to the electrooptic crystal/dielectric layer interface of a two layer device, with

$$V(\omega) = \frac{q/\omega}{\varepsilon_{eo}\coth\omega t_1 + \varepsilon_{bl}\coth\omega t_3} \tag{8}$$

in agreement with the solution for this case derived previously (9).

The modulation transfer function (MTF) relating the output image modulation to the input image modulation may be obtained from the expression (9):

$$MTF = \frac{1}{m}\left[\frac{I_{max} - I_{min}}{I_{max} + I_{min}}\right] \tag{9}$$

where

$$I_{out} = \frac{I_0}{2}\sin^2\left[\frac{\pi V(0)}{2V_{\lambda/2}}\left\{1 + m\frac{V(\omega)}{V(0)}\cos\omega x\right\}\right] \tag{10}$$

and where m is the spatial modulation of the imposed charge distribution, $V_{\lambda/2}$ is the electrooptic crystal half-wave voltage, and $V(0) \equiv V(\omega=0)$. Physically, V(0) is the average value of the potential difference across the electrooptic crystal layer. In Eq. (9), $I_{max}$ and $I_{min}$ are the values of $I_{out}$ for $\cos\omega x=1$ and $\cos\omega x=-1$, respectively. From Eq. (10), it can be seen that the character of the solution for each case is fully expressed by V(ω) or V(ω)/V(0). Since the MTF for a given device will be both exposure [V(0)] and modulation (m) dependent, a more fundamental indication of expected device performance is obtained by presentation and discussion of the un-normalized [V(ρ)] and normalized [V(ω)/V(0)] potential difference functions.

Before proceeding to a detailed presentation and interpretation of the results, it should be pointed out that the un-normalized potential differences V(ρ) and the normalized functions V(ρ)/V(0) have a direct interpretation useful for both comparison of distinct devices of different constitutive characteristics, and for comparison of the implications of distinct charge distributions within a given device. In particular, graphs of V(ρ) as a function of ω parametrized by different device constitutive properties assume equal

exposure conditions (identical charge distributions), while graphs of $V(\omega)/V(0)$ assume optimum exposure conditions for each compared device (i.e. sufficient exposure for each device such that $V(\omega)$ is optimized in the limit of low spatial frequencies). These types of comparisons are familiar from the case of photographic film, where the typical resolution/sensitivity trade-off forces a similar comparison of film properties on the basis of either response to equal exposure, or response to optimum exposure.

## III. Features of the solution for discrete charge distributions

The nature of the spatial frequency dependence of the potential difference $V(\omega)$ can be more easily appreciated if the high and low spatial frequency responses are examined. These limiting forms are given by:

$$[V(\omega)]_{\omega \to 0} = q\left[\frac{t_4(t_2+t_3)-t_1t_2}{\epsilon_{bl}(t_2+t_3)+\epsilon_{eo}t_1}\right] \tag{11}$$

$$[V(\omega)]_{\omega \to \infty} = \frac{q}{(\epsilon_{bl}+\epsilon_{eo})\omega}\left[e^{-\omega\Delta_1}-e^{-\omega\Delta_2}\right] \tag{12}$$

where $\Delta_1=t_1-t_4$ and $\Delta_2=t_4$. The parameters $\Delta_1$ and $\Delta_2$ represent the distance of the point charge from each dielectric blocking layer/electrooptic crystal interface.

From Eq. (11), it is apparent that the low spatial frequency limit of $V(\omega)$ depends on the layer thicknesses and dielectric constants, as well as on the charge location. In particular, if we consider the case of a symmetric device (i.e. a device with two identical blocking layers), $V(\omega)$ decreases linearly to zero and then increases to its initial value as the charge moves from one interface to the other. This is intuitively appealing since no voltage drop is expected across the electrooptic crystal for a point charge in the center of a symmetric device. The low frequency response is in addition independent of spatial frequency.

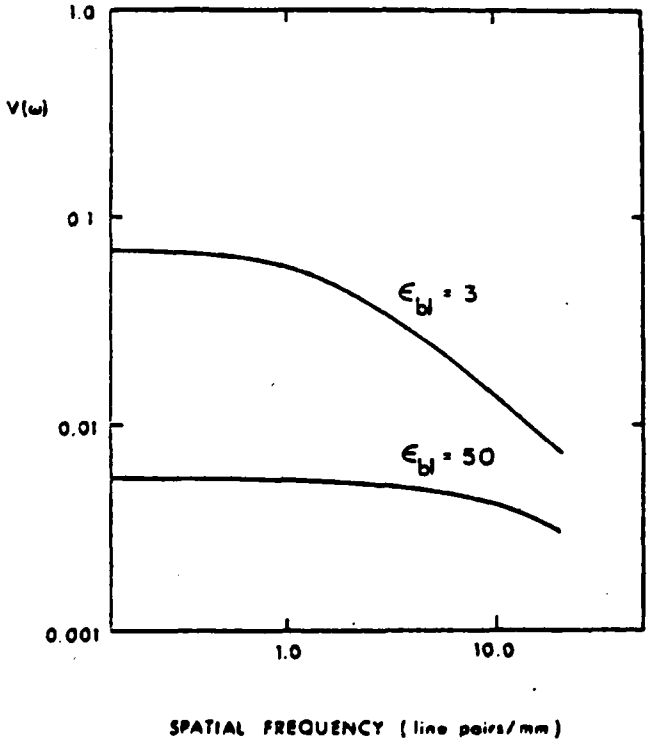


Figure 3. Effect of dielectric blocking layer dielectric constant on the spatial frequency response of $V(\omega)$. A symmetric PROM device is assumed, with geometric and constitutive parameters as shown in Figure 1. The vertical scale is arbitrary, but is the same for Figures 3,5,7, and 9.

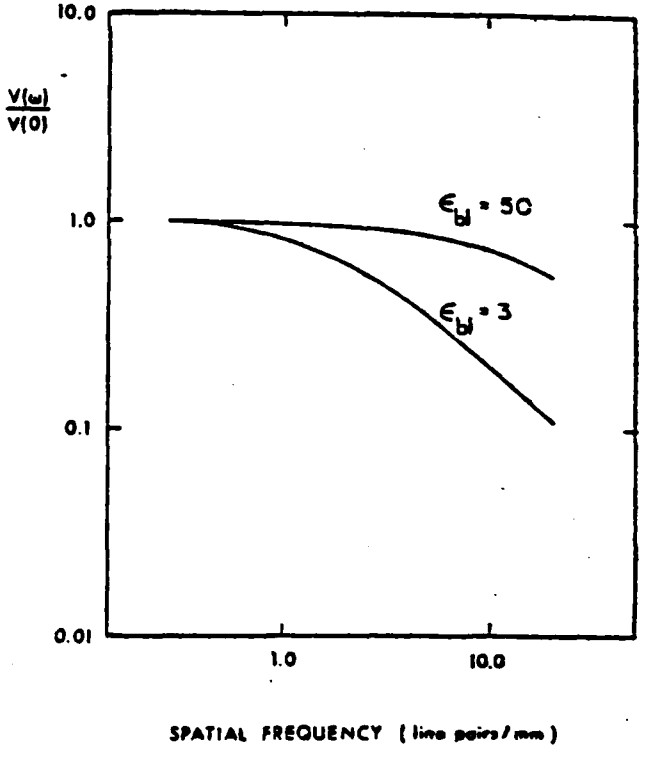


Figure 4. Effect of dielectric blocking layer dielectric constant on the spatial frequency response of $V(\omega)/V(0)$.

The high frequency limiting form of $V(\omega)$ given in Eq. (12) is a function only of the dielectric constants of the layers, the spatial frequency, and the distances of the charge from each of the blocking layer/crystal interfaces. If the point charge resides on either interface, $V(\omega)$ falls off inversely with increasing spatial frequency. For even small separations of the charge from either interface, however, the high spatial frequencies will be exponentially attenuated. Note that as in the low spatial frequency case, $V(\omega)$ is zero when the charge is in the center of the device.

The dependence of $V(\omega)$ and $V(\omega)/V(0)$ on the dielectric constant of the blocking layers (assumed identical) is shown in Figures 3 and 4, respectively. The effect of increasing the blocking layer dielectric constant is seen to reduce the device sensitivity (see Figure 3), while increasing the high spatial frequency response for optimum exposure in both cases (see Figure 4).

The dependence of $V(\omega)$ and $V(\omega)/V(0)$ on the thickness of the blocking layers is shown in Figures 5 and 6, respectively. The effect of decreasing the blocking layer thickness reduces the device sensitivity (see Figure 5) but improves the relative response at high spatial frequencies (see Figure 6). In Figures 3-6, a single point charge is located at one of the dielectric blocking layer/electrooptic crystal interfaces.

The solutions for cases involving multiple point charges can be obtained by a linear superposition of the solutions for each separate point charge. In particular, the effect of an electron-hole pair can be modeled if the point charges are assigned opposite signs. The results of such a calculation as a function of the charge separation are shown in Figures 7 and 8. In this calculation, the hole and electron were assumed initially constrained to opposite interfaces, and were subsequently displaced symmetrically into the bulk of the electrooptic crystal layer. In Figures 7 and 8, each curve is labeled by the positions of each point charge according to the following convention: the electrooptic crystal layer is 500 μm thick and the coordinate pairs labeling each curve are the z coordinates of each of the two point charges. Thus (0,500) represents a positive charge at the $z = -500$ μm interface and a negative charge at the $z = 0$ μm interface. The device parameters are those of the typical PROM configuration shown in Figure 1. From Figure 7, it is observed that displacement of the point charges away from the dielectric blocking layer/electrooptic crystal interfaces strongly degrades the high spatial frequency response, and in addition reduces the sensitivity at low spatial frequencies. The

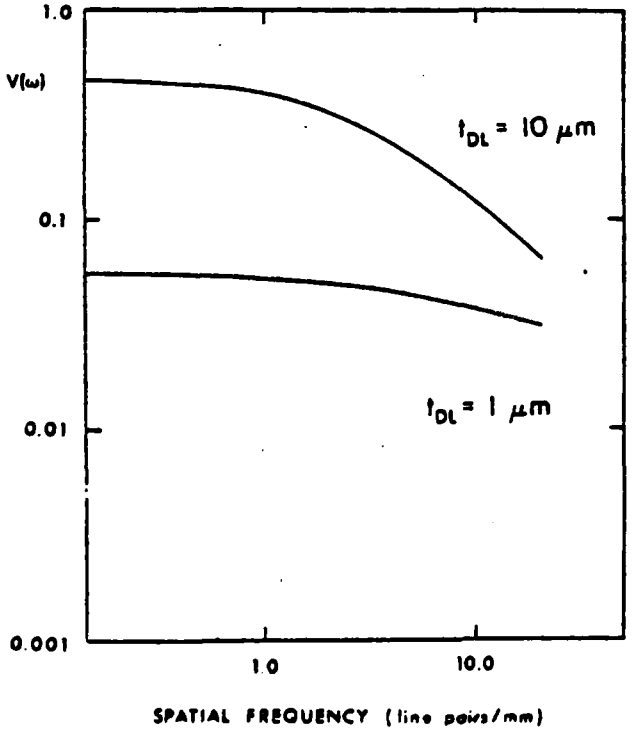


Figure 5. Effect of dielectric blocking layer thickness on the spatial frequency response of $V(\omega)$. The dielectric constant of the blocking layer is $\varepsilon_{bl} = 10\varepsilon_0$.

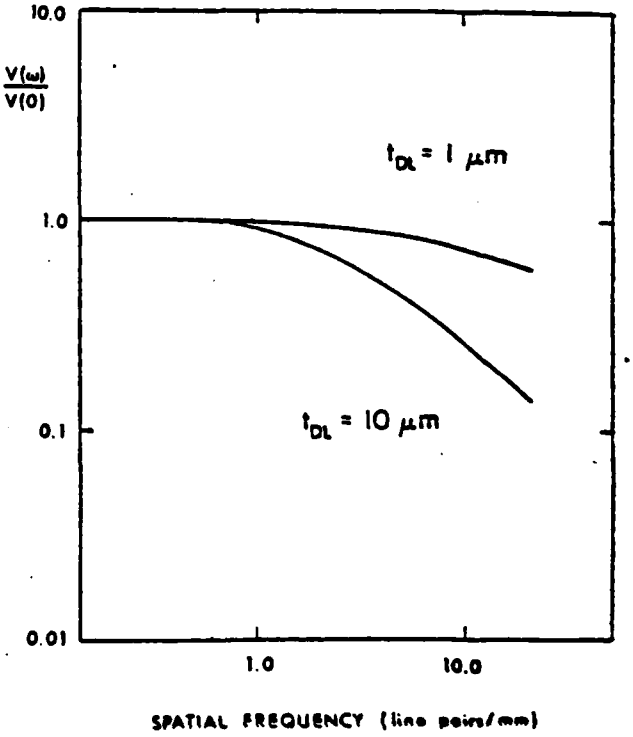


Figure 6. Effect of dielectric blocking layer thickness on the spatial frequency response of $V(\omega)/V(0)$.

exponential modification of the high spatial frequency behavior is shown more clearly in the graphs of $V(\omega)/V(0)$ shown in Figure 8. Due to the assumption of a symmetric device configuration in this calculation, it should be noted that charges of opposite sign symmetrically placed on opposite sides of the electrooptic crystal layer contribute equally to the total potential. Thus the results shown in Figure 8 for the dual charge calculation are equally applicable to the case of a single charge of appropriate sign placed at the same distances from either interface (i.e. 0, 50 and 100 μm).

The effects of asymmetric charge location within a symmetric PROM device are shown in Figures 9 and 10. A positive point charge is located at one dielectric blocking layer/electrooptic crystal interface ($z = -500$ μm), and a negative point charge is placed at varying distances from the opposite interface ($z = 0$ μm). This configuration models a hypothetical writing process in which the incident illumination is characterized by a large absorption coefficient so that the (immobile) hole distribution is constrained to one interface, while the electron distribution is forced into the bulk electrooptic layer by the applied field. The resultant charge separation will thus be a function of the constitutive device properties and the voltage across the device during the writing cycle. The resultant $V(\omega)$ curve for the case of the negative charge at the opposite interface (labeled "(0)" in Figure 9) is exactly the same as the (0,500) case discussed with respect to Figure 7. As the negative charge is moved in from the interface toward the center of the crystal, the response at high spatial frequencies decreases more rapidly at first than the response at low spatial frequencies. As the negative charge reaches the center of the electrooptic crystal layer ($z = -250$ μm) and continues to approach the positive charge, the response at low spatial frequencies decreases faster than the reduction in high spatial frequency response. For both charges in the same half of the electrooptic crystal, the response characteristic becomes nonmonotonic, as can be seen in Figure 9 and even more graphically in Figure 10.

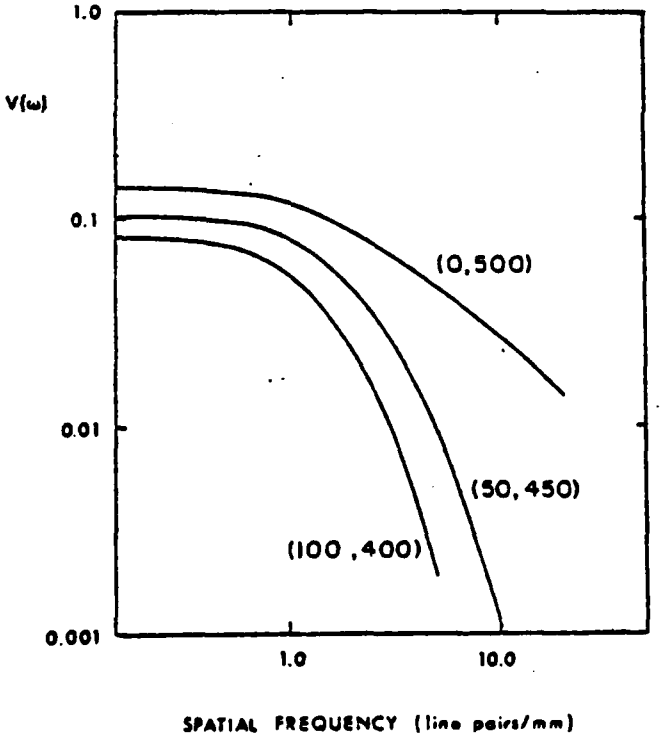


Figure 7. Effect of longitudinal charge position within the electrooptic crystal layer on the spatial frequency response of $V(\omega)$. In each case, two point charges of opposite sign are symmetrically placed relative to the center of the device. Each curve is labeled by the distance in μm of the (negative, positive) charge from the electrooptic crystal/dielectric blocking layer interface at $z = 0$μm.

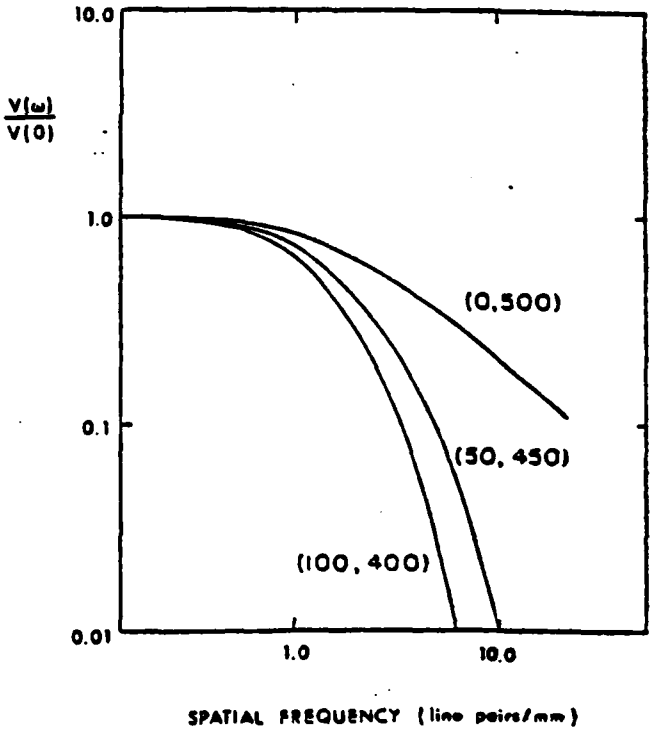


Figure 8. Effect of longitudinal charge position within the electrooptic crystal layer on the spatial frequency response of $V(\omega)/V(0)$. Note the marked attenuation of the high spatial frequency response as the charges are increasingly displaced from their respective interfaces.

This remarkable nonmonotonic behavior of the spatial frequency response can be explained with the aid of Figure 11, which details the contributions of each charge to the total potential. In Figure 11(a), the signs and magnitudes of the potential contributions from both charges are positive, and the resultant potential has the same response characteristic as that of a single charge positioned at an interface. In Figure 11(b), the negative charge is 125 μm (one quarter of the electrooptic crystal thickness) from the interface, and hence contributes a reduced low spatial frequency response and an exponentially attenuated high spatial frequency response. At the center of the crystal, the negative charge does not contribute to the potential due to symmetry, and the form of the frequency response is the same as that for a single point charge at an interface [as shown in Figure 11(c)]. The most interesting case is shown in Figure 11(d), in which the charge separation is one quarter of the electrooptic crystal thickness. Here the contributions to the total potential from both charges have opposite signs. This situation is equivalent to taking the difference between the V(ω) curves for two positive charges at the same locations, as shown in the Figure. The nonmonotonic behavior is thus seen to arise directly from the exponential attenuation of the high spatial frequency components of the potential due to the negative charge.

## IV. Device implications

The dependence of the spatial frequency response on the dielectric constants and thicknesses of the dielectric blocking layers (as shown in Figures 3-6) indicates that new PROM devices can be envisioned with modulation transfer functions constant to much higher spatial frequencies than are characteristic of presently available devices. Gains in MTF behavior due to choice of dielectric blocking layer properties will be accompanied by an overall reduction in device sensitivity. Such new devices, however, would provide significantly improved image fidelity and resolution in applications where requirements on device sensitivity can be relaxed, similar to the familiar tradeoff in the case of photographic film. In order to improve PROM resolution, high dielectric constant, high dielectric breakdown strength, high resistivity dielectric blocking layers are required.

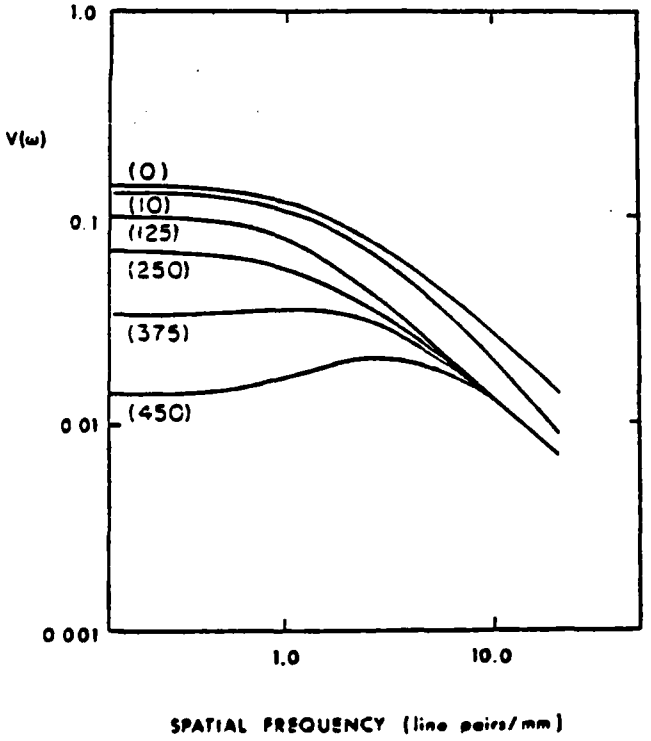


Figure 9. Effect of asymmetric charge locations on the spatial frequency response of V(ω). A positive charge is located at the z= -500μm electrooptic crystal/dielectric blocking layer interface. Each curve is labeled by the distance in μm of a negative charge from the electrooptic crystal/dielectric blocking layer interface at z= 0μm.

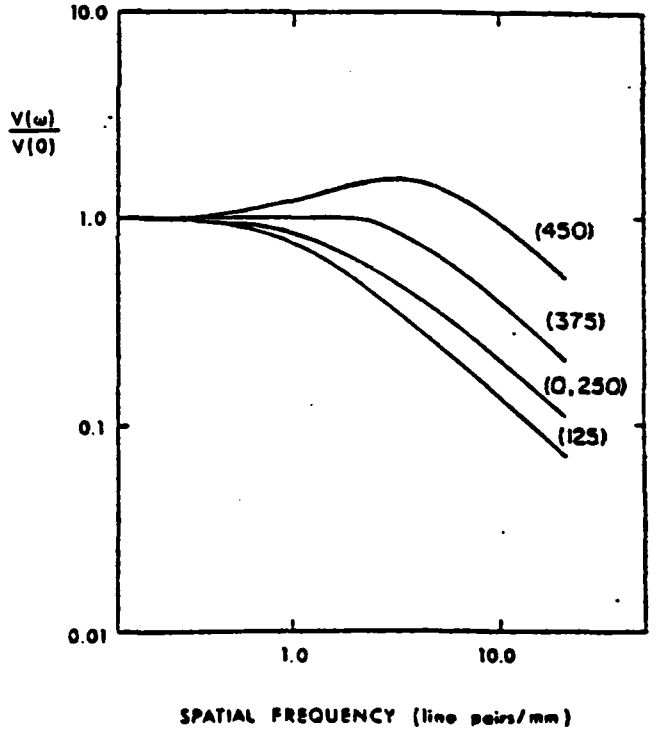


Figure 10. Effect of asymmetric charge locations on the spatial frequency response of V(ω)/V(0). Note the nonmonotonic behavior of V(ω)/V(0) when both charges are in the same half of the electrooptic crystal. The curves for the negative charge at z= 0μm and z= -250μm are identical.

The effect of exposure-induced charge distribution throughout the bulk of the electrooptic crystal layer is seen to have an adverse effect on the high spatial frequency response characteristics of the image storage process. The optimum resolution and sensitivity within a given PROM device structure are obtained when the hole distribution is constrained to the interface nearest the negative electrode, and the entire electron distribution is swept to the interface nearest the positive electrode during the writing cycle. The actual resolution and sensitivity obtained for a given device are thus strongly dependent on the absorption coefficient of the electrooptic layer at the writing illumination wavelength, on the external applied voltage and voltage division between the multiple layers during the writing cycle, and on the mobility-lifetime product of photogenerated electrons in the electrooptic crystal. Such bulk charge distribution effects will also strongly affect the resolution and sensitivity for cases where the image-wise modulated charge pattern is induced by high energy electron beam (6) and x-ray (5) sources.

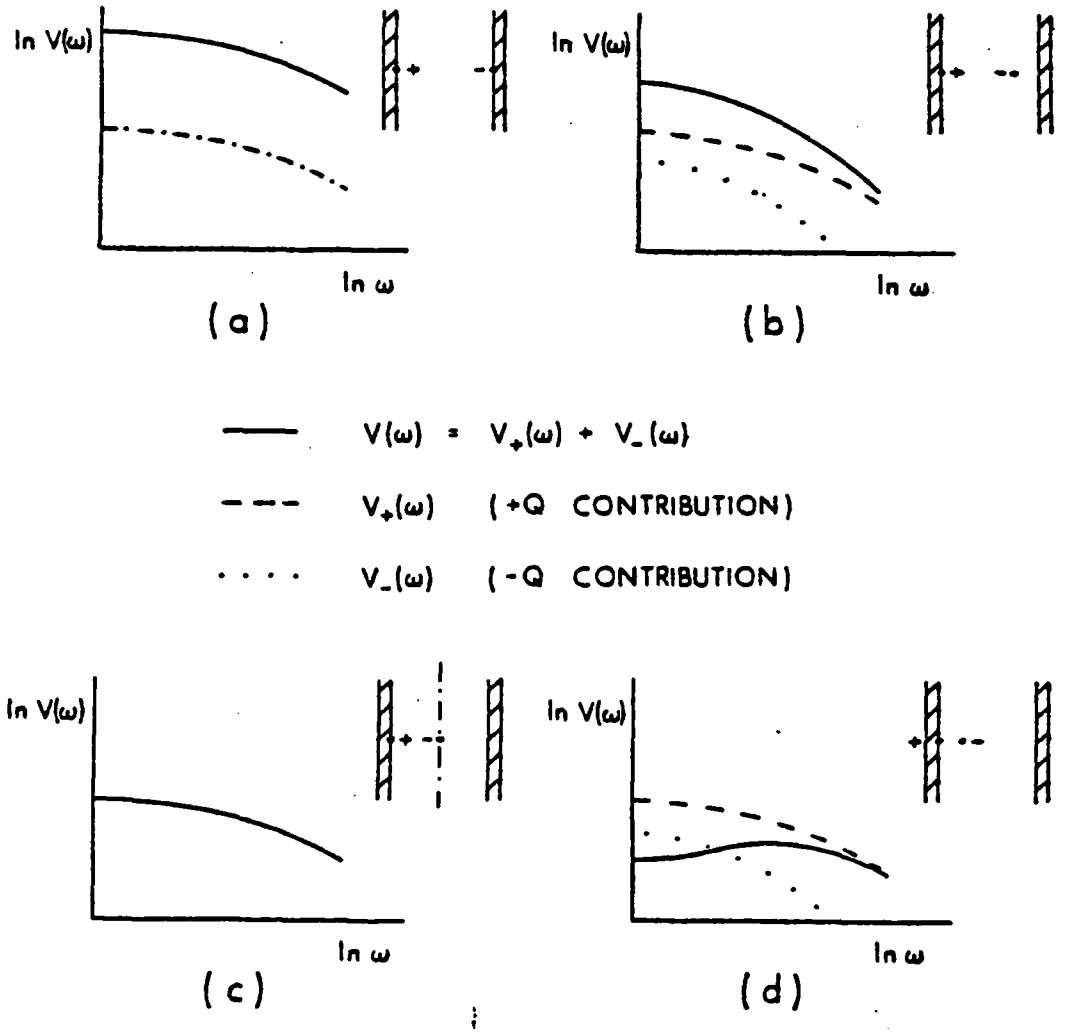


Figure 11. Schematic explanation of the effect of asymmetric charge locations on the spatial frequency response of $V(\omega)$ and $V(\omega)/V(0)$. (a) Both charges are at their respective interfaces; thus $V_+(\omega) = V_-(\omega)$, and the total $V(\omega)$ is simply twice the potential difference expected for a single point charge ($V(\omega) = 2V_+(\omega)$). (b) Here the negative charge is displaced from the interface, exponentially attenuating the high spatial frequency response of $V_-(\omega)$. The sum of the terms due to each charge thus decreases monotonically, with diminished high spatial frequency response relative to case (a) (see Figure 10). (c) The negative charge is placed at the center of the symmetric PROM. Hence, it does not contribute to $V(\omega)$ and $V(\omega) = V_+(\omega)$. (d) The negative charge is in the same half of the crystal as the positive charge; the total $V(\omega)$ can be obtained by taking the difference between $V_+(\omega)$ and $-V_-(\omega)$, since $V_+(\omega)$ and $V_-(\omega)$ have opposite signs. Since $V_+(\omega)$ and $V_-(\omega)$ decrease at unequal rates, $V(\omega)$ no longer decreases monotonically.

## V. Summary

A generalized expression for the spatial frequency response of a three layer electrooptic spatial light modulator is presented, which gives explicitly the dependence of the response on the thicknesses and dielectric constants of the layers, and on an arbitrary longitudinal charge position within the electrooptic crystal layer. This solution is applied specifically to the case of the Pockels Readout Optical Modulator (PROM), wherein the importance of the inclusion of bulk charge distribution effects is clearly demonstrated. Extension of these results to cases involving continuous longitudinal charge distributions in order to model specific device operational modes and writing cycle parameters is straightforward due to the inherent linearity of the Fourier (Hankel) transform (12,15). Application to other ESLM's with anisotropic electrooptic materials exhibits device geometric, constitutive, and charge distribution effects similar to those described herein (15). Research on the implications of including two-dimensional charge diffusion effects during the writing process is currently in progress.

## Appendix I: Derivation of $V(\omega)$ for a three layer device

The device geometry is as shown in Figures 1 and 2. The dielectric constants of the blocking layers are assumed equal ($\varepsilon_{b1}$), and the thicknesses of the layers are given by $t_2$ and $t_3$. The dielectric constant of the electrooptic crystal layer is denoted $\varepsilon_{eo}$, and the thickness of the layer by $t_1$. A single point charge q is placed within the electrooptic crystal a distance $t_4$ from the dielectric blocking layer/electrooptic crystal interface as shown in Figure 2. Transparent electrodes are placed in the planes $z=t_2$ and $z=-(t_1+t_3)$, at the external boundaries of the dielectric blocking layers; both electrodes are assumed grounded during readout.

The cylindrical symmetry of the problem about the z-axis is utilized by expressing the potential within the layers in cylindrical coordinates as a Hankel transform:

$$V(\rho,\theta,z) = V(\rho,z) = \frac{1}{2\pi}\int_0^\infty V(\omega,z)J_0(\omega\rho)\omega d\omega \tag{1}$$

The potential within any of the four regions shown in Figure 2 automatically satisfies Laplace's equation if it is written in the form:

$$V(\rho,z) = \int_0^\infty G(\omega)e^{\pm\omega z}J_0(\omega\rho)\,d\omega \tag{2}$$

The potential in each of the four regions may then be expressed explicitly as:

$$\text{I.}\quad V_I(\rho,z) = \int_0^\infty A_1(\omega)\sinh\omega(z+a)J_0(\omega\rho)\,d\omega \tag{3}$$

$$\text{II.}\quad V_{II}(\rho,z) = \int_0^\infty A_2(\omega)\sinh\omega(z-b)J_0(\omega\rho)\,d\omega \tag{4}$$

$$\text{III.}\quad V_{III}(\rho,z) = \int_0^\infty A_3(\omega)\sinh\omega(z+t_1+t_3)J_0(\omega\rho)\,d\omega \tag{5}$$

$$\text{IV.}\quad V_{IV}(\rho,z) = \int_0^\infty A_4(\omega)\sinh\omega(z-t_2)J_0(\omega\rho)\,d\omega \tag{6}$$

This form insures that the potential in regions III and IV is zero at the $z=-(t_1+t_3)$ and $z=t_2$ ground planes. The parameters a and b correspond to imaginary ground planes at $z=-a$ and $z=-b$, and are determined below from the application of appropriate boundary conditions.

The boundary conditions are:

$$V(-t_1^+) = V(-t_1^-) \tag{7}$$

$$-\varepsilon_{eo}\frac{\partial V(-t_1^+)}{\partial z} + \varepsilon_{b1}\frac{\partial V(-t_1^-)}{\partial z} = 0 \tag{8}$$

$$V(-t_4^+) = V(-t_4^-) \tag{9}$$

$$V(0^+) = V(0^-) \tag{10}$$

$$-\varepsilon_{b1}\frac{\partial V(0^+)}{\partial z} + \varepsilon_{eo}\frac{\partial V(0^-)}{\partial z} = 0 \tag{11}$$

$$-\frac{\partial V(-t_4^+)}{\partial z} + \frac{\partial V(-t_4^-)}{\partial z} = \frac{\sigma_0}{\varepsilon_{eo}} \tag{12}$$

where $\sigma_0$, the charge density at $z=-t_4$, is given by:

$$\sigma_0 = \frac{q\delta(\rho)}{2\pi\rho} = \frac{q}{2\pi}\int_0^\infty J_0(\omega\rho)\omega d\omega \tag{13}$$

and $\delta(\rho)$ is the unit impulse function. Application of the boundary conditions by direct substitution of Eqs. (3)-(6) into Eqs. (7)-(13) yields:

$$A_1(\omega) = \frac{q}{2\pi\varepsilon_{eo}}\left[\cosh\omega(a-t_4)\left\{1-\frac{\coth\omega(b-t_4)}{\coth\omega(a-t_4)}\right\}\right]^{-1} \tag{14}$$

$$A_2(\omega) = \frac{q}{2\pi\varepsilon_{eo}}\left[\cosh\omega(b-t_4)\left\{\frac{\coth\omega(a-t_4)}{\coth\omega(b-t_4)}-1\right\}\right]^{-1} \tag{15}$$

where a and b are given by:

$$a = t_1 + \frac{1}{\omega}\coth^{-1}\left(\frac{\varepsilon_{b1}}{\varepsilon_{eo}}\coth\omega t_3\right) \tag{16}$$

$$b = \frac{1}{\omega}\coth^{-1}\left(\frac{\varepsilon_{b1}}{\varepsilon_{eo}}\coth(-\omega t_2)\right) \tag{17}$$

The voltage across the electrooptic crystal is given by:

$$V_{eo}(\rho) = V_I(\rho,-t_1) - V_{II}(\rho,0) \tag{18}$$

Writing $V_{eo}(\rho)$ as a Hankel transform (as in Eq. (1)) and substituting Eqs. (3), (4), (14)-(17) into Eq. (18), we obtain the final expression for the spatial frequency dependence of the potential difference across the electrooptic crystal layer:

$$V(\omega) = \frac{q}{\varepsilon_{eo}\omega}\left\{\frac{\sinh\omega(a-t_1)}{\cosh\omega(a-t_4)\left[1-\frac{\coth\omega(b-t_4)}{\coth\omega(a-t_4)}\right]} + \frac{\sinh\omega b}{\cosh\omega(b-t_4)\left[1-\frac{\coth\omega(a-t_4)}{\coth\omega(b-t_4)}\right]}\right\} \tag{19}$$

## Acknowledgements

This research was supported in part by the National Science Foundation (Grant No. ENG-7805517) and in part by the Joint Services Electronics Program. One of us (Y.O.) gratefully acknowledges the support of a Xerox Graduate Fellowship.

## References

1. B.A. Horwitz and F.J. Corbett, "The PROM-Theory and Applications for the Pockels Readout Optical Modulator," Opt. Eng., 17, 353, (1978).
2. G. Marie, "Large-Screen Projection of Television Pictures With an Optical-Relay Tube Based on the Pockels Effect," Philips Tech. Rev., 30, 292, (1969).
3. G. Marie, J. Donjon, and J.-P. Hazan, "Pockels Effect Imaging Devices and Their Applications," in Advances in Image Pickup and Display, Vol. 1, B. Kazan, Ed., Academic Press, New York, (1974), 225.
4. C. Warde, A. Weiss and A. Fisher, "$LiTaO_3$ and $LiNbO_3$ Microchannel Spatial Light Modulators," Proc. SPIE Los Angeles Technical Symposium, 218, (1980).
5. G.J. Berzins and M. Graser, Jr., "Response of a $Bi_{12}SiO_{20}$ Pockels Readout Optical Modulator to X-rays," Appl. Phys. Lett., 34 (8), 500, (1979).
6. J.C.H. Spence, "Prospects for On-Line Optical Image Processing of Atomic Resolution Images Using a PROM," Proc. SPIE Los Angeles Technical Symposium, 218, (1980).
7. I.M. Krittman, "Resolution of Electrostatic Storage Targets," IEEE Trans. Elec. Dev., ED-10, 404, (1963).
8. R.M. Schaffert, "The Nature and Behavior of Electrostatic Images," Photographic Science and Engineering, 6 (4), 197, (1962).
9. W.R. Roach, "Resolution of Electrooptic Light Valves," IEEE Trans. Elec. Dev., ED-21, 453, (1974).
10. A.R. Tanguay, Jr., "The Czochralski Growth and Optical Properties of Bismuth Silicon Oxide," Thesis, Yale University, (1977).
11. A.R. Tanguay, Jr. and R.C. Barker, "Implications of Concurrent Optical Activity and Electric Field Induced Birefringence for Pockels Readout Optical Memory Performance," 1978 Annual Meeting of the Optical Society of America, San Francisco, California, (1978); to be published.
12. Y. Owechko and A.R. Tanguay, Jr., "Exposure-Induced Charge Distribution Effects on the MTF of Electrooptic Spatial Light Modulators," Proc. SPIE Los Angeles Technical Symposium, 218, (1980).
13. R.A. Sprague, "Effect of Bulk Carriers on PROM Sensitivity," J. Appl. Phys., 46 (4), 1673, (1975).
14. J.W. Goodman, Introduction to Fourier Optics, McGraw-Hill, New York, (1968), 12.
15. Y. Owechko and A.R. Tanguay, Jr., "Theoretical Resolution Limitations of Electrooptic Spatial Light Modulators," 1979 Annual Meeting of the Optical Society of America, Rochester, New York, (1979); to be published.

APPENDIX II

# Exposure-induced charge distribution effects on the modulation transfer function (MTF) of electrooptic spatial light modulators

Y. Owechko, A. R. Tanguay, Jr.
Departments of Electrical Engineering and Materials Science
University of Southern California, University Park, Los Angeles, California 90007

## Abstract

The theoretical resolution of an electrooptic spatial light modulator [such as the Pockels Readout Optical Modulator (PROM)] is a function of the electrostatic field distribution arising from stored point charges located within the active electrooptic crystal layer. The Fourier transform of the voltage distribution (which can be directly related to the modulation transfer function) is expressed as a function of the charge location within the electrooptic crystal. In addition, the resultant analytic expression contains the dielectric constants of the blocking layers and electrooptic crystal, and the thicknesses of the three layers. This formulation allows the effects of charge trapping within the bulk of the electrooptic crystal to be modeled. In particular, the low spatial frequency response decreases linearly and the high spatial frequency response decreases exponentially with the distance of the point charge from the dielectric blocking layer/electrooptic crystal interface. Thus the overall sensitivity and resolution are degraded strongly by charge storage in the bulk away from the interface. Utilizing superposition, this formulation can be readily extended to accommodate arbitrary charge distributions arising from different exposure parameters. The spatial frequency response of the PROM is calculated for both analytic (exponential hole/gaussian electron) and iterative (exposure-induced charge transport) continuous charge distributions. The limiting form of the high spatial frequency response is shown to be independent of the particular distribution of volume charge. The implications of these results for device design and operation are discussed.

## I. Introduction

Several electrooptic spatial light modulators (ESLM's) have been investigated for numerous applications in coherent optical signal processing, including the Pockels Readout Optical Modulator (PROM) (1), TITUS (2), PHOTOTITUS (3), and the Microchannel Spatial Light Modulator (MSLM) (4). Such devices record two-dimensional image information in the form of a charge pattern which modulates the voltage across an active (electrooptic) single crystal layer. The charge pattern is typically induced either by intensity modulation of light incident on a photoconductive layer, or by direct electron beam charge deposition. More recently, image storage in ESLM's has been accomplished by exposure to x-ray sources (5) and by high energy electron beam charge implantation (6). In each case, the image-wise modulated voltage is sensed using polarized light by means of the linear electrooptic effect.

One extremely important parameter in the characterization of candidate spatial light modulators is the limiting resolution attainable with each such device. In addition, the shape of the modulation transfer function (MTF) strongly influences the resultant image fidelity, and consequently limits the accuracy of subsequent optical processing algorithms. The resolution of an electrooptic spatial light modulator is in general determined by the field spreading within the electrooptic crystal layer. The electric field distribution is a function of the dielectric constants and thicknesses of the dielectric blocking layers and electrooptic crystal layer, and of the charge distribution within the electrooptic crystal.

A method for calculating the sine wave response of a multi-layered structure due to the impulse response of a point charge was developed by Krittman (7), who applied the method to electrostatic storage targets. Schaffert (8) has performed related work on electrostatic images with emphasis on applications to the xerographic developing process. Roach (9) derived an expression for the modulation transfer function of electrooptic light valves consisting of an isotropic dielectric layer and a dielectrically anisotropic electrooptic crystal sandwiched between two transparent conducting electrodes, for the case of a sinusoidal modulation in charge density introduced at the dielectric layer/electrooptic crystal interface. These previous analyses of resolution effects in multi-layered electrostatic structures share a common limitation, in that each model constrains the charge distribution to lie at the interface between a dielectric layer and

the electrooptic crystal. Due to the nature of the charge pattern generating process in numerous applications of ESLM's, however (notably in the cases of the PROM and MSLM, and for the recent applications of x-ray exposure and high energy electron beam excitation), the resultant charge distribution is known to reside within the bulk of the electrooptic crystal layer. A complete treatment of resolution in electrooptic spatial light modulators, therefore, must include the effects of exposure-induced longitudinal charge distributions in addition to the geometric and constitutive properties of the layer structure.

Recently, an analytic expression has been derived for the Fourier transform of the voltage distribution (which can be directly related to the modulation transfer function) as a function of the location of point charges within the electrooptic crystal (10). In addition, this expression contains the dielectric constants of the blocking layers and electrooptic crystal, and the thicknesses of the three layers. This formulation allows the effects of charge trapping within the bulk of the electrooptic crystal to be modeled. In succeeding sections, the theoretical background of the analytic solution is explored, and features of the solution for single and multiple point charge cases are described to emphasize the essential behavior of the device response characteristics. The theoretical model is then extended to include the effects of continuous charge distributions throughout the electrooptic layer. Examples of both analytic and iterative exposure-induced charge distributions are presented and discussed in terms of the essential features of the theoretical point charge model. Finally, the implications of these results for device design and operation are discussed.

## II. Theoretical development

In order to simplify the theoretical treatment of resolution in electrooptic spatial light modulators, the Pockels Readout Optical Modulator (PROM) will be employed as a specific example, since the dielectric constant of the electrooptic crystal is isotropic. Extension of this analysis to other ESLM's (such as the TITUS device) with anisotropic electrooptic layers is relatively straightforward (9,15). A schematic diagram of a typical PROM structure is shown in Figure 1. The device is comprised of a photoconductive

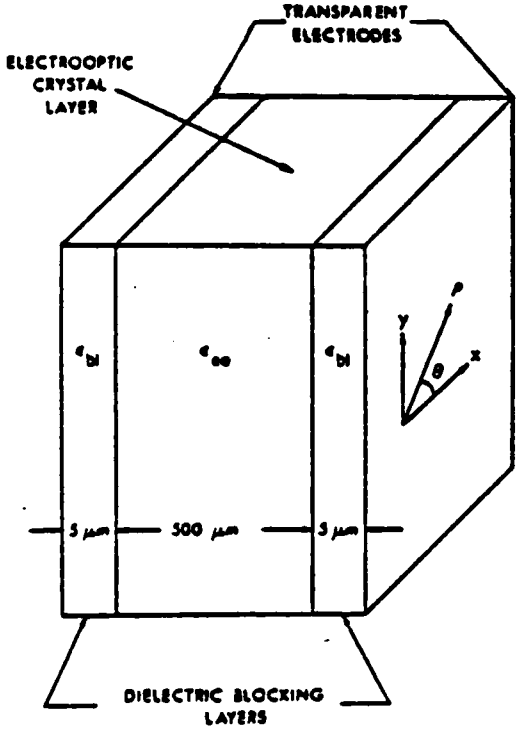


Figure 1. Structure of a typical PROM. In current PROM's, the electrooptic crystal layer is bismuth silicon oxide ($Bi_{12}SiO_{20}$, $\epsilon_{eo}= 56\epsilon_0$) and the dielectric blocking layers are parylene C ($\epsilon_{bl}=3\epsilon_0$). The transverse coordinate system used in the derivation of V(ω) is also shown.

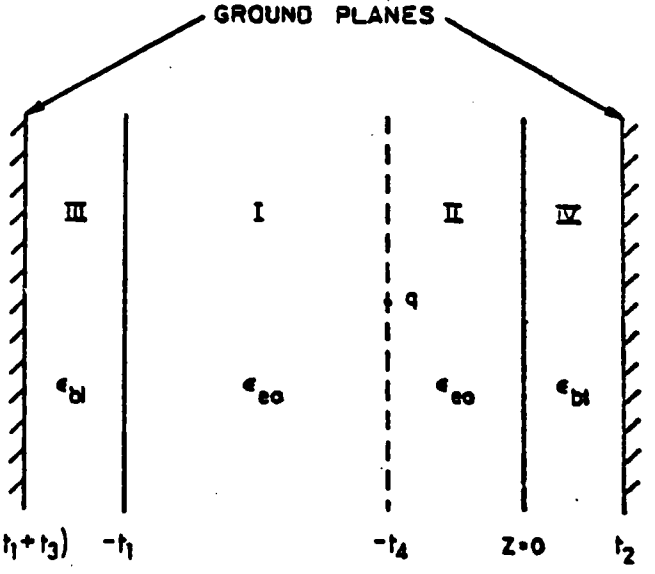


Figure 2. Longitudinal coordinate system used in the derivation of V(ω) (see Appendix I). The position of the point charge within the electrooptic crystal layer is at $z= -t_4$, while $t_1$, $t_2$, and $t_3$ are the electrooptic crystal thickness and dielectric blocking layer thicknesses, respectively.

electrooptic crystal ($Bi_{12}SiO_{20}$) sandwiched between two thin dielectric blocking layers. The blocking layers are coated with transparent electrodes.

In the simplest mode of PRCM operation, a voltage (typically 2000V) is applied to the electrodes, dividing between the three layers in inverse proportion to the capacitance of each layer. Since the electrooptic crystal is also photoconductive, illumination from the negative electrode side with image-wise modulated blue light causes electron-hole pair generation at a rate proportional to the incident intensity at each location. The generated charges then separate in the applied field (by electron drift into the bulk, since holes are relatively immobile in $Bi_{12}SiC_{20}$) giving rise to a reduction in voltage across the electrooptic crystal in illuminated regions. Since in the absence of illumination (subsequent to the writing process) the dielectric relaxation time ($\varepsilon\varepsilon_0\rho$) of bismuth silicon oxide is unusually large (of order several thousand seconds), the electron distribution is trapped in the bulk; hence, the written charge pattern is stored. The resultant two dimensional voltage distribution induces a birefringence (through the linear longitudinal electrooptic effect) which alters the polarization of linearly polarized readout light oriented to bisect the principal birefringent axes, producing an image-wise modulated amplitude when viewed through a crossed analyzer. The readout amplitude transmitted through a PRCM between ideal crossed polarizers may be expressed as

$$A(x,y) = \frac{A_0}{\sqrt{2}} \sin\left(\frac{\pi V(x,y)}{2V_{\lambda/2}}\right) \qquad (1)$$

where $A_0$ is the incident readout light amplitude, $V_{\lambda/2}$ is the half-wave voltage of the electrooptic crystal, and $V(x,y)$ is the voltage across the electrooptic crystal at image coordinates $(x,y)$. It should be noted that in the above expression it is assumed that the readout wavelength and intensity are chosen such that insignificant photoconductive charge redistribution occurs, and that the effects of natural optical activity in the bismuth silicon oxide crystal may be neglected (11,12). Thus the output amplitude is a monotonic function of the input intensity (for applied voltage less than the electrooptic half-wave voltage); such a transfer relationship is desirable for incoherent-to-coherent conversion and subsequent coherent optical signal processing operations.

From the nature of Eq. (1), it can be seen that the resolution of an electrooptic spatial light modulator depends directly on the relationship between a periodic (spatial frequency $\omega$) variation in the writing intensity, and the resultant spatial modulation of the voltage across the electrooptic crystal. The cubic symmetry (I23) of bismuth silicon oxide in conjunction with the orientation of the electrooptic crystal slice (<001>) assures that only longitudinal components of the electric field contribute to the induced birefringence through the electrooptic effect (see Appendix I). Therefore, the modulation in output amplitude [see Eq. (1)] depends only on the voltage difference $V(x,y)$ between opposite sides of the electrooptic crystal at each image point $(x,y)$. In the absence of significant two-dimensional diffusion effects in comparison with the drift-aided charge separation of photogenerated electron-hole pairs (13), $V(x,y)$ will be a function of the dielectric constants and thicknesses of the electrooptic and blocking layers, the locations (in the z-direction) of the trapped hole and electron distributions resulting from the writing (image recording) process, and the spatial frequency of the charge (writing intensity) modulation in the $(x,y)$ plane. In summary, we seek to express the dependence of each Fourier component of $V(x,y)$ (denoted $V(\omega)$) on the corresponding Fourier component of the lateral charge distribution, as a function of the device parameters and the longitudinal charge distribution.

If the longitudinal charge distribution is assumed to be such that charges are constrained to the blocking layer/electrooptic crystal interfaces, the spatial frequency dependence of the potential $V(\omega)$ may be obtained by straightforward solution (9) of the electrostatic boundary conditions with a surface charge $\sigma(x,y,z)$ given by:

$$\sigma(x,y,z) = \sigma_0\{1+\cos\omega x\}\delta(z). \qquad (2)$$

Since the absorption coefficient of the writing light is not infinite, and since in addition the drift length of a photoexcited electron is significantly smaller than or on the order of the typical electrooptic layer thickness, consideration of charge distributions within the bulk of the electrooptic crystal is necessary in order to formulate a realistic resolution model.

Consider a single point charge $\zeta$ located at $(x,y,z)=(0,0,-t_4)$ within the electrooptic crystal layer as shown schematically in Figure 2. Determination of the Fourier components of the potential difference $V(\omega)$ due to such a point charge is equivalent to calculation of the potential difference due to a periodic charge distribution given by

$$\sigma(x,y,z) = \sigma_0\{1+\cos\omega x\}\delta(z+t_4) \tag{3}$$

as a function of spatial frequency $\omega$. This approach has the advantage that once the solution for a single point charge has been obtained, the inherent linearity of the Fourier transform may be utilized to solve multiple charge cases by summation of single charge solutions, and continuous charge distribution cases by simple integration.

The axial symmetry of the problem can be exploited by transformation to cylindrical coordinates $(\rho,\theta,z)$ where $(\rho,\theta)$ are in the $(x,y)$ plane and $z$ is the longitudinal coordinate, as shown in Figure 1. Since the problem is invariant with respect to the angular coordinate $\theta$, the rectilinear two-dimensional Fourier transformation becomes a Hankel transform. The voltage across the electrooptic crystal can then be written in the form:

$$V(\rho) \equiv V(\rho,-t_1)-V(\rho,0) = \frac{1}{2\pi}\int_0^\infty V(\omega)J_0(\omega\rho)\omega d\omega \tag{4}$$

where $J_0(\omega\rho)$ is the zeroth order Bessel function and $\omega$ is a radial spatial frequency (14). Expressing $V(\omega)$ as a Hankel transform leads to a striking simplification of the calculation, since the Hankel transform of the delta function charge distribution (point charge) is a constant. Hence the difficulties associated with discontinuities in the real space boundary conditions due to charge singularities are automatically removed in Fourier space.

The real space potential difference $V(\rho)$ must satisfy Laplace's equation in all four regions depicted in Figure 2, and must also satisfy the boundary conditions at both electrodes, at both electrooptic crystal/blocking layer interfaces, and at the plane defined by the location of the point charge $(z=-t_4)$. Once $V(\rho)$ is determined, $V(\omega)$ is easily found by extracting the kernel of the Hankel transform (10), with the following result:

$$V(\omega) = \frac{\sigma}{\varepsilon_{eo}\omega}\left\{\frac{\sinh\omega(a-t_1)}{\cosh\omega(a-t_1)\left[1-\frac{\coth\omega(b-t_4)}{\coth\omega(a-t_4)}\right]} + \frac{\sinh\omega b}{\cosh\omega(b-t_4)\left[1-\frac{\coth\omega(a-t_4)}{\coth\omega(b-t_4)}\right]}\right\} \tag{5}$$

where

$$a = t_1 + \frac{1}{\omega}\coth^{-1}\left(\frac{\varepsilon_{b1}}{\varepsilon_{eo}}\coth\omega t_3\right) \tag{6}$$

and

$$b = \frac{1}{\omega}\coth^{-1}\left(\frac{\varepsilon_{b1}}{\varepsilon_{eo}}\coth(-\omega t_2)\right) \tag{7}$$

Note that as desired, $V(\omega)$ is a function of the electrooptic crystal thickness $t_1$, the dielectric blocking layer thicknesses $t_2$ and $t_3$, the dielectric constants $\varepsilon_{eo}$ and $\varepsilon_{b1}$ of the respective layers, as well as on the location of the point charge $t_4$. In this calculation, the electrodes are both assumed to be grounded.

In the special case $t_1=t_4$, and $t_2=0$, the problem reduces to that of a charge pattern confined to the electrooptic crystal/dielectric layer interface of a two layer device, with

$$V(\omega) = \frac{\sigma/\omega}{\varepsilon_{eo}\coth t_1 + \varepsilon_{b1}\coth t_3} \tag{8}$$

in agreement with the solution for this case derived previously (9).

The modulation transfer function (MTF) relating the output image modulation to the input image modulation may be obtained from the expression (9):

$$\text{MTF} = \frac{1}{m}\left[\frac{I_{max} - I_{min}}{I_{max} + I_{min}}\right] \tag{9}$$

where

$$I_{out} = \frac{I_0}{2} \sin^2 \left[ \frac{\pi V(0)}{2V_{\lambda/2}} \left\{ 1 + m \frac{V(\omega)}{V(0)} \cos\omega x \right\} \right] \tag{10}$$

and where m is the spatial modulation index of the imposed charge distribution, $V_{\lambda/2}$ is the electrooptic crystal half-wave voltage, and $V(0) \equiv V(\omega=0)$. Physically, V(0) is the average value of the potential difference across the electrooptic crystal layer. In Eq. (9), $I_{max}$ and $I_{min}$ are the values of $I_{out}$ for $\cos\omega x=1$ and $\cos\omega x=-1$, respectively. From Eq. (10), it can be seen that the character of the solution for each case is fully expressed by $V(\omega)$ or $V(\omega)/V(0)$. Since the MTF for a given device will be both exposure [V(0)] and modulation (m) dependent, a more fundamental indication of expected device performance is obtained by presentation and discussion of the un-normalized [$V(\omega)$] and normalized [$V(\omega)/V(0)$] potential difference functions.

Before proceeding to a detailed presentation and interpretation of the results, it should be pointed out that the un-normalized potential differences $V(\omega)$ and the normalized functions $V(\omega)/V(0)$ have a direct interpretation useful for both comparison of distinct devices of different constitutive characteristics, and for comparison of the implications of distinct charge distributions within a given device. In particular, graphs of $V(\omega)$ as a function of $\omega$ parametrized by different device constitutive properties assume equal exposure conditions (identical charge distributions), while graphs of $V(\omega)/V(0)$ assume optimum exposure conditions for each compared device (i.e. sufficient exposure for each device such that $V(\omega)$ is optimized in the limit of low spatial frequencies). These types of comparisons are familiar from the case of photographic film, where the typical resolution/sensitivity trade-off forces a similar comparison of film properties on the basis of either response to equal exposure, or response to optimum exposure.

## III. Features of the solution for discrete charge distributions

The nature of the spatial frequency dependence of the potential difference $V(\omega)$ can be more easily appreciated if the high and low spatial frequency responses are examined. These limiting forms are given by:

$$\{V(\omega)\}_{\omega \to 0} = q \left[ \frac{t_4(t_2+t_3)-t_1t_2}{\epsilon_{eo}(t_2+t_3)+\epsilon_{bl}t_1} \right] \tag{11}$$

$$\{V(\omega)\}_{\omega \to \infty} = \frac{q}{(\epsilon_{bl}+\epsilon_{eo})\omega} \left[ e^{-\omega\Delta_1} - e^{-\omega\Delta_2} \right] \tag{12}$$

where $\Delta_1=t_1-t_4$ and $\Delta_2=t_4$. The parameters $\Delta_1$ and $\Delta_2$ represent the distance of the point charge from each dielectric blocking layer/electrooptic crystal interface.

From Eq. (11), it is apparent that the low spatial frequency limit of $V(\omega)$ depends on the layer thicknesses and dielectric constants, as well as on the charge location. In particular, if we consider the case of a symmetric device (i.e. a device with two identical blocking layers), $V(\omega)$ decreases linearly to zero and then increases to its initial value as the charge moves from one interface to the other. This is intuitively appealing since no voltage drop is expected across the electrooptic crystal for a point charge in the center of a symmetric device. The low frequency response is in addition independent of spatial frequency.

The high frequency limiting form of $V(\omega)$ given in Eq. (12) is a function only of the dielectric constants of the layers, the spatial frequency, and the distances of the charge from each of the blocking layer/crystal interfaces. If the point charge resides on either interface, $V(\omega)$ falls off inversely with increasing spatial frequency. For even small separations of the charge from either interface, however, the high spatial frequencies will be exponentially attenuated. Note that as in the low spatial frequency case, $V(\omega)$ is zero when the charge is in the center of the device.

The dependence of $V(\omega)$ and $V(\omega)/V(0)$ on the dielectric constant of the blocking layers (assumed identical) is shown in Figures 3 and 4, respectively. The effect of increasing the blocking layer dielectric constant is seen to reduce the device sensitivity (see Figure 3), while increasing the high spatial frequency response for optimum exposure in both cases (see Figure 4). Similarly, the effect of decreasing the blocking layer thickness reduces the device sensitivity but improves the relative response at high spatial frequencies (10). In Figures 3 and 4, a single point charge is located at one of the dielectric blocking layer/electrooptic crystal interfaces.

The solutions for cases involving multiple point charges can be obtained by a linear superposition of the solutions for each separate point charge. In particular, the effect of an electron-hole pair can be modeled if the point charges are assigned opposite signs. The results of such a calculation as a function of the charge separation are shown in Figures 5 and 6. In this calculation, the hole and electron were assumed initially constrained to opposite interfaces, and were subsequently displaced symmetrically into the bulk of the electrooptic crystal layer. In Figures 5 and 6, each curve is labeled by the positions of each point charge according to the following convention: the electrooptic crystal layer is 500 μm thick and the coordinate pairs labeling each curve are the z coordinates of each of the two point charges. Thus (500,0) represents a positive charge at the z=-500 μm interface and a negative charge at the z= 0 μm interface. The device parameters are those of the typical PROM configuration shown in Figure 1. From Figure 5, it is observed that displacement of the point charges away from the dielectric blocking layer/electrooptic crystal interfaces strongly degrades the high spatial frequency response, and in addition reduces the sensitivity at low spatial frequencies. The exponential modification of the high spatial frequency behavior is shown more clearly in the graphs of $V(\omega)/V(0)$ shown in Figure 6. Due to the assumption of a symmetric device configuration in this calculation, it should be noted that charges of opposite sign symmetrically placed on opposite sides of the electrooptic crystal layer contribute equally to the total potential. Thus the results shown in Figure 6 for the dual charge calculation are equally applicable to the case of a single charge of appropriate sign placed at the same distances from either interface (i.e. 0, 50 and 100 μm).

The effects of asymmetric charge location within a symmetric PROM device are shown in Figures 7 and 8. A positive point charge is located at one dielectric blocking layer/electrooptic crystal interface (z=-500 μm), and a negative point charge is placed at varying distances from the opposite interface (z= 0 μm). The device constitutive parameters are those shown in Figure 1. This configuration models a hypothetical writing process in which the incident illumination is characterized by a large absorption coefficient so that the (immobile) hole distribution is constrained to one interface, while the electron distribution is forced into the bulk electrooptic layer by the applied field. The resultant charge separation will thus be a function of the constitutive device

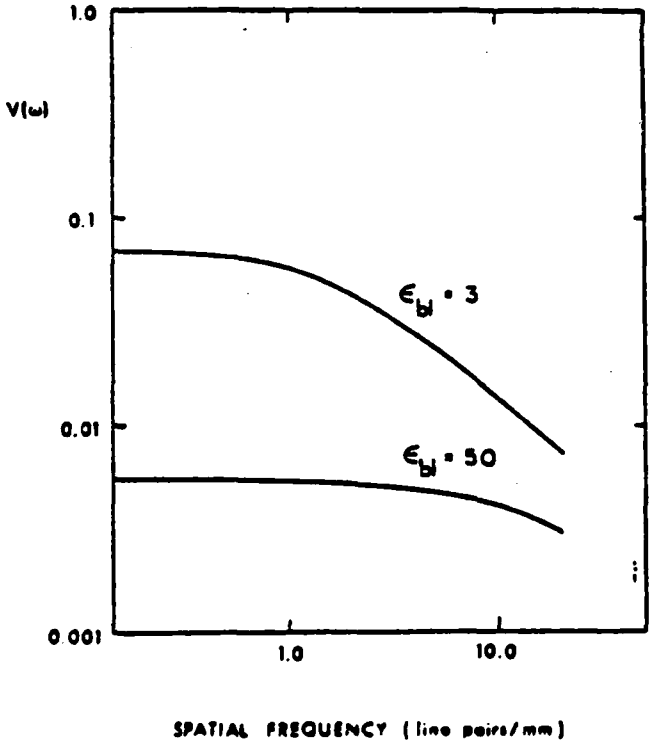


Figure 3. Effect of dielectric blocking layer dielectric constant on the spatial frequency response of V(ω). A symmetric PROM device is assumed, with geometric and constitutive parameters as shown in Figure 1. The vertical scale is arbitrary, but is the same for Figures 3, 5, and 7.

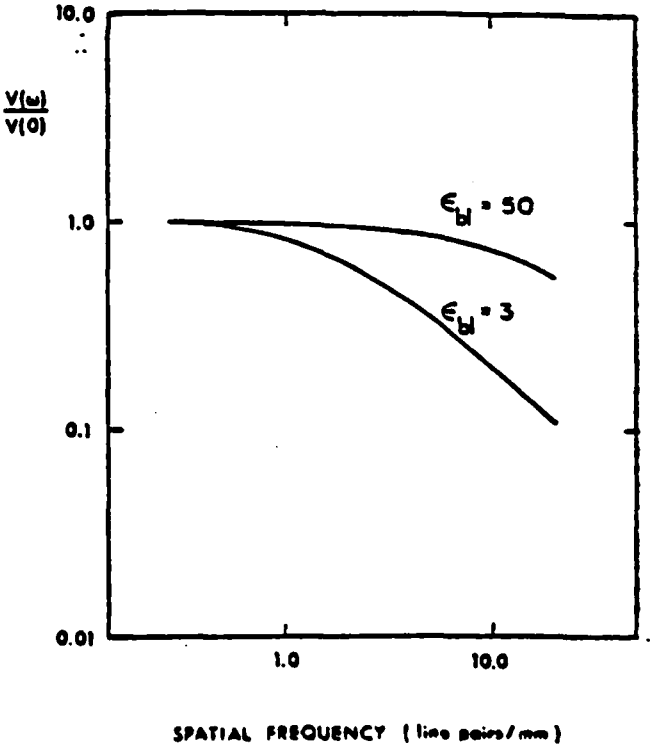


Figure 4. Effect of dielectric blocking layer dielectric constant on the spatial frequency response of $V(\omega)/V(0)$.

properties and the voltage across the device during the writing cycle. The resultant V(ω) curve for the case of the negative charge at the opposite interface (labeled "(0)" in Figure 7) is exactly the same as the (0,500) case discussed with respect to Figure 5. As the negative charge is moved in from the interface toward the center of the crystal, the response at high spatial frequencies decreases more rapidly at first than the response at low spatial frequencies. As the negative charge reaches the center of the electrooptic crystal layer (z=-250 μm) and continues to approach the positive charge, the response at low spatial frequencies decreases faster than the reduction in high spatial frequency response. For both charges in the same half of the electrooptic crystal, the response characteristic becomes nonmonotonic, as can be seen in Figure 7 and even more graphically in Figure 8.

This remarkable nonmonotonic behavior of the spatial frequency response can be explained with the aid of Figure 9, which details the contributions of each charge to the total potential. In Figure 9(a), the signs and magnitudes of the potential contributions from both charges are positive, and the resultant potential has the same response characteristic as that of a single charge positioned at an interface. In Figure 9(b), the negative charge is 125 μm (one quarter of the electrooptic crystal thickness) from the interface, and hence contributes a reduced low spatial frequency response and an exponentially attenuated high spatial frequency response. At the center of the crystal, the negative charge does not contribute to the potential due to symmetry, and the form of the frequency response is the same as that for a single point charge at an interface [as shown in Figure 9(c)]. The most interesting case is shown in Figure 9(d), in which the charge separation is one quarter of the electrooptic crystal thickness. Here the contributions to the total potential from both charges have opposite signs. This situation is equivalent to taking the difference between the V(ω) curves for two positive charges at the same locations, as shown in the Figure. The nonmonotonic behavior is thus seen to arise directly from the exponential attenuation of the high spatial frequency components of the potential due to the negative charge.

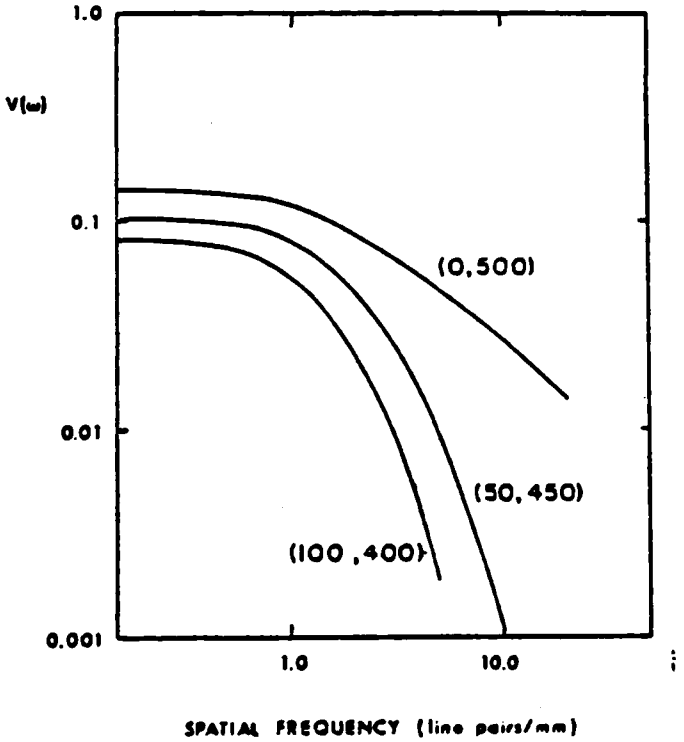


Figure 5. Effect of longitudinal charge position within the electrooptic crystal layer on the spatial frequency response of V(ω). In each case, two point charges of opposite sign are symmetrically placed relative to the center of the device. Each curve is labeled by the distance in μm of the (negative, positive) charge from the electrooptic crystal/dielectric blocking layer interface at z= 0μm.

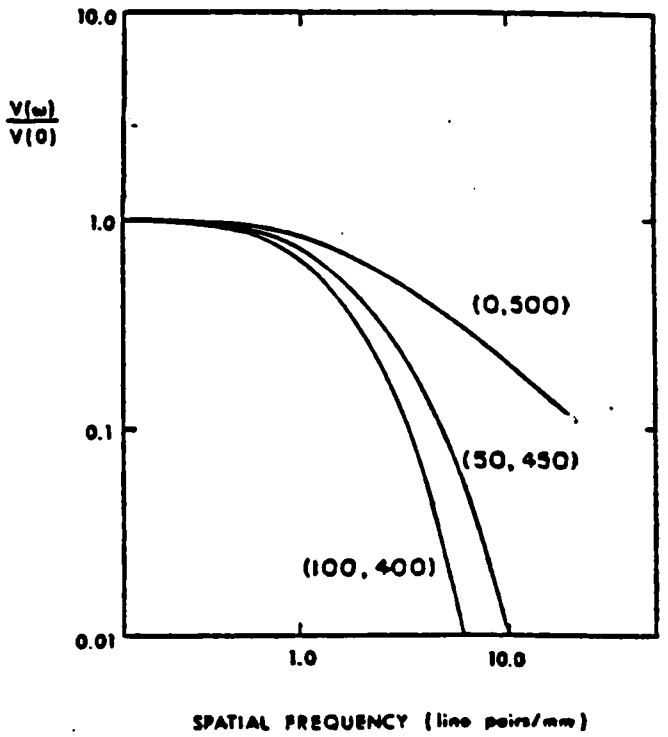


Figure 6. Effect of longitudinal charge position within the electrooptic crystal layer on the spatial frequency response of V(ω)/V(0). Note the marked attenuation of the high spatial frequency response as the charges are increasingly displaced from their respective interfaces.

## IV. Features of the solution for continuous charge distributions

As in the cases involving multiple point charges, the solutions for cases involving continuous charge distributions can be obtained by superposition due to the inherent linearity of the Fourier (Hankel) transform. Consider an arbitrary charge distribution $\rho(z)$ confined to the bulk of the electrooptic crystal layer ($-t_1 \leq z \leq 0$ in Figure 2). In the case of the PROM, wherein charge redistribution is effected either by electron-hole pair generation or by photon-assisted detrapping, charge neutrality must be enforced such that:

$$\int_{-t_1}^{0} \rho(z)dz = 0. \tag{13}$$

Such an assumption will not apply explicitly in cases involving electron-beam addressed electrooptic spatial light modulators. The contribution to the Fourier component $V(\omega)$ of the overall potential difference across the electrooptic crystal layer from the charge density at a given longitudinal coordinate z will be weighted by the Fourier component $V(\omega,z)$ generated by a point charge at the same longitudinal coordinate. Hence the total integrated response is

$$V(\omega) = \int_{-t_1}^{0} \rho(z)V(\omega,z)dz. \tag{14}$$

This relation can be readily utilized to calculate the spatial frequency response resulting from any arbitrary charge distribution function. In particular, the process of photogenerated electron-hole pair generation and field-induced separation is of considerable interest since it describes the response of the electrooptic spatial light modulator to optical exposure. By way of illustration, such a writing process may be simply modeled as shown schematically in Figure 10 by assuming an immobile exponential

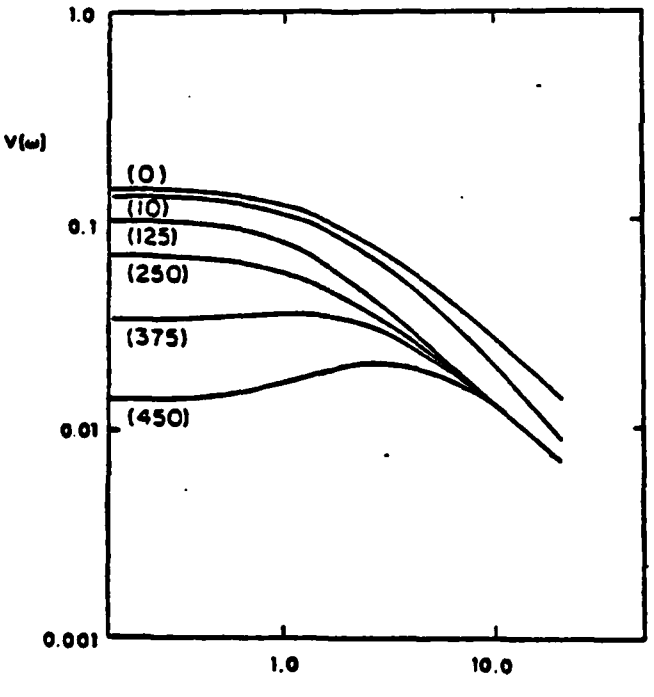


Figure 7. Effect of asymmetric charge locations on the spatial frequency response of $V(\omega)$. A positive charge is located at the z= -500μm electrooptic crystal/dielectric blocking layer interface. Each curve is labeled by the distance in μm of a negative charge from the electrooptic crystal/dielectric blocking layer interface at z= 0μm.

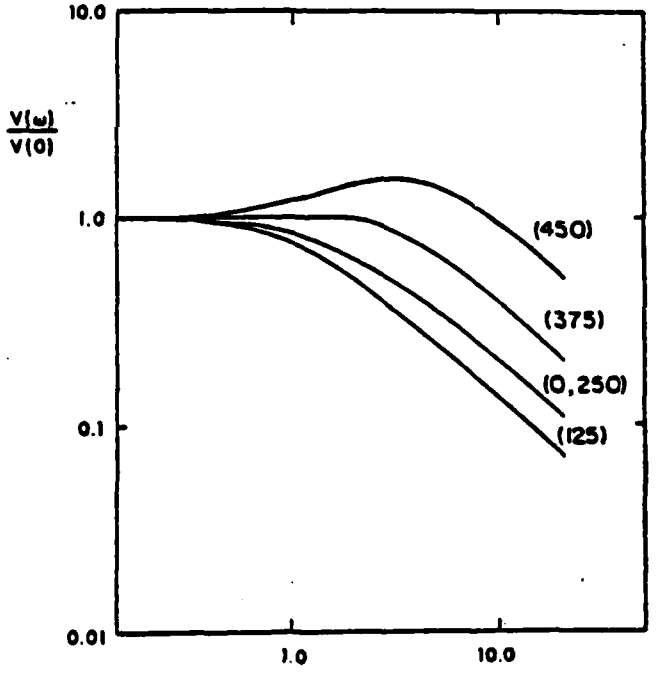


Figure 8. Effect of asymmetric charge locations on the spatial frequency response of $V(\omega)/V(0)$. Note the nonmonotonic behavior of $V(\omega)/V(0)$ when both charges are in the same half of the electrooptic crystal. The curves for the negative charge at z= 0μm and z= - 250μm are identical.

hole distribution given by (for $0 \leq z \leq t_{eo}$ in Figure 10)

$$\rho_h(z) = \rho_h \exp(-\alpha z) \tag{15}$$

corresponding to the absorption profile of the writing illumination, and a gaussian electron distribution given by

$$\rho_e(z) = \rho_e \exp\left(-\frac{4(z-z_0)^2}{\sigma^2}\right) \tag{16}$$

such that the total charge density is $\rho(z) = \rho_h(z) + \rho_e(z)$.

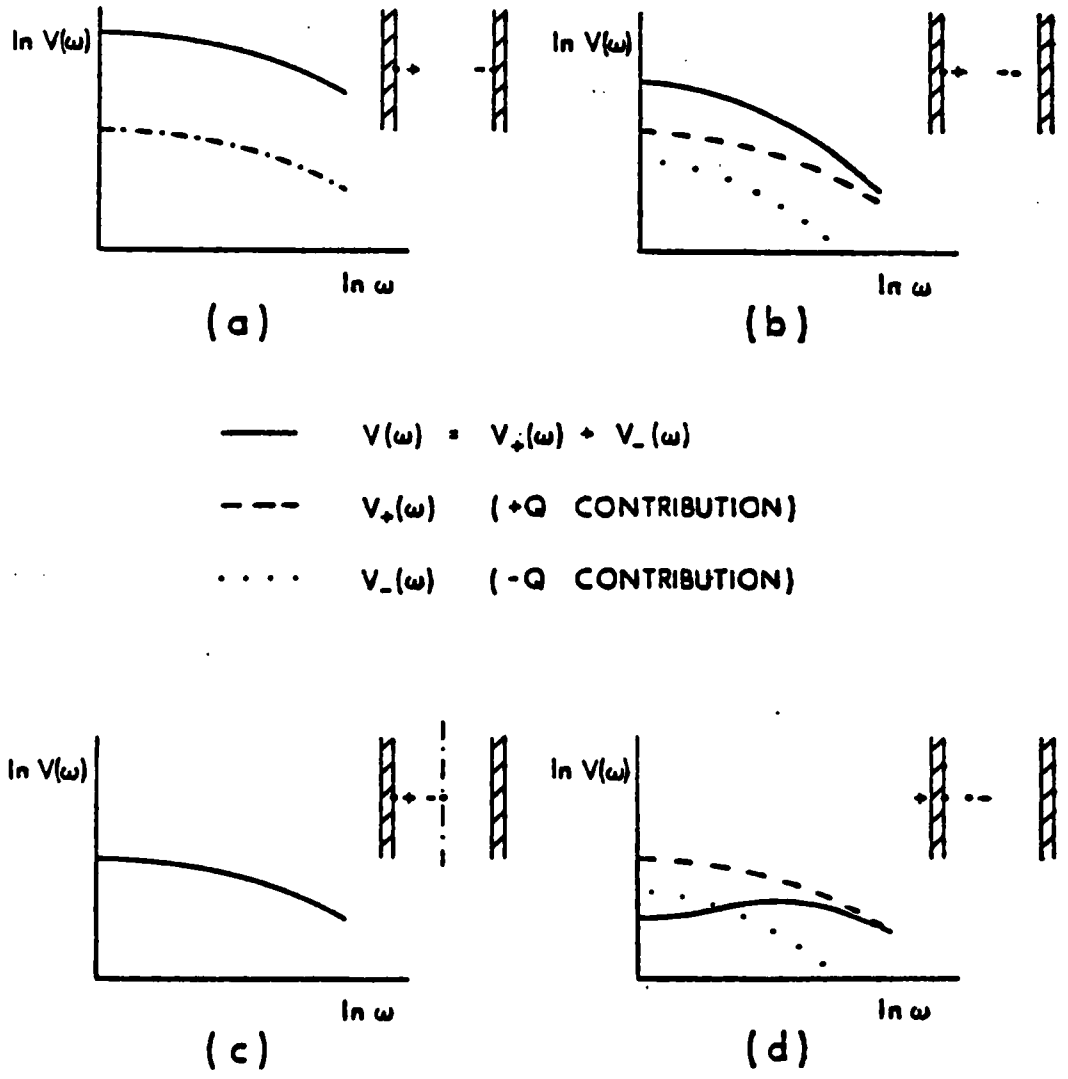


Figure 9. Schematic explanation of the effect of asymmetric charge locations on the spatial frequency response of V(ω) and V(ω)/V(0). (a) Both charges are at their respective interfaces; thus $V_+(\omega) = V_-(\omega)$, and the total V(ω) is simply twice the potential difference expected for a single point charge ($V(\omega) = 2V_+(\omega)$). (b) Here the negative charge is displaced from the interface, exponentially attenuating the high spatial frequency response of $V_-(\omega)$. The sum of the terms due to each charge thus decreases monotonically, with diminished high spatial frequency response relative to case (a) (see Figure 10). (c) The negative charge is placed at the center of the symmetric PROM. Hence, it does not contribute to V(ω) and $V(\omega) = V_+(\omega)$. (d) The negative charge is in the same half of the crystal as the positive charge; the total V(ω) can be obtained by taking the difference between $V_+(\omega)$ and $-V_-(\omega)$, since $V_+(\omega)$ and $V_-(\omega)$ have opposite signs. Since $V_+(\omega)$ and $V_-(\omega)$ decrease at unequal rates, V(ω) no longer decreases monotonically.

The assumption of analytic forms for $\rho_h(z)$ and $\rho_e(z)$ allows the total integrated response (Eq. (14)) to be evaluated numerically in a straightforward manner. The results of two such calculations are presented in Figure 11. The curve labeled (140;80,400) represents an exponential hole distribution of characteristic width (1/e point) 71.4 μm, and a electron distribution centered at 400 μm with a characteristic width of 80 μm. These distributions produce a spatial frequency response exhibiting monotonic behavior as expected from the discussion relating to Figure 9, since the majority of electrons and holes are on opposite sides of the electrooptic crystal layer. The curve labeled (280;40,50) represents an exponential hole distribution of width 35.7 μm, and a gaussian electron distribution centered at 50 μm of width 40 μm. Here the electrons and holes are primarily on the same side of the electrooptic crystal layer, giving rise to striking nonmonotonic behavior of the spatial frequency response. The response for two point charges located at opposite interfaces is reproduced for comparison.

Note that in both cases shown in Figure 11, the high spatial frequency response decreases more rapidly than the $\omega^{-1}$ dependence predicted from the single point charge analysis for charges confined to the interfaces, and yet does not decrease as rapidly as the $\exp(-\omega\Delta)$ dependence predicted for point charges in the bulk away from the interface. This behavior can be understood by reference to Figure 12, which schematically illustrates the form of the integrand in Eq. (14). Since $V(\omega,z)$ decreases exponentially from its interface values as the distance from either interface increases, charges near the interfaces are preferentially weighted in the summation. In the limit of large spatial frequencies, the limiting form of $V(\omega,z)$ given in Eq. 12 may be employed. Hence

$$\underset{\omega\to\infty}{\{V(\omega)\}} = \frac{-q}{\omega(\varepsilon_{eo}+\varepsilon_{bl})}\int_0^{t_{eo}} \rho(z)\left[e^{-\omega(t_{eo}-z)} - e^{-\omega z}\right] dz \tag{17}$$

$$\sim \frac{-q}{\omega^2(\varepsilon_{eo}+\varepsilon_{bl})}\left[\rho(t_{eo}) - \rho(0)\right] .$$

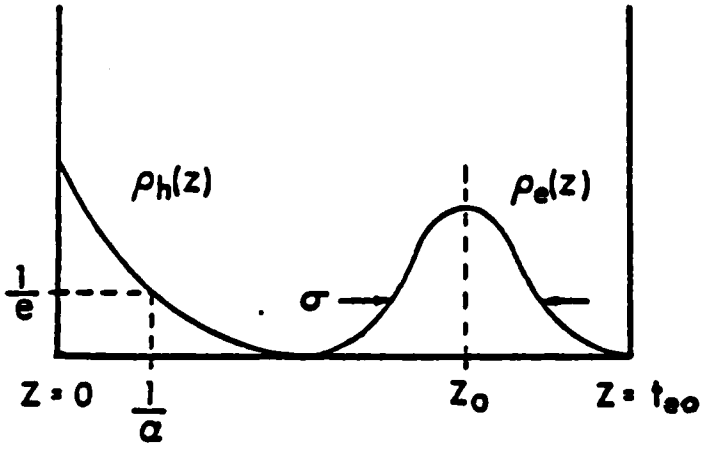


Figure 10. Example of an analytic longitudinal charge distribution representing exposure-induced charge separation. The assumed hole distribution is described by an exponential absorption profile $\rho_h(z)$ with absorption coefficient α. The electron distribution $\rho_e(z)$ is gaussian with width σ centered at $z=z_0$.

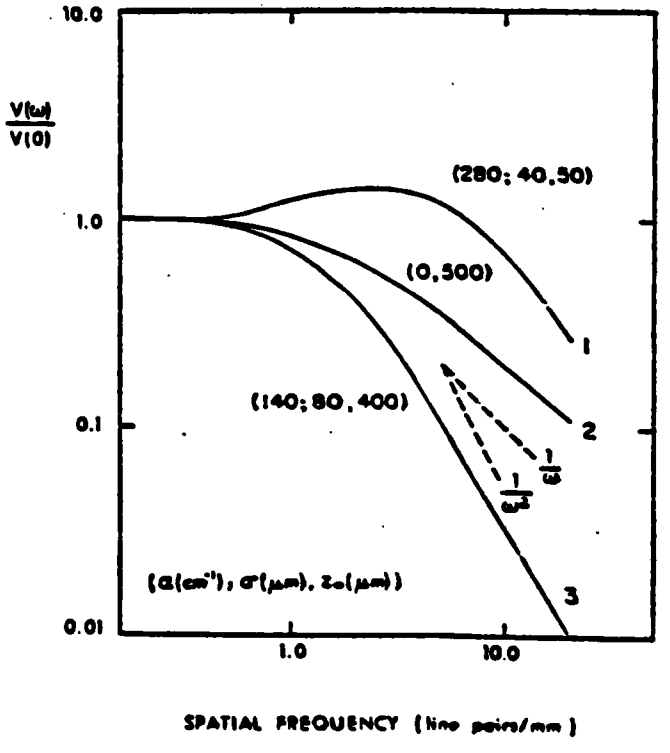


Figure 11. Effect of analytic longitudinal charge distribution parameters on the spatial frequency response of $V(\omega)/V(0)$. The response for the case of point charges at opposite interfaces (0,500) is presented for comparison.

Thus at large spatial frequencies, the response decreases as $\omega^{-2}$, and the absolute sensitivity depends only on the charge densities at or near the dielectric layer/electrooptic crystal layer interface. Since this relation holds true independent of the assumed z dependence of the charge density, both cases described above are expected to approach $\omega^{-2}$ asymptotically, as confirmed by reference to Figure 11. Further support for this prediction is provided by experimental measurements of the modulation transfer function in PROM structures (1,16), which also indicate asymptotic behavior proportional to $\omega^{-2}$. It should be noted that the shape of the longitudinal charge distribution influences the onset of the high spatial frequency regime, such that distributions primarily confined to the interfaces will approach the $\omega^{-2}$ asymptote at higher spatial frequencies than those distributions extending significantly into the bulk electrooptic crystal layer.

A more refined estimate of the device spatial frequency response resulting from optical exposure may be obtained from iterative solutions of the charge transport equations under simulated exposure conditions (13). Charge distributions so obtained are subject to the assumptions that the minority carrier lifetime is independent of minority carrier density, that diffusion terms in the transport equations can be neglected, and that the variation in the electric field during the charge migration comprising each iteration can be neglected. In addition, it is important to include the effects of finite electrooptic crystal layer thickness and to enforce self-consistency between the incremented charge distribution and the resultant electric field distribution at each iteration stage (15), in contrast to the method proposed in Ref. (13).

Sample charge distribution results corresponding to exposure wavelengths of 450 nm and 375 nm for device constitutive properties as described in Figure 1 are shown in Figure 13. The absorption coefficients ($\alpha$=30 $cm^{-1}$ @ $\lambda$=450 nm; $\alpha$=830 $cm^{-1}$ @ $\lambda$=375 nm) are such that the 375 nm case is characterized by close confinement of the hole distribution near the input interface with shallow electron penetration into the bulk, whereas the 450 nm case is characterized by significant electron-hole pair generation throughout the electrooptic crystal layer, resulting in a sizeable accumulation of electrons at the far interface, as shown in Figure 13.

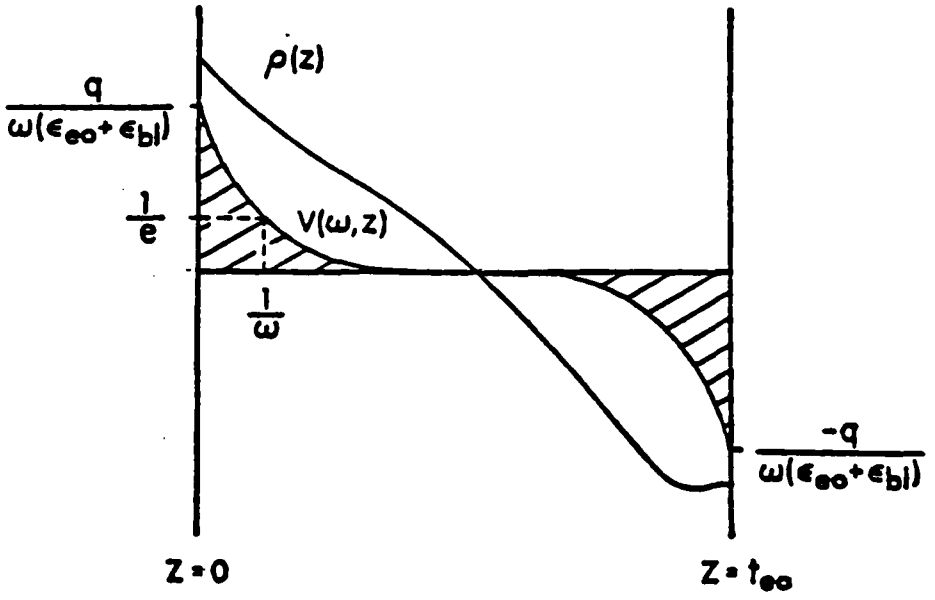


Figure 12. Origin of $\omega^{-2}$ asymptotic behavior for continuous charge distribution cases. The total response $V(\omega)$ at high spatial frequencies is given by the integral throughout the electrooptic crystal layer of the high frequency form (Eq. 12) of $V(\omega,z)$ weighted by the charge density $\rho(z)$. In the limit of large $\omega$, the exponential attenuation with z of $V(\omega,z)$ emphasizes the contribution from charges at or near the respective interfaces.

The spatial frequency responses calculated from these widely disparate charge distributions are shown in Figure 14. As expected, the closely confined charge in the 375 nm case produces a nonmonotonic spatial frequency response, whereas the volume excitation present in the 450 nm case generates a monotonic frequency response. This situation is quite similar to that described previously with reference to the exponential/gaussian analytic distribution cases. One interesting feature of the 450 nm case is the presence of a large density of accumulated electrons at the $z=t_{eo}$ interface (due to the fact that the drift length is of the same order as the crystal thickness) (see Figure 13). The high spatial frequency response of such a highly confined charge density at an interface is expected to decrease nearly as $\omega^{-1}$ (see Eq. 12) at intermediate spatial frequencies, approaching the required $\omega^{-2}$ asymptote only at extremely high spatial frequencies. This contribution is evident in Figure 14, inasmuch as the $\lambda$=450 nm asymptote lies between $\omega^{-1}$ and $\omega^{-2}$ over the spatial frequency range shown. Similar limiting behavior is evident in the $\lambda$=375 nm case, due to the close confinement of the hole distribution to the z=0 interface.

## V. Device implications

The dependence of the spatial frequency response on the dielectric constants and thicknesses of the dielectric blocking layers (as shown in Figures 3 and 4, and in Figures 5 and 6 of Ref. (10)) indicates that new PROM devices can be envisioned with modulation transfer functions constant to much higher spatial frequencies than are characteristic of presently available devices. Gains in MTF behavior due to choice of dielectric blocking layer properties will be accompanied by an overall reduction in device sensitivity. Such new devices, however, would provide significantly improved image fidelity and resolution in applications where requirements on device sensitivity can be relaxed, similar to the familiar tradeoff in the case of photographic film. In order to improve PROM resolution, high dielectric constant, high dielectric breakdown strength, high resistivity dielectric blocking layers are required.

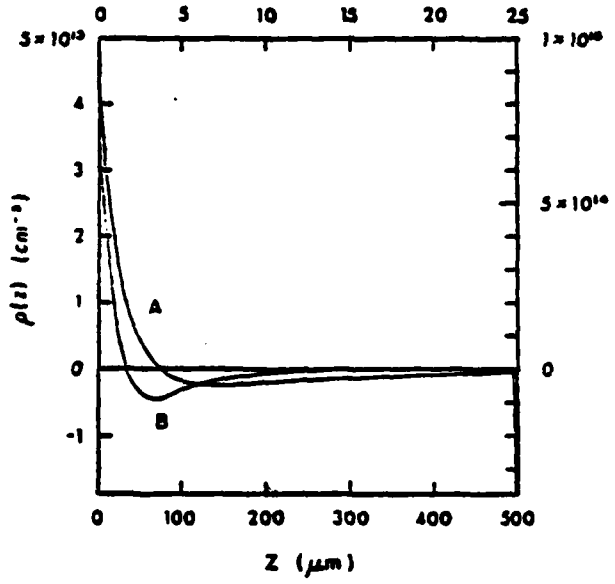


Figure 13. Longitudinal charge distributions $\rho(z)$ calculated numerically using an iterated electron drift model for two exposure wavelengths (and corresponding absorption coefficients). Curves A and B result from exposure wavelengths of 450 nm and 375 nm, respectively. The left and lower scales correspond to curve A, while the right and upper scales correspond to curve B.

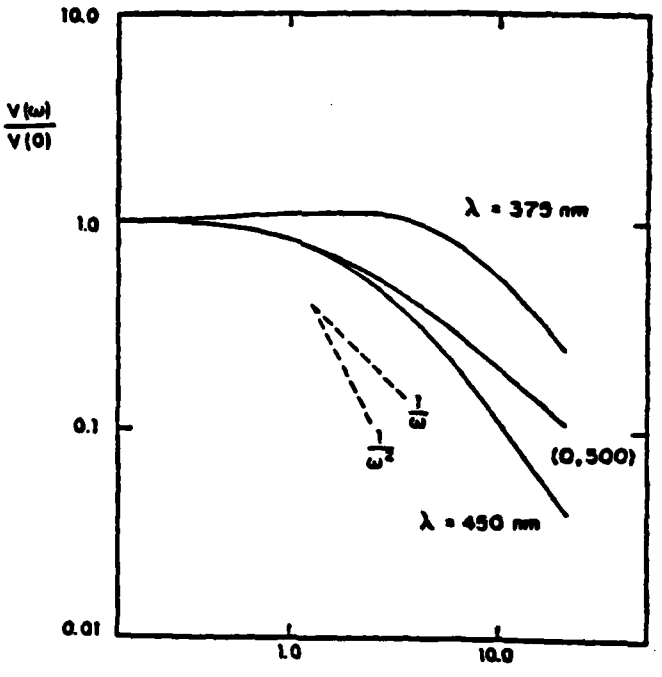


Figure 14. Normalized frequency responses $V(\omega)/V(0)$ for the calculated longitudinal charge distributions of Figure 13. The normalized response of point charges at the two interfaces is included for comparison.

The effect of exposure-induced charge distribution throughout the bulk of the electrooptic crystal layer is seen to have an adverse effect on the high spatial frequency response characteristics of the image storage process. The optimum resolution and sensitivity within a given PROM device structure are obtained when the hole distribution is constrained to the interface nearest the negative electrode, and the entire electron distribution is swept to the interface nearest the positive electrode during the writing cycle. The actual resolution and sensitivity obtained for a given device are thus strongly dependent on the absorption coefficient of the electrooptic layer at the writing illumination wavelength, on the external applied voltage and voltage division between the multiple layers during the writing cycle, and on the mobility-lifetime product of photogenerated electrons in the electrooptic crystal. Such bulk charge distribution effects will also strongly affect the resolution and sensitivity for cases where the image-wise modulated charge pattern is induced by high energy electron beam (6) and x-ray (5) sources.

## VI. Summary

A generalized expression for the spatial frequency response of a three layer electrooptic spatial light modulator is presented, which gives explicitly the dependence of the response on the thicknesses and dielectric constants of the layers, and on an arbitrary longitudinal charge position within the electrooptic crystal layer. This solution is applied specifically to the case of the Pockels Readout Optical Modulator (PROM), wherein the importance of the inclusion of bulk charge distribution effects is clearly demonstrated. These results are extended to several cases involving continuous longitudinal charge distributions, including both analytic (exponential hole/gaussian electron) and iterative (exposure-induced) charge density functions. The spatial frequency response in the continuous distribution cases reflects the essential features of the point charge solutions. The generalized formulation developed herein can be utilized to model specific device operational modes and writing cycle parameters. Application to other ESLM's with anisotropic electrooptic materials exhibits device geometric, constitutive, and charge distribution effects similar to those described herein (15). Research on the implications of including two-dimensional charge diffusion effects during the writing process is currently in progress.

## Appendix I. Transverse contribution to PROM electrooptic effect

The contribution to the electrooptic effect of the electric field components transverse to the light propagation direction can be determined by consideration of the index ellipsoid. For a crystal of I23 symmetry such as $Bi_{12}SiO_{20}$ the only nonzero electrooptic coefficients are (in the usual contracted notation)

$$r_{41} = r_{52} = r_{63} \tag{A-1}$$

If the longitudinal direction (corresponding to both the direction of the applied field and the direction of light propagation) is taken to be the z-axis, then the transverse field components $E_x$ and $E_y$ modify the index ellipsoid such that

$$\frac{x^2}{n_o^2} + \frac{y^2}{n_o^2} + \frac{z^2}{n_o^2} + r_{41}E_x yz + r_{41}E_y xz = 1 \tag{A-2}$$

where the longitudinal field $E_z$ is taken to be zero for simplicity, and $n_o$ is the zero field index of refraction. In the usual PROM geometry, the light propagation direction is along the crystallographic <001> axis. The polarization eigenstates are determined by the intersection of the ellipsoid with the plane normal to the light propagation direction (z = 0 plane), which is described by

$$\frac{x^2}{n_o^2} + \frac{y^2}{n_o^2} = 1 \tag{A-3}$$

Since the intersection is circularly symmetric, the transverse fields $E_x$ and $E_y$ do not contribute to the electrooptic effect for light propagating along the z axis. Consequently, only the longitudinal component of the electric field need be considered in calculating the field induced birefringence.

## Acknowledgements

This research was supported in part by the National Science Foundation (Grant No. Eng-7805617), the Joint Services Electronics Program, and the U.S. Army Research Office. One of us (Y.O.) gratefully acknowledges the support of a Xerox Graduate Fellowship.

## References

1. B.A. Horwitz and F.J. Corbett, "The PROM-Theory and Applications for the Pockels Readout Optical Modulator," Opt. Eng., 17, 353, (1978).
2. G. Marie, "Large-Screen Projection of Television Pictures With an Optical-Relay Tube Based on the Pockels Effect," Philips Tech. Rev., 30, 292 (1969).
3. G. Marie, J. Donjon, and J.-P. Hazan, "Pockels Effect Imaging Devices and Their Applications," in Advances in Image Pickup and Display, Vol. 1, B. Kazan, Ed., Academic Press, New York, (1974), 225.
4. C. Warde, A. Weiss and A. Fisher, "$LiTaO_3$ and $LiNbO_3$ Microchannel Spatial Light Modulators," Proc. SPIE Los Angeles Technical Symposium, 218, (1980).
5. G.J. Berzins and M. Graser, Jr., "Response of a $Bi_{12}SiO_{20}$ Pockels Readout Optical Modulator to X-rays," Appl. Phys. Lett., 34 (8), 500, (1979).
6. J.C.H. Spence, "Prospects for On-Line Optical Image Processing of Atomic Resolution Images Using a PROM," Proc. SPIE Los Angeles Technical Symposium, 218, (1980).
7. I.M. Krittman, "Resolution of Electrostatic Storage Targets," IEEE Trans. Elec. Dev., ED-10, 404, (1963).
8. R.M. Schaffert, "The Nature and Behavior of Electrostatic Images," Photographic Science and Engineering, 6 (4), 197, (1962).
9. W.R. Roach, "Resolution of Electrooptic Light Valves," IEEE Trans. Elec. Dev., ED-21, 453, (1974).
10. Y. Owechko and A.R. Tanguay, Jr., "Effects of Charge Dynamics and Device Parameters on the Resolution of Electrooptic Spatial Light Modulators," Proc. SPIE International Symposium, San Diego, 202, (1979).
11. A.R. Tanguay, Jr., "The Czochralski Growth and Optical Properties of Bismuth Silicon Oxide," Thesis, Yale University, (1977).
12. A.R. Tanguay, Jr. and R.C. Barker, "Implications of Concurrent Optical Activity and Electric Field Induced Birefringence for Pockels Readout Optical Memory Performance," 1978 Annual Meeting of the Optical Society of America, San Francisco, California, (1978); to be published.
13. R.A. Sprague, "Effect of Bulk Carriers on PROM Sensitivity," J. Appl. Phys., 46 (4), 1673, (1975).
14. J.W. Goodman, Introduction to Fourier Optics, McGraw-Hill, New York, (1968), 12.
15. Y. Owechko and A.R. Tanguay, Jr., "Theoretical Resolution Limitations of Electrooptic Spatial Light Modulators," 1979 Annual Meeting of the Optical Society of America, Rochester, New York, (1979); to be published.
16. M.P. Petrov, A.V. Khomenko, V.I. Berezkin, and M.V. Krasinkova, "Optical Information Recording in $Bi_{12}SiO_{20}$," Ferroelectrics, 22, 651, (1978).

# SPATIAL LIGHT MODULATORS FOR REAL TIME OPTICAL PROCESSING

Armand R. Tanguay,Jr.
Image Processing Institute
Departments of Electrical Engineering
and Materials Science
University of Soutnern California
University Park, Los Angeles, California 90007

## Abstract

Several candidate real time spatial light modulator technologies for conerent optical processing applications are reviewed. Physical principles of operation are described, as are current technological and fundamental physical limitations on device performance. A number of promising directions for current and future research on spatial light modulators are presented.

## I. Introduction

Following the advent of the laser, and directly stimulated by its ready availability, tremendous progress has been achieved during the past two decades in the development of conerent and incoherent optical processing techniques. However, the many advantages of two-dimensional parallel processing are not fully exploitable in image and data processing systems without the availability of appropriate real time spatial lignt modulators. Although a wide range of candidate spatial light modulator technologies nave been proposed and extensively researched and developed, no single candidate has as of yet emerged that at once satisfies the system requirements of low cost, reliability, and ease of operation while simultaneously exhibiting the requisite tecnnical performance characteristics demanded by increasingly complex optical processing applications.

Several factors have primarily contributed to the present gap between the level of sophistication of optical processing techniques and the development status of spatial light modulators necessary for real time implementations of such techniques. First and foremost, device research and development is inherently expensive due to large capital equipment requirements, necessary parallel research and development efforts in growth, deposition, and characterization of materials, and multiple iterations of device design on the basis of operational characterization and application-dependent criteria. To date, the prospective market for such devices nas not generally been viewed as large enough to encourage the type of major investments that stimulated rapid progress in such areas as information displays and solid state lasers. An added complication arises from the fact that all of the current candidate spatial light modulators are active devices, and as such require extensive parametric characterization coupled with comprehensive understanding of the fundamental device physics for optimum results in diverse applications. Major progress in both of these areas has been a relatively recent development. Finally, it has become increasingly apparent that no single spatial light modulator (at least of those presently envisioned) is capable of satisfying the wide range of at times conflicting demands stemming from the great diversity of proposed real time optical processing applications.

In the past few years, research has been initiated in a number of laboratories on the physical principles of operation of generic classes of spatial light modulators, on the requisite materials technologies, on methods of device characterization and analysis, and on new types of spatial light modulators for special applications. Such research has demonstrated encouraging results, particularly in the areas of increased physical understanding of optimum device operational modes and design parameters, and of novel device technologies.

In view of the numerous extensive reviews of spatial light modulators that nave already been published (1-7) the purpose of this paper is to present a survey of recent results in the research areas described above. In particular, emphasis will be placed on our present understanding of some of the fundamental physical limitations inherent in several of the more promising spatial light modulator technologies. In succeeding sections of this paper, performance parameters of spatial light modulators are briefly described with emphasis on several difficulties inherent in such performance evaluation and specification. Current progress in three major types of spatial light modulators (electrooptic, liquid crystal, and photorefractive) is then described. Finally, some future directions for research in several of these areas are suggested.

## II. Performance Evaluation of Spatial Light Modulators

A wide range of potential applications exists for real time, recyclable spatial light modulators in systems implementations of coherent optical processing techniques. These applications include use as the input incoherent-to-coherent image transducer in optical correlators and convolvers, programmable Fourier plane filters, serial-to-parallel (two-dimensional) buffer memories, page composers for holographic memories, real time holographic recording media, and holographic Fourier plane filters. In addition, many optical processing applications demand considerable image preprocessing, including contrast variation, contrast enhancement, contrast reversal, edge enhancement, image addition/subtraction, thresholding, level slicing, and minimization or elimination of the zeroth diffracted order in the Fourier plane.

Performance evaluation of each of the candidate spatial light modulator technologies is complicated by the innerently diverse requirements demanded by such a wide range of applications and desirable features. A number of performance parameters important in coherent optical processing applications are presented in Table I. This listing characterizes device parameters required for primarily "linear" applications, in which the SLM output amplitude is optimally a linear function of the input intensity. Additional parameters should be added for characterization of SLM's designed for "nonlinear" applications, including ideality of the implemented nonlinear function (e.g., logarithmic for homomorphic filtering, or step for thresholding), programmability of the nonlinearity (e.g., variable level slicing), extended resolution requirements (e.g., halftoning) and the necessity for post-modulator thresholding (i.e., electronic or optical).

TABLE I: PERFORMANCE PARAMETERS FOR SPATIAL LIGHT MODULATORS: "LINEAR" APPLICATIONS.

| | |
|---|---|
| linearity | cycle time |
| sensitivity | optical quality |
| resolution; MTF | optical uniformity |
| contrast | phase dependence |
| address mechanism | operational complexity |
| write/read wavelengths | fabrication complexity |
| erase mechanism | lifetime |
| grey scale (dynamic range) | cost |
| storage capability/time | special features |
| phase or amplitude readout | reciprocity behavior |
| Fourier plane signal-to-noise ratio | |

The difficulty of side-by-side comparison of SLM's is readily apparent from the considerable number of characteristics presented in Table I. The suitability of an individual SLM also depends critically on the particular application for which it is envisioned. Furthermore, data describing several of these performance parameters can be highly misleading due to differences in definition and measurement techniques (1,8). For example, device sensitometry (linearity and sensitivity), resolution (modulation transfer function), Fourier plane signal-to-noise ration, uniformity (global vs. local), and exposure-dependent phase present particular complications in specification and interpretation. Sensitometry, resolution, and exposure-dependent phase depend on a wide range of parameters (including, for example, wavelength input, exposure magnitude, exposure pulse duration, operational mode (biasing conditions), readout mode, magnitude of baseline subtraction) since SLM's are truly active devices. Resolution (MTF) specifications also depend strongly on the measurement technique and analytical method employed (8) due to physical differences in device response to, for example, holographic fringe exposure as opposed to incoherent grating exposure at a given wavelength. Measurement of Fourier plane signal-to-noise ratio and device uniformity are largely dependent on defect densities that vary greatly from device to device due to lack of appropriate manufacturing process control.

The problems noted above with regard to accurate parametric- and application-dependent characterization of SLM's are by no means insurmountable. Rather, they point out the importance of continued advances in the fundamental physical understanding of device design and operation. As will be illustrated in several cases below, such improved understanding can indicate optimum design criteria, new operational modes, and new applications for traditional SLM's, as well as provide direction for the development of novel SLM technologies.

In the following three sections, current progress in each of three categories of spatial light modulators is highlighted, with emphasis on the physical principles of device

operation, principal advantages and disadvantages for potential applications, and where appropriate on current technological vs. fundamental limitations of device performance. The scope of this paper is necessarily limited, and the goals are to describe recent results that demonstrate the importance of advances in device understanding on SLM operation, as well as to point out a number of promising novel SLM technologies. This focus has necessitated some selectivity in the types of devices treated. Spatial light modulators based on thermoplastic, deformable oil film, deformable membrane, electrooptic ceramics (PLZT), magnetooptic, photochromic and photodichroic effects have been reviewed previously (see Refs. 1-7). In Section III, progress in electrooptic spatial light modulators is described, including the Pockels Readout Optical Modulator (PROM), the Microchannel Spatial Light Modulator (MSLM), and the photo- and electron beam-DKDP devices. Section IV covers recent advances in liquid crystal spatial light modulators, including the hybrid field effect liquid crystal light valve (LCLV), the Si-addressed LCLV, and the newly developed CCD-addressed LCLV. In addition, two novel liquid crystal devices are described for nonlinear processing applications: the multiple period LCLV for parallel A/D conversion and the variable grating mode liquid crystal device for implementation of arbitrary point nonlinearities and optical logic and computing applications. Photorefractive effect spatial light modulators for applications in correlation/convolution, edge enhancement, double-exposure holographic testing, and phase conjugate image generation are described in Section V.

## III. Electrooptic Spatial Light Modulators

Electrooptic spatial light modulators (ESLM's) have been investigated for numerous applications in coherent optical signal processing, including the Pockels Readout Optical Modulator (PROM) (9), the Microchannel Spatial Light Modulator (MSLM) (10,11), the electron beam-DKDP SLM (TITUS) (12,13), and the photo-DKDP SLM (PHOTOTITUS) (14,15). Such devices record two-dimensional image information in the form of a charge pattern which modulates the voltage across an active (electrooptic) single crystal layer. The charge pattern is typically induced either by intensity modulation of light incident on a photoconductive layer, or by direct electron beam charge deposition. More recently, image storage in ESLM's has been accomplished by exposure to x-ray sources (13,16) and by high energy beam charge implantation (13,17). In each case, the image-wise modulated voltage is sensed using polarized light by means of the linear electrooptic effect.

Since all four of these electrooptic spatial light modulators have a number of similar operational features, the description of their essential characteristics will be simplified by examining the physical operation of the PROM first as an example, followed by discussions of each of the other devices.

### III.1 Pockels Readout Optical Modulator (PROM)

A schematic diagram of a typical PROM structure is shown in Figure 1. The device is comprised of a photoconductive, electrooptic crystal wafer ($Bi_{12}SiO_{20}$) sandwiched between two thin dielectric blocking layers. The blocking layers are coated with transparent electrodes. The operation of the PROM is shown schematically in Figure 2. A voltage (typically 2 kV) is applied to the device, dividing between the dielectric and electrooptic layers in inverse proportion to the capacitance of each layer. A pulse of uniform uv illumination generates free electron-hole pairs which are subsequently separated by the applied field. Since the mobility-lifetime product of electrons is much larger than for holes in $Bi_{12}SiO_{20}$, illumination of the negative electrode provides the most efficient field reduction per absorbed photon. In this "erase/prime" step (Figure 2), sufficient uv illumination is provided to effectively cancel the internal field in the BSO layer. Note that the dielectric blocking layer thicknesses must be sufficient to witnstand 1/2 $V_{app}$. When the applied bias $V_{app}$ is now reversed, the applied field and the field due to the stored (displaced) charges add rather than cancel, resulting in approximately $2V_{app}$ dropped across the BSO layer. Illumination from the negative electrode side with image-wise modulated blue light causes electron-hole pair generation and subsequent charge separation at a rate proportional to the incident intensity at each location, giving rise to a reduction in voltage across the electrooptic crystal in illuminated regions. Since in the absence of illumination (subsequent to the writing process) the dielectric relaxation time ($\varepsilon\varepsilon_0\rho$) of bismuth silicon oxide is unusually large (of order several thousand seconds), the electron distribution is trapped in the bulk; hence, the written charge distribution is stored. The resultant two-dimensional voltage distribution induces a birefringence (through the linear longitudinal electrooptic effect) which alters the polarization of linearly polarized readout light oriented to bisect the principal birefringent axes, producing an image-wise modulated amplitude when viewed through a crossed analyzer (see Figure 3). The readout amplitude transmitted through a PROM between ideal crossed polarizers may be expressed as

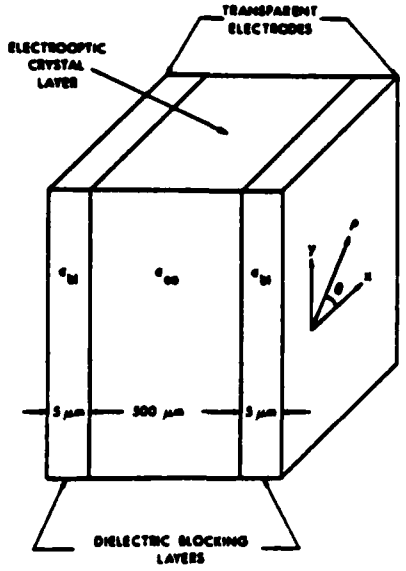


Figure 1. Structure of a typical PROM. In current PROM's, the electrooptic crystal layer is bismuth silicon oxide ($Bi_{12}SiO_{20}$, $\varepsilon_{eo}=56\varepsilon_0$) and the dielectric blocking layers are parylene C ($\varepsilon_{bl}=3\varepsilon_0$).

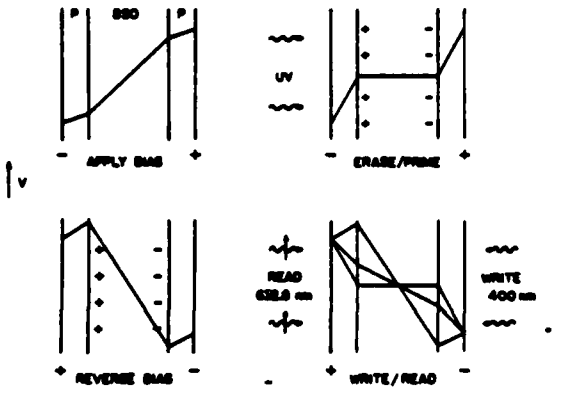


Figure 2. Diagram of basic PROM operational sequence, showing the potential distribution within the parylene and $Bi_{12}SiO_{20}$ layers following each step in the erase/prime and write/read sequence.

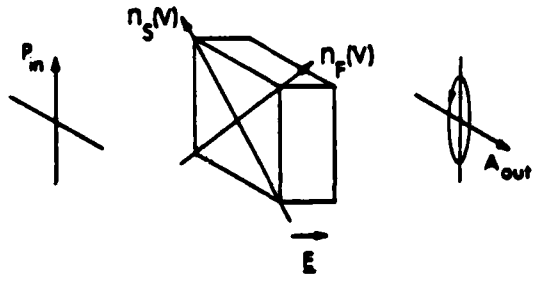


$$A_{out} = A_0 \sin\left(\frac{\pi V}{2 V_\pi}\right) \sim A_1 V \qquad \{V \ll V_\pi\}$$

Figure 3. Electrooptic spatial light modulator readout configuration through crossed polarizers.

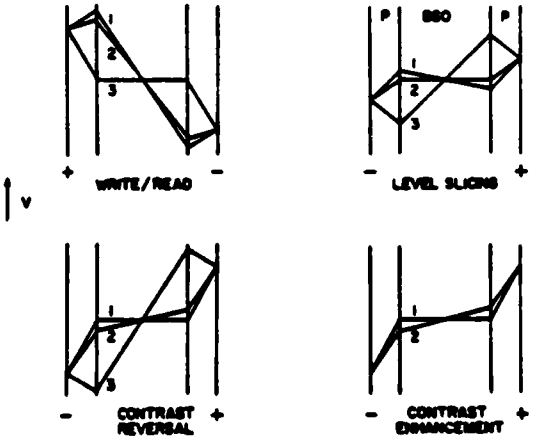


Figure 4. Diagram of several PROM optical processing operations. Shown are the potential distribution within the parylene and $Bi_{12}SiO_{20}$ layers for the negative write/read, level slicing, contrast reversal, and contrast enhancement functions.

$$A(x,y) = \frac{A_0}{\sqrt{2}} \sin\left(\frac{\pi V(x,y)}{2V_{\lambda/2}}\right) \quad (1)$$

where $A_0$ is the incident readout light amplitude, $V_{\lambda/2}$ is the half-wave voltage of the electrooptic crystal, and $V(x,y)$ is the voltage across the electrooptic crystal at image coordinate $(x,y)$. It should be noted that in the above expression it is assumed that the readout wavelength and intensity are chosen such that insignificant photoconductive charge redistribution occurs, and the effects of natural optical activity in the bismuth silicon oxide crystal may be neglected (18,19). Thus the output amplitude is a monotonic function of the input intensity (for applied voltages less than the electrooptic half-wave voltage); such a transfer relationship is desirable for incoherent-to-coherent conversion and subsequent coherent signal processing operations.

The write/read mode described above is presented again in Figure 4, where three different levels of exposure are depicted. Note that in this mode of operation a negative of the input image is produced on readout. An image positive may be created easily by reversing the sense of the applied voltage, creating a contrast reversal, as shown. In addition, contour generation (level slicing) is achievable by varying the external bias, causing various internal field regions to be cancelled by the external applied field. In the illustration chosen in Figure 4, the region labeled "2" has been brought to the null condition by suitable reduction of the applied voltage. Contrast enhancement of highly underexposed images results from external bias adjustment to disperse the exposed regions about the zero field condition, as shown.

Recent progress has been achieved in the analysis of the fundamental resolution limitations of the PROM as well as of the other electrooptic spatial light modulators (20-22). From the nature of Eq. (1), it can be seen that the resolution of an electrooptic spatial light modulator depends directly on the relationship between a periodic (spatial frequency $\omega$) variation in the writing intensity, and the resultant spatial modulation of the voltage across the electrooptic crystal. The cubic symmetry (I23) of bismuth silicon oxide in conjunction with the orientation of the electrooptic crystal slice (<001>) assures that only longitudinal components of the electric field contribute to the induced birefringence through the electrooptic effect. Therefore, the modulation in output amplitude [see Eq. (1)] depends only on the voltage difference $V(x,y)$ between opposite sides of the electrooptic crystal at each image point $(x,y)$. In the absence of significant two-dimensional diffusion effects in comparison with the drift-aided charge separation of photogenerated electron-hole pairs, $V(x,y)$ will be a function of the dielectric constants and thicknesses of the electrooptic and blocking layers, the locations (in the z-direction) of the trapped hole and electron distributions resulting from the writing (image recording) process, and the spatial frequency of the charge (writing intensity) modulation in the $(x,y)$ plane.

From an exact solution of the device multi-layer structure containing a single point charge, the Fourier transform of the voltage distribution (which can be directly related to the modulation transfer function) was derived as a function of the charge location within the electrooptic crystal and the device layer parameters (20). Since the modulation transfer function (MTF) for a given device will be both exposure and modulation dependent, a more fundamental indication of expected device performance is obtained by presentation and discussion of the un-normalized $[V(\omega)]$ and normalized $[V(\omega)/V(0)]$ potential difference functions.

At this point, it should be mentioned that the un-normalized potential differences $V(\omega)$ and the normalized function $V(\omega)/V(0)$ have a direct interpretation useful for both comparison of distinct devices of different constitutive characteristics, and for comparison of the implications of distinct charge distributions (resulting from different exposure parameters) within a given device. In particular, graphs of $V(\omega)$ as a function of $\omega$ parameterized by different device constitutive properties assume equal exposure conditions (identical charge distributions) while graphs of $V(\omega)/V(0)$ assume optimum exposure conditions for each compared device (i.e., sufficient exposure for each device such that $V(\omega)$ is optimized in the limit of low spatial frequencies. These types of comparisons are familiar from the case of photographic film (23) where the typical resolution/sensitivity trade-off forces a similar comparison of film properties on the basis of either response to equal exposure, or response to optimum exposure (see Figure 5).

This situation is graphically illustrated by reference to Figures 6 and 7, which depict the spatial frequency dependence of $V(\omega)$ and $V(\omega)/V(0)$ for PROM device parameters as shown in Figure 7, with the dielectric constant of the dielectric blocking layer as a parameter. The effect of increasing the blocking layer dielectric constant is seen to reduce the device sensitivity (see Figure 6), while increasing the high spatial frequency response for optimum exposure in both cases (see Figure 7). In Figures 6 and 7, a single point charge is located

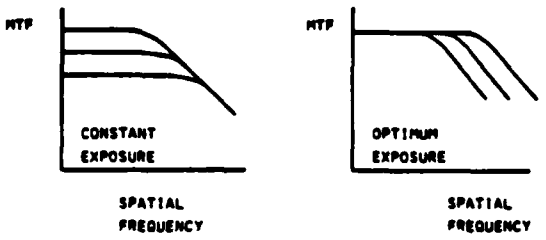


Figure 5. Resolution/sensitivity tradoff for photographic film. The unnormalized curve shows the reduction in sensitivity that accompanies increased resolution capability.

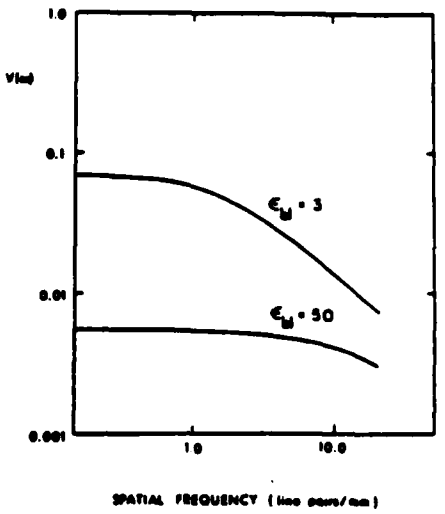


Figure 6. Effect of dielectric blocking layer dielectric constant on the spatial frequency response of $V(\omega)$. A symmetric PROM device is assumed, with geometric and constitutive parameters as shown in Figure 1.

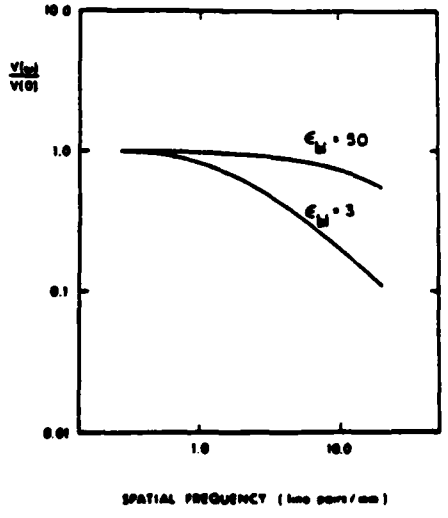


Figure 7. Effect of dielectric blocking layer dielectric constant on the spatial frequency response of $V(\omega)/V(0)$.

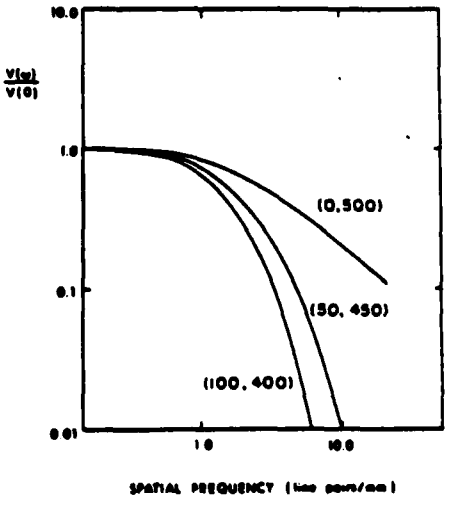


Figure 8. Effect of longitudinal charge position within the electrooptic crystal layer on the spatial frequency response of $V(\omega)/V(0)$. Note the marked attenuation of the high spatial frequency response as the charges are increasingly displaced from their respective interfaces.

at one of the dielectric blocking layer/electrooptic crystal interfaces.

The dependence of the spatial frequency response on the dielectric constants and thicknesses of the dielectric blocking layers (as shown in Figures 6 and 7, and in Figures 5 and 6 of Ref. (20)) indicates that new PROM devices can be envisioned with modulation transfer functions constant to much higher spatial frequencies than are characteristic of presently available devices. Gains in MTF behavior due to choice of dielectric blocking layer properties will be accompanied by an overall reduction in device sensitivity. Such new devices, however, would provide significantly improved image fidelity and resolution in applications where requirements on device sensitivity can be relaxed (as is the case with photographic film). In order to improve PROM resolution, high dielectric constant, high dielectric breakdown strength, high resistivity dielectric blocking layers are required.

In an effort to understand the effects of exposure-induced charge distributions throughout the bulk of the electrooptic crystal layer on PROM resolution, solutions for cases involving multiple point charges were obtained by a linear superposition of the solutions for each separate point charge (21). In particular, the effect of an electron-hole pair can be modeled if the point charges are assigned opposite signs. The results of such a calculation as a function of the charge separation are shown in Figure 8. In this calculation, the hole and electron were assumed initially constrained to opposite interfaces, and were subsequently displaced symmetrically into the bulk of the electrooptic crystal layer. Three cases are depicted in Figure 8, in which the hole and electron were first constrained to opposite dielectric blocking layer/electrooptic crystal interfaces (0,500), and were subsequently displaced symmetrically into the electrooptic crystal layer by 50 μm (50,450) and 100 μm (100,400), respectively. From Figure 8, it is observed that charges displaced from the dielectric blocking layer/electrooptic crystal interfaces strongly degrade the high spatial frequency response. In addition, such displacement reduces the sensitivity at low spatial frequencies (21).

An estimate of the device spatial frequency response resulting from optical exposure may be obtained from iterative solutions of the charge transport equations under simulated exposure conditions (24,21). Sample charge distribution results corresponding to exposure wavelengths of 450 nm and 375 nm for device constitutive properties as described in Figure 1 are shown in Figure 9. The absorption coefficients ($\alpha$= 30 $cm^{-1}$ @ $\lambda$ = 450 nm; $\alpha$ = 830 $cm^{-1}$ @

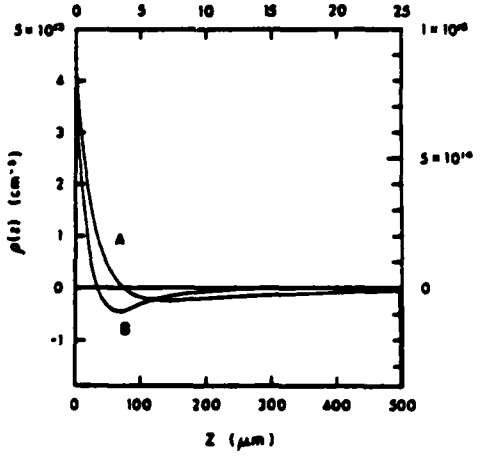


Figure 9. Longitudinal charge distribution $\rho(z)$ calculated numerically using an iterated electron drift model for two exposure wavelengths (and corresponding absorption coefficients). Curves A and B result from exposure wavelengths of 450 nm and 375 nm, respectively. The left and lower scales correspond to curve A, while the right and upper scales correspond to curve B.

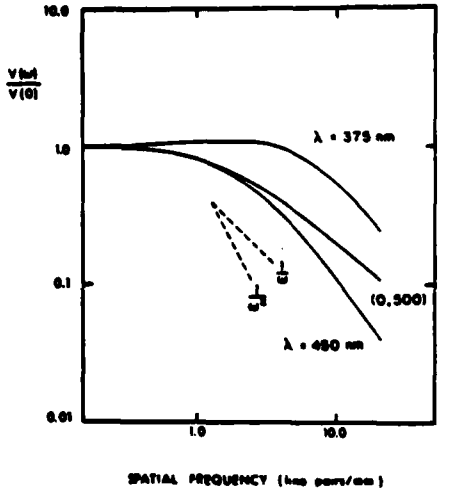


Figure 10. Normalized frequency responses $V(\omega)/V(0)$ for the calculated longitudinal charge distributions of Figure 9. The normalized response of point charges at the two interfaces is included for comparison.

$\lambda$ = 375 nm) are such that the 375 nm case is characterized by close confinement of the hole distribution near the input interface with shallow electron penetration into the bulk. In contrast, the 450 nm case is characterized by significant electron-hole pair generation throughout the electrooptic crystal layer, which results in a sizeable accumulation of electrons at the far interface (as shown in Figure 9).

The spatial frequency responses calculated from these widely disparate charge distributions are shown in Figure 10. The closely confined charge in the 375 nm case produces a nonmonotonic spatial frequency response (20-22), whereas the volume excitation present in the 450 nm case generates a monotonic frequency response. In both cases, the high spatial frequency response asymptotically approaches $\omega^{-2}$, in contrast to the $\omega^{-1}$ asymptote applicable to cases where all charges are confined to the interface (21).

The effect of exposure-induced charge distribution throughout the bulk of the electrooptic crystal layer is seen to have a marked effect on the high spatial frequency response characteristics of the image storage process. The optimum resolution and sensitivity within a given PROM device structure are obtained when the hole distribution is constrained to the interface nearest the negative electrode, and the entire electron distribution is swept to the interface nearest the positive electrode during the writing cycle. The actual resolution and sensitivity obtained for a given device are thus strongly dependent on the absorption coefficient of the electrooptic layer at the writing illumination wavelength, on the external applied voltage and voltage division between the multiple layers during the writing cycle, and on the mobility-lifetime product of photogenerated electrons in the electrooptic crystal. Such bulk charge distribution effects will also strongly affect the resolution and sensitivity for cases where the image-wise modulated charge pattern is induced by high energy electron beam (13,17) and x-ray (16 sources. Specification of the exposure wavelength (in addition to exposure level, bias exposure, operational mode, and MTF test method (8)) is thus seen to be critical for proper device evaluation and comparison. Research on the physics of the device operational modes (prime, erase, exposure, and "superprime" (9)) utilizing the charge transport and resolution models described above is currently in progress.

The PROM will continue to be utilized in applications requiring either temporal storage or time integration. Current PROM's exhibit excellent contrast and Fourier plane signal-to-noise ratio, moderate sensitivity and resolution, and provide a number of active image preprocessing functions. The principal shortcomings of the PROM relative to certain applications are nonlinear sensitometry effects at high exposure levels, the necessity of blue write wavelengths for optimum sensitivity and resolution, and the lack of a completely nondestructive readout mode (which limits the available readout gain).

### III.2 Microchannel Spatial Light Modulator (MSLM)

The Microchannel Spatial Light Modulator (MSLM) (10,11) is under development for coherent optical processing applications requiring high sensitivity, such as stellar speckle interferometry or low-visibility optical communication. The MSLM is shown schematically in Figure 11, consisting primarily of an evacuated cell (which may be either sealed or demountable), a photocathode, a microchannel array plate, a dielectric mirror, and a thin electrooptic crystal layer. The microchannel array plate consists of an array of semiconducting glass-lined pores (~10 $\mu$m diameter), and is bounded by two semi-transparent electrodes. The pores are oriented at an angle to the plate normal, so that incident electrons impact the pore walls, giving rise to electron multiplication by successive secondary electron emission. The microchannel plate is separated from the electrooptic crystal by a gap (~500-1000 $\mu$m). In combination with the dielectric multilayer mirror, this gap serves a voltage division function similar to the dielectric blocking layer in the PROM.

In operation, an initial electron distribution is emitted from the photocathode in response to an incoherent or coherent control image (within the wavelength region of photosensitivity of the photocathode). After electron multiplication in the appropriately biased microchannel array plate, the amplified electron image is proximity focused onto the dielectric mirror. Either positive or negative charge distributions can be written on the mirror surface, depending on whether the ratio of secondary (emitted) electrodes to primary (incident) electrons is greater or less than unity (see Figure 12). The charge distribution induces a spatially varying longitudinal electric field field in the electrooptic crystal layer, which modulates the local refractive indices through the Pockels effect. As in the case of the PROM, either phase or amplitude modulation can be achieved on reflective readout by appropriate readout polarization and/or orientation of the electrooptic crystal. In current devices (11), both $LiNbO_3$ and $LiTaO_3$ z-cut plates have been utilized to produce pure phase modulation.

The dynamic operation of the MSLM can be understood with reference to Figure 13, which depicts lines of stable equilibria (full bold lines) and a line of unstable equilibria (broken bold line) in the state-space of the device (gap energy $eV_g$ as a function of

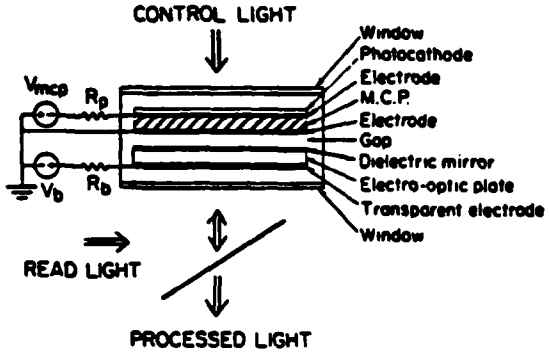


Figure 11. The microchannel spatial light modulator (MSLM): proximity-focussed configuration. (After Warde, Ref. 10).

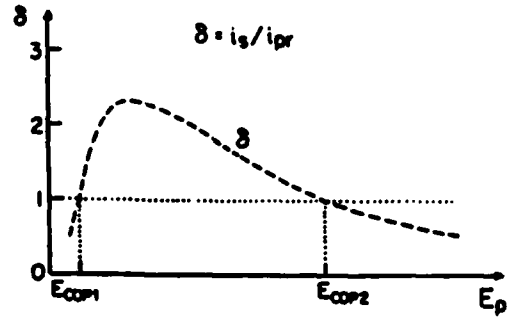


Figure 12. Secondary electron emission characteristics of a typical insulator. (After Warde, Ref. 11).

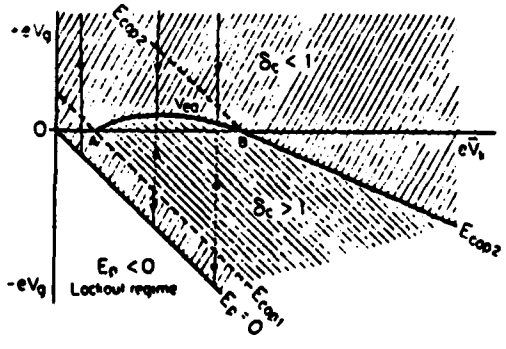


Figure 13. State-space plot illustrating the dynamic operation of the MSLM. (After Warde, Ref. 11).

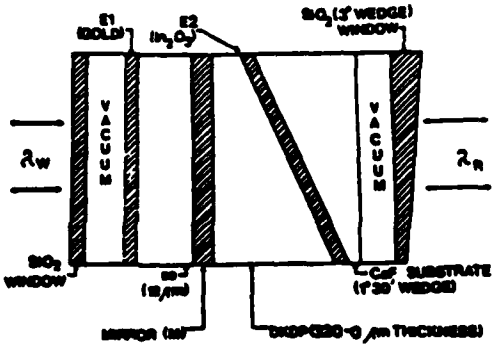


Figure 14. Schematic diagram of the photo-DKDP spatial light modulator. (After Casasent, Ref. 14).

effective cathode potential $e\bar{V}_k$). The effective cathode potential is a function of the secondary emission characteristics of the dielectric mirror/crystal surface, the gap voltage $V_g$, the microchannel plate voltage $V_{mcp}$, and the shape of the electron energy distribution emitted from the microchannel plate. The parameter $\delta_c$ is the ratio of secondary electrons collected by other parts of the system to primary electrons. With no illumination incident on the photocathode, the gap voltage may be altered by raising or lowering $V_b$ (see Figure 11). If the gap voltage is initially biased into the region where $\delta_c<1$, illumination of a particular region of the photocathode will induce electron deposition on the crystal, causing the local gap voltage to drop along one of the vertical lines shown in Figure 13. Saturation in this region will occur when the total local exposure exceeds the level required to drive the gap voltage onto the stable equilibrium curve. The image can be erased by subsequently lowering the bias into the region $\delta_c>1$ and uniformly or selectively illuminating the photocathode, such that net electrons are emitted from the surface, raising the local gap voltage along one of the dashed lines shown. The lower dashed bold line labeled $E_{cop1}$ represents unstable equilibria, since lowering of the gap voltage below this line causes entry to a second $\delta_c<1$ region, such that illumination drives the gap voltage toward the line $E_p = 0$ along which the incident primary electron energy at the crystal surface is zero. Hence once a local region of the crystal surface resides on this line, the local potential cannot be further altered without changing the bias level $V_b$.

Charge distributions have been successfully stored directly on a 500 μm thick $LiTaO_3$ crystal (without a dielectric mirror) for periods as long as two weeks (11). Although the surface and bulk resistivities of $LiTaO_3$ are such as to result in large dielectric relaxation time constants, it is likely that deep surface trap states with extraordinarily long relaxation times must be involved in the electron-induced charge storage mechanism. Research on the nature of such trap levels by spectroscopically selective photoemission is currently in progress (25). The existence of image storage capability can be used in concert with programmable variation of the bias voltage $V_b$ to allow implementation of several useful image preprocessing functions. Image addition and subtraction can be performed by temporal integration and sequential selective write/erasure, respectively. Contrast enhancement and reversal can be implemented by bias adjustment following exposure, as described earlier in the case of the PROM. Utilization of the erasure saturation characteristic described above provides a form of variable level thresholding. In addition, edge enhancement is possible due to variation of the secondary electron emission characteristics in the presence of fringing fields in a region of exposure discontinuity.

One of the most promising features of the MSLM configuration is its inherent flexibility in both choice of electrooptic crystal and choice of photocathode material (which together determine the readout and writing wavelength response regions for the device, respectively). Since the microchannel array plate is inherently responsive from x-ray to near-uv wavelengths, no photocathode is required for operation in this regime. The device exhibits extremely high sensitivity, and the physical separation of the write and read functions allows further inherent throughput gain in image amplifier applications. The combination of long term storage with (at present) near-TV frame rates allows great flexibility in system design. Current MSLM's exhibit resolutions (~3 lp/mm) limited by the thickness of the electrooptic crystal, the relatively thick dielectric blocking layer (gap), and the low dielectric constant of the gap. Although the implementation of the active image preprocessing functions described above involves rapid programmability of relatively hign voltages, the almost purely capacitive loading presented by the MSLM should minimize such difficulties.

### III.3 Photo-DKDP Spatial Light Modulator

The photo-DKDP Spatial Light Modulator (also called "PHOTOTITUS" (15)) has been developed and is currently manufactured by Laboratoires d'Electronique et de Physique Appliquee in France, and has only recently become available for experimentation in the United States (26). A schematic diagram of the photo-DKDP device is shown in Figure 14. A wedged electrooptic crystal layer of deuterated potassium dihydrogen phosphate (DKDP) is sandwiched between a dielectric mirror and a transparent electrode on a CaF substrate. A photoconductive layer of amorphous selenium is deposited on the dielectric mirror, and is overcoated with a second transparent electrode. This assembly is incorporated in an evacuated two-stage Peltier cooler to allow operation near the ferroelectric Curie point of DKDP (~-50°C), which enhances the resolution and storage time of the device while significantly reducing the half-wave voltage of DKDP to approximately 300V. This reduction in operating voltage is critical in order to allow the incorporation of the Se photoconductor, which effectively separates the read and write functions.

Operation of the photo-DKDP SLM is similar in most respects to the PROM operational modes described above, as is depicted schematically in Figure 15. In Figure 15(a), initial application of a positive voltage $V_0$ to the Se electrode produces a voltage division among the various layers. Exposure to appropriate wavelength write illumination (typically 440-520 nm) induces hole transport across the Se layer, reducing the voltage across the

photoconductor and increasing the voltage across the electrooptic DKDP crystal (Figure 15(b)). In Figure 15(c), the electrodes have been short-circuited to produce a positive readout image. The small residual voltage $V_2$ in the dark (unilluminated) region arises from the finite dark conductivity of the photoconductive layer during the writing cycle. Erasure is accomplished by subsequent uniform illumination of the photoconductor to induce electron transport to the mirror interface, thereby reducing the stored electrostatic field to zero. It should be noted that exposure wavelengths on the long wavelength side of the selenium photoconductivity response will initiate bulk electron-hole pair generation with resultant ambipolar diffusion. Since the mobility-lifetime product for electrons is significantly smaller than that for holes, sensitometry curves resulting from primarily electron transport differ from those characterized by primarily hole transport. These differences are especially important for image subtraction applications (14).

The photo-DKDP spatial light modulator has been utilized in a wide range of coherent optical data processing applications, and has demonstrated processing accuracies comparable to those achievable with photographic film inputs (26). The device as presently configured has moderate sensitivity, storage capability, and the availability of image subtraction in addition to other image preprocessing functions. The resolution is enhanced relative to that exhibited by current PROM's due to the increase in dielectric anisotropy resulting from Curie point operation. On the other hand, this very feature limits the contrast available in non-collimated readout configurations due to large natural birefringence. The necessity of cooling to achieve proper device performance can led to nonuniformities in device characteristics, since small temperature differences yield large changes in the magnitude and ratio of the dielectric constants. The hygroscopic nature of DKDP necessitates the use of an evacuated cell; however, even with this constraint the reported optical quality of current devices is excellent (14).

### III.4 Electron-Beam DKDP Spatial Light Modulator

The electron-beam DKDP SLM has been under development for many years for coherent optical processing applications, and has been implemented during the past ten years in two similar versions (12,13). The primary difference between this electrooptic spatial light modulator and the three previously described is the mode of address. As shown in Figure 16,

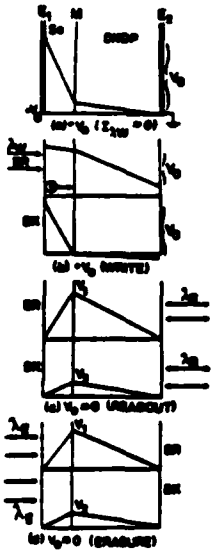

Figure 15. Distribution of voltage as a function of distance in the photo-DKDP SLM at different operational steps for illuminated (BR) and unilluminated (DK) regions. (After Casasent, Ref. 14).

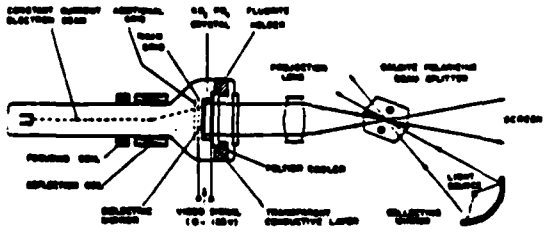

Figure 16. Electron-beam-addressed Pockels effect imaging device using a DKDP ($KD_2PO_4$) crystal plate operated in the reflection mode. A constant current electron beam is used and the video signal is applied between the transparent conductive layer and the main grid placed at about 40 μm from the target. (After Marie, Ref. 13).

charge is deposited on a dielectric mirror/electrooptic crystal layer by an axial (13) or off-axis(12) electron gun driven in a raster pattern and grid-modulated by a serial (usually video) input. The physics of operation ot this device thus combines several features of the MSLM and the photo-DKDP SLM. The design, operation, and applications of this SLM have been extensively documented (12,13) and are not treated herein. In addition to a wide range of applications in optical data processing, the electron-beam DKDP spatial light modulator has been successfully utilized for large-screen multi-color television projection display (13).

## IV. Liquid Crystal Spatial Light Modulators

A number of spatial light modulator technologies are based on the utilization of liquid crystals. The attractiveness of liquid crystal layers for this application arises primarily from several unusual characteristics of nematic liquid crystals, including large dielectric anisotropies (resulting in low operating voltages), large birefringences (resulting in sizeable polarization effects even in the thin cells necessary for rapid response times), and a wide variety of possible alignment configurations. In this section, several liquid crystal spatial light modulators are discussed, including some potentially exciting modifications of the Hughes liquid crystal light valve, as well as two novel liquid crystal devices for nonlinear coherent optical processing applications.

### IV.1 Hybrid Field Effect Liquid Crystal Light Valve

By far the most advanced spatial light modulator employing a liquid crystal layer as the active electrooptic element is the hybrid field effect liquid crystal light valve (LCLV) (27,28). The typical device configuration of the LCLV is presented in Figure 17. A transparent electrode and a chemically inert insulating layer ($SiO_2$) are deposited on an optically flat glass substrate. The insulating $SiO_2$ layer prevents dc current flow through the device while simultaneously functioning as a preferred direction alignment layer for the liquid crystal and as an ionic blocking layer to prevent cell poisoning effects. A biphenyl nematic liquid crystal layer is confined laterally by a deposited thin film spacer, and longitudinally by a second $SiO_2$ alignment layer. The liquid crystal layer is photoconductively-addressed by a thin film of cadmium sulfide deposited on a transparent electrode-coated optically flat glass substrate. Separation of the read and write functions is accomplished by incorporation of a dielectric mirror and cadmium telluride light blocking layer between the liquid crystal layer and the CdS photoconductor, as shown.

In order to optimize the electrooptic properties of the liquid crystal layer for coherent optical processing applications, a hybrid field effect operational configuration is employed (27). In this configuration, the uniaxial liquid crystal molecules are preferentially aligned (by means of appropriate surface treatment of the $SiO_2$ alignment layers) with their long axes parallel to the electrode surfaces (homogeneous alignment). In addition, the alignment directions on the two opposed surfaces are oriented to form an included angle of 45°. This 45° twist imparts a continuous rotation of the liquid crystal molecules from one surface to the other, as shown schematically in Figure 18. Since the nematic liquid crystal employed in this device exhibits large birefringence (difference in refractive indices for light polarized parallel and perpendicular to the molecular long axis), the resultant twisted layer can be modeled as a succession of thin birefringent layers, each oriented at a slight angle with respect to the immediately preceding and following layers. Such an optical configuration has been shown to be equivalent under certain conditions to a purely optically active layer (29), so that the polarization of light traversing the layer undergoes a pure rotation of 45°.

The operation of the hybrid field effect liquid crystal layer can be explained with reference to Figure 19. In the "off" state with no voltage applied across the liquid crystal layer, input light polarized parallel to the preferential alignment direction of the entrance electrode experiences a positive 45° polarization rotation on traversing the layer, and a negative 45° rotation following reflection from the dielectric mirror and a second pass through the cell. Hence the emergent polarization is parallel to the incident polarization, and can be extinguished with a crossed analyzer to provide a dark off state. When voltage is applied across the liquid crystal layer, the resulting longitudinal electric field tends to align the liquid crystal molecules with the field direction (due to the positive dielectric anisotropy of the molecules). This "tilt" toward perpendicular alignment from parallel alignment varies continuously between the two surfaces, and is largest in the center of the layer where the surface alignment forces are weakest. Due to the physical nature of the intermolecular forces, as the tilt angle increases in a given layer, the transmittance of the twist angle is weakened. Hence as the voltage is increased, molecules in the layer center approach a perpendicular orientation, allowing molecules near each surface to relax toward an untwisted state with orientation parallel to the induced surface orientation. The polarization of incident light will thus be relatively unaltered by the front half of the cell on the first pass, but will encounter a birefringent layer oriented at 45° in the rear half of the cell, causing the polarization of light striking the dielectric mirror to be elliptical. Since birefringence adds on reflection (rather than cancels as in the case of optical activity), the emergent polarization from the cell will in

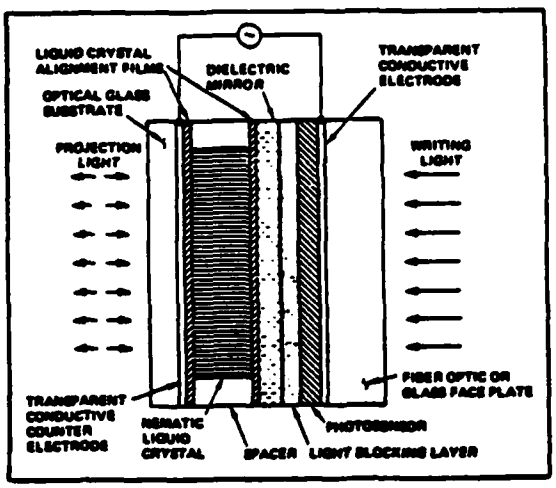


Figure 17. Cross-sectional schematic of the hybrid field effect liquid crystal light valve. (After Bleha, Ref. 27).

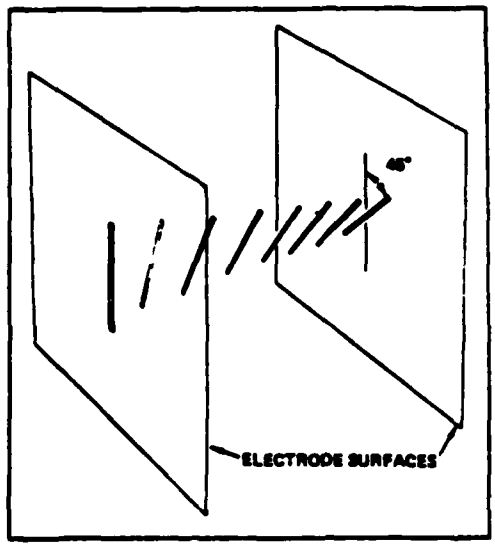


Figure 18. Schematic of 45° twisted nematic liquid crystal alignment (hybrid field effect model). (After Bleha, Ref. 27).

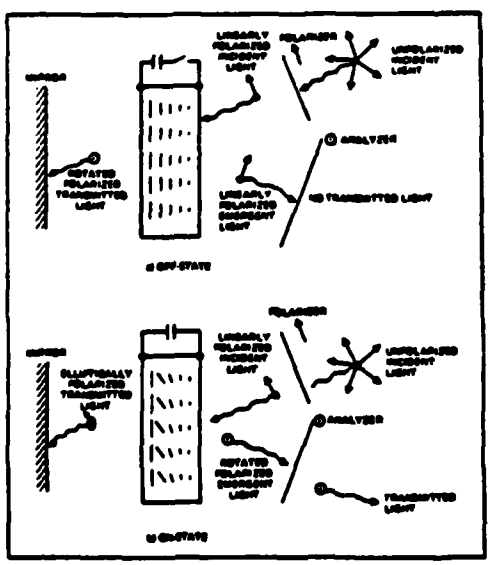

Figure 19. Operation of the hybrid field effect liquid crystal light valve: (a) the off-state; (b) the on-state. (After Bleha, Ref. 27).

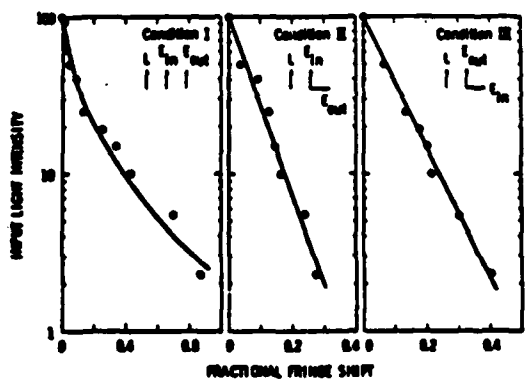


Figure 20. The phase response (in multiples of $2\pi$ rad) of the hybrid field effect LCLV as a function of input irradiance. The arrows indicate the relative configuration of the polarization of the coherent beam entering the device ($E_{in}$), the molecular orientation at this point (L), and the orientation of the analyzer ($E_{out}$). (After Gara, Ref. 37).

general be elliptical, such that the appropriate component will be passed by the crossed analyzer. A detailed analysis of the cell transmission as a function of voltage has recently been performed (30-32).

In order to function as an optical-to-optical converter, the LCLV requires a mechanism for spatially-dependent variation of the liquid crystal layer voltage in response to an input image intensity distribution. This function is performed by the CdS/CdTe heterojunction in series with the capacitance of the multilayer dielectric mirror. Analysis of the operation of this structure (33,34) shows that photocapacitive as well as photoconductive processes must be considered to fully explain the observed LCLV sensitometry behavior. The LCLV requires low operating voltages (5-10 V rms) at intermediate frequencies (1-10 kHz).

The principal advantages of the hybrid field effect liquid crystal light valve for coherent optical processing applications are good sensitivity and resolution characteristics, full separation of the write/read functions (which allows for the possibility of single wavelength optical feedback, for example), simplicity of operation, and low power requirements. The sensitometry characteristics of the LCLV depend rather strongly on the magnitude and frequency of the applied voltage (35,36); this feature can be used to advantage in some applications, but also contributes to device nonuniformity effects (36). Device uniformity in both the off and on states has been shown to be a quite sensitive function of liquid crystal layer thickness (30-32), which is particularly difficult to control in such a multilayer structure. Device reproducibility (both within a given device and from device to device) is dependent primarily on the deposition characteristics of the cadmium sulfide and cadmium telluride layers, since the optical and electronic properties of II-VI compounds are strong functions of deposition conditions. The device response time varies as a function of input intensity (primarily due to the characteristics of the CdS photoconductor), which when coupled with the lack of storage capability leads to temporal variations of the diffracted orders in the Fourier plane during operation, and in some cases to image ghosting with slow decay time constants in brightly exposed regions of the images. A number of these difficulties are due primarily to the utilization of CdS as the photoconductor, and should be eliminated with the advent of the Si-LCLV described below. Finally, it is important to note that the hybrid field effect structure gives rise to an input-intensity-dependent phase shift of the output wavefront that is a further function of the relative orientation of the LCLV, polarizer, and analyzer (37).

## IV.2 Silicon Liquid Crystal Light Valve

Recently, a major potential technological advance in liquid crystal light valve technology has been reported (38), resulting from incorporation of a silicon photoconductor in a hybrid field effect device. The structure of this novel light valve is shown in Figure 21. The active liquid crystal layer is the same as that described previously for the CdS-addressed LCLV. The CdTe layer has been replaced with a cermet light blocking layer, composed of a multilayer structure of metallic (tin) islands dispersed in insulating ($SiO_x$) layers. A silicon dioxide gate insulator is coupled to a very high resistivity $\pi$-silicon wafer to form an MOS structure. A thin degenerately doped $p^{++}$ layer forms the rear device electrode, and is overcoated with a thermally grown protective oxide coating. A square p-doped grid just beneath the $SiO_2$ gate insulator serves to enhance the device resolution (as described below), and $p^+$ isolation channel stops surround the periphery of the wafer to minimize minority carrier injection into the active region.

When the $Si/SiO_2$ interface is biased into accumulation, recombination at the interface erases any residual image and readies the device for the active mode. The $Si/SiO_2$ interface is then biased into depletion (depleting not only the p-grid but also the entire $\pi$-silicon layer), and the $\pi$-silicon side is illuminated with the input image. Illumination produces local electron-hole pair generation near the back contact, with electrons subsequently swept to the $Si/SiO_2$ interface by the field across the $\pi$-silicon layer. Calculations show there to be only negligible spreading of the swept-electron distribution during traversal across the wafer (39). In addition, the depleted p-grid is more negative than the surrounding $\pi$-regions, which acts to focus the incoming electrons into the $\pi$-buckets near the $Si/SiO_2$ interface. The p-grid also prevents significant charge spreading during the readout cycle. Due to the sequential accumulation/depletion cycle, the mode of operation is fully ac, which significantly extends the lifetime of the liquid crystal layer. Once the image-induced charge pattern has been established at the $Si/SiO_2$ interface, the electric field across the liquid crystal layer will be modulated such that the device may be read out in reflection just as described above for the CdS/CdTe LCLV.

Current performance parameters of the Si/LCLV are quite encouraging, with limiting resolution of 25 lp/mm at present limited by a 20 μm period grid, 20 $\mu W/cm^2$ sensitivity, and a contrast ratio of 30:1 (39). The device has been successfully operated at TV frame rates. With the incorporation of a grid with 6 μm period, the limiting resolution should be

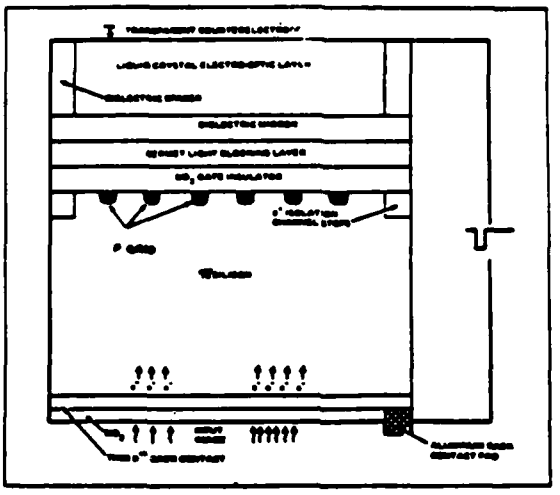

Figure 21. Schematic diagram of the photo-activated silicon liquid crystal light valve. (After Braatz, Ref. 38).

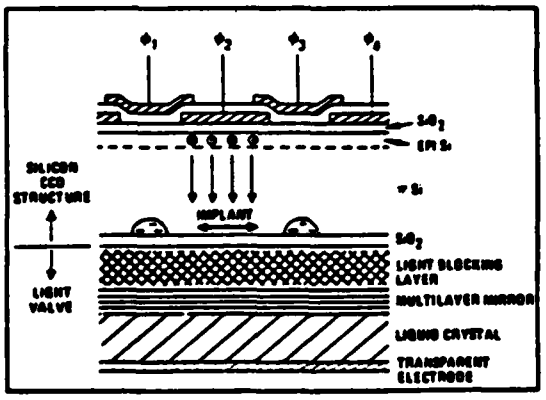


Figure 22. Cross-sectional schematic of the CCD-addressed liquid crystal light valve. (After Grinberg, Ref. 40).

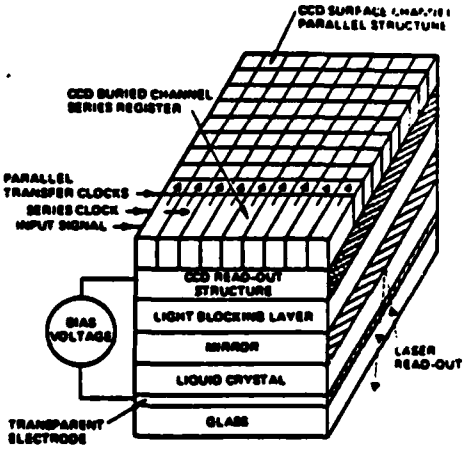


Figure 23. Functional schematic of the CCD-addressed liquid crystal light valve. (After Grinberg, Ref. 40).

extendable to 150 lp/mm. The liquid crystal layer is expected to accommodate such high spatial frequencies, since the presence of grid lines 3 μm wide has been observed in several test structures (39). The silicon photosensitivity spectrum extends from the near uv (400 nm) into the near ir (1.1 μm) with high quantum efficiency. Hence such Si-LCLV's should find numerous applications in optical data processing, including real-life scene input situations.

## IV.3 CCD-Addressed Liquid Crystal Light Valve

Much of the new technology evident in the Si-LCLV is being utilized to mate a high bandwidth serial/parallel CCD register to a modified Si-LCLV for optical processing applications requiring a serial input format (40). As illustrated in Figure 22, the CCD-LCLV is similar in configuration to the Si-LCLV described above. The difference between the two consists primarily in the placement on the uppermost π-silicon surface of a surface channel CCD array. Proper sequencing of the clock lines $\phi_1$-$\phi_4$ propagates electron packets under each gate. Subsequent positive bias of the liquid crystal electrode drives the electron packets to the $Si/SiO_2$ interface, where they are focused and prevented from lateral diffusion by the implanted p-grid. A functional schematic diagram of the CCD array is shown in Figure 23. The input is serially transferred by the series clock into the CCD buried channel series register until an entire line of data is recorded. The line of data is then transferred in parallel to the adjacent CCD surface channel parallel structure as shown. When all CCD registers are full, representing a complete frame of input information, the bias voltage is changed to drive the entire stored electron packet array to the $Si/SiO_2$ interface. At this point, the two-dimensional image can be read out in reflection by polarized illumination from the liquid crystal side of the device, as shown. The buried channel serial array is necessitated by the 100 MHz design clock frequency, while the slower (100 kHZ) parallel array requires surface channel technology to allow for subsequent charge transfer to the $Si/SiO_2$ interface.

Current CCD-LCLV devices are 64x64 arrays of elements on 1.3 mil centers (total active area 83 mils square) (39). A 256x256 element array is presently under development, with an eventual goal of a 1000x1000 element array operating at 100 kHz per line. Such a device would operate at an overall frame rate approaching 100 HZ. Several difficult technical problems currently under investigation include the quality of image transfer from the CCD to the LC layer, development of the novel buried channel serial/surface channel parallel CCD approach, uniformity of processing of the very high resistivity π-silicon wafer, and the processing delicacy required for the 5 mil thinned wafers. Achievement of these design goals will represent a long-awaited major breakthrough in serial input/parallel output spatial light modulator technology.

## IV.4 Multiple Period Liquid Crystal Light Valve

A technique for optically performing parallel analog-to-digital conversion on incoherent two-dimensional inputs at real-time rates utilizing a multiple period liquid crystal light valve has been recently described (41). This MP LCLV is similar in construction to the hybrid field effect LCLV with the notable exception that the liquid crystal layer was homeotropically aligned (long molecular axes perpendicular to the electrode in the "off" state). The liquid crystal chosen has negative dielectric anisotropy, so that application of a voltage across the layer tends to rotate the molecules parallel to the electrodes. The magnitude of the rotation is a function of the applied voltage, so that readout light polarized at 45° with respect to the projection of the long molecular axis on the electrode surface (in the partially rotated state) will experience pure birefringence on traversal of the cell. For liquid crystals with large optical anisotropies (and for thick enough cells), the total phase retardation can be many multiples of 2π. Since the local voltage across the liquid crystal layer can be photoconductively-addressed, the overall relationship between the intensity transmittance of the device and the incident intensity at any point is given ideally by the sinusoidal ($\sin^2$) curve shown by a dashed line in Figure 24. In Figure 24(a), optical or electronic thresholding of the device transmittance at one half produces the least significant bit of the reflected or Gray code. Rescaling the input intensity by a factor of one half produces the device transmittance curve shown in Figure 24(b). Thresholding of this curve at one half produces the next most significant bit, and so on. Sequential rescaling as shown in Figure 24(a-c) produces the 3 least significant Gray-code bit planes in sequence. Parallel rescaling is also possible utilizing 3 periodically repeated attenuating strips on the device surface of attenuation factors 1, 1/2, and 1/4, respectively (41).

Due to the nonlinear sensitometry effects associated with the cadmium sulfide photoconductor described in Section IV.1, the actual device response curve departs significantly from the ideal behavior of Figure 24. The response curve of the actual device utilized for the A/D conversion experiments is shown in Figure 25. The aperiodic nature of the device response curve necessitated nonuniform quantization level assignments, as shown in the figure. Nevertheless, real time parallel three-bit A/D conversion was performed successfully with this device (41), with an estimated potential A/D conversion rate of

$1.2 \times 10^8$ points per second for currently available device parameters. Development of a LCLV with a more nearly periodic response function would significantly advance the potential of this technique, but requires linearization of both the photoconductor response and the relationship between applied voltage and effective birefringence.

## IV.5 Variable Grating Mode Liquid Crystal Device

Variable grating mode (VGM) liquid crystal devices offer a new approach to the problem of optical transducers (42-44) for nonlinear optical processing and optical logic and computing applications. The basic function of the VGM device is to perform an intensity-to-spatial frequency conversion over a two-dimensional image field. In this process, the intensity variations of an input image are converted to local spatial frequency variations in a phase grating structure within the liquid crystal layer. Due to this intensity-to-spatial frequency conversion, a standard spatial filtering system can be used to manipulate the input intensities.

The principal element of the variable grating mode device is a thin layer of liquid crystal that is observed to form periodic stripe domains in the presence of an applied voltage. The formation of the domains results in a phase grating characterized by a spatial frequency that depends on the magnitude of the voltage across the liquid crystal layer. The grating period can be optically controlled by placing a two-dimensional photoconductive layer in series with the layer of liquid crystal. The structure of the photoactivated device is shown schematically in Figure 26. The sputter-deposited ZnS photoconductor and the liquid crystal layer are sandwiched between indium tin oxide transparent electrodes deposited on optically flat glass substrates. To operate this device, a dc voltage is impressed across the electrodes. The thin film structure is designed to accept most of the drive voltage when the photoconductor is not illuminated, such that the fraction of the voltage that drops across the liquid crystal layer is below the activation threshold of the VGM effect. Illumination incident on a given area of the photoconductor reduces its impedance, thereby increasing the voltage drop across the liquid crystal layer and driving the liquid crystal into its activated state. Thus, due to the VGM effect, the photoconductor converts an input intensity distribution into a local variation of the phase grating spatial frequency. The variation of optical frequency with voltage across the liquid crystal layer is quite linear for a wide range of VGM liquid crystals, as shown in Figure 27. The fundamental origin of the VGM effect is not well understood, and is the

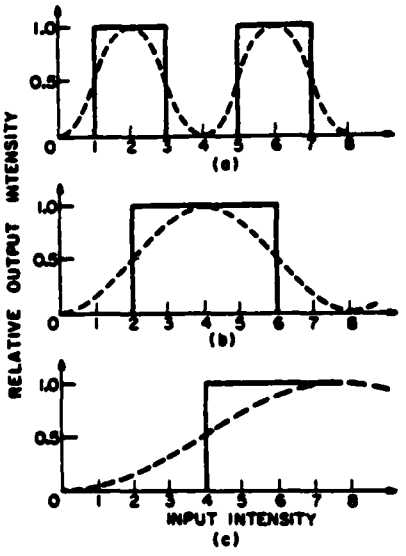


Figure 24. Nonlinear characteristic curves required for the three-bit Gray code. Solid curves are the desired characteristics for the bit plane outputs. Dashed curves are the ideal responses of a multiple period liquid crystal light valve. Parts (a) through (c) represent increasingly significant output bits. (After Armand, Ref. 41).

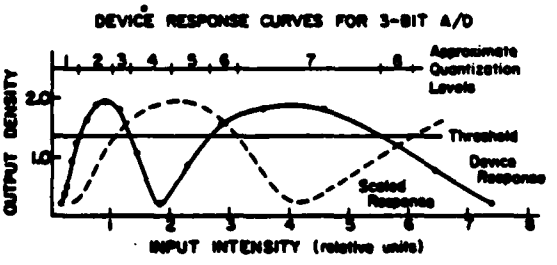


Figure 25. Response curve of the multiple period liquid crystal device used for the three-bit A/D conversion. The solid curve is the measured response. The dashed curve represents the same response with a fixed attenuation of the input. (After Armand, Ref. 41).

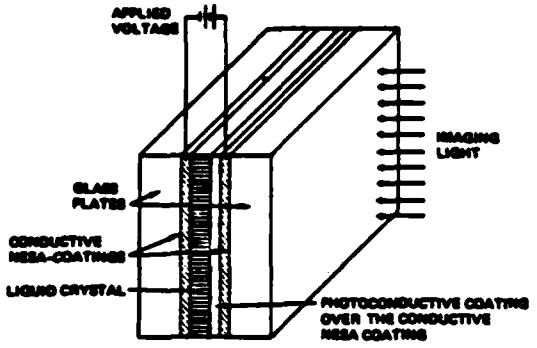


Figure 26. Schematic diagram of the Variable Grating Mode liquid crystal device. (After Soffer, Ref. 43).

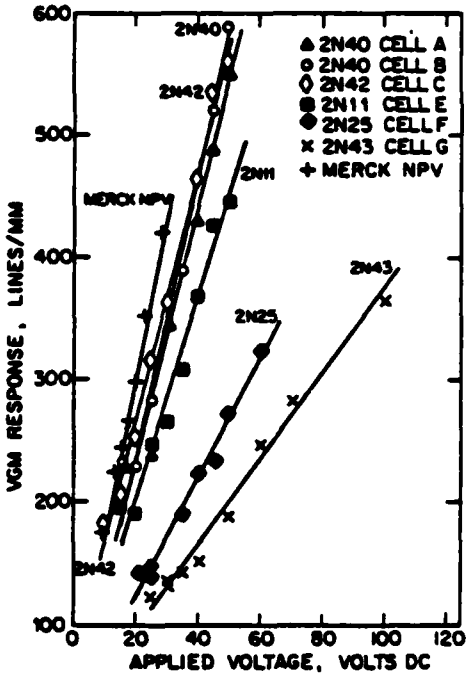


Figure 27. Spatial frequency of VGM domains as a function of applied voltage for various liquid crystals. (After Soffer, Ref. 43).

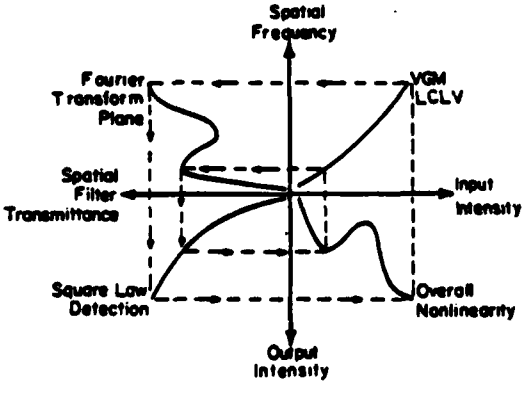


Figure 28. Nonlinear processing utilizing the intensity-to-spatial frequency conversion characteristic of the VGM liquid crystal device. (After Soffer, Ref. 44).

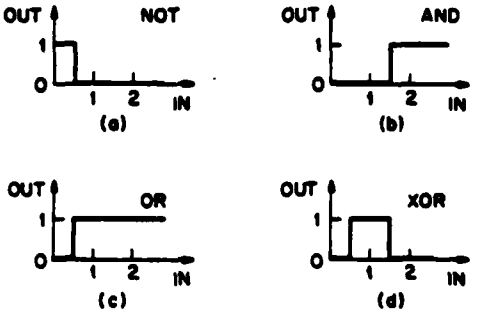


Figure 29. Logic functions as simple nonlinearities. Given an input consisting of the sum of two binary inputs, different logical operations can be effected by means of the depicted nonlinear characteristics. (After Chavel, Ref. 42).

subject of current investigation.

The intensity-to-spatial frequency conversion capability of the VGM device allows the implementation of arbitrary point nonlinearities with simple Fourier plane filters. As discussed above, when an input image illuminates the photoconductive layer of this device, the intensity variations of the input image change the local grating frequency. If conerent light is utilized to Fourier transform the processed image, different spatial frequency components (corresponding to different input intensities) of the encoded image appear at different locations in the Fourier plane. Thus, by placing appropriate spatial filters in this plane it is possible to obtain different transformations of the input intensity in the output plane as depicted in Figure 28. This figure describes the variable grating mode nonlinear processing function graphically. The input intensity variation is converted to a spatial frequency variation by the characteristic function of the VGM device (upper right-hand quadrant). These variations are Fourier transformed by the optical system and the spectrum is modified by a filter in the Fourier plane (upper left-hand quadrant). Finally, a square-law-detection produces the intensity observed in the output plane (lower left-hand quadrant). Considered together, these transformations yield the overall nonlinearity (lower right-hand quadrant). Design of a proper spatial filter for a desired transformation is a relatively easy task. For example, a level slice transformation requires only a simple slit that passes a certain frequency band or bands.

To visualize how the VGM device can be used to implement logic operations, one need only realize that the function of a logic circuit can be represented as a simple binary nonlinearity. The input-output characteristics of the common logic functions are shown in Figure 29. The input in this figure is the simple arithmetic sum of two input image intensities corresponding to logic levels 0 or 1, as shown in the experimental arrangement depicted in Figure 30. For example, NOT is simply a hard-clipping inverter, AND and OR are hard-clippers with different thresholds and XOR is a level slice function. In the VGM approach, such binary nonlinearities can be directly implemented by means of simple slit apertures (41). Thus the particular binary logic function implemented is fully programmable merely by altering the (low resolution) Fourier plane filter. In addition, the input and output functions are physically separate, which provides for the possibility of level restoration of degraded inputs. This feature is essential to the production of a reliable logic system that is immune to noise and systematic errors.

Many logic functions which would normally require multiple gates to implement can be obtained directly with a single VGM cell. An important example is the full-adder where two input bit planes and the carry bit plane are imaged simultaneously onto the VGM device, generating four possible input intensity levels as shown in Figure 31. The four resulting diffracted orders can be filtered to generate the sum bit plane using the positive orders and simultaneously the carry bit plane using the negative orders. Thus, a full addition can be performed in a single pass through the device. Functions requiring matrix-addressable look-up tables can be generated by utilizing two orthogonally oriented VGM devices in conjunction with a two-dimensional Fourier plane filter. Several such functions are required for optical implementation of residue arithmetic. Finally, in addition to the combinatorial logic functions discussed above, sequential logic may also be implemented with appropriate feedback.

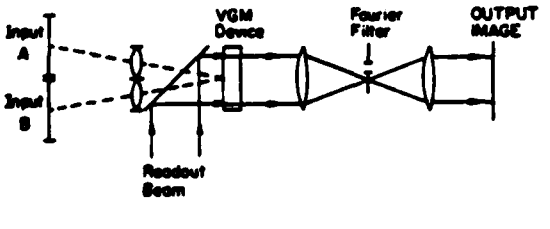


Figure 30. Experimental arrangement for performing logical operations on 2-D binary inputs with a VGM device. (After Chavel, Ref. 42).

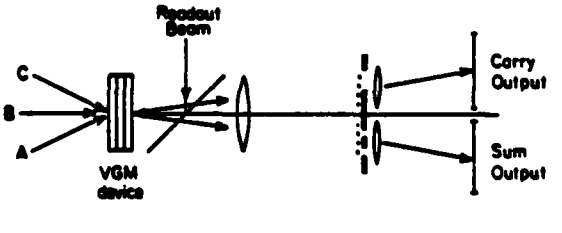


Figure 31. Implementation of a single pass full adder with a VGM device. The inputs A and B represent two binary images (bit-planes) to be added, while input C represents the carry-bit-plane from the previous operation.

The wide range of nonlinear optical processing applications described above demonstrates the tremendous flexibility inherent in the intensity-to-spatial frequency conversion process. It is unfortunate that at present, the VGM device represents the only available real time implementation of this operation. The present major shortcomings of the device are grating imperfections (which give rise to broadening of the diffracted orders), speed of response (on the order of one second), and lifetime. Improvements in all of these areas may be anticipated, since the VGM liquid crystal device is at an early stage of development.

## V. Photorefractive Spatial Light Modulators

Until quite recently, the recording of volume holograms in photorefractive materials has been primarily investigated for applications in archival storage and high resolution holographic memories. Applications to coherent optical processing were limited by extremely low writing sensitivities in available electrooptic materials. Recently, however, a number of electrooptic materials have been investigated which exhibit holographic recording sensitivities comparable to that of photographic film, including iron-doped lithium niobate (45), strontium barium niobate (46), bismuth silicon oxide and bismuth germanium oxide (47), and barium titanate (48). The availability of appropriate materials for real time volume holographic storage has spawned interest in several optical data processing applications, incuding phase-conjugate wavefront generation (49), double-exposure and time average holographic interferometry for non-destructive testing (50,51), real time correlation/convolution (52,53), and edge enhancement (54,55). The use of photorefractive materials as spatial light modulators necessitates the use of coherent input and output beams, and as such represents a departure from the traditional function of incoherent-to-coherent conversion in SLM's. However, such devices may be utilized as Fourier plane holographic filters in conjunction with an incoherent-to-coherent or electron-beam-addressed SLM, and in applications (such as multiple exposure holographic interferometry and phase-conjugate wavefront generation) requiring coherent sources.

The physical origin of the photorefractive effect is shown schematically in Figure 32 (56). The intensity interference pattern of two monochromatic coherent plane waves with angular separation $2\theta$ is characterized by a grating vector $k = 4\pi(\sin\theta)/\lambda$ oriented perpendicular to the acute bisector of the plane wave propagation vectors. Within the photorefractive material, either electron-hole pair generation, or electron (hole) excitation from trap states to the conduction (valence) band, or both may occur at a rate proportional to the local intensity. Free carriers so created will diffuse due to the spatially-varying concentration gradient, and will subsequently be trapped preferentially in regions of lower intensity. This charge redistribution can be enhanced by application of an electric field parallel to the grating wave vector. The resultant spatial variation in the charge distribution replicates the grating spacing of the intensity interference pattern, generating a periodic modulation of the local space charge field, which in turn modulates the local refractive indices through the Pockels (electrooptic) effect. The refractive index grating so formed creates a volume phase hologram within the bulk of the electrooptic material, which can be read out by a third monochromatic beam of appropriate polarization counterpropagating along either of the two writing beams. Both transmission and refection holograms may be stored dependent on the orientation of the crystal with respect to the writing beams, as well as on the included angle $2\theta$. The sensitivity and maximum diffraction efficiency of the photorefractive holographic storage process are functions of the density of carriers available for photoexcitation, the density of available traps for charge redistribution, the magnitude of the electrooptic coefficient, the relative intensities of the writing beams, the magnitude of the applied field (if any), the mobility-lifetime product of the liberated photocarriers, and the grating period, in addition to numerous geometrical factors. Simultaneous optimization of these considerations places many constraints on the selection of appropriate electrooptic materials, and consequently emphasizes continued research on desirable material modifications (primarily doping and improvements in growth techniques for enhanced optical quality) and characterization of the relevant optoelectronic properties of electrooptic materials.

Photorefractive materials have several notable advantages for coherent optical processing applications. Since both image plane and Fourier plane holograms can be recorded will equal ease, great flexibility in optical processing configurations can be made use of. For example, an optical system that is capable of performing real time correlations and convolutions is shown schematically in Figure 33 (52). A similar system configuration that allows implementation of image edge enhancement is shown schematically in Figure 34 (55). In this latter application, use is made of the nonlinear dependence of the diffraction efficiency on the modulation index of the two writing beams by adjusting the reference beam intensity to lie between the bright and dark object intensity levels to enhance the diffraction efficiency in the transition regions where the modulation index approaches unity. A second notable feature of photorefractive materials is extremely high resolution, as depicted graphically in Figure 35. The marked dependence of the amplitude modulation function on the magnitude of the applied field (see Figure 35) allows the possibility of

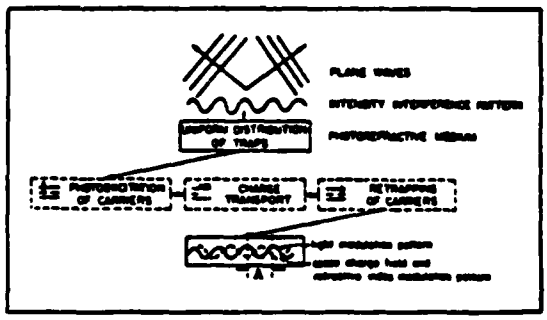

Figure 32. Schematic explanation of the photorefractive effect. (After Kim, Ref. 56).

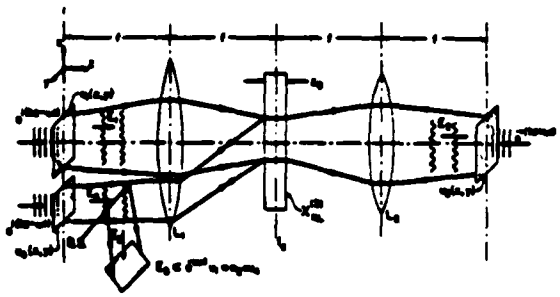

Figure 33. Real time degenerate four-wave mixing convolution/correlation geometry. All input optical fields are at frequency $\omega$. The beam splitter (BS) is necessary to view the desired output, $E_3$, which is evaluated at a plane located a distance f from lens $L_1$. (After Pepper, Ref. 52).

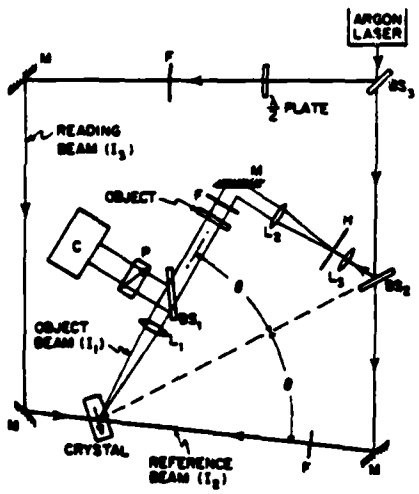


Figure 34. Experimental setup for real time edge enhancement using the photorefractive effect in $BaTiO_3$. Writing beams with intensities $I_1$ and $I_2$ (ordinary polarization) and reading beam with intensity $I_3$ (extraordinary polarization) are shown, as is the C axis of the $BaTiO_3$ crystal. (After Feinberg, Ref. 55).

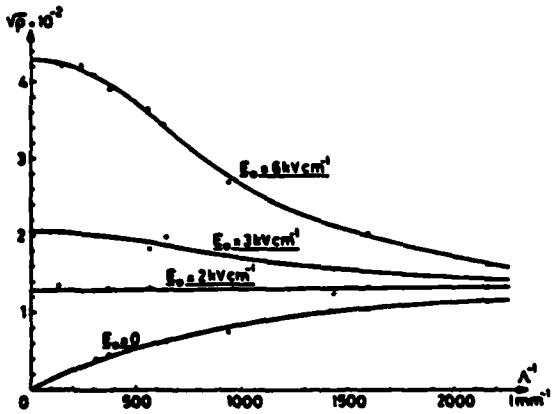


Figure 35. Amplitude modulation transfer function for pnotorefractive volume holographic storage in $Bi_{12}SiO_{20}$. (After Huignard, Ref. 57).

achieving spatial light modulation with essentially flat MTF characteristics out to spatial frequencies in excess of 1000 line pairs/mm.

## VI. Future Directions for Research

In this concluding section, a number of potentially profitable directions for research are presented in addition to those indicated in preceeding sections. Research on the fundamental physical limitations of each candidate spatial light modulator technology is critical both to optimization of current device design and performance, and to meaningful performance comparisons irrespective of current technological limitations. Such comparisons are essential in the assessment of the ultimate potential of each technological approach. This research must be broadly extended to include increased efforts in the materials growth, deposition, processing, and characterization areas, since most of the devices discussed above have been shown to require relatively unique materials properties simultaneously in several distinct materials classes (e.g., the liquid crystal light valves require high resistivity photoconductors, thin film blocking layers, thin film dielectric mirrors, and appropriate liquid crystals). Very little work to date has been reported on attempts to develop high speed spatial light modulators for high frame rate applications. All of the approaches described above are inherently slow and cannot be expected to significantly exceed TV frame rates. Limited frame rate capability will become a major bottleneck in the development of advanced real time optical processing systems and subsystems. Research on the optoelectronic properties of photorefractive materials may yield improvements in both sensitivity and maximum diffraction efficiency. Realization of such improvements would result in widespread availability of inexpensive, real time holographic storage and processing devices. The enormous processing flexibility for linear, nonlinear, combinatorial logic, and sequential logic point operations inherent in the intensity-to-spatial frequency conversion process will hopefully stimulate other possible approaches in addition to that offered by the variable grating mode liquid crystal device. In the area of real time parallel nonlinear optical processing, strong demand exists for high quality two-dimensional variable level slice and threshold functions. Although recent progress in optical bistability has been substantial, most current approaches are either one-dimensional or even single channel. Many "linear" optical processing operations such as correlation, convolution, and Fourier plane filtering require some form of threshold at the output for eventual system implementation.

## Acknowledgements

Valuable discussions with C. Warde, D. Casasent, R. Aldrich, J. Grinberg, U. Efron, A.A. Sawchuk, T. Strand, and J. Feinberg are gratefully acknowledged. Research on the physics of operation, materials growth and characterization, and device characterization of real time spatial light modulators is supported in part by the National Science Foundation, the Joint Services Electronics Program, the Air Force Office of Scientific Research, the Army Research Office, and the Ford Motor Company.

## REFERENCES

1. D. Casasent, "Spatial Light Modulators," Proc. IEEE, 65, 143-157, (1977).

2. D. Casasent, "Recyclable Input Device and Spatial Filter Materials," in Laser Applications, M. Ross, Ed., Academic Press, New York, (1977).

3. D. Casasent, "Materials and Devices for Coherent Optical Computing," in Optical Information Processing, G.W. Stroke et al. Eds., Plenum Press, New York, (1976).

4. S. Lipson, "Recyclable Incoherent-to-Coherent Image Converters," in Advances in Holography, N. Farhat, Ed., Marcel Dekker, New York, (1976).

5. G. Knight, "Interface Devices and Memory Materials," in Optical Data Processing, S.H. Lee, Ed., Springer-Verlag, Heidelberg, Germany, (1976).

6. J. Flannery, Jr., "Light-Controlled Light Valves," IEEE Trans. Elec. Dev., Ed-20, 941-953, (1973).

7. K. Preston, Jr., Coherent Optical Computers, McGraw Hill, New York, (1972).

8. D. Casasent, "Performance Evaluation of Spatial Light Modulators," Appl. Opt., 18, 2445-2453, (1979).

9. B.A. Horwitz and F.J. Corbett, "The PROM-Theory and Applications for the Pockels Readout Optical Modulator," Opt. Eng., 17, 353-364, (1978).

10. C. Warde, A.D. Fisher, D.M. Cocco, and M.Y. Burmawi, "Microchannel Spatial Light Modulator," Opt. Lett., 3, 196-198, (1978).

11. C. Warde, A. Weiss, and A. Fisher, "$LiTaO_3$ and $LiNbO_3$ Microchannel Spatial Light Modulators," Proc. SPIE Los Angeles Technical Symposium, 218, 59-66, (1980).

12. D. Casasent, "E-Beam DKDP Light Valves," Opt. Eng., 17, 344-352, (1978).

13. G. Marie, J. Donjon, and J.-P. Hazan, "Pockels Effect Imaging Devices and Their Applications," in Advances in Image Pickup and Display. Vol. 1, B. Kazan, Ed., Academic Press, New York, (1974), 225-302.

14. D. Casasent, S. Natu, T. Luu, G. Lebreton, and E. DeBazelaire, "New Birefringence Theory and Uses of the Photo-DKDP Spatial Light Modulator in Optical Data Processing," Proc. SPIE, 202, 122-131, (1980).

15. J. Donjon, F. Dumont, M. Grenot, J.-P. Hazan, G. Marie, and J. Pergrale, "A Pockels-Effect Light Valve: Phototitus. Applications to Optical Image Processing," IEEE Trans. Elec. Dev., ED-20, 1037-1042, (1973).

16. G.J. Berzins and M. Graser, Jr., "Response of a $Bi_{12}SiO_{20}$ Pockels Readout Optical Modulator to X-rays," Appl. Phys. Lett., 34(8), 500-502, (1979).

17. J.C.H. Spence and A. Olsen, "Use of Pockels Readout Optical Modulators (PROMs) for Atomic Resolution Electron Image Processing," Proc. SPIE Los Angeles Technical Symposium, 218, 154-160, (1980).

18. A.R. Tanguay, Jr., "The Czochralski Growth and Optical Properties of Bismuth Silicon Oxide," Thesis, Yale University, (1977).

19. A.R. Tanguay, Jr. and R.C. Barker, "Implications of Concurrent Optical Activity and Electric Field Induced Birefringence for Pockels Readout Optical Memory Performance," 1978 Annual Meeting of the Optical Society of America, San Francisco, California, (1978); to be published.

20. Y. Owechko and A.R. Tanguay, Jr., "Effects of Charge Dynamics and Device Parameters on the Resolution of Electrooptic Spatial Light Modulators," Proc. SPIE, 202, 110-121, (1979).

21. Y. Owechko and A.R. Tanguay, Jr., "Exposure-Induced Charge Distribution Effects on the MTF of Electrooptic Spatial Light Modulators," Proc. SPIE Los Angeles Technical Symposium, 218, 67-80, (1980).

22. Y. Owechko and A.R. Tanguay, Jr., "Theoretical Resolution Limitations of Electrooptic Spatial Light Modulators," 1979 Annual Meeting of the Optical Society of America, Rochester, New York, (1979); to be published.

23. J.C. Dainty and R. Shaw, Image Science: Principles, Analysis, and Evaluation of Photographic-Type Imaging Processes, Academic Press, New York, (1974), 140.

24. R.A. Sprague, "Effect of Bulk Carriers on PROM Sensitivity," J. Appl. Phys., 46 (4), 1673-1678, (1975).

25. C. Warde, Private Communication.

26. D. Casasent and T.K. Luu, "Photo-DKDP Light Valve in Optical Data Processing," App. Opt., 18, 3307-3314, (1979).

27. W.P. Bleha, L.T. Lipton, E. Wiener-Avnear, J. Grinberg, P.G. Reif, D. Casasent, H.D. Brown, and B.V. Markevitch, "Application of the Liquid Crystal Light Valve to Real-Time Optical Data Processing," Opt. Eng., 17(4), 371-384, (1978).

28. P.G. Reif, A.D. Jacobson, W.P. Bleha, and J. Grinberg, "Hybrid Liquid Crystal Light Valve-Image Tube Devices for Optical Data Processing," Proc. SPIE, 83, 34-43, (1976).

29. R.C. Jones, "A New Calculus for the Treatment of Optical Systems. III. The Sohncke Theory of Optical Activity," J. Opt. Soc. Am., 13, 500-503, (1941).

30. G.P. Montgomery, Jr., "Effect of Liquid-Crystal Thickness on the Optical Performance of a Liquid Crystal Image Transducer," Proc. SPIE, 202, 103-109, (1979).

31. G.P. Montgomery, Jr., "Optical Properties of a Liquid Crystal Image Transducer at Normal Incidence, I. Mathematical Analysis and Application to the Off-State," J. Opt. Soc. Am., 70, 287-300, (1980).

32. G.P. Montgomery, Jr., "Optical Properties of a Liquid Crystal Image Transducer at Normal Incidence. II. The On-State," J. Opt. Soc. Am., 70, 843-856, (1980).

33. L.M. Fraas, J. Grinberg, W.P. Bleha, and A.D. Jacobson, "Novel Charge-Storage-Diode Structure For Use With Light-Activated Displays," J. Appl. Phys., 47(2), 576-583, (1976).

34. L.M. Fraas,, W.P. Bleha, J. Grinberg, and A.D. Jacobson, "AC Photoresponse of a Large-Area Imaging CdS/CdTe Heterojunction," J. Appl. Phys., 47(2), 584-590, (1976).

35. S. Natu and D. Casasent, "Sensitometry Control of a Hybrid Field-Effect Liquid Crystal Light Valve," Opt. Comm., 31(2), 135-138, (1979).

36. D. Casasent and S. Natu, "Spatial Variations in a Hybrid Field-Effect Liquid Crystal Light Valve," Appl. Phys., 20, 171-174, (1979).

37. A.D. Gara, "Phase Response of a Liquid Crystal Image Transducer," Appl. Opt., 17(23), 3696-3698, (1978).

38. P.O. Braatz, K. Chow, U. Efron, J. Grinberg, and M.J. Little, "A Fast Silicon Photoconductor-Based Liquid Crystal Light Valve," Proc. Int. Elec. Dev. Mtng., 540-542, (1979).

39. J. Grinberg and U. Efron, Private Communications.

40. J. Grinberg, W.P. Bleha, P.O. Braatz, K. Chow, D.H. Close, A.D. Jacobson, M.J. Little, N. Masseti, R.J. Murphy, J.G. Nash, and M. Waldner, "Liquid-Crystal Electro-Optical Modulators for Optical Processing of Two-Dimensional Data," Proc. SPIE, 128, 253-266, (1977).

41. A. Armand, A.A. Sawchuk, T.C. Strand, D. Boswell, and B.H. Soffer, "Real-Time Parallel Optical Analog-to-Digital Conversion," Opt. Lett., 5(3), 129-131, (1980).

42. P. Chavel, A.A. Sawchuk, T.C. Strand, A.R. Tanguay, Jr., and B.F. Soffer, "Optical Logic With Variable Grating Mode Liquid Crystal Devices," Opt. Lett., 5, 398-400, (1980).

43. B.H. Soffer, D. Boswell, A.M. Lackner, A.R. Tanguay, Jr., T.C. Strand, and A.A. Sawchuk, "Variable Grating Mode Liquid Crystal Device for Optical Processing," Proc. SPIE, 218, 81-87, (1980).

44. B.H. Soffer, D. Boswell, A.M. Lackner, P. Chavel, A.A. Sawchuk, T.C. Strand, and A.R. Tanguay,Jr., "Optical Computing with Variable Grating Mode Liquid Crystal Devices," Proc. SPIE, 232, (1980) (in press).

45. D. Staebler and W. Philips, "Fe-Doped $LiNbO_3$ for Read-Write Applications," Appl. Opt., 13, 788-794, (1974).

46. K. Megumi, H. Kozuka, M. Kobayashi, and Y. Furuhata, "High-Sensitive Holgoraphic Storage in Ce-Doped SBN," Appl. Phys. Lett., 30(12), 631-633, (1977).

47. J.P. Huignard and F. Micheron, "High-Sensitivity Read-Write Volume Holographic Storage in $Bi_{12}SiO_{20}$ and $Bi_{12}GeO_{20}$ Crystals," Appl. Phys. Lett., 29(9), 591-593, (1976).

48. J. Feinberg, D. Heiman, A.R. Tanguay, Jr., and R.W. Hellwarth, "Photorefractive Effects and Light-Induced Charge Migration in Barium Titanate," J. Appl. Phys., 51(3), 1297-1305, (1980).

49. J.P. Huignard, J.P. Herriau, P. Auborg, and E. Spitz, "Phase-Conjugate Wavefront Generation Via Real-Time Holography in $Bi_{12}SiO_{20}$ Crystal," Opt. Lett., 4(1), 21-33, (1979).

50. J.P. Huignard and J.P. Herriau, "Real-Time Double-Exposure Interferometry With $Bi_{12}SiO_{20}$ Crystals in Transverse Electrooptic Configuration," Appl. Opt., 16(7), 1807-1809, (1977).

51. J.P. Huignard, J.P. Herriau, and T. Valentin, "Time Average Holographic Interferometry With Photoconductive Electrooptic $Bi_{12}SiO_{20}$ Crystal," Appl. Opt., 16(11), 2796-2798, (1977).

52. D.M. Pepper, J. AuYeung, D. Fekete, and A. Yariv, "Spatial Convolution and Correlation of Optical Fields Via Degenerate Four-Wave Mixing," Opt. Lett., 3(1), 7-9, (1978).

53. J.O. White and A. Yariv, "Real-Time Image Processing Via Four-Wave Mixing in a Photorefractive Medium," Appl. Phys. Lett., 37(1), 5-7, (1980).

54. J.P. Huignard and J.P. Herriau, "Real-Time Coherent Object Edge Enhancement with $Bi_{12}SiO_{20}$ Crystals," Appl. Opt., 17(17), 2671-2672, (1978).

55. J. Feinberg, "Real-Time Edge Enhancement Using the Photorefractive Effect," Opt. Lett., 5(8), 330-332, (1980).

56. D.M. Kim, T.A. Rabson, R.R. Shah, and F.K. Tittel, "Photorefractive Materials for Optical Storage and Display," Opt. Eng., 16(2), 189-196, (1977).

57. J.P. Huignard, J.P. Herriau, G. Rivet, and P. Gunter, "Phase-Conjugation and Spatial-Frequency Dependence of Wave-Front Reflectivity in $Bi_{12}SiO_{20}$ Crystals," Opt. Lett., 5(3), 102-104, (1980).

# Effects of operating mode on electrooptic spatial light modulator resolution and sensitivity

Y. Owechko and A. R. Tanguay, Jr.

*Departments of Electrical Engineering and Materials Science, University of Southern California, Los Angeles, California 90089*

Received August 20, 1982

The strikingly opposite dependences of PROM and PRIZ electrooptic spatial light modulator resolution and sensitivity on operating mode have been modeled by including the effects of bulk charge distributions on the longitudinal and transverse fields. It is shown that the relative performance of PROM and PRIZ devices is strongly influenced by the choice of operating mode and by the quality of the dielectric blocking layers.

Electrooptic spatial light modulators (ESLM's) such as the PROM[1] and the PRIZ[2] have been proposed for use as incoherent-to-coherent transducers in coherent optical processors for applications in which both real-time operation and image storage are required. Recently it was reported that, under certain operating conditions, the PRIZ can have substantially larger diffraction efficiency and enhanced resolution relative to the PROM.[3] In this Letter we show that specification of operating mode is vital in any device comparison because of its strikingly strong and opposite effects on the two devices.

ESLM's can be classified into two categories: those devices that utilize an electrooptic effect induced by longitudinal fields parallel to the direction of readout light propagation and those devices that utilize transverse fields perpendicular to the light-propagation direction. These fields arise from charge distributions within the electrooptic crystal layer photoinduced by the input image. The PROM and the PRIZ are examples of longitudinal- and transverse-effect ESLM's, respectively. These devices utilize bismuth silicon oxide ($Bi_{12}SiO_{20}$, BSO) as the electrooptic and photoconductive medium in which the charge distribution is induced. The BSO crystal layer is positioned between two transparent dielectric blocking layers, with transparent electrodes deposited on both sides of the device. The two devices differ in the crystallographic orientation of the BSO layer, which determines those components of the electric field that contribute to the electrooptic effect. The PROM utilizes a ⟨001⟩ orientation[1] and the PRIZ a ⟨111⟩ or a ⟨110⟩ orientation.[2,3]

The amplitude of a plane wave that has passed through an ESLM situated between crossed polarizers oriented to bisect the induced principal axes is given by[4]

$$A(x,y) = iA_0 \sin G(x,y), \tag{1}$$

where $G(x,y)$ is one half of the spatially varying birefringence induced by the input image, $A_0$ is the readout light amplitude, and $(x,y)$ are image coordinates in the plane transverse to the light-propagation direction $z$. A phase factor that is present in the PRIZ case has been suppressed in Eq. (1). This factor can have an important deleterious influence on PRIZ performance.[5] In addition, the effects of natural optical activity in BSO on Eq. (1) have been neglected.[6]

The dependence of $G$ on the relevant fields can be readily determined from the electrcoptic tensor ($I23$ symmetry) and crystallographic orientation of the BSO crystal for each device:

$$G(x,y) = \begin{cases} \pi V_L(x,y)/2V_\pi & \text{(PROM)} \\ \pi V_T(x,y)/\sqrt{6}V_\pi & \text{(⟨111⟩ PRIZ)} \end{cases}, \tag{2}$$

where

$$V_{L,T}(x,y) = \int_0^d E_{L,T}(x,y,z)\,dz. \tag{3}$$

The longitudinal field is given by $E_L(x, y, z)$, the transverse field by $E_T(x,y,z)$, and the BSO thickness by $d$; $V_\pi$ is the ⟨001⟩ half-wave voltage of $Bi_{12}SiO_{20}$. The generalized voltages $V_L$ and $V_T$ have units of volts, although it should be kept in mind that $V_T$ represents an integral of transverse fields in the longitudinal direction.

In order to model ESLM resolution and sensitivity for various operating modes, it is necessary first to derive the generalized voltages $V_L(x,y)$ and $V_T(x,y)$ for the case of a single point charge in the BSO crystal bulk. Solutions of Poisson's equation for a point charge located at an arbitrary position within a three-layer dielectric stack have been obtained by a Hankel transform technique that takes advantage of the cylindrical symmetry of the problem.[7] This results in analytic expressions for the transfer functions $V_L(\omega;\xi)$ and $V_T(\omega;\xi)$ [the Hankel (Fourier) transforms of the single-point-charge voltages $V_T(x,y;\xi)$ and $V_L(x,y;\xi)$], where $\omega$ is the radial spatial frequency and $\xi$ is the $z$ coordinate of the point charge.[7,8] The advantage of this approach is that the ESLM response at all spatial frequencies can immediately be calculated as a function of point charge position and device constitutive parameters (thicknesses and dielectric constants of the layers). Once the charge distribution is known, the ESLM response for continuous charge distributions can be determined by taking advantage of the linearity of Poisson's equation and integrating through the BSO crystal thickness, using the single-point-charge solution as a Green's function. The ESLM response as a function of spatial frequency is then determined by

0146-9592/82/120587-03$1.00/0 

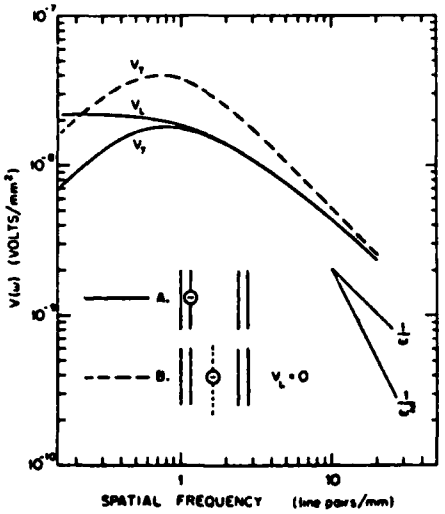


Fig. 1. Generalized single-point-charge voltage transfer functions for two charge positions, 0 $\mu$m (Case A) and 250 $\mu$m (Case B) from the BSO-crystal surface. Blocking layer and BSO thicknesses are assumed to be 5 and 500 $\mu$m, respectively.

$$G(\omega) = \begin{cases} \pi V_L(\omega)/2V_\pi & \text{(PROM)} \\ \pi V_T(\omega)/\sqrt{6}V_\pi & \text{(⟨111⟩ PRIZ)} \end{cases}, \quad (4)$$

where

$$V_{L,T}(\omega) = \int_0^d V_{L,T}(\omega; z)\rho(z)\mathrm{d}z. \quad (5)$$

The longitudinal charge density induced by the input exposure is represented by $\rho(z)$. The resolution and the sensitivity of the ESLM [as described by G($\omega$)] are strongly influenced by $\rho(z)$, which is in turn determined by the sign and the magnitude of the applied field (collectively referred to as the operating mode) as well as by a number of device, material, and exposure parameters. The effects of $\rho(z)$ on PROM and PRIZ resolution and sensitivity can be envisaged by considering cases in which $\rho(z)$ consists of one or two point charges, i.e., one electron or an electron–hole pair. The discussion can then be extended to include a continuous charge distribution by using Eq. (5).

In Fig. 1, $V_L(\omega)$ and $V_T(\omega)$ have been plotted for a single point charge at two different locations in the BSO crystal. The device is assumed to consist of a 500-$\mu$m-thick BSO crystal with 5-$\mu$m-thick dielectric blocking layers ($\epsilon_{eo} = 56$, $\epsilon_{bl} = 3$). Note the bandpass nature of $V_T(\omega)$ caused by the lack of transverse-field excitation from uniform components of the input image. In Case A the point charge is at the BSO–blocking-layer interface, whereas in Case B the point charge is placed in the center of the BSO-crystal layer. It is evident that, for a single point charge on the interface, $V_L(\omega)$ and $V_T(\omega)$ are asymptotically equal for high spatial frequencies, although according to Eq. (4) the PRIZ response is actually a factor of $2/\sqrt{6}$ smaller than the PROM when $V_L(\omega) = V_T(\omega)$. The PROM response drops precipitously relative to that of the PRIZ as the single point charge moves into the BSO crystal bulk. This can be explained by considering the symmetry of the electric field configuration around a point charge in the BSO crystal bulk, as illustrated for both Case A and Case B in Fig. 2. The longitudinal field components have opposite values on opposite sides of the charge in Case B; hence they cancel, resulting in a $V_L(\omega)$ identically equal to zero, as compared with nonzero values in Case A. The transverse field components, on the other hand, have equal values on opposite sides of the charge in Case B, resulting in a larger $V_T(\omega)$ than in Case A. Since the PROM and the PRIZ spatial-frequency responses are described by $V_L(\omega)$ and $V_T(\omega)$, respectively, the charge distribution that results in optimum resolution and sensitivity is quite different for the two devices.

It cannot be concluded, however, that the PRIZ is necessarily more sensitive than the PROM by considering only one charge. Realistic charge distributions consist of electrons and positively charged traps or holes, which are photoinduced in pairs, resulting in equal numbers of each. In order to model the effects of charge conservation on the relative sensitivities of the PROM and the PRIZ, $V_L(\omega)$ and $V_T(\omega)$ have been plotted in Fig. 3 for two distinct charge distributions, each consisting of a positive and a negative charge. The device parameters are identical with those of Fig. 1. In Case C the charge distribution is symmetric, consisting of a negative charge at one BSO-crystal–blocking-layer interface and a positive charge at the opposite interface. This charge distribution models the forward-operating mode in which the illuminated electrode is maintained at a negative potential during exposure so that electrons are transported in the direction of light propagation into the BSO-crystal bulk until they reach the far interface. In Case D the charge distribution is asymmetric, consisting of a positive charge at one interface and a negative charge in the center of the device. This charge distribution models the reverse mode, in which the illuminated electrode is maintained at a positive potential during exposure so that electron transport is opposite the light-propagation direction, confining electrons near the illuminated electrode.

Again it is evident that the PRIZ sensitivity dependence on charge position is opposite that of the PROM. The largest PROM sensitivity is achieved for symmetric charge distributions, as in Case C, in which oppositely signed charges are fully separated; whereas the PRIZ

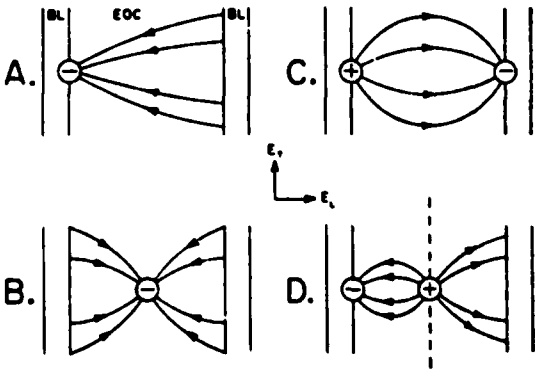


Fig. 2. Schematic diagrams of the electric field configurations for the charge distributions of Figs. 1 and 3.

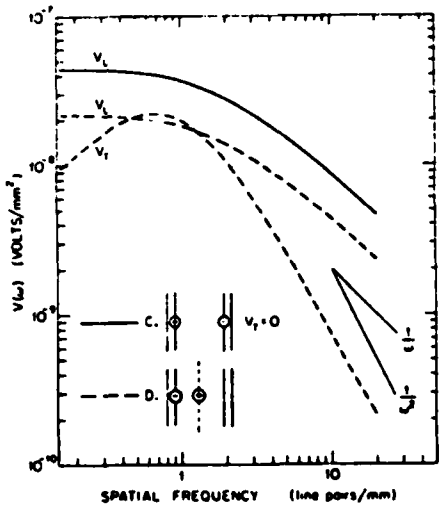


Fig. 3. Generalized voltage-transfer functions for $\rho(z)$ consisting of two opposite point charges. Values for two charge distributions corresponding to forward (Case C) and reverse (Case D) operating modes are shown. Device parameters are unchanged from those of Fig. 1. Charge positions are given in the text.

sensitivity is identically zero for the same charge distributions. This is seen to be physically reasonable on consideration of the electric field configuration for a symmetric charge distribution consisting of oppositely signed charges, as illustrated in Fig. 2. The transverse field components cancel on integration through the bulk, resulting in zero PRIZ response, whereas the longitudinal field components add, enhancing the PROM response. Asymmetric charge distributions, as in Case D, increase the PRIZ response and decrease the PROM response, again because the transverse fields have the same sign and the longitudinal fields have opposite signs on opposite sides of a point charge. These considerations show that PROM and PRIZ sensitivity and resolution will in general be optimized for quite different operating modes and resultant charge distributions. Comparison of these two quite different devices under conditions of identical operating mode will necessarily favor one over the other. The effects of continuous charge distributions have been modeled by using Eq. (5) and an iterative charge-transport model.[9] The essential results presented here are unchanged in the continuous case and in addition are confirmed by experiment.[9]

Another factor that will favor one device over the other in terms of resolution and sensitivity is charge conservation. If overall charge neutrality is maintained so that equal numbers of positive and negative charges are present in the BSO layer, then the PROM response will be enhanced relative to that of the PRIZ, as is evident from Fig. 3. However, if unequal numbers of positive and negative charges are present, the PRIZ response will be enhanced relative to that of the PROM, as illustrated in Fig. 1. The high-spatial-frequency limit of $V_T(\omega)$ is independent of charge position[8]; therefore PRIZ high spatial frequencies are greatly attenuated if equal numbers of oppositely signed charges are present. The high-spatial-frequency limit of $V_L(\omega)$,[7,11] on the other hand, is strongly dependent on charge position; therefore PROM high spatial frequencies are not attenuated by charge conservation. The quality of the dielectric blocking layers directly affects charge conservation in the PROM and the PRIZ and, consequently, the relative performances of the two devices. Poor-quality blocking layers that allow electrons to bleed away from the BSO–blocking-layer interface enhance the PRIZ response and degrade the PROM response, resulting in larger PRIZ diffraction efficiencies relative to those of the PROM.[3] Such leaky blocking layers result in relatively short storage times of a few minutes.[3]

We have demonstrated in this Letter the strong dependence of ESLM sensitivity and resolution on the operating mode used. The PROM and the PRIZ show essentially opposite dependences, making specification of the operating mode mandatory for meaningful device comparisons. Decreasing the dielectric blocking layer quality was found to be beneficial for PRIZ resolution and sensitivity but detrimental for those of the PROM. The effects of orientation on ESLM phase distortions will be reported separately,[5] as will conditions for optimum operating modes of both types of device.[9,2]

This research was supported in part by the U.S. Army Research Office and the Joint Services Electronics Program.

## References

1. B. A. Horwitz and F. J. Corbett, Opt. Eng. 17, 353 (1978).
2. M. P. Petrov *et al.*, Sov. Phys. Tech. Phys. 25, 752 (1980).
3. D. Casasent, F. Caimi, and A. Khomenko, Appl. Opt. 20, 4215 (1981).
4. R. A. Sprague and P. Nisenson, Opt. Eng. 17, 256 (1981).
5. Y. Owechko and A. R. Tanguay, Jr., "Effects of crystallographic orientation on electrooptic spatial light modulator amplitude and phase responses," submitted to Opt. Commun.
6. A. R. Tanguay, Jr., Ph.D. Thesis (Yale University, New Haven, Conn., 1977).
7. Y. Owechko and A. R. Tanguay, Jr., Proc. Soc. Photo-Opt. Instrum. Eng. 202, 110 (1979).
8. Y. Owechko and A. R. Tanguay, Jr., "Theoretical resolution limitations of electrooptic spatial light modulators. II: Effects of crystallographic orientation," submitted to J. Opt. Soc. Am.
9. Y. Owechko and A. R. Tanguay, Jr., "Theoretical resolution limitations of electrooptic spatial light modulators. III: Effects of continuous charge distributions," submitted to J. Opt. Soc. Am.
10. Y. Owechko and A. R. Tanguay, Jr., Proc. Soc. Photo-Opt. Instrum. Eng. 218, 67 (1980).
11. Y. Owechko and A. R. Tanguay, Jr., "Theoretical resolution limitations of electrooptic spatial light modulators. I: Fundamental considerations," submitted to J. Opt. Soc. Am.
12. Y. Owechko and A. R. Tanguay, Jr., "Theoretical resolution limitations of electrooptic spatial light modulators. IV: Effects of operational mode," submitted to J. Opt. Soc. Am.

Volume 44, number 4 OPTICS COMMUNICATIONS 15 January 1983

# EFFECTS OF CRYSTALLOGRAPHIC ORIENTATION ON ELECTROOPTIC SPATIAL LIGHT MODULATOR AMPLITUDE AND PHASE RESPONSES

Y. OWECHKO and A.R. TANGUAY, Jr.

*Departments of Electrical Engineering and Materials Science, University of Southern California, Los Angeles, CA 90089, USA*

Received 4 October 1982

**The effects of crystallographic orientation on output amplitude and signal-dependent phase distortions in electrooptic spatial light modulators such as the PROM and PRIZ are described.**

Real time coherent optical processing systems often utilize Electrooptic Spatial Light Modulators (ESLM's) as input transducers for converting incoherent input images into coherent form. In evaluating the suitability of an ESLM for a particular application, the amplitude and phase responses are among numerous device characteristics that must be considered. In this paper the effects of crystallographic orientation on ESLM amplitude and signal-dependent phase responses are described in detail.

The PROM [1] and PRIZ [2] spatial light modulators are examples of ESLM's. These devices consist of an electrooptic and photoconductive crystal (bismuth silicon oxide: the chemical compound $Bi_{12}SiO_{20}$ (BSO)) sandwiched between two transparent dielectric blocking layers. Transparent electrodes contact opposite faces of each device. The PROM utilizes a ⟨001⟩ orientation of the electrooptic crystal, and the PRIZ either ⟨111⟩ or ⟨110⟩. The incoherent input image is recorded during exposure as a photoinduced charge distribution in the photoconductive BSO layer. The electric fields arising from the charge redistribution induce modulation of the refractive indices along principal axes in the BSO crystal through the linear electrooptic (Pockels) effect. The crystallographic orientation and electrooptic tensor (123 symmetry) of BSO determine which components of the electric field contribute to the electrooptic effect and hence to the point spread function (amplitude and phase) of the output image. The effects of volume charge distributions on the development of electric field components in the PROM and PRIZ have been discussed previously [3].

The output amplitude $A$ of an ESLM situated between crossed polarizers with the input polarization oriented to bisect the induced principal electrooptic axes can be calculated using the Jones matrix formalism in the principal axis coordinate system (neglecting the natural optical activity of BSO) as

$$A = \tfrac{1}{2} A_0 (1 \quad -1) \begin{pmatrix} e^{i\phi_1} & 0 \\ 0 & e^{i\phi_2} \end{pmatrix} \begin{pmatrix} 1 \\ 1 \end{pmatrix}$$

$$= i A_0 \, e^{i\phi} \sin(G) \qquad (1)$$

where the retardation $G = (\phi_1 - \phi_2)/2$ is one half of the phase difference induced between the two principal axes and $\phi = (\phi_1 + \phi_2)/2$ is the ESLM phase response. The phase shifts along the principal axes induced by the electric fields are given by $\phi_1$ and $\phi_2$, and $A_0$ represents the readout light amplitude. The output amplitude is directly proportional to $G$ for small signal amplitudes such that $G \ll 1$.

It is clear from eq. (1) that for an arbitrary crystallographic orientation (such that $\phi_1 \neq -\phi_2$), the output amplitude image can be multiplied by a phase image. This signal-dependent phase distortion can increase the device harmonic distortion in applications

0 030-4018/83/0000–0000/S 03.00 

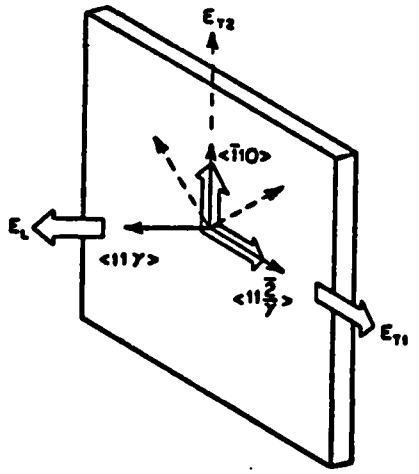


Fig. 1. Orientations of longitudinal and transverse electric fields, and their respective induced principal axes, for $Bi_{12}SiO_{20}$ (I23 symmetry). The longitudinal field ($E_L$) and one transverse field ($E_{T1}$) induce the same set of principal axes (open arrows), while the other transverse field ($E_{T2}$) induces a set of principal axes rotated by 45° (dashed arrows).

for which pure amplitude modulation is desirable, as will be shown below. The quantities $\phi$ and $G$ can be induced by electric fields longitudinal or transverse to the light propagation direction or a mixture of both, depending on the crystallographic orientation. Fig. 1 illustrates the orientation and labeling of the longitudinal ($E_L$) and transverse ($E_{T1}$, $E_{T2}$) fields with respect to the light propagation direction for crystallographic orientations between ⟨001⟩ and ⟨110⟩. The modified Miller notation ⟨11γ⟩ is used to represent the crystallographic orientation, where $\gamma = +\infty$ corresponds to ⟨001⟩ and $\gamma = 0$ corresponds to ⟨110⟩. This range of orientations was chosen from the many possible as representative of the expected effects, and because both the PROM (⟨001⟩) and PRIZ (⟨111⟩, ⟨110⟩) cases are included. The principal axes induced by the fields $E_L$, $E_{T1}$, and $E_{T2}$ are also indicated in fig. 1.

Plots of $G$ and $\phi$ induced by each of the three orthogonal field components as functions of the crystallographic orientation between ⟨001⟩ and ⟨110⟩ are shown in figs. 2 and 3. The principal axes and the phase shifts $\phi_1$ and $\phi_2$ were obtained by diagonalization of the index ellipsoid cross section normal to the direction of light propagation (⟨11γ⟩). The angle $\psi$ between the ⟨001⟩ axis and the crystallographic orientation ⟨11γ⟩ is related to $\gamma$ by

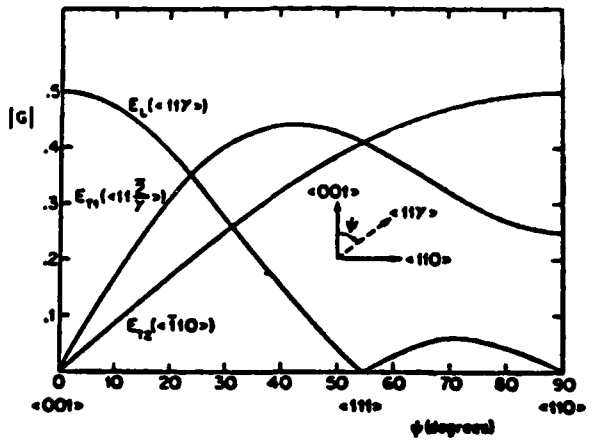


Fig. 2. Magnitude of retardation $G$ induced by the three orthogonal field components defined in fig. 1 as a function of crystallographic orientation. The value of $G$ is given in units of $\pi V_\alpha / V_\pi$ where $\alpha$ = L, T1, or T2; the quantities $V_L$, $V_{T1}$, and $V_{T2}$ are defined in the text.

$$\gamma = \sqrt{2}\cot(\psi) \qquad (2)$$

In figs. 2 and 3, $V_\pi = \lambda/2n_0^3 r_{41}$ is the half wave voltage for BSO in the ⟨001⟩ orientation, where $\lambda$ is the readout wavelength, $n_0$ is the refractive index of BSO, and $r_{41}$ is the BSO electrooptic coefficient. For $\lambda$ = 632.8 nm, $V_\pi$ = 3900 V [4]. It is assumed that the input polarization is oriented to bisect the principal axes induced by the relevant field component.

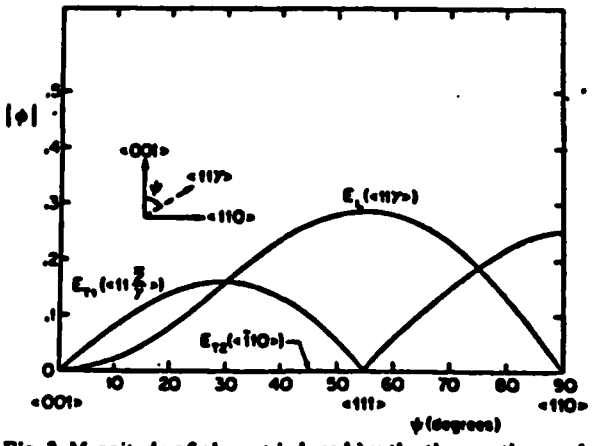


Fig. 3. Magnitude of phase $\phi$ induced by the three orthogonal field components defined in fig. 1 as a function of crystallographic orientation. The value of $\phi$ is given in units of $\pi V_\alpha / V_\pi$ where $\alpha$ = L, T1, or T2; the quantities $V_L$, $V_{T1}$, and $V_{T2}$ are defined in the text.

Table 1
Values of $G$ and $\phi$ for three orthogonal fields and three crystallographic orientations used in the PROM and PRIZ. The generalized voltages $V_L$, $V_{T1}$, and $V_{T2}$ are defined in the text.

| BSO orientation | ⟨001⟩ (PROM) | | | ⟨111⟩ (PRIZ) | | | ⟨110⟩ (PRIZ) | | |
|---|---|---|---|---|---|---|---|---|---|
| Field orientation | $E_L$ ⟨001⟩ | $E_{T2}$ ⟨$\bar{1}$10⟩ | $E_{T1}$ ⟨110⟩ | $E_L$ ⟨111⟩ | $E_{T2}$ ⟨$\bar{1}$10⟩ | $E_{T2}$ ⟨11$\bar{2}$⟩ | $E_L$ ⟨110⟩ | $E_{T2}$ ⟨$\bar{1}$10⟩ | $E_{T1}$ ⟨00$\bar{1}$⟩ |
| Phase $\phi$ | 0 | 0 | 0 | $\frac{\pi V_L}{2\sqrt{3}V_\pi}$ | 0 | 0 | 0 | 0 | $\frac{\pi V_{T1}}{4V_\pi}$ |
| Signal $G$ | $\frac{\pi V_L}{2V_\pi}$ | 0 | 0 | 0 | $\frac{\pi V_{T2}}{\sqrt{6}V_\pi}$ | $\frac{\pi V_{T1}}{\sqrt{6}V_\pi}$ | 0 | $\frac{\pi V_{T2}}{2V_\pi}$ | $\frac{\pi V_{T1}}{4V_\pi}$ |

It is apparent from figs. 2 and 3 that in the PROM (⟨110⟩ orientation) no phase distortion is caused by any of the field components. In addition, only the longitudinal field $E_L$ contributes to $G$. On the other hand, phase distortions do exist for both PRIZ orientations (⟨111⟩ and ⟨110⟩). Such phase distortions are caused by the transverse field $E_{T1}$ in the ⟨110⟩ orientation, while in the ⟨111⟩ orientation the longitudinal field $E_L$ is reponsible. In both PRIZ orientations, contributions to the amplitude image through $G$ are made only by the transverse fields, which leads to the suppression of zero spatial frequency components [2]. These results for the PROM and PRIZ are summarized in table 1. In table 1, the generalized voltages $V_L$, $V_{T1}$, and $V_{T2}$ are given by

$$V_\alpha = \int_0^d E_\alpha \, dz,$$

$$\alpha = L, T2, T1 \qquad (3)$$

where $d$ is the BSO crystal thickness. The above expressions are longitudinal integrals of the field components through the BSO and have units of volts.

One approach to analyzing the effects of the signal-dependent phase $\phi$ of the PRIZ is to consider the second harmonic distortion (SHD) of the device for a sinusoidal input distribution. The SHD is readily calculated as the square root of the ratio of second to first order diffraction efficiencies [5]. Using the ⟨111⟩ PRIZ as a specific example, it is assumed that a sinusoidal intensity distribution of spatial frequency $\omega/2\pi$ and wave vector parallel to the $E_{T1}$ direction exposes the PRIZ, generating related sinusoidal distributions of the longitudinal field $E_L$ and the transverse field $E_{T1}$. The polarizer and analyzer are assumed crossed, and in addition oriented to bisect the principal electrooptic axes induced by these fields as shown in fig. 1. According to table 1, $G$ and $\phi$ are given by

$$G(x) = (\pi V_{T1}/\sqrt{6}V_\pi)\cos(\omega x), \qquad (4)$$

$$\phi(x) = (\pi V_L/2\sqrt{3}V_\pi)\sin(\omega x), \qquad (5)$$

where an unimportant constant term in the phase has been suppressed and nonlinear sensitometry effects [6] have been neglected. The maxima of $\phi(x)$ are shifted by $\pi/2$ relative to $G(x)$ because by symmetry the transverse fields are strongest midway between the input exposure maxima and minima while the longitudinal fields are strongest at the maxima. The PRIZ first and second order diffraction efficiencies can be found by first expanding eq. (1) using a small signal approximation

$$A \approx iA_0(1 + i\phi)G, \qquad (6)$$

and, since the far field diffracted amplitude is the Fourier transform of eq. (1), by extracting the fundamental and harmonic frequency components. The first and second order PRIZ diffraction efficiencies are given by

$$\eta_1 = (\pi V_{T1}/2\sqrt{6}V_\pi)^2, \qquad (7)$$

$$\eta_2 = (\pi^2 V_{T1} V_L/24\sqrt{2}V_\pi^2)^2. \qquad (8)$$

the PRIZ SHD due to the phase contribution is therefore given by

$$\mathrm{SHD} \equiv (\eta_2/\eta_1)^{1/2} = \pi V_L/4\sqrt{3}V_\pi. \quad (9)$$

In the ⟨111⟩ PRIZ, the first order diffraction efficiency is determined by the transverse fields, while the longitudinal fields contribute to the SHD. Operating modes and exposure parameters that result in large longitudinal fields will increase $\phi$, resulting in large contributions to the SHD. For example, an exposure that results in $V_L$ equal to 1000 V induces a SHD of 12%. It should be noted here that in addition to the phase effects, pronounced nonlinear sensitometry characteristics also contribute to the SHD in the PRIZ [6].

In conclusion, it has been shown that the effects of all field components must be considered in evaluating the amplitude and phase responses of electrooptic spatial light modulators. In the ⟨111⟩ PRIZ, for example, the transverse fields modulate the output amplitude while the longitudinal fields modulate the phase. Such signal-dependent phase nonuniformities should be taken into consideration in evaluating ESLM's for applications in which phase response is important [5]. For example, the signal-dependent phase distortion could be used to increase the signal-to-noise ratio in an optical correlator [7]. Such phase distortions would be detrimental, however, in coherent optical processing applications where distortions in the Fourier plane cannot be tolerated, as in Fourier plane filtering.

The PRIZ also possesses additional phase effects apart from those described herein which arise from the symmetry properties of its point spread function. These effects can result in asymmetries in the PRIZ imaging properties. A full analysis will be published elsewhere [8–11].

This research was supported in part by the Army Research Office and the Joint Services Electronics Program. The authors are pleased to acknowledge many stimulating conversations with Professor Cardinal Warde, including a critical reading of the manuscript.

## References

[1] B.A. Horwitz and F.J. Corbett, Opt. Eng. 17 (1978) 353.
[2] M.P. Petrov, V.I. Marakhonov, M.G. Shlyagin, A.V. Khomenko and M.V. Krasin'kova, Sov. Phys. Tech. Phys. 25 (1980) 752.
[3] Y. Owechko and A.R. Tanguay, Jr., Optics Letters, in press (1982).
[4] R.E. Aldrich, S.L. Hou and M.L. Harvill, J. Appl. Phys. 42 (1971) 493.
[5] D. Casasent, Appl. Optics 18 (1979) 2445.
[6] Y. Owechko and A.R. Tanguay, Jr., Effects of crystallographic orientation on electrooptic spatial light modulator linearity, to be published.
[7] W.M. Gopfert and A.A. Read, Proc. Soc. Photo-Opt. Instrum. Eng. 83 (1976) 146.
[8] Y. Owechko and A.R. Tanguay, Jr., Theoretical resolution limitations of electrooptic spatial light modulators. I: Fundamental considerations, submitted to Journal of the Optical Society of America.
[9] Y. Owechko and A.R. Tanguay, Jr., Theoretical resolution limitations of electrooptic spatial light modulators. II: Effects of crystallographic orientation, submitted to Journal of the Optical Society of America.
[10] Y. Owechko and A.R. Tanguay, Jr., Theoretical resolution limitations of electrooptic spatial light modulators. III: Effects of continuous charge distributions, to be published.
[11] Y. Owechko and A.R. Tanguay, Jr., Theoretical resolution limitations of electrooptic spatial light modulators. IV: Effects of operational mode, to be published.

# Theoretical resolution limitations of electrooptic spatial light modulators. I. Fundamental considerations

Y. Owechko* and A. R. Tanguay, Jr.

*Departments of Electrical Engineering and Materials Science, and Image Processing Institute, University of Southern California, Los Angeles, California 90089-0483*

Received October 8, 1982; accepted February 28, 1984

The sensitivity and resolution of electrooptic spatial light modulators (ESLM's) such as the Pockels Readout Optical Modulator (PROM) and Microchannel Spatial Light Modulator (MSLM) are shown to be functions of the potential distribution arising from charges located within the active electrooptic-crystal layer. The Fourier transform of the potential distribution (which can be directly related to the modulation transfer function) is derived as a function of the charge location within the electrooptic crystal. The resultant analytic expression in addition exhibits the dependence of sensitivity and resolution on the dielectric constants of the blocking layers and electrooptic crystal and on the thicknesses of the three layers. It is shown that the overall sensitivity and resolution are affected strongly by charge storage in the bulk away from the electrooptic-crystal/dielectric-blocking-layer interfaces. In particular, the effects of various operating modes can be qualitatively explained by utilizing superposition to calculate the potential distribution for a positive–negative charge pair located at various positions in the electrooptic crystal. The implications of these results for device design and operation are discussed.

## 1. INTRODUCTION

An important component of numerous proposed real-time coherent optical-processing systems is an input device for performing incoherent-to-coherent conversion of data at a rate high enough to take advantage of the inherent parallelism of the processor. Electrooptic spatial light modulators (ESLM's), such as the Pockels Readout Optical Modulator (PROM),[1] PRIZ,[2–4] TITUS,[5] PHOTOTITUS,[6] and the Microchannel Spatial Light Modulator (MSLM),[7] have been proposed as such input devices and have been described in several review papers.[8,9] ESLM's record two-dimensional image information as exposure-dependent charge distributions, which induce electric fields within an active electrooptic-crystal layer. The induced electric fields in turn modulate polarized readout light through the electrooptic effect. The charge distributions can be induced by intensity modulation of light incident on a photoconductive layer,[1] by direct electron-beam charge deposition,[10] or by x-ray exposure.[11] Both longitudinal and transverse electric-field components can be sensed in readout. In this paper, the resolution and sensitivity of ESLM's that utilize the longitudinal electrooptic effect will be analyzed. Resolution, sensitivity, and phase effects in transverse-effect ESLM's will be described separately.[12]

The resolution of an ESLM is, in general, limited by electric-field spreading within the active electrooptic-crystal layer. To describe the resolution and sensitivity of an ESLM, it is necessary to determine the transfer process between the image-induced charge distribution and the resultant field distribution. This process is modeled herein as a space-invariant linear system that is characterized by a transfer function. A method for calculating the transfer function of a multilayered structure by introducing a single point charge at an interface was developed by Krittman.[13] Roach[11] derived an expression for the transfer function of an ESLM that has a two-layer structure consisting of an isotropic dielectric layer and a dielectrically anisotropic electrooptic crystal, assuming a sinusoidal charge distribution at the interface between the two layers. These previous analyses of resolution effects in layered electrostatic structures share a common limitation in that the charge distribution is confined to the interface between a dielectric layer and the electrooptic crystal. Because of the nature of the charge-pattern generating process in numerous applications of ESLM's, however (notably in the cases of the PROM and PRIZ and for the applications involving x-ray exposure and high-energy electron-beam excitation), the resultant charge distribution extends throughout the bulk of the electrooptic-crystal layer. Petrov *et al.*[2,15] have investigated the effects of bulk charge distributions by calculating the PROM and PRIZ responses for a charge density that is distributed in a step function near the electrooptic-crystal surface. Such a distribution, however, cannot take into account the presence of oppositely signed charges, the effects of operating mode, and the attenuated absorption of the incident writing illumination. The strikingly different resolutions and sensitivities obtained for different operating modes, such as forward, reverse, and superprime,[16] are caused by substantial differences in the bulk charge distributions associated with each operating mode.

In this paper, a more complete point-charge model is developed; this model includes the effects of charge trapping within the bulk of the electrooptic crystal as well as the geometric and material properties of the ESLM. The model is also generalized to a full three-layer dielectric structure consisting of an electrooptic crystal between two blocking layers; such a structure is representative of a number of current ESLM configurations. The contribution of single point charges to the sensitivity and resolution of ESLM's is shown to be dramatically dependent on the separation of the point charge from the electrooptic-crystal/dielectric-blocking-layer interface. The solutions for single point charges in numerous configurations are shown to illustrate the fundamental physical origins of observed device performance, including the dependence on operating mode[17] and on crystallographic

0740-3232/84/060635-09$02.00 

orientation.[18] By utilizing the principle of superposition, the solution for a charge distribution consisting of a positive–negative charge pair is used to explain the increased resolution obtained in the PROM by employing the superprime mode. The model will be extended to continuous longitudinal charge distributions in succeeding papers in this series by using the single-point-charge solution, derived here as a Green's function. Such distributions are obtained from iterative charge-transport models that depend on numerous device and material parameters and as such are not as generally applicable as the results described herein.

## 2. THEORETICAL DEVELOPMENT

The PROM will be used as a specific example of an ESLM that utilizes the longitudinal electrooptic effect in the following derivation. It is instructive to compare the resultant characteristics with those of the PRIZ, a transverse-effect device that is structurally identical to the PROM except for the crystallographic orientation of the electrooptic crystal. Such a comparison is treated in the second paper of this series.[12]

A schematic diagram of a typical PROM structure is shown in Fig. 1. The device consists of a photoconductive electrooptic crystal ($Bi_{12}SiO_{20}$, or BSO; dielectric constant $\epsilon_{eo} = 56$) oriented in the ⟨001⟩ direction and sandwiched between two thin, transparent dielectric blocking layers. The blocking layers typically consist of parylene (dielectric constant $\epsilon_{bl} = 3$)[1] and are coated with transparent electrodes. The orientation of the BSO-crystal layer ensures that only longitudinal-field components contribute to the electrooptic effect (Appendix A).

In the simplest mode of PROM operation,[1] a voltage (typically 2000 V) is applied to the electrodes and is divided among the three layers in inverse proportion to the capacitance of each layer. Since the electrooptic crystal is also photoconductive, illumination from the negative electrode side with image-modulated light at a photosensitive wavelength causes charge generation at a rate proportional to the incident intensity at each spatial location. The generated charges then separate in the applied field (by electron drift into the bulk, since holes are relatively immobile in BSO[19]), giving rise to a reduction in voltage across the electrooptic crystal in the illuminated regions. Since in the absence of illumination the dielectric relaxation time of BSO is unusually large (several thousand seconds), the electron distribution subsequent to exposure is trapped in the bulk, resulting in storage of the image. The resultant field distribution induces a birefringence (through the linear longitudinal electrooptic effect), which alters the polarization of linearly polarized readout light oriented to bisect the principal birefringent axes. The exposure-induced polarization produces an image-modulated amplitude when viewed through a crossed analyzer (as used in a typical optical-processing application requiring an amplitude image; other applications may be optimized for phase modulation by utilizing parallel polarizer/analyzer combinations). Since, for the purposes of light propagation, an ESLM may be considered to be optically thin[20] (in other words, diffraction within the ESLM can be ignored), the readout amplitude transmitted through a PROM situated between crossed polarizers may be expressed as[1]

$$A(x,y) = iA_0 \sin\left[\frac{\pi V_L(x,y)}{2V_\pi}\right], \tag{1}$$

where $A_0$ is the incident readout-light amplitude (appropriately corrected for interface reflection losses); $V_\pi = \lambda/2n_0^3 r_{41}$ is the longitudinal half-wave voltage of BSO in the ⟨001⟩ orientation, where $\lambda$ is the wavelength of the readout light, $n_0$ is the refractive index of BSO, and $r_{41}$ is the electrooptic coefficient of BSO; and $V_L(x,y)$ is the voltage across the BSO layer at image coordinates $(x,y)$. It should be noted that in the above expression it is assumed that the readout wavelength and intensity are chosen such that insignificant photoconductive charge redistribution occurs and that the effects of natural optical activity in BSO may be neglected.[21,22] Thus the output amplitude is a monotonic function of the input intensity (for applied voltages less than the half-wave voltage). Such a transfer relationship is desirable for incoherent-to-coherent conversion in optical-signal-processing operations.[23]

The mapping of the input exposure into the output amplitude can be described by the cascaded transformations shown in Fig. 2. In this paper, we are modeling the transformation from the induced charge distribution to the voltage distribution as a space-invariant linear system with a well-defined transfer function that describes the effects of the system in the spatial-frequency domain.[23] An assumption that is implicit in the transfer-function treatment of ESLM resolution is that the resolution is limited by field fringing effects and not by transverse drift or diffusion of the input exposure-induced charge distribution $\rho(x,y,z)$ (both of which are inherently nonlinear processes).

From the nature of Eq. (1), it can be seen that the resolution of an ESLM depends directly on the relationship between a periodic variation in the writing exposure and the resultant spatial modulation of the voltage across the electrooptic crystal. The voltage $V_L(x,y)$ will be a function of the dielectric constants and thicknesses of the electrooptic and blocking layers, the longitudinal locations of electrons and positive charges resulting from the writing process, and the spatial frequency of the charge (writing intensity) modulation in the transverse $(x,y)$ plane. To describe the sensitivity and resolution of the device, we seek to derive the dependence of each Fourier component of $V_L(x,y)$ on the corresponding Fourier component of the transverse charge distribution as a function of the device parameters and the longitudinal

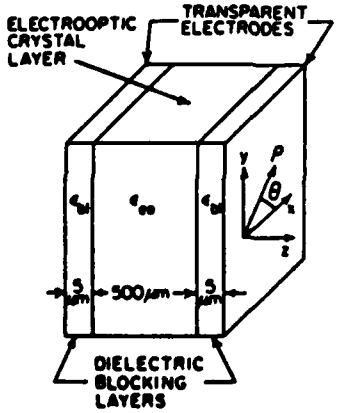


Fig. 1. Typical PROM structure and coordinate system used in derivation of $V_L(\omega;\xi)$.

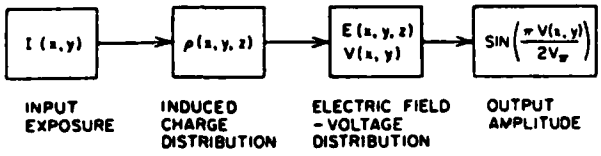


Fig. 2. Transformation of input exposure to output amplitude in electrooptic spatial light modulators.

charge distribution. This dependence is described by the voltage transfer function $V_L(\omega)$. As shown in linear systems theory,[23] the transfer function of a linear system is the Fourier transform of the impulse response. In this case, the impulse response corresponds to the voltage distribution arising from a delta-function input exposure distribution in the transverse dimensions.

If the charges are constrained to the blocking-layer/electrooptic-crystal interfaces, the spatial-frequency dependence of $V_L(\omega)$ may be obtained by straightforward solution[14] of the electrostatic boundary conditions with a surface charge $\sigma(x, y, z)$ given by

$$\sigma(x, y, z) = \sigma_0 \delta(z)[1 + \cos(\omega x)], \tag{2}$$

where $\sigma_0$ is the average value of the surface charge density and $\delta(z)$ is the unit impulse function. However, since the absorption coefficient of the electrooptic crystal is finite and since, in addition, the drift length of a photoexcited electron can be of the order of the typical electrooptic-layer thickness,[24] consideration of charge distributions within the bulk of the electrooptic crystal is necessary to formulate a realistic resolution model.

The effects of such a bulk charge distribution can be modeled by considering a single point charge $q$ located at $(x, y, z) = (0, 0, -\xi)$ within the electrooptic-crystal layer as shown in Fig. 3. Determination of the voltage transfer function $V_L(\omega; \xi)$ resulting from such a point charge is equivalent to calculation of the potential difference resulting from a periodic charge distribution in the bulk given by

$$\sigma(x, y, z) = \sigma_0 \delta(z + \xi)[1 + \cos(\omega x)] \tag{3}$$

as a function of spatial frequency $\omega$. This approach has the advantage that, once the solution for a single point charge has been obtained, the linearity of the Fourier transform may be utilized to solve multiple-charge cases by summation of single-charge solutions and continuous-charge distribution cases by simple integration.

The axial symmetry of the problem can be exploited by transformation to cylindrical coordinates $(\rho, \theta, z)$, where $(\rho, \theta)$ are in the $(x, y)$ plane and $z$ is the longitudinal coordinate, as shown in Fig. 1. Since the problem is invariant with respect to the angular coordinate $\theta$, the rectilinear two-dimensional Fourier transform becomes a Hankel transform. The voltage across the electrooptic crystal can then be written in the form

$$V_L(\rho; \xi) = \frac{1}{2\pi} \int_0^\infty V_L(\omega; \xi) \omega J_0(\omega \rho) \mathrm{d}\omega, \tag{4}$$

where $J_0$ is the zero-order Bessel function and $\omega$ is the circular spatial frequency.[23] Expressing $V_L(\rho; \xi)$ as a Hankel transform simplifies the calculation since the Hankel transform of the delta-function charge distribution is a constant. Hence the difficulties associated with discontinuities in the real-space boundary conditions that result from charge singularities are automatically removed in Fourier space.

The real-space potential difference $V_L(\rho; \xi)$ must satisfy Laplace's equation in all four regions depicted in Fig. 3, and it must also satisfy the boundary conditions at both electrodes, at both electrooptic-crystal/blocking-layer interfaces, and at the plane defined by the location of the point charge ($z = -\xi$). Once $V_L(\rho; \xi)$ is determined, $V_L(\omega; \xi)$ is easily found by extracting the kernel of the Hankel transform, as shown explicitly in Appendix B with the following result:

$$V_L(\omega; \xi) = \frac{q}{\epsilon_{eo}\epsilon_0 \omega} \left( \frac{\sinh[\omega(a-d)]}{\cosh[\omega(a-\xi)] \left\{ 1 - \dfrac{\coth[\omega(b-\xi)]}{\coth[\omega(a-\xi)]} \right\}} + \frac{\sinh(\omega b)}{\cosh[\omega(b-\xi)] \left\{ 1 - \dfrac{\coth[\omega(a-\xi)]}{\coth[\omega(b-\xi)]} \right\}} \right), \tag{5}$$

where

$$a = d + \frac{1}{\omega} \coth^{-1} \left[ \frac{\epsilon_{bl}}{\epsilon_{eo}} \coth(\omega d_2) \right]$$

and

$$b = \frac{1}{\omega} \coth^{-1} \left[ \frac{\epsilon_{bl}}{\epsilon_{eo}} \coth(-\omega d_1) \right].$$

Note that, as expected, $V_L(\omega; \xi)$ is a function of the electrooptic-crystal thickness $d$, the dielectric-blocking-layer thicknesses $d_1$ and $d_2$, and the dielectric constants $\epsilon_{eo}$ and $\epsilon_{bl}$ of the respective layers as well as on the location $\xi$ of the point charge. In this calculation both of the electrodes are assumed to be grounded.

In the special case $\xi = d$ and $d_1 = 0$, the problem reduces to that of a charge pattern confined to the electrooptic-crystal/dielectric-layer interface of a two-layer device, with

$$V_L(\omega; d) = \frac{q}{\omega \epsilon_0 [\epsilon_{eo} \coth(\omega d) + \epsilon_{bl} \coth(\omega d_2)]}, \tag{6}$$

in agreement with the solution for this case derived previously.[14] In addition, the above results reduce to the expressions given by Barrera *et al.*[25] as the blocking-layer thicknesses approach infinity.

The nature of the spatial-frequency dependence of the transfer function $V_L(\omega; \xi)$ can be more easily appreciated if the low- and high-spatial-frequency limits are examined. These limiting forms are given by

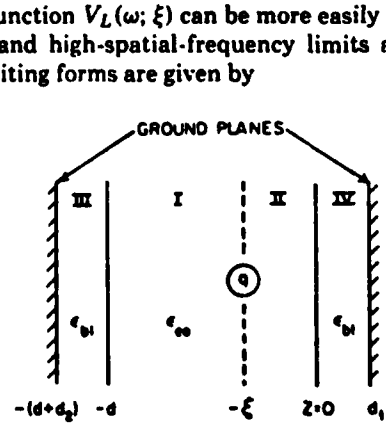


Fig. 3. Location of point charge $q$ in electrooptic-crystal bulk.

$$\lim_{\omega \to 0} V_L(\omega; \xi) = \frac{q}{\epsilon_0}\left[\frac{\xi(d_1 + d_2) - dd_1}{\epsilon_{eo}(d_1 + d_2) + \epsilon_{bl}d}\right], \tag{7}$$

$$\lim_{\omega \to \infty} V_L(\omega; \xi) \simeq \frac{q}{\omega\epsilon_0(\epsilon_{bl} + \epsilon_{eo})}[\exp(-\omega\Delta_1) - \exp(-\omega\Delta_2)], \tag{8}$$

where $\Delta_1 = d - \xi$ and $\Delta_2 = \xi$. The parameters $\Delta_1$ and $\Delta_2$ represent the distance of the point charge from each dielectric-blocking-layer/electrooptic-crystal interface. It should be noted here that the measured diffraction efficiency may not decrease with spatial frequency at the rate predicted by the magnitude squared of Eq. (8), as might be expected from Eq. (1). This is because Eq. (8) must be used as a Green's function and integrated over the actual longitudinal charge distribution. Qualitative trends may, however, be extracted from the single-point-charge solution.

From Eq. (7), it is apparent that the low-spatial-frequency limit of $V_L(\omega; \xi)$ depends on the layer thicknesses and dielectric constants as well as on the charge location. In particular, if we consider the case of a symmetric device (i.e., a device with two identical blocking layers), $V_L(\omega; \xi)$ decreases linearly to the negative of its initial value as the charge position varies from one interface to the other. This is intuitively appealing since zero voltage drop is expected across the electrooptic crystal for a point charge in the center of a symmetric device. The low-frequency response is, in addition, independent of spatial frequency.

The high-frequency limiting form of $V_L(\omega; \xi)$ given in Eq. (8) is a function only of the dielectric constants of the layers, the spatial frequency, and the distance of the charge from either of the blocking-layer/electrooptic-crystal interfaces. If the point charge is positioned on either interface, $V_L(\omega; \xi)$ falls off inversely with increasing spatial frequency. For even small separations of the charge from either interface, however, the high spatial frequencies will be exponentially attenuated. Noted that, as in the low-spatial-frequency limit for a symmetric device, $V_L(\omega; \xi)$ is zero when the charge is in the center of the device.

The modulation transfer function (MTF) relating the output image intensity modulation to the input image intensity modulation may be obtained from the expression[14]

$$\text{MTF} = \frac{1}{m}\left(\frac{I_{max} - I_{min}}{I_{max} + I_{min}}\right), \tag{9}$$

where the output intensity is given by

$$I = I_0 \sin^2\left\{\frac{\pi V_L(0)}{2V_\pi}\left[1 + m\frac{V_L(\omega)}{V_L(0)}\cos(\omega x)\right]\right\} \tag{10}$$

and where $m$ is the spatial modulation index of the input charge distribution and $V_L(0; \xi) = \lim_{\omega \to 0} V_L(\omega; \xi)$. Physically, $V_L(0; \xi)$ is the average value in the transverse dimension of the potential difference across the electrooptic crystal. In Eq. (9), $I_{max}$ and $I_{min}$ are the values of I for $\cos(\omega x) = 1$ and $\cos(\omega x) = -1$, respectively. From Eq. (10), it can be seen that the character of the solution for each case is fully expressed by $V_L(\omega; \xi)$ or $V_L(\omega; \xi)/V_L(0; \xi)$. Since the MTF for a given device will be both exposure $[V_L(0; \xi)]$ and modulation $(m)$ dependent, a more fundamental indication of expected device performance is obtained by discussion of the unnormalized $[V_L(\omega; \xi)]$ and normalized $[V_L(\omega; \xi)/V_L(0; \xi)]$ transfer functions.

Before proceeding to a detailed presentation and interpretation of the results, it should be pointed out that the unnormalized and normalized transfer functions have direct interpretations useful both for comparison of different devices and comparison of the effects of different charge distributions within a given device. In particular, graphs of $V_L(\omega; \xi)$ as a function of $\omega$ parameterized by different device properties represent equal exposure conditions (identical charge distributions), whereas graphs of $V_L(\omega; \xi)/V_L(0; \xi)$ represent optimum exposure conditions for each compared device [i.e., sufficient exposure for each device that $V_L(\omega; \xi)$ is optimized in the limit of the low spatial frequencies]. These types of comparison are familiar from the case of photographic film, for which the typical resolution/sensitivity trade-off forces a similar comparison of film properties on the basis of response to either equal exposure or optimum exposure.

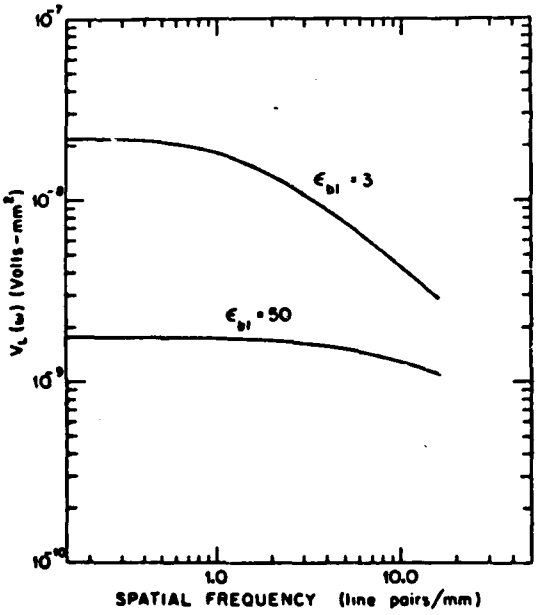


Fig. 4. Dependence of transfer function $V_L(\omega; \xi)$ on blocking-layer dielectric constant.

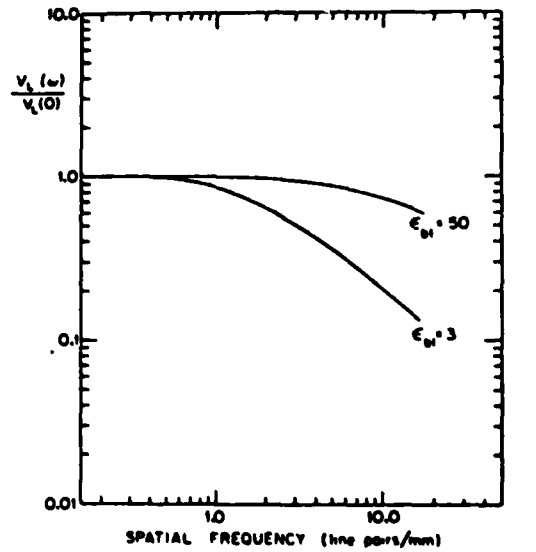


Fig. 5. Dependence of normalized transfer function $V_L(\omega; \xi)/V_L(0; \xi)$ on blocking-layer dielectric constant.

AD-A146 210 DIELECTRIC AND OPTICAL PROPERTIES OF SPUTTERED THIN FILMS(U) UNIVERSITY OF SOUTHERN CALIFORNIA LOS ANGELES OPTICAL MATERIA... A R TANGUAY JUL 84 USC/OMDL-1101 2/2

UNCLASSIFIED ARO-16291.3-PH DAAG29-79-C-0175 F/G 20/6 NL

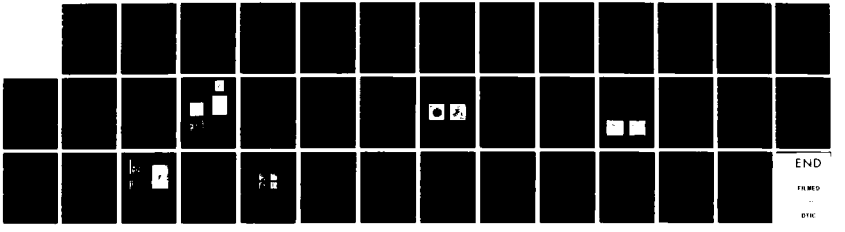

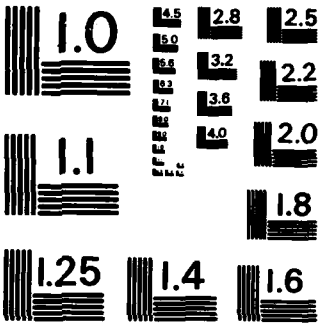

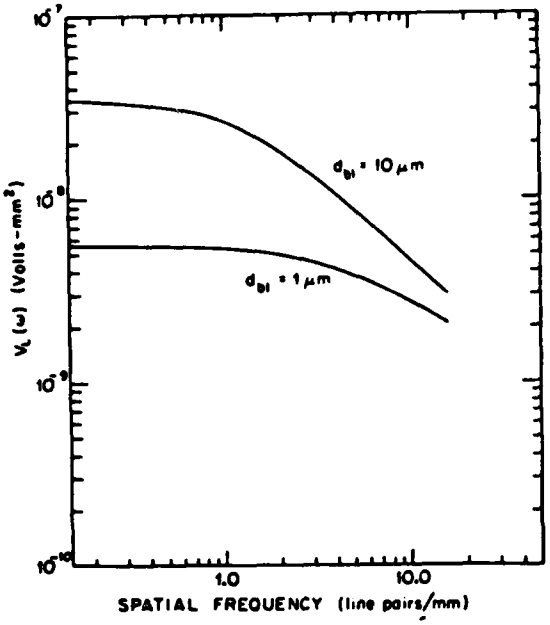


Fig. 6. Dependence of transfer function $V_L(\omega; \xi)$ on blocking-layer thicknesses.

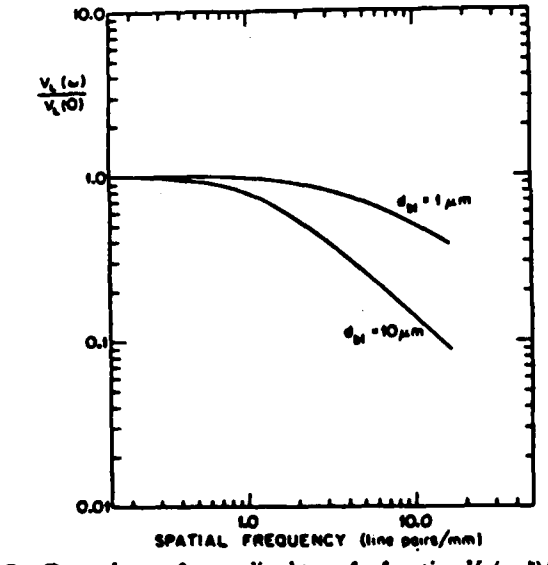


Fig. 7. Dependence of normalized transfer function $V_L(\omega; \xi)/V_L(0; \xi)$ on blocking-layer thicknesses.

## 3. FEATURES OF THE SOLUTION FOR DISCRETE CHARGE DISTRIBUTIONS

The dependences of $V_L(\omega; \xi)$ and $V_L(\omega; \xi)/V_L(0; \xi)$ on the dielectric constant of the blocking layers are shown in Figs. 4 and 5, respectively, for a symmetric device with the point charge on the blocking-layer/electrooptic-crystal interface. The layer thicknesses are given in Fig. 1. [Increasing the blocking-layer dielectric constant reduces the device sensitivity (Fig. 4) and increases the resolution or high-spatial-frequency relative response (Fig. 5).] Decreasing the thicknesses of the two dielectric blocking layers has a similar effect, as shown in Figs. 6 and 7. The resolution and sensitivity also exhibit the same behavior when the electrooptic-crystal thickness is decreased, as illustrated in Figs. 8 and 9.

Perhaps the most interesting behavior of the transfer function $V_L(\omega; \xi)$ occurs when the point charge is displaced from the surface into the bulk of the electrooptic crystal. The high-spatial-frequency amplitude response of a PROM for a charge distribution confined to the blocking-layer/electrooptic-crystal interface should decrease inversely with spatial frequency, as first determined by Roach.[14] Experimentally measured PROM MTF's, however, decrease with spatial frequency at a faster rate, especially at low exposures.[16] In Section 2 it was shown that the high-spatial-frequency response decreased exponentially and that the low-spatial-frequency response decreased linearly with separation of the point charge from the interface. This results in the degradation of the sensitivity as well as the resolution by movement of the charge into the electrooptic-crystal bulk, as illustrated by the graphs of $V_L(\omega; \xi)$ and $V_L(\omega; \xi)/V_L(0; \xi)$ in Figs. 10 and 11. Trapping of charges in the electrooptic-crystal bulk can

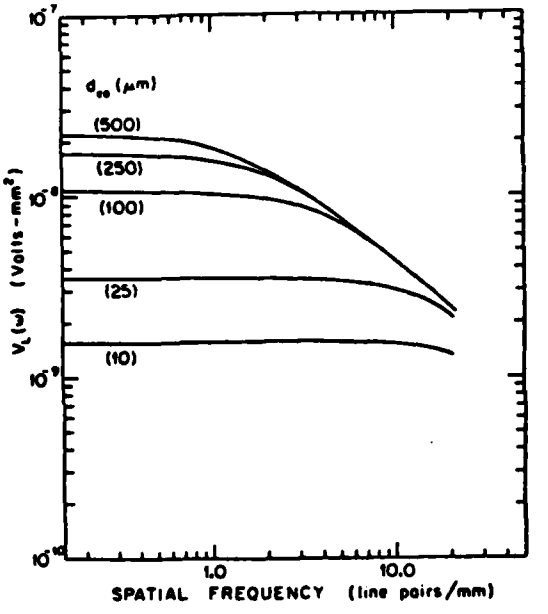


Fig. 8. Dependence of transfer function $V_L(\omega; \xi)$ on electrooptic-crystal thickness.

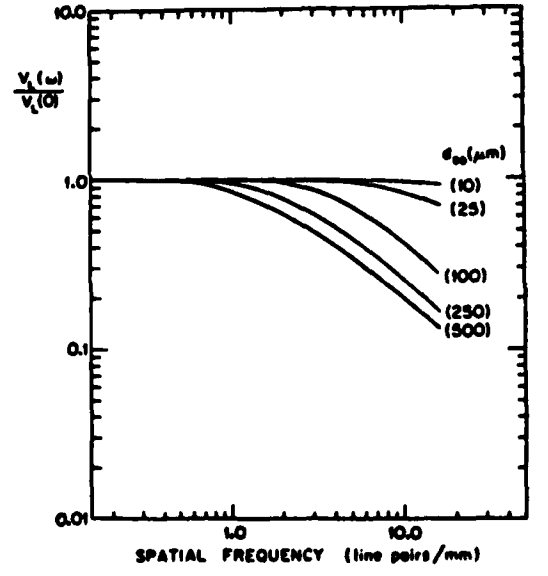


Fig. 9. Dependence of normalized transfer function $V_L(\omega; \xi)/V_L(0; \xi)$ on electrooptic-crystal thickness.

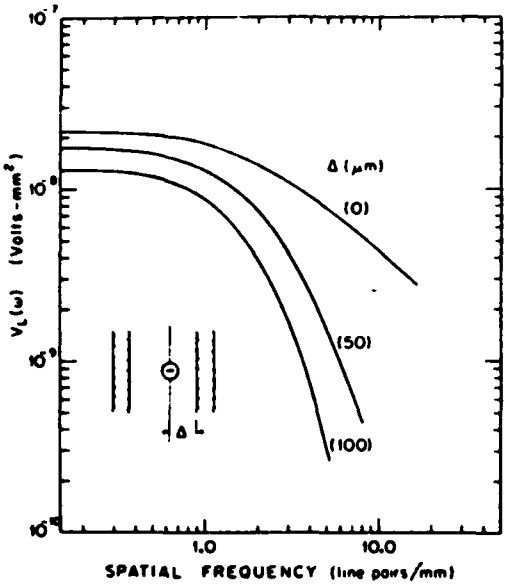


Fig. 10. Dependence of transfer function $V_L(\omega;\xi)$ on point-charge position.

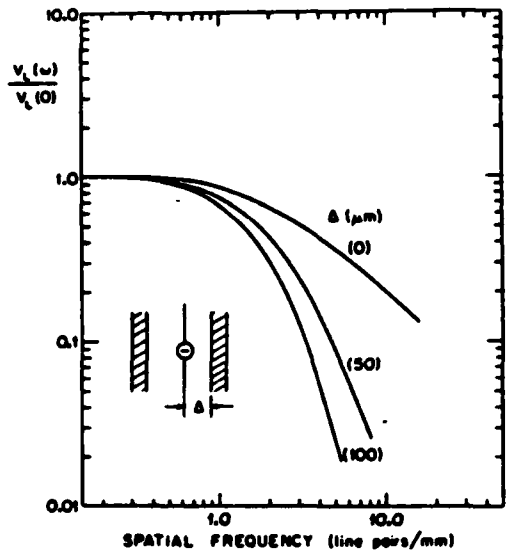


Fig. 11. Dependence of normalized transfer function $V_L(\omega;\xi)/V_L(0;\xi)$ on point-charge position.

therefore explain the measured degradation of PROM MTF's relative to resolution models that confine the charges to the interface.

The solutions for cases involving multiple point charges can be obtained by a linear superposition of the solutions for each separate point charge. In particular, since realistic charge distributions consist of input-exposure-induced positive-negative charge pairs, the effects of such pairs (and the operating modes that generate them) can be modeled if the point charges are assigned opposite signs. The results of such a calculation for asymmetric charge configurations within a symmetric PROM device are shown in Figs. 12 and 13. A positive point charge is located at one interface ($z = -500\,\mu m$), and a negative point charge is placed at varying distances from the opposite interface. The device parameters are those of the typical symmetric PROM shown in Fig. 1. This charge configuration is a zero-order approximation of an exposure process in which the incident illumination is characterized by a large absorption coefficient, so that the positive charge distribution (which is assumed immobile[19]) is constrained to one interface, whereas the electron distribution is forced into the bulk electrooptic layer by the applied field. The resultant charge separation will be a function of the device constitutive parameters and the voltage across the device during writing (operating mode). Because of the assumption of a symmetric device, the $V_L(\omega)$ curve for the case of the negative charge at the opposite interface [labeled (0) in Fig. 12] is exactly a factor of 2 larger than the curve in Fig. 10 for a single point charge at an interface. (In a symmetric device, charges of opposite sign symmetrically placed on opposite sides of the electrooptic

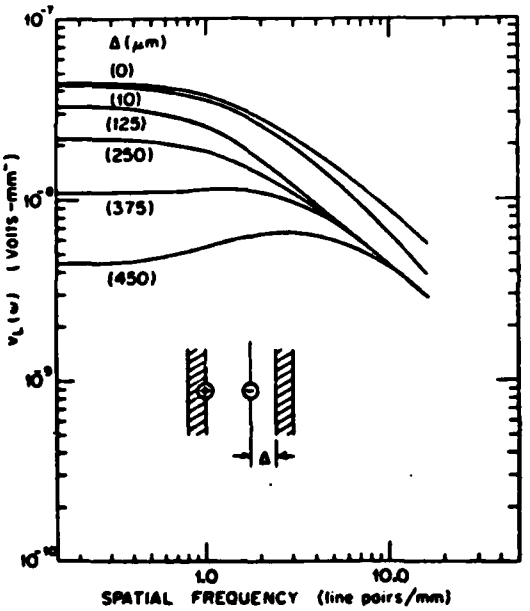


Fig. 12. Transfer function $V_L(\omega;\xi)$ for asymmetric charge distributions consisting of two point charges of opposite sign.

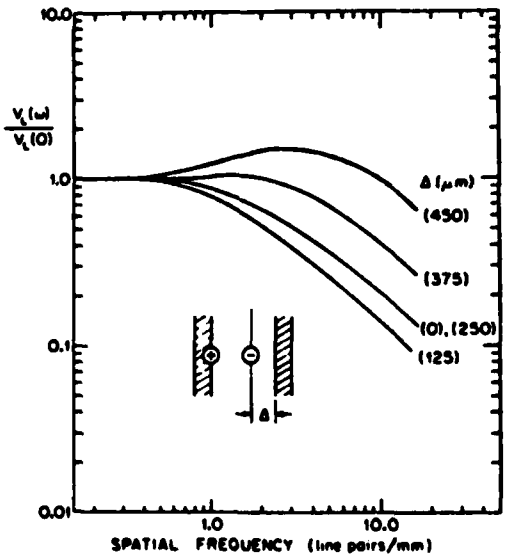


Fig. 13. Normalized transfer function $V_L(\omega;\xi)/V_L(0;\xi)$ for asymmetric charge distributions consisting of two point charges of opposite sign.

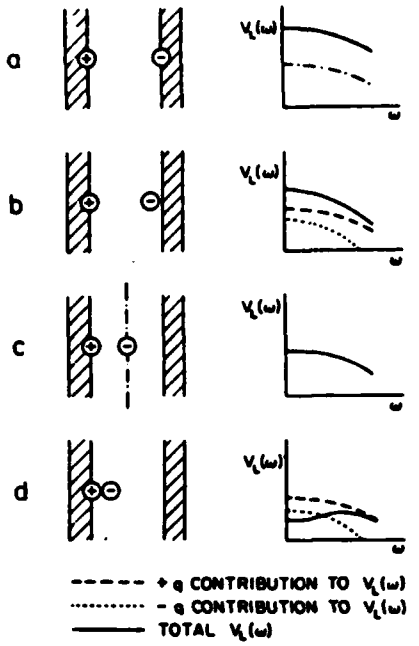


Fig. 14. Explanation of nonmonotonic spatial-frequency response of Figs. 12 and 13 in terms of contributions of each point charge to the total transfer function $V_L(\omega; \xi)$.

crystal contribute equally to the total potential.) As the negative charge is moved from the interface toward the center of the crystal, the response at high spatial frequencies decreases more rapidly at first than the response at low frequencies. As the negative charge reaches the center of the electrooptic crystal ($z = -250\ \mu m$) and continues to approach the positive charge, the response at low spatial frequencies decreases faster than the reduction in high-frequency response. For both charges in the same half of the crystal, the response characteristic becomes nonmonotonic, as shown in Figs. 12 and 13. In the operating mode called superprime,[16] a voltage reversal in mid-exposure is used to generate a closely confined distribution of positive and negative charges near one interface. The increase in resolution obtained with the superprime mode is a direct consequence of the relative enhancement of high spatial frequencies by this nonmonotonic effect.

The nonmonotonic behavior of the voltage transfer function can be explained with the aid of Fig. 14, which details the contributions of each charge to the total transfer function. In Fig. 14a, the signs and magnitudes of the response contributions from both charges are positive, and the resultant response has the same characteristic as that of a single charge positioned at an interface. In Fig. 14b the negative charge is 125 $\mu m$ (one quarter of the electrooptic-crystal thickness) from the interface and, hence, contributes a linearly reduced low-spatial-frequency response and an exponentially reduced high-spatial-frequency response as compared with Fig. 14a. At the center of the crystal, the negative charge does not contribute to the response because of symmetry considerations, and the form of the response is the same as that for a single point charge at an interface (as shown in Fig. 14c). The most interesting case is shown in Fig. 14d, in which the contributions to the total response from the two charges have opposite signs. This situation is equivalent to taking the difference between the $V_L(\omega; \xi)$ curves for two positive charges at the same locations, as shown in the figure. The nonmonotonic behavior is seen to arise directly from the exponential attenuation of the high-spatial-frequency components of the response contributed by the negative charge.

## 4. DEVICE IMPLICATIONS

The dependence of the voltage transfer function on the dielectric constants and thicknesses of the blocking layers and on the thickness of the electrooptic layer (as shown in Figs. 4–9) indicates that new PROM devices can be envisaged with MTFs constant to much higher spatial frequencies than are characteristic of currently available devices. Gains in MTF behavior that result from the appropriate choice of layer properties will be accompanied by an overall reduction in device sensitivity. Such new devices, however, would provide significantly improved image fidelity and resolution in applications for which requirements on device sensitivity can be relaxed, similar to the familiar trade-off in the case of photographic film. In order to improve PROM resolution, high dielectric constant, high dielectric breakdown strength, and high resistivity dielectric blocking layers are required. Alternatively, decreasing the device layer thicknesses would also improve PROM resolution.

The form of the exposure-induced charge distribution in the bulk of the electrooptic crystal is seen to have a strong influence on the response of the image storage process. For normal writing modes, the optimum resolution and sensitivity within a given PROM structure are obtained when the positive charge distribution is constrained to the interface nearest the negative electrode and the entire electron distribution is swept to the interface nearest the positive electrode during the writing process. The actual resolution and sensitivity obtained for a given device are thus strongly dependent on a number of factors, including the absorption coefficient of the electrooptic crystal at the writing wavelength, the external applied voltage, the device layer thicknesses, and the mobility-lifetime product of photogenerated electrons in the electrooptic crystal. A model of charge transport in BSO developed by Sprague[26] has been adapted to incorporate the effects of bulk charge storage and the above variables on ESLM resolution and will be detailed in subsequent papers in this series. Bulk charge-distribution effects will also strongly affect the resolution and sensitivity for cases in which the image-modulated charge pattern is induced by high-energy electron-beam[10] and x-ray[11] sources. The use of voltage modulation techniques (such as reversing the applied voltage in mid-exposure in the superprime mode) can also improve device resolution by utilizing the bulk charge-distribution effects of Fig. 14. Further details of operating mode effects on resolution and sensitivity will be published separately.

## 5. SUMMARY

A generalized expression for the voltage transfer function of a point charge in a three-layer electrooptic spatial light modulator was derived that depends explicitly on the thicknesses and dielectric constants of the layers and on the longitudinal charge position within the electrooptic crystal. This solution was applied explicitly to the analysis of the sensitivity and resolution of the PROM, and the importance of bulk charge-distribution effects was demonstrated. In subsequent

papers, extensions of the solution will be made to ESLM's that use novel electrooptic-crystal orientations to sense transverse fields[12] and to ESLM's that utilize anisotropic electrooptic crystals. The continuous bulk charge-distribution case will also be treated, along with the effects of various operating modes.

## APPENDIX A. TRANSVERSE CONTRIBUTION TO PROM ELECTROOPTIC EFFECT

The contribution to the electrooptic effect of the electric-field components transverse to the light propagation direction can be determined by consideration of the index ellipsoid. For a crystal of $I23$ symmetry, such as $Bi_{12}SiO_{20}$, the only nonzero electrooptic coefficients are (in the usual contracted notation)

$$r_{41} = r_{52} = r_{63}. \tag{A1}$$

If the longitudinal direction (corresponding to both the direction of the applied field and the direction of light propagation) is taken to be the $z$ axis, then the transverse-field components $E_x$ and $E_y$ modify the index ellipsoid such that

$$\frac{x^2 + y^2 + z^2}{{n_0}^2} + 2r_{41}(E_x yz + E_y zx + E_z xy) = 1, \tag{A2}$$

where the longitudinal field $E_z$ is taken to be zero for simplicity and $n_0$ is the zero field index of refraction. In the usual PROM geometry, the light propagation direction is along the crystallographic ⟨001⟩ axis. The polarization eigenstates are determined by the intersection of the ellipsoid with the plane normal to the light-propagation direction ($z = 0$ plane), which is described by

$$\frac{x^2 + y^2}{{n_0}^2} = 1. \tag{A3}$$

Since the intersection is circularly symmetric, the transverse fields $E_x$ and $E_y$ do not contribute to the electrooptic effect for light propagation along the $z$ axis. Consequently, only the longitudinal component of the electric field need be considered in calculating the field-induced birefringence.

## APPENDIX B. DERIVATION OF $V_L(\omega; \xi)$ FOR A THREE-LAYER DEVICE

In this appendix, we derive the expression given in Eq. (5) for the voltage transfer function $V_L(\omega; \xi)$ in a three-layer ESLM. The device geometry is shown in Figs. 1 and 3. The dielectric constants of the blocking layers are assumed equal ($\epsilon_{bl}$), and the thicknesses of the layers are given by $d_1$ and $d_2$. The dielectric constant of the electrooptic-crystal layer is denoted by $\epsilon_{eo}$ and the thickness of the layer by $d$. A single point charge $q$ is placed within the electrooptic crystal at a distance $\xi$ from the dielectric blocking-layer/electrooptic-crystal interface, as shown in Fig. 3. Transparent electrodes are placed in the planes $z = d_1$ and $z = -(d + d_2)$, which are the external boundaries of the dielectric blocking layers. Both electrodes are assumed grounded during readout.

The cylindrical symmetry of the problem about the $z$ axis is utilized by expressing the potential within the layers in cylindrical coordinates as a Hankel transform:

$$V(\rho, \theta, z) = V(\rho, z) = \frac{1}{2\pi}\int_0^\infty V(\omega, z)\omega J_0(\omega\rho)\mathrm{d}\omega. \tag{B1}$$

The potential within any of the four regions shown in Fig. 3 automatically satisfies Laplace's equation if the potential is written in the form

$$V(\rho, z) = \int_0^\infty G(\omega)\exp(\pm\omega z)J_0(\omega\rho)\mathrm{d}\omega. \tag{B2}$$

The potential in each of the four regions may then be expressed explicitly as

$$\text{I.}\quad V_I(\rho, z) = \int_0^\infty A_1(\omega)\sinh[\omega(z + a)]J_0(\omega\rho)\mathrm{d}\omega, \tag{B3}$$

$$\text{II.}\quad V_{II}(\rho, z) = \int_0^\infty A_2(\omega)\sinh[\omega(z + b)]J_0(\omega\rho)\mathrm{d}\omega, \tag{B4}$$

$$\text{III.}\quad V_{III}(\rho, z) = \int_0^\infty A_3(\omega)\sinh[\omega(z + d + d_2)]J_0(\omega\rho)\mathrm{d}\omega, \tag{B5}$$

$$\text{IV.}\quad V_{IV}(\rho, z) = \int_0^\infty A_4(\omega)\sinh[\omega(z - d_1)]J_0(\omega\rho)\mathrm{d}\omega. \tag{B6}$$

This form ensures that the potentials in regions III and IV are zero at the $z = -(d + d_2)$ and $z = d_1$ ground planes. The parameters $a$ and $b$ are determined below from the application of appropriate boundary conditions.

The boundary conditions are

$$V(\rho, -d^+) = V(\rho, -d^-), \tag{B7}$$

$$\epsilon_{eo}\frac{\partial}{\partial z}V(\rho, -d^+) = \epsilon_{bl}\frac{\partial}{\partial z}V(\rho, -d^-), \tag{B8}$$

$$V(\rho, -\xi^+) = V(\rho, -\xi^-), \tag{B9}$$

$$\frac{\partial}{\partial z}V(\rho, -\xi^+) - \frac{\partial}{\partial z}V(\rho, -\xi^-) = \frac{\sigma(\rho, \xi)}{\epsilon_{eo}\epsilon_0}, \tag{B10}$$

$$V(\rho, 0^+) = V(\rho, 0^-), \tag{B11}$$

$$\epsilon_{bl}\frac{\partial}{\partial z}V(\rho, 0^+) = \epsilon_{eo}\frac{\partial}{\partial z}V(\rho, 0^-), \tag{B12}$$

where $\sigma(\rho, \xi)$, the charge density at $z = -\xi$, is given by

$$\sigma(\rho, \xi) = \frac{q\delta(\rho)}{2\pi\rho} = \frac{q}{2\pi}\int_0^\infty \omega J_0(\omega\rho)\mathrm{d}\omega \tag{B13}$$

and $\delta(\rho)$ is the unit impulse function. Application of the boundary conditions by direct substitution of Eqs. (B3)–(B6) into Eqs. (B7)–(B12) yields

$$A_1(\omega) = \frac{q}{2\pi\epsilon_{eo}\epsilon_0}\left(\cosh[\omega(a - \xi)]\left\{1 - \frac{\coth[\omega(b - \xi)]}{\coth[\omega(a - \xi)]}\right\}\right)^{-1}, \tag{B14}$$

$$A_2(\omega) = \frac{q}{2\pi\epsilon_{eo}\epsilon_0}\left(\cosh[\omega(b - \xi)]\left\{\frac{\coth[\omega(a - \xi)]}{\coth[\omega(b - \xi)]} - 1\right\}\right)^{-1}, \tag{B15}$$

where $a$ and $b$ are given by

$$a = d + \frac{1}{\omega}\coth^{-1}\left[\frac{\epsilon_{bl}}{\epsilon_{eo}}\coth(\omega d_2)\right], \tag{B16}$$

$$b = \frac{1}{\omega}\coth^{-1}\left[\frac{\epsilon_{bl}}{\epsilon_{eo}}\coth(-\omega d_1)\right]. \tag{B17}$$

The voltage across the electrooptic crystal is given by

$$V_L(\rho) = V_I(\rho, -d) - V_{II}(\rho, 0). \tag{B18}$$

By writing $V(\rho, z)$ as a Hankel transform [as in Eq. (B1)] and by substituting Eqs. (B3), (B4), and (B14)–(B17) into Eq. (B18), we obtain the final expression for the spatial-frequency dependence of the potential drop across the electrooptic-crystal layer:

$$V_L(\omega;\xi) = \frac{q}{\epsilon_{eo}\epsilon_0\omega}\left(\frac{\sinh[\omega(a-d)]}{\cosh[\omega(a-\xi)]\left\{1-\dfrac{\coth[\omega(b-\xi)]}{\coth[\omega(a-\xi)]}\right\}}\right.$$

$$\left. + \frac{\sinh(\omega b)}{\cosh[\omega(b-\xi)]\left\{1-\dfrac{\coth[\omega(a-\xi)]}{\coth[\omega(b-\xi)]}\right\}}\right). \tag{B19}$$

This is the result presented in Eq. (5).

## ACKNOWLEDGMENTS

This research was supported in part by the National Science Foundation, the Joint Services Electronics Program, the U.S. Army Research Office, and the Defense Advanced Research Projects Agency. Y. Owechko gratefully acknowledges the support of Xerox and Schlumberger Graduate Fellowships. Many stimulating conversations with Ralph Aldrich (Itek Corporation), Cardinal Warde (Massachusetts Institute of Technology), and David Casasent (Carnegie-Mellon University) are gratefully acknowledged.

* Present address, Hughes Research Laboratories, 3011 Malibu Canyon Road, Malibu, California 90265.

## REFERENCES

1. B. A. Horwitz and F. J. Corbett, "The PROM—theory and applications for the Pockels Readout Optical Modulator," Opt. Eng. 17, 353–364 (1978).
2. M. P. Petrov, A. V. Khomenko, M. V. Krasin'kova, V. I. Marakhonov, and M. G. Shlyagin, "The PRIZ image converter and its use in optical data processing systems," Sov. Phys. Tech. Phys. 26, 816–821 (1981).
3. D. Casasent, F. Caimi, and A. Khomenko, "Test and evaluation of the Soviet PROM and PRIZ spatial light modulators," Appl. Opt. 20, 4215–4220 (1981).
4. D. Casasent, F. Caimi, M. P. Petrov, and A. V. Khomenko, "Applications of the PRIZ light modulator," Appl. Opt. 21, 3846–3854 (1982).
5. G. Marie, "Large-screen projection of television pictures with an optical-relay tube based on the Pockels effect," Philips Tech. Rev. 30, 292–298 (1969).
6. G. Marie, J. Donjon, and J. P. Hazan, "Pockels effect imaging devices and their applications," in *Advances in Image Pickup and Display*, B. Kazan, ed. (Academic, New York, 1974), Vol. 1.
7. C. Warde, A. M. Weiss, A. D. Fisher, and J. I. Thackara, "Optical information processing characteristics of the microchannel spatial light modulator," Appl. Opt. 20, 2066–2074 (1981).
8. D. Casasent, "Spatial light modulators," Proc. IEEE 65, 143–157 (1977).
9. A. R. Tanguay, Jr., "Spatial light modulators for real time optical processing," in *Proceedings of the ARO Workshop on Future Directions for Optical Information Processing* (Army Research Office, Research Triangle Park, N.C., 1981).
10. J. C. H. Spence, "Prospects for on-line image processing of atomic resolution images using a PROM," Proc. Soc. Photo-Opt. Instrum. Eng. 218, 154–160 (1980).
11. G. J. Berzins and M. Graser, Jr., "Response of a $Bi_{12}SiO_{20}$ Pockels-readout optical modulator to x-rays," Appl. Phys. Lett. 34, 500–503 (1979).
12. Y. Owechko and A. R. Tanguay, Jr., "Theoretical resolution limitations of electrooptic spatial light modulators. II. Effects of crystallographic orientation," J. Opt. Soc. Am. A 1, 644–652 (1984).
13. I. M. Krittman, "Resolution of electrostatic storage targets," IEEE Trans. Electron Devices ED-10, 404–409 (1963).
14. W. R. Roach, "Resolution of electrooptic light valves," IEEE Trans. Electronic Devices ED-21, 453–459 (1974).
15. M. P. Petrov, A. V. Khomenko, V. I. Berezkin, and M. V. Krasin'kova, "Optical information recording in $Bi_{12}SiO_{20}$," Ferroelectrics 22, 651–652 (1978).
16. R. A. Sprague and P. Nisenson, "The PROM—a status report," Opt. Eng. 17, 256–266 (1978).
17. Y. Owechko and A. R. Tanguay, Jr., "Effects of operating mode on electrooptic spatial light modulator resolution and sensitivity," Opt. Lett. 7, 587–589 (1982).
18. Y. Owechko and A. R. Tanguay, Jr., "Effects of crystallographic orientation of electrooptic spatial light modulator amplitude and phase responses," Opt. Commun. 44, 239–242 (1983).
19. R. E. Aldrich, S. L. Hou, and M. L. Harvill, "Electrical and optical properties of $Bi_{12}SiO_{20}$," J. Appl. Phys. 42, 493–494 (1971).
20. T. K. Gaylord and M. G. Moharam, "Thin and thick gratings: terminology clarification," Appl. Opt. 20, 3271–3273 (1981).
21. A. R. Tanguay, Jr., "Czochralski growth and optical properties of bismuth silicon oxide," Ph.D. Dissertation (Yale University, New Haven, Conn., 1977).
22. A. R. Tanguay, Jr. and R. C. Barker, "Implications of concurrent optical activity and electric field induced birefringence for Pockels Readout Optical Modulator performance," J. Opt. Soc. Am. 68, 1449 (A) (1978).
23. J. W. Goodman, *Introduction to Fourier Optics* (McGraw-Hill, New York, 1968).
24. S. L. Hou, R. B. Lauer, and R. E. Aldrich, "Transport processes of photoinduced carriers in $Bi_{12}SiO_{20}$," J. Appl. Phys. 44, 2652–2658 (1973).
25. R. G. Barrera, O. Guzman, and B. Balaguer, "Point charge in a three-layer dielectric medium with planar interfaces," Am. J. Phys. 46, 1172–1179 (1978).
26. R. A. Sprague, "Effect of bulk carriers on PROM sensitivity," J. Appl. Phys. 46, 1673–1678 (1975).

APPENDIX VII



# Theoretical resolution limitations of electrooptic spatial light modulators. II. Effects of crystallographic orientation

Y. Owechko* and A. R. Tanguay, Jr.

*Departments of Electrical Engineering and Materials Science and Image Processing Institute, University of Southern California, Los Angeles, California 90089-0483*

Received October 8, 1982; accepted February 28, 1984

The point-spread function (PSF) of an electrooptic spatial light modulator (ESLM), such as the Pockels Readout Optical Modulator (PROM) or the PRIZ, is derived for various electrooptic crystal orientations and for charge distributions consisting of one or two point charges located in the electrooptic-crystal bulk. It is shown that phase modulation occurs for crystallographic orientations other than (001), resulting in signal-dependent phase distortions in the image plane and increased harmonic distortion in the Fourier plane. By utilizing linear systems theory, ESLM sensitivity and resolution are analyzed by means of generalized voltage transfer functions. Strikingly strong dependences on crystallographic orientation and charge position are shown. The effects of readout polarization on the angular dependence of the phase and amplitude of the PSF for various crystallographic orientations are also derived.

## 1. INTRODUCTION

Electrooptic spatial light modulators (ESLM's) have been proposed for use in place of photographic film as the input media in optical-processing systems for applications in which real-time operation is required. These devices store images as charge patterns induced in a photoconductor by the input image. The charge patterns modulate the electrostatic fields in an electrooptic crystal, creating a modulated field-induced birefringence or electrooptic effect that, in turn, modulates the polarization state of a coherent readout beam. The amplitude (or phase or both) of the readout beam is related to the intensity of the original input image when the ESLM is read out between crossed (or suitably oriented) polarizers, allowing various coherent optical-processing algorithms to be performed on the image. Examples of ESLM's are the Pockels Readout Optical Modulator (PROM),[1] PRIZ,[2-4] the Microchannel Spatial Light Modulator (MSLM),[5] PHOTOTITUS, and TITUS[6] devices.

The resolution and sensitivity of an ESLM are of vital importance to its performance in a coherent optical processor. An important limitation of ESLM resolution and sensitivity is field fringing. A delta-function input image results in a charge distribution that is sharply confined in the transverse dimensions (neglecting diffusion and transverse drift), but the electric-field lines arising from it will, in general, spread throughout the volume of the electrooptic crystal, affecting both the resolution and the sensitivity of the device. The effects of field fringing are analyzed in Ref. 7 for the case of a charge distribution of one or two point charges in the electrooptic-crystal bulk and a crystallographic orientation of the electrooptic crystal that ensures that only longitudinal electric-field components parallel to the light-propagation direction contribute to the electrooptic effect. The PROM, which utilizes bismuth silicon oxide ($Bi_{12}SiO_{20}$, or BSO) in a (001) orientation, was used as a specific example of an ESLM. (The physical geometry and principles of operation of the PROM have been described previously.[1]) The (001) orientation and $I23$ symmetry of BSO result in no contribution to the electrooptic effect by electric fields transverse to the light propagation direction.[7] The total integrated electrooptic effect for such a case is proportional to the voltage across the electrooptic crystal and, as we showed in Ref. 7, the conversion process from the input image-generated charge pattern to the output light amplitude can be treated as a linear system described by a transfer function. It was shown that ESLM sensitivity and resolution are strongly affected by device layer thicknesses and dielectric constants and especially by charge position within the bulk of the electrooptic-crystal layer.

In this paper, we investigate the effects on ESLM sensitivity and resolution of varying the electrooptic-crystal orientation so that transverse fields can contribute to the electrooptic effect, as first suggested by Petrov *et al.*[2] To this end we again utilize both single- and multiple-point-charge models. Such models are necessary to take into account the effects of oppositely signed charges and exposure-dependent bulk charge distributions. These effects were not included in earlier models,[2,8] which assumed that the charge distribution is confined to a step function near the electrooptic-crystal surface. Enhancement of harmonic distortion by signal-dependent phase errors is shown to occur for certain crystallographic orientations. Finally, the effects of the readout-light polarization state on the amplitude and phase of the ESLM point-spread function (PSF) are demonstrated.

## 2. POINT-SPREAD-FUNCTION RADIAL DEPENDENCE

The following analysis of ESLM resolution, sensitivity, and phase response is performed in terms of the device PSF for a charge distribution consisting of a single point charge located at an arbitrary position within the electrooptic crystal. (The radial variation of the PSF determines the response of the ESLM to one-dimensional sinusoidal gratings as a function of the spatial frequency $\omega$ of the grating.) This analysis is analogous to that applicable to the (001) PROM device,[7]

0740-3232/84/060644-09$02.00 

except that here the crystallographic orientation is treated as a variable parameter, such that all three orthogonal electric-field components arising from the point charge can potentially contribute to the electrooptic effect. Before a quantity analogous to the PROM voltage transfer function $V_L(\omega)$[7] describing the resolution and sensitivity of an ESLM of arbitrary crystallographic orientation can be determined, the effects of the three orthogonal field components on the optical properties of the crystal must be derived.

If an electric field is applied to an initially isotropic cubic crystal of $I23$ symmetry (such as BSO in the case of the PROM or PRIZ), its effect on the crystal birefringence can be described by the following deformed index ellipsoid:

$$\frac{x^2+y^2+z^2}{{n_0}^2} + 2r_{41}(E_x yz + E_y zx + E_z xy) = 1, \quad (1)$$

where $E_x$, $E_y$, and $E_z$ are the components of the field in the directions of the three crystallographic axes and $r_{41}$ is the electrooptic coefficient of the crystal. Since BSO is cubic, $r_{41} = r_{52} = r_{63}$, and all other components of the electrooptic tensor vanish. The elliptical cross section of the index ellipsoid perpendicular to the light-propagation direction determines the new principal axes and indexes. If the ESLM is read out between crossed polarizers oriented to bisect the principal axes, the output amplitude can be shown to be

$$A = iA_0 e^{i\phi} \sin G, \quad (2)$$

where

$$\phi = (\phi_1 + \phi_2)/2,$$

$$G = (\phi_1 - \phi_2)/2,$$

in which $\phi_1$ and $\phi_2$ are the incremental phase shifts of the components of the readout light along the two principal axes and $A_0$ is the readout-light amplitude (corrected for surface-reflection losses). The retardation $G$ represents one half of the phase difference between the two axes induced by the field; for small signals, the output amplitude is proportional to $G$. A phase error or distortion of the output wave front is represented by the phase $\phi$, which is caused by a circular (uniform) expansion of the index-ellipsoid cross section induced by the electric fields. The above expression neglects the effects of natural optical activity in BSO.[9,10]

The phase $\phi$ and retardation $G$ were calculated for each of the three orthogonal field components and for various crystallographic orientations by rotating the coordinate system until the $z$ axis coincided with the light-propagation direction and then by rotating about the new $z'$ axis until Eq. (1) was diagonalized. The new $x'$ and $y'$ axes then define the principal axes of the index-ellipsoid cross section, and $\phi$ and $G$ can be easily extracted from the equation for the cross section in the new coordinate system.

The directions of the three orthogonal field components $E_{T1}$, $E_{T2}$, and $E_L$ and their respective induced principal axes are illustrated in Fig. 1 for an $I23$-class crystal of orientation $\langle 11\gamma\rangle$, where $\gamma$ can vary from zero ($\langle 110\rangle$) to infinity ($\langle 001\rangle$). This range of orientations was chosen over the many possible others because it includes all three orientations currently used in PROM and PRIZ constructions ($\langle 001\rangle$, $\langle 111\rangle$, and $\langle 110\rangle$). In particular, $E_L$ is the longitudinal field along $\langle 11\gamma\rangle$, and $E_{T2}$ and $E_{T1}$ are the two orthogonal transverse fields along $\langle \bar{1}10\rangle$ and $\langle 11(\bar{2}/\gamma)\rangle$, respectively. The field $E_{T2}$ induces a set of principal axes rotated 45° from the axes induced by both $E_L$ and $E_{T1}$.

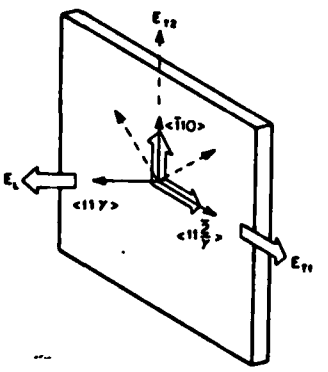


Fig. 1. Orientations of longitudinal and transverse electric fields and their respective induced principal axes for $Bi_{12}SiO_{20}$ ($I23$ symmetry). The longitudinal field ($E_L$) and one transverse field ($E_{T1}$) induce the same set of principal axes (open arrows), whereas the other transverse field ($E_{T2}$) induces a set of principal axes rotated by 45° (dashed arrows).

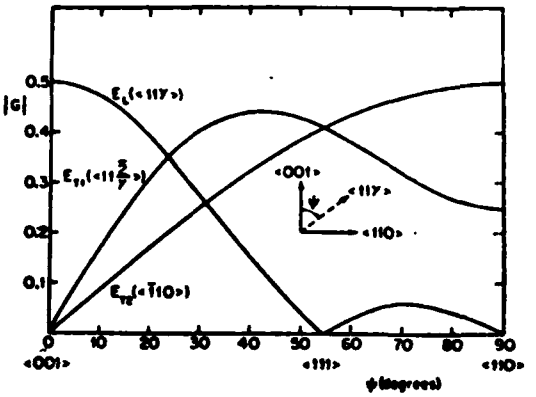


Fig. 2. Magnitude of retardation $G$ induced by the three orthogonal field components defined in Fig. 1 as a function of crystallographic orientation. The generalized voltages $V_{T1}$, $V_{T2}$, and $V_L$ are defined in the text; $G$ is given in units of $\pi V_\alpha/V_\pi$, where $\alpha = T1$, $T2$, or $L$.

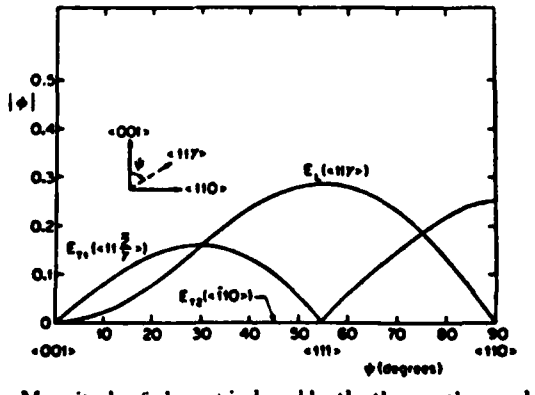


Fig. 3. Magnitude of phase $\phi$ induced by the three orthogonal field components defined in Fig. 1 as a function of crystallographic orientation. The generalized voltages $V_{T1}$, $V_{T2}$, and $V_L$ are defined in the text; $\phi$ is given in units of $\pi V_\alpha/V_\pi$, where $\alpha = T1$, $T2$, or $L$.

The results of the calculations of $G$ and $\phi$ for the three orthogonal field components as functions of crystallographic orientation between $\langle 001\rangle$ and $\langle 110\rangle$, assuming a crystal of $I23$ symmetry, such as BSO, are presented in Figs. 2 and 3. It

is assumed that the readout light is incident normal to the electrooptic-crystal surface. The results are expressed in terms of generalized voltages, defined as longitudinal integrals of the relevant field component through the electrooptic crystal in the direction of the readout-light propagation:

$$V_\alpha = \int_0^d E_\alpha dz,$$

$$\alpha = L, T2, T1, \tag{3}$$

where $d$ is the electrooptic-crystal thickness. (Because of the blocking layers present in these devices, $V_L$, the voltage across the electrooptic crystal, can be spatially modulated by the input image even though, during operation, a constant voltage is applied across the device.[7]) Figure 2 illustrates the relative contributions of the fields to the retardation $G$. For the ⟨001⟩ orientation, only the longitudinal field $E_L$ contributes to G. The $E_L$ contribution decreases to zero and the transverse fields $E_{T2}$ and $E_{T1}$ have nonzero contributions for both the ⟨111⟩ and ⟨110⟩ orientations. The immediate conclusion can be drawn that, for the ⟨111⟩ and ⟨110⟩ orientations, the ESLM will pass only nonzero spatial frequencies, since uniform (zero-spatial-frequency) components do not induce any transverse fields. These devices will therefore act as spatial bandpass filters. The two transverse-field retardations are equal in the ⟨111⟩ orientation but differ by a factor of 2 in the ⟨110⟩ orientation. Figure 3 shows the orientation dependence of the phase $\phi$ for the same fields and orientations as in Fig. 2. No phase distortions resulting from the electrooptic effect exist in the ⟨001⟩ PROM orientation, but nonzero phase distortions that result from at least one field component are present in all other orientations between ⟨001⟩ and ⟨110⟩, including the ⟨111⟩ and ⟨110⟩ orientations used in the PRIZ devices.[2] These results for the PROM and PRIZ are summarized in Table 1.

The phase error due to the longitudinal field $E_L$ in the ⟨111⟩ orientation results in a phase image that premultiplies the transverse field-induced amplitude image. This phase image will increase the second-harmonic distortion (SHD) of the ESLM as measured in the Fourier plane. For example, consider the case of a sinusoidal exposure distribution of circular spatial frequency $\omega$ imaged onto the ⟨111⟩ PRIZ with its wave vector parallel to the $T1$ direction. According to Table 1, the phase $\phi$ and retardation $G$ are given by

$$\phi(x) = \frac{\pi V_L}{2\sqrt{3}\,V_\pi}\sin(\omega x), \tag{4}$$

$$G(x) = \frac{\pi V_{T1}}{\sqrt{6}\,V_\pi}\cos(\omega x), \tag{5}$$

**Table 1. Values of G and $\phi$ for Three Orthogonal Fields and Three Crystallographic Orientations Used in the PROM and PRIZ[a]**

| BSO ORIENTATION | ⟨001⟩ (PROM) | | | ⟨111⟩ (PRIZ) | | | ⟨110⟩ PRIZ | | |
|---|---|---|---|---|---|---|---|---|---|
| FIELD ORIENTATION | $E_L$ ⟨001⟩ | $E_{T2}$ ⟨110⟩ | $E_{T1}$ ⟨110⟩ | $E_L$ ⟨111⟩ | $E_{T2}$ ⟨110⟩ | $E_{T1}$ ⟨112⟩ | $E_L$ ⟨110⟩ | $E_{T2}$ ⟨110⟩ | $E_{T1}$ ⟨001⟩ |
| PHASE $\phi$ | 0 | 0 | 0 | $\frac{\pi V_L}{2\sqrt{3}V_\pi}$ | 0 | 0 | 0 | 0 | $\frac{\pi V_{T1}}{4V_\pi}$ |
| SIGNAL G | $\frac{\pi V_L}{2V_\pi}$ | 0 | 0 | 0 | $\frac{\pi V_{T2}}{\sqrt{6}V_\pi}$ | $\frac{\pi V_{T1}}{\sqrt{6}V_\pi}$ | 0 | $\frac{\pi V_{T2}}{2V_\pi}$ | $\frac{\pi V_{T1}}{4V_\pi}$ |

[a] The generalized voltages $V_{T1}$, $V_{T2}$, and $V_L$ are defined in the text.

where an unimportant constant term in $\phi$ has been suppressed. The half-wave voltage for the ⟨001⟩ orientation, $V_\pi = \lambda/2n_0^3 r_{41}$ (where $\lambda$ is the wavelength of the readout light, $n_0$ is the refractive index of BSO, and $r_{41}$ is the electrooptic coefficient of BSO), is equal to 4430 V for a readout wavelength of 632.8 nm.[9] The maxima of $\phi(x)$ are shifted by $\pi/2$ relative to $G(x)$ because, by symmetry, the transverse fields are strongest midway between the input exposure maxima and minima, whereas the longitudinal fields are strongest at the maxima. The effects of the phase image on the SHD can be estimated by inserting Eqs. (4) and (5) into Eq. (2), expanding in a power series to first order in $\phi$ and $G$, and extracting the coefficients of the fundamental- and harmonic-frequency components. The first- and second-order diffraction efficiencies, $\eta_1$ and $\eta_2$, can be obtained by taking the magnitude squared of the corresponding coefficients with the following results:

$$\eta_1 = \left(\frac{\pi V_{T1}}{2\sqrt{6}\,V_\pi}\right)^2, \tag{6}$$

$$\eta_2 = \left(\frac{\pi^2 V_{T1} V_L}{24\sqrt{2}\,V_\pi^2}\right)^2. \tag{7}$$

The SHD resulting from $\phi(x)$ is given by

$$\mathrm{SHD} = (\eta_2/\eta_1)^{1/2} = \frac{\pi V_L}{4\sqrt{3}\,V_\pi}. \tag{8}$$

The effect of the phase image, therefore, is to increase the amount of light diffracted into the second order, which increases the SHD. For example, an exposure that induces a $V_L$ equal to 2000 V results in a SHD of 20%. Phase distortions in the image plane translate into amplitude distortions in the Fourier plane. Such distortions have a deleterious effect on the fidelity of optical-processing algorithms that require Fourier-plane filtering operations. Another source (not considered here) of possible phase errors in both the PROM and the PRIZ is the natural optical activity of BSO. As discussed elsewhere,[9,10] concurrent optical activity and electric-field-induced birefringence can distort the output phase of an ESLM. Pronounced nonlinear sensitometry characteristics also contribute to the SHD in the PRIZ.[11]

According to Eq. (2), the output amplitude is equal to the retardation $G$ if the phase $\phi$ is neglected and if the small-signal approximation ($G \ll 1$) is used. The retardation that results from the $E_{T1}$ transverse-field component for a ⟨111⟩-oriented ESLM is given by

$$G_{T1}(x, y) = \frac{\pi}{\sqrt{6}\,V_\pi}\int_0^d E_{T1}(x, y, z)dz. \tag{9}$$

It is assumed in Eq. (9) that the input polarization is linear and oriented to bisect the principal axes induced by $E_{T1}$. If the small-signal approximation is used, the PSF (output amplitude) is proportional to $G(x, y)$ for a delta-function input exposure. The PSF can be determined from Eq. (9) for the case of a point charge in the electrooptic-crystal bulk. The potential resulting from a single point charge is circularly symmetric about the $z$ axis or light-propagation direction, so that $E_{T1}$ can be expressed in cylindrical coordinates as the component of the potential gradient in the $T1$ direction:

$$E_{T1}(\rho, \theta, z) = \frac{\partial}{\partial \rho} V(\rho, z; \xi)\cos\theta, \tag{10}$$

where $\rho$ and $\theta$ are the radial and angular coordinates, respectively, in the transverse plane, $z$ is the longitudinal coordinate, and $V(\rho, z; \xi)$ is the potential resulting from a single point charge located within the electrooptic crystal at position $z = -\xi$. When expressed in terms of $V(\omega, z; \xi)$ [the Fourier–Hankel transform of $V(\rho, z; \xi)$ with respect to the radial coordinate], the PSF [Eq. (9)] can be rewritten, using Eq. (10), as

$$G_{T1}(\rho, \theta; \xi) = \frac{\pi}{\sqrt{6}\, V_\pi} \times \int_0^d \frac{\partial}{\partial \rho}\left[\frac{1}{2\pi}\int_0^\infty \omega V(\omega, z; \xi) J_0(\omega\rho)\mathrm{d}\omega\right](\cos\theta)\mathrm{d}z. \quad (11)$$

The transfer function of the ESLM is obtained by Fourier transforming the PSF (Appendix A):

$$H_{T1}(\omega, \theta; \xi) = \frac{i\pi}{\sqrt{6}\, V_\pi} V_T(\omega; \xi)\cos\theta, \quad (12)$$

where

$$V_T(\omega; \xi) = \omega \int_0^d V(\omega, z; \xi)\mathrm{d}z.$$

An analytic expression for the potential $V(\omega, z; \xi)$ was derived in Ref. 7. The generalized voltage transfer function $V_T(\omega; \xi)$ is given by

$$V_T(\omega; \xi) = \frac{q}{\epsilon_{eo}\epsilon_0\omega}\left(\frac{\cosh[\omega(a-d)] - \cosh[\omega(a-\xi)]}{\cosh[\omega(a-\xi)]\left\{\dfrac{\coth[\omega(b-\xi)]}{\coth[\omega(a-\xi)]} - 1\right\}} + \frac{\cosh[\omega(b-\xi)] - \cosh(\omega b)}{\cosh[\omega(b-\xi)]\left\{1 - \dfrac{\coth[\omega(a-\xi)]}{\coth[\omega(b-\xi)]}\right\}}\right),$$

$$a = d + \frac{1}{\omega}\coth^{-1}\left[\frac{\epsilon_{bl}}{\epsilon_{eo}}\coth(\omega d_2)\right],$$

$$b = \frac{1}{\omega}\coth^{-1}\left[\frac{\epsilon_{bl}}{\epsilon_{eo}}\coth(-\omega d_1)\right], \quad (13)$$

where $d_1$, $d_2$, and $\epsilon_{bl}$ are the blocking layer thicknesses and dielectric constant; $d$ and $\epsilon_{eo}$ are the electrooptic layer thickness and dielectric constant; and $\xi$ is the point-charge position. The function $V_T(\omega; \xi)$ is analogous to the voltage transfer function $V_L(\omega; \xi)$ calculated in Ref. 7 for the ⟨001⟩ orientation, in which only longitudinal fields contribute to the output, and has the same dimensions (voltage × area). The function $V_T(\omega; \xi)$ describes how each image spatial-frequency component is weighted by the ESLM if only transverse-field components contribute to the PSF. The high- and low-spatial-frequency limits of $V_T(\omega; \xi)$ are given by

$$\lim_{\omega \to \infty} V_T(\omega; \xi) \cong \frac{q}{\omega\epsilon_{eo}\epsilon_0} \times \left\{1 - \frac{\epsilon_{bl}}{\epsilon_{bl} + \epsilon_{eo}}[\exp(-\omega\Delta_1) + \exp(-\omega\Delta_2)]\right\}, \quad (14)$$

$$\lim_{\omega \to 0} V_T(\omega; \xi) = 0, \quad (15)$$

where $\Delta_1$ and $\Delta_2$ are the distances of the point charge from the two electrooptic-crystal/dielectric-blocking-layer interfaces. The function $V_T(\omega; \xi)$ decreases inversely with spatial frequency in the limit of large spatial frequencies and is a function of the dielectric constants of the ESLM layers. It has only a weak dependence on the charge position, in contrast to the voltage transfer function $V_L(\omega; \xi)$, which, as was shown in Ref. 7, decreases exponentially with the separation of the point charge from the electrooptic-crystal/blocking-layer interface in the large-spatial-frequency limit. It should be noted here that the measured diffraction efficiency may not decrease with spatial frequency at the rate predicted by the magnitude squared of Eq. (14), as might be expected from Eq. (6). This is because Eq. (14) must be used as a Green's function and integrated over the actual longitudinal charge distribution. Qualitative trends, however, may be extracted from the single-point-charge solution.

Single-point-charge transfer functions are compared in Fig. 4 for two distinct charge positions. In Case A, the point charge is at an electrooptic-crystal/blocking-layer interface, and, in Case B, the point charge is in the center of the electrooptic crystal. The ESLM is assumed to consist of a 500-$\mu$m-thick electrooptic crystal (BSO, $\epsilon_{eo} = 56$) with symmetric 5-$\mu$m-thick blocking layers, which usually consist of parylene,[1] an organic polymer ($\epsilon_{bl} = 3$). A ⟨111⟩ crystallographic orientation is assumed for the transverse-field device and a ⟨001⟩ orientation for the longitudinal-field device. It is evident from Fig. 4 that, as the point charge is displaced off the dielectric-blocking-layer/electrooptic-crystal interface, the transverse and longitudinal transfer functions display strikingly opposite behavior. The longitudinal transfer function $V_L(\omega; \xi)$ is zero for a point charge in the center of the electrooptic crystal. As derived in Ref. 7, the high-spatial-frequency form of $V_L(\omega; \xi)$ decreases exponentially and the low-spatial-frequency form decreases linearly with the separation of the point charge from the interface. For the transverse transfer function $V_T(\omega; \xi)$, however, the dependence on charge displacement is opposite that for $V_L(\omega; \xi)$.

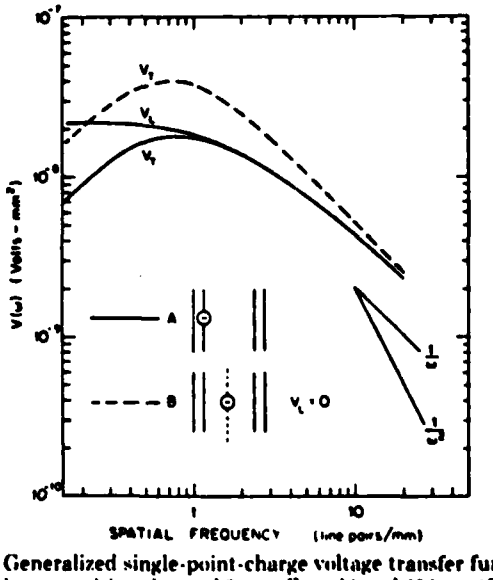


Fig. 4. Generalized single-point-charge voltage transfer functions for two charge positions located 0 $\mu$m (Case A) and 250 $\mu$m (Case B) from the BSO crystal surface. Blocking-layer and BSO thicknesses are assumed to be 5 and 500 $\mu$m, respectively.

The response is enhanced as the point charge is moved away from the interface, with larger relative enhancements for lower spatial frequencies. These different dependences on point-charge position are reasonable from an intuitive point of view. For a point charge in the center of a symmetric ESLM, the contributions from longitudinal-field components on either side of the charge will cancel, leaving no net response. The transverse field contributions, on the other hand, will add instead of cancel, resulting in an enhanced response (see Fig. 6). These results seem to suggest that ESLM's that utilize transverse fields should be more sensitive than longitudinal-field ESLM's if there is significant charge storage in the electrooptic-crystal bulk. However, it is important to realize that physically realistic charge distributions contain equal numbers of oppositely signed charges. In most ELSM's, including the PROM and PRIZ devices, charges are generated by the input image in a photoconductive process in which electrons and positively charged centers or holes are photogenerated in pairs. So long as no charge transport occurs across the dielectric blocking layers, charge conservation must hold. It should be pointed out, however, that if significant transverse drift occurs so that electrons (which are the mobile carriers in BSO) undergo some transverse smearing, then charge conservation may be effectively violated, since the smeared electrons will no longer contribute to nonzero spatial frequencies.

In order to model the effects of charge conservation, we will consider two cases. Case C (Fig. 5), in which two oppositely signed charges are situated at the interfaces, models the forward operating mode, in which the sign of the applied voltage results in electron transport in the direction of light propagation. Case D, in which a negative point charge is located at an interface and the positive charge is in the center of the electrooptic crystal, models the reverse operating mode, in which the polarity of the applied voltage is reversed so that electron transport is opposite the direction of light propagation. The device parameters are the same as those of Fig. 4.

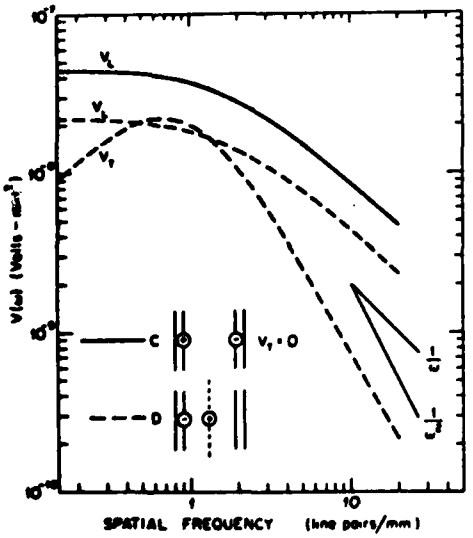


Fig. 5. Generalized voltage transfer functions for a charge distribution consisting of two oppositely signed point charges. Values for two charge distributions corresponding to forward (Case C) and reverse (Case D) operating modes are shown. Device parameters are the same as those for Fig. 4. Charge positions are given in the text.

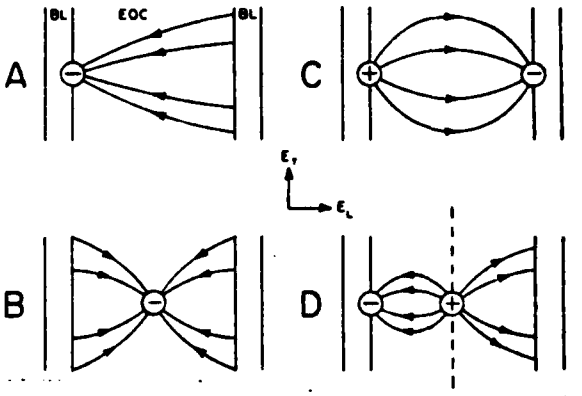


Fig. 6. Schematic diagrams of the electrostatic-field configurations for the charge distributions of Figs. 4 and 5.

(The electrostatic field configurations for Cases A through D are illustrated in Fig. 6.) By utilizing the principle of superposition, the response for two point charges is simply the sum of the individual responses. The longitudinal response is now greatly enhanced as compared with the transverse response, especially for large spatial frequencies. The decrease in the transverse response for two point charges as compared with one can be explained by referring to the high-spatial-frequency limit of $V_T(\omega;\xi)$, given by Eq. (14). For large $\omega$, $V_T(\omega;\xi)$ approaches the same value for all values of the charge position. Consequently, for two point charges of opposite sign at different longitudinal positions in the PRIZ, the sum of the individual charge contributions will rapidly approach zero at higher spatial frequencies. The longitudinal $V_L(\omega;\xi)$ response, on the other hand, varies greatly with charge position. Therefore the contributions from two oppositely signed charges in different longitudinal positions in the PROM will not necessarily cancel at high spatial frequencies (as they do in the PRIZ case). Therefore cases in which equal numbers of positive and negative charges contribute to the image modulation tend to favor the PROM response relative to the PRIZ. If unequal numbers of positive and negative charges contribute to the image modulation, whether because of leaky blocking layers or transverse drift, then the PRIZ response will be improved relative to the PROM. PROM and PRIZ sensitivity and resolution have strong but opposite dependences on the specific nature of the charge distribution.[12] Quantitative comparisons of ESLM performance must, therefore, be made in terms of a continuous charge-distribution model that includes the effects of operating modes optimized for each device. Such a model has been developed and will be discussed in the third and fourth papers of this series.

## 3. POINT-SPREAD-FUNCTION ANGULAR DEPENDENCE

The angular variation of the PSF determines the response of the ESLM to one-dimensional sinusoidal gratings as a function of the orientation of the grating wave vector. In order to determine the angular variations in both the phase and amplitude of the ESLM PSF, the index-ellipsoid cross section along the light-propagation direction must be found for a field distribution that contains components along all three ($T1$, $T2$, and $L$) orthogonal directions. Additionally, although in Section 2 the input polarization was chosen to select only one

transverse-field component, for a complete description of the PSF, the effects of arbitrary input polarizations on the PSF angular dependence must be included. The PSF is angularly isotropic in the ⟨001⟩ PROM because only longitudinal fields (which are cylindrically symmetric about a point charge) contribute to the electrooptic effect. Furthermore, because the induced principal axes do not vary in orientation, the PSF is angularly isotropic in both the phase and the amplitude, regardless of the polarization used to read out the PROM. To illustrate the angular anisotropy in both the phase and the amplitude of the PSF in ESLM's of $I23$-symmetry crystal orientations other than ⟨001⟩, the ⟨111⟩ orientation used in the PRIZ will be analyzed.

Equation (1) represents the index ellipsoid for a crystal of $I23$ symmetry, such as $Bi_{12}SiO_{20}$, when electric fields are applied along all three orthogonal crystallographic directions. In order to determine the index-ellipsoid cross section along the light propagation direction, the coordinate system is rotated until the $z'$ axis is parallel to the ⟨111⟩ direction. The equation for the cross section is obtained by setting $z' = 0$, resulting in

$$\left[\frac{1}{n_0^2}+\frac{1}{3}r_{41}(E_z-2E_y-2E_x)\right]x'^2+\left(\frac{1}{n_0^2}-r_{41}E_z\right)y'^2 - \frac{2}{\sqrt{3}}r_{41}(E_y-E_x)x'y'=1, \tag{16}$$

where $x'$ is along $\langle 11\bar{2}\rangle$, $y'$ is along $\langle \bar{1}10\rangle$, and $z'$ is along ⟨111⟩; $E_x$, $E_y$, and $E_z$ are fields along the crystallographic directions; $n_0$ is the unperturbed refractive index; and $r_{41}$ is the electrooptic coefficient. The cross section is diagonalized by rotation of the coordinate system about $z'$. The angle $\theta_p$ between the principal axes and the $(x', y')$ axes is

$$\theta_p=\frac{1}{2}\tan^{-1}\left[\frac{\sqrt{3}(E_y-E_x)}{E_x+E_y-2E_z}\right]. \tag{17}$$

The angle $\theta_p$ varies from 0° to 45° as the transverse electric-field vector rotates 90° from $\langle 11\bar{2}\rangle$ to $\langle \bar{1}10\rangle$ in the transverse plane. One of the principal axes induced by the transverse field $E_{T1}$ along the $\langle 11\bar{2}\rangle$ direction is parallel to $E_{T1}$, whereas the other principal axis is normal to it. The transverse field $E_{T2}$ along $\langle \bar{1}10\rangle$ normal to $E_{T1}$ induces another set of principal axes, both of which are situated at a 45° angle with respect to $E_{T2}$. It will be shown below that this variation of $\theta_p$ with the transverse-field orientation leads to interesting modifications of the PSF phase and amplitude, which are not present in ESLM's that utilize longitudinal effects, such as the PROM. The equation for the index-ellipsoid cross section in the new rotated coordinate system is

$$\left(\frac{1}{n_0^2}+A+B\right)x''^2+\left(\frac{1}{n_0^2}+A-B\right)y''^2=1, \tag{18}$$

where

$$A=-\frac{r_{41}}{3}(E_x+E_y+E_z)$$

and

$$B=\frac{2}{3}r_{41}(E_x^2+E_y^2+E_z^2-E_xE_y-E_yE_z-E_zE_z)^{1/2}.$$

A circularly symmetric expansion or contraction of the ellipsoid cross section is represented by the quantity $A$. It is the source of the phase factor of Eq. (2). For the ⟨111⟩ orientation, $A$ is nonzero if fields are present in the ⟨111⟩ longitudinal direction, as is usually the case. The quantity $B$ represents a field-induced birefringence and is the source of the retardation factor of Eq. (2). Although the induced birefringence from the longitudinal field is zero, $B$ is nonzero for fields in the transverse plane.

Equations (17) and (18) define the index-ellipsoid cross section for arbitrary fields. To determine the form of the PSF for various input polarizations, the above relations must be combined with knowledge of the electric fields associated with the point charge. The point-charge field in cylindrical coordinates is described by

$$\mathbf{E}(\rho,\theta,z)=(\hat{\mathbf{E}}_{T1}\cos\theta+\hat{\mathbf{E}}_{T2}\sin\theta)E_T(\rho,z)+\hat{\mathbf{E}}_LE_L(\rho,z) \tag{19}$$

where

$$\hat{\mathbf{E}}_L=\frac{1}{\sqrt{3}}(1,1,1),\quad \hat{\mathbf{E}}_{T2}=\frac{1}{\sqrt{2}}(-1,1,0),$$
$$\hat{\mathbf{E}}_{T1}=\frac{1}{\sqrt{6}}(1,1,-2)$$

are unit vectors in the longitudinal and two transverse directions, $E_L$ and $E_T$ are the longitudinal and transverse fields, respectively, $\theta$ and $\rho$ are the angular and radial coordinates, respectively, in the $(x', y')$ plane, and $z'$ is the longitudinal coordinate, as shown in Fig. 7.

Substituting Eq. (19) into Eqs. (17) and (18) results in

$$\theta_p=\frac{1}{2}\left(\theta+\frac{\pi}{2}\right) \tag{20}$$

for the orientation of the principal axes. This linear variation of the orientation of the principal axes with the transverse-field orientation leads to an anisotropic PSF for both linear and circular input polarizations, as shown below. The diagonalized equation for the index-ellipsoid cross section becomes

$$\left[\frac{1}{n_0^2}-\frac{1}{\sqrt{3}}r_{41}E_L(\rho,z)+\sqrt{\frac{2}{3}}r_{41}E_T(\rho,z)\right]x''^2 + \left[\frac{1}{n_0^2}-\frac{1}{\sqrt{3}}r_{41}E_L(\rho,z)-\sqrt{\frac{2}{3}}r_{41}E_T(\rho,z)\right]y''^2=1. \tag{21}$$

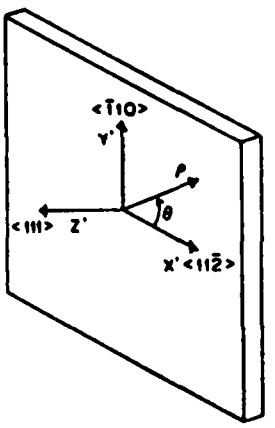


Fig. 7. Coordinate system used in derivation of ⟨111⟩ PRIZ PSF.

The incremental phase retardations along the principal axes are

$$\phi_1 = \frac{\pi}{\sqrt{6}\,V_\pi}\left[\frac{V_L(\rho)}{\sqrt{2}} - V_T(\rho)\right],$$
$$\phi_2 = \frac{\pi}{\sqrt{6}\,V_\pi}\left[\frac{V_L(\rho)}{\sqrt{2}} + V_T(\rho)\right]. \quad (22)$$

As derived by Jones,[13] the polarization transfer matrix $M(\theta_p)$, which describes a birefringence rotated by angle $\theta_p$, is given by

$$M(\theta_p) = \begin{bmatrix}\cos\theta_p & -\sin\theta_p \\ \sin\theta_p & \cos\theta_p\end{bmatrix}\begin{bmatrix}\exp(i\phi_1) & 0 \\ 0 & \exp(i\phi_2)\end{bmatrix}\begin{bmatrix}\cos\theta_p & \sin\theta_p \\ -\sin\theta_p & \cos\theta_p\end{bmatrix}. \quad (23)$$

First, consider linearly polarized input light with polarization vector

$$\mathbf{A}_0 = \begin{pmatrix}\cos\beta \\ \sin\beta\end{pmatrix}, \quad (24)$$

where $\beta$ is the angle between the polarization vector and the $x'$ axis ($\langle 11\bar{2}\rangle$ direction). With an orthogonal analyzer placed after the ESLM, the PSF for linear polarization is given by

$$h(\rho,\theta) = (\sin\beta - \cos\beta)M(\theta_p)\begin{pmatrix}\cos\beta \\ \sin\beta\end{pmatrix}$$
$$= i\cos(2\beta-\theta)\exp[i\phi(\rho)]\sin G(\rho), \quad (25)$$

where Eq. (20) has been used to substitute $\theta$ for $\theta_p$. The radial variations in the PSF are contained in the phase and retardation terms

$$\phi(\rho) = \frac{\pi V_L(\rho)}{2\sqrt{3}V_\pi},$$
$$G(\rho) = \frac{\pi V_T(\rho)}{\sqrt{6}V_\pi}. \quad (26)$$

Phase modulation is caused by the longitudinal field. The transverse fields contribute to the retardation. As shown in Fig. 8a, the PSF for linear input polarization consists of two lobes of opposite sign, the orientation of which depends on the orientation of the linear input polarization. Therefore, for a sinusoidal grating input exposure, the phase of the output amplitude depends on both the amplitude of the longitudinal fields and the grating-wave-vector orientation [through the sign of $\cos(2\beta-\theta)$].

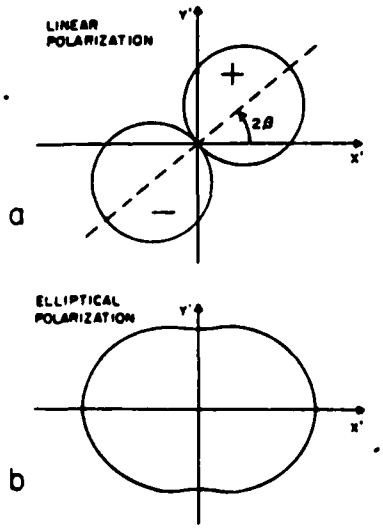


Fig. 8. Angular variations in magnitude of (111) PRIZ PSF for (a) linear and (b) elliptical readout polarizations. The PSF is circularly symmetric in magnitude for circularly polarized readout.

If elliptically polarized light is used to read out the ESLM, its polarization may be given by

$$\mathbf{A}_0 = \begin{pmatrix}\cos\beta \\ i\sin\beta\end{pmatrix}, \quad (27)$$

where $\beta$ is now a parameter that determines the ellipticity. Circularly polarized light results if $\beta = \pi/4$. The PSF for elliptically polarized readout with an orthogonal elliptical analyzer placed in back of the ESLM is

$$h(\rho,\theta) = (\sin\beta \quad i\cos\beta)M(\theta_p)\begin{pmatrix}\cos\beta \\ i\sin\beta\end{pmatrix}$$
$$= (i\cos\theta - \sin 2\beta\sin\theta)\exp[i\phi(\rho)]\sin G(\rho), \quad (28)$$

where, again, Eq. (20) has been used to substitute $\theta$ for $\theta_p$. The form of the PSF is shown in Fig. 8b for $\beta = \pi/8$. For general elliptical polarizations, the PSF is anisotropic in both phase and amplitude. In the case of circularly polarized readout light, Eq. (28) reduces to

$$h(\rho,\theta) = i\exp(i\theta)\exp[i\phi(\rho)]\sin G(\rho). \quad (29)$$

The amplitude of the PSF for circular polarization is circularly symmetric, but the phase variations cover the entire unit circle in the complex plane. Physically, this is caused by the rotation of the principal axes as the transverse field rotates [see Eq. (20)], which alters the phase of the output. (Buhrer *et al.*[14] have used this effect in (111)-oriented cubic crystals to achieve optical single-sideband suppressed-carrier transmission with a transverse electrooptic modulator.) As in the linear polarization case, a signal-dependent phase is present. The change in sign of the PSF on reflection through the origin for both linear and elliptical polarization ensures that the PRIZ has no zero spatial-frequency response since the two-dimensional spatial integral of the PSF is zero. The above results extend the analysis by Petrov and Khomenko[15] of the angular variations in the PRIZ PSF to include the effects of the longitudinal fields and the readout-light polarization state on the PSF phase.

The phase effects in the PRIZ can be made visible in the image plane by a constant bias $F_0$. Such a constant bias can be caused by nonzero extinction of the polarizers or by strain-induced birefringence in the electrooptic crystal. If the radial dependence of the PRIZ PSF is incorporated in $f(\rho)$, then the PSF's for linear and circular polarization with bias $F_0$ can be written as

$$h(\rho,\theta) = f(\rho)\cos(2\beta-\theta) + F_0 \quad (30)$$

for linear polarization and

$$h(\rho,\theta) = f(\rho)ie^{i\theta} + F_0 \quad (31)$$

for circular polarization. The effects of $F_0$ on the angular symmetry of the PRIZ PSF can be determined by defining $F_0$ as equal to some fraction $f_0$ of $f(\rho)$ at a particular $\rho = \rho_0$. It then becomes clear from Eqs. (30) and (31) that constructive and destructive interference occurs between $F_0$ and different lobes of the PSF, resulting in asymmetric PSF's. The angular

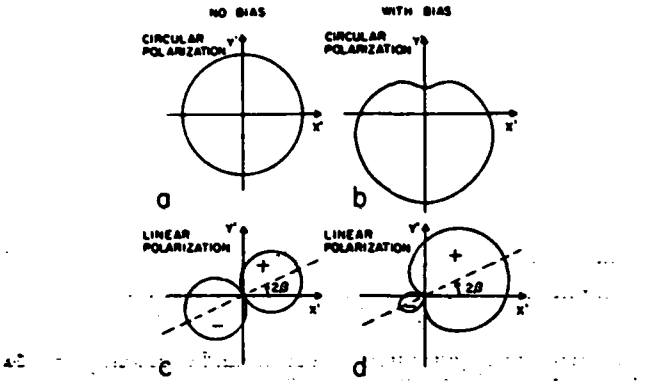


Fig. 9. Effects of constant background leakage on angular variations in magnitude of ⟨111⟩ PRIZ PSF.

dependence of the magnitudes of the PSF's for linear and circular polarizations (for a value of $f_0 = 0.5$) is illustrated in Fig. 9. The effect of the bias is to destroy the inversion symmetry of the PRIZ PSF's, which results in asymmetric imaging properties. The visual effect of these asymmetries is shadowing or reliefing of the image in which edges on one side of an object are brighter than edges on the other side. Such asymmetries are not present in the PROM because the phase of its PSF does not change on reflection through the origin, resulting in no constructive or destructive interference with the bias term.

The PRIZ transfer functions corresponding to the PSF's for linearly and circularly polarized light given by Eqs. (25) and (29) are

$$H(\omega, \theta; \xi) = -\cos(2\beta - \theta)\frac{\pi V_T(\omega; \xi)}{\sqrt{6}\, V_\pi} \tag{32}$$

for linear polarization and

$$H(\omega, \theta; \xi) = -e^{i\theta}\frac{\pi V_T(\omega; \xi)}{\sqrt{6}\, V_\pi} \tag{33}$$

for circular polarization. The radial and angular polar coordinates in the Fourier plane are given by $\omega$ and $\theta$, respectively, $\beta$ is the orientation of the linear polarization, and $V_T(\omega; \xi)$ is given by Eq. (13). A small-signal approximation was used, and the signal-dependent phase was neglected. (The angular dependences of the magnitude of the amplitude agree with previous derivations and experimental measurements of the diffraction efficiency.[15]) Note that the angular phase variations present in the PSF are also present in the Fourier plane. The output phase of gratings imaged onto the PRIZ will vary with the orientation of the grating wave vector. The phase can vary over the entire unit circle in the complex plane. These phase anisotropies in the PRIZ transfer functions may affect the use of PRIZ ESLM's in applications in which phase uniformity is important.

## 4. CONCLUSIONS

In this study we have derived the point-spread functions and transfer functions for electrooptic spatial light modulators of various crystallographic orientations, specifically the PROM and PRIZ devices, for the cases of one or two point charges in the electrooptic-crystal bulk. It has been shown that the sensitivity and resolution depend strongly on the charge distribution and on the crystallographic orientation. In addition, the importance of treating charge conservation in any model of ESLM performance was demonstrated. Since the relative performance of the PROM and PRIZ devices depends strongly on the operating mode used and on the resultant charge distribution, quantitative comparisons of the devices in terms of sensitivity and resolution can be made only in the context of a more realistic continuous charge-distribution model, using operating modes optimized for each device. Such a model will be described in subsequent papers in this series.

Signal-dependent phase effects are present in the PRIZ that distort the phase of the output wave front and increase the SHD. (Another strong contribution to the SHD in the PRIZ is its nonlinear sensitometry characteristics.[11]) Polarization-dependent phase effects are also present in the PRIZ because of the simultaneous excitation of two sets of principal axes by the three orthogonal electric-field components. Neither of these effects is present in the PROM. The PRIZ polarization-dependent phase distortions can be made visible by a constant bias caused either by strain-induced birefringence in the electrooptic crystal or by incomplete polarizer–analyzer extinction. The phase and amplitude distortions mentioned above, which occur when novel crystallographic orientations are used in ESLM construction, are important factors to consider in the design of real-time optical-processing systems.

## APPENDIX A. CALCULATION OF THE TRANSVERSE-EFFECT ESLM TRANSFER FUNCTION

The PSF of a transverse effect ESLM (⟨111⟩ PRIZ) for a readout polarization that selects the $E_{T1}$ transverse-field component was given in Eq. (11) and is rewritten below in rectangular coordinates with the order of integration reversed:

$$G_{T1}(x, y; \xi) = \frac{\pi}{\sqrt{6}V_\pi}\hat{\mathbf{E}}_{T1}\cdot\left(\hat{\mathbf{x}}\frac{\partial}{\partial x} + \hat{\mathbf{y}}\frac{\partial}{\partial y}\right) \times \int_{-\infty}^{+\infty}\int_{-\infty}^{+\infty}\left[\int_0^d V(\omega_x, \omega_y, z; \xi)dz\right] \times \exp[i(\omega_x x + \omega_y y)]d\omega_x d\omega_y. \tag{A1}$$

As was mentioned in Section 2, the above expression for the PSF is accurate only in the small-signal approximation for which the output is proportional to the retardation $G$. The ESLM transfer function is given by the Fourier transform of Eq. (A1):

$$H_{T1}(\omega_x, \omega_y; \xi) = \frac{i\pi}{\sqrt{6}V_\pi}\hat{\mathbf{E}}_{T1}\cdot(\hat{\mathbf{x}}\omega_x + \hat{\mathbf{y}}\omega_y) \times \int_0^d V(\omega_x, \omega_y, z; \xi)dz. \tag{A2}$$

Since $V(\omega_x, \omega_y, z; \xi)$ is circularly symmetric about the $z$ axis and since $E_{T1}$ is parallel to the $x$ axis, the above transfer function can be rewritten in polar coordinates as

$$H_{T1}(\omega, \theta; \xi) = \frac{i\pi}{\sqrt{6}\, V_\pi} V_T(\omega; \xi)\cos\theta, \tag{A3}$$

where

$$V_T(\omega; \xi) = \omega\int_0^d V(\omega, z; \xi)dz.$$

This is the result presented in Eq. (12).

## ACKNOWLEDGMENTS

This research was supported in part by the National Science Foundation, the Joint Services Electronics Program, the U.S. Army Research Office, and the Defense Advanced Research Projects Agency. Y. Owechko gratefully acknowledges the support of Xerox and Schlumberger Graduate Fellowships. Many stimulating conversations with Ralph Aldrich (Itek Corporation), Cardinal Warde (Massachusetts Institute of Technology), and David Casasent (Carnegie-Mellon University) are gratefully acknowledged.

* Present Address, Hughes Research Laboratories, 3011 Malibu Canyon Road, Malibu, California 90265.

## REFERENCES

1. B. A. Horwitz and F. J. Corbett, "The PROM—theory and applications for the Pockels Readout Optical Modulator," Opt. Eng. 17, 353–364 (1978).
2. M. P. Petrov, A. V. Khomenko, M. V. Krasin'kova, V. I. Marakhonov, and M. G. Shlyagin, "The PRIZ image converter and its use in optical data processing systems," Sov. Phys. Tech. Phys. 26, 816–821 (1981).
3. D. Casasent, F. Caimi, and A. Khomenko, "Test and evaluation of the Soviet PROM and PRIZ spatial light modulators," Appl. Opt. 20, 4215–4220 (1981).
4. D. Casasent, F. Caimi, M. P. Petrov, and A. V. Khomenko, "Applications of the PRIZ light modulator," Appl. Opt. 21, 3846–3854 (1982).
5. C. Warde, A. M. Weiss, A. D. Fisher, and J. I. Thackara, "Optical information processing characteristics of the microchannel spatial light modulator," Appl. Opt. 20, 2066–2074 (1981).
6. G. Marie, J. Donjon, and J. P. Hazan, "Pockels effect imaging devices and their applications," in *Advances in Image Pickup and Display*, B. Kazan, ed. (Academic, New York, 1974), Vol. 1.
7. Y. Owechko and A. R. Tanguay, Jr., "Theoretical resolution limitations of electrooptic spatial light modulators. I. Fundamental considerations," J. Opt. Soc. Am. A 1, 635–643 (1984).
8. M. P. Petrov, A. V. Khomenko, V. I. Berezkin, and M. V. Krasin'kova, "Optical information recording in $Bi_{12}SiO_{20}$," Ferroelectrics 22, 651–652 (1978).
9. A. R. Tanguay, Jr., "Czochralski growth and optical properties of bismuth silicon oxide," Ph.D. Dissertation (Yale University, New Haven, Conn., 1977).
10. A. R. Tanguay, Jr. and R. C. Barker, "Implications of concurrent optical activity and electric field induced birefringence for Pockels Readout Optical Modulator performance," J. Opt. Soc. Am. 68, 1449 (A) (1978).
11. Y. Owechko, "Effects of charge transport and crystallographic orientation on electrooptic spatial light modulator resolution and sensitivity," Ph.D. Dissertation (University of Southern California, Los Angeles, Calif., 1983).
12. Y. Owechko and A. R. Tanguay, Jr., "Effects of operating mode on electrooptic spatial light modulator resolution and sensitivity," Opt. Lett. 7, 587–589 (1982).
13. R. C. Jones, "A new calculus for the treatment of optical systems. I. Description and discussion of the calculus," J. Opt. Soc. Am. 31, 488–503 (1941).
14. C. F. Buhrer, L. R. Bloom, and D. H. Baird, "Electro-optic light modulation with cubic crystals," Appl. Opt. 2, 839–846 (1963).
15. M. P. Petrov and A. V. Khomenko, "Anisotropy of the photorefractive effect in $Bi_{12}SiO_{20}$ crystals," Sov. Phys. Solid State 23, 789–792, (1981).

APPENDIX VIII

## Photorefractive incoherent-to-coherent optical converter

Y. Shi, D. Psaltis, A. Marrakchi, and A. R. Tanguay, Jr.

Y. Shi and D. Psaltis are with California Institute of Technology, Division of Engineering & Applied Science, Pasadena, California 91125; the other authors are with University of Southern California, Departments of Electrical Engineering and Materials Science, Optical Materials & Devices Laboratory, Los Angeles, California 90089.

Received 17 September 1983.
Sponsored by William T. Rhodes, Georgia Institute of Technology.
0003-6935/83/233665-03$01.00/0.



Photorefractive materials have been extensively used in recent years as real-time recording media for optical holography.[1,2] One prospective application of real-time holography is in the area of optical information processing; for example, the correlation between two mutually incoherent images has recently been demonstrated in real time in a four-wave mixing geometry.[3] Often, however, the information to be processed exists only in incoherent form. High performance spatial light modulators[4] are thus necessary in many optical information processing systems to convert incoherent images to coherent replicas for subsequent processing. We report in this Communication the successful demonstration of real-time incoherent-to-coherent image transduction through the use of holographic recording in photorefractive crystals. Several possible configurations and experimental results are presented.

The interference of two coherent beams in the volume of a photorefractive crystal generates nonuniformly distributed free carriers, which are redistributed spatially by diffusion and/or drift in an external applied field. The subsequent trapping of the free carriers in relatively immobile trapping sites results in a stored space-charge field, which in turn modulates the index of refraction through the linear electrooptic effect.[5] Thus a volume phase hologram is recorded. If the two coherent beams are plane waves, a uniform phase grating is established. An incoherent image focused in the volume of the photorefractive material will spatially modulate the charge distribution stored in the crystal. This spatial modulation can be transferred onto a coherent beam by reconstructing the holographic grating. The spatial modulation of the coherent reconstructed beam will then be a negative replica of the input incoherent image. The holographic

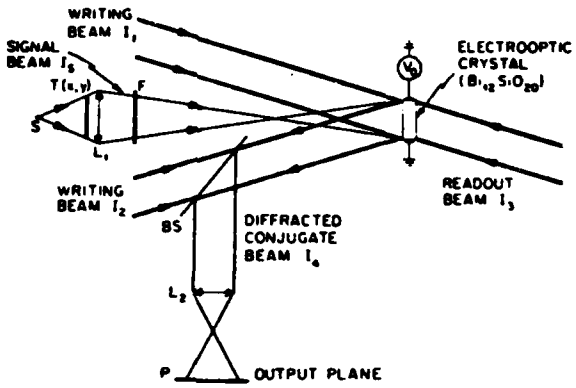


Fig. 1. Experimental setup for incoherent-to-coherent conversion with phase conjugation in four-wave mixing. The writing beams $I_1$ and $I_2$ and the reading beam $I_3$ are generated from an argon laser ($\lambda$ = 514 nm). The phase conjugate beam $I_4$ is diffracted at the same wavelength. The transparency $T(x,y)$ is illuminated with a xenon arc lamp $S$ and imaged on the BSO crystal with the optical system $L_1$ through a filter $F(\lambda = 545$ nm). $BS$ is a beam splitter, and $P$ is a polarizer placed in the output plane.

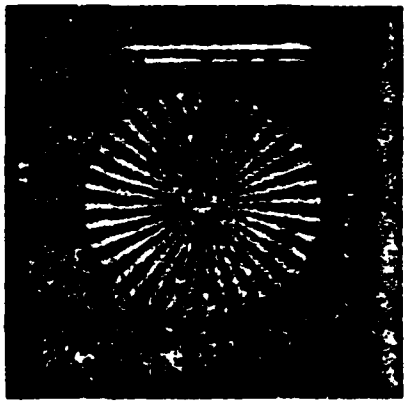

(a)

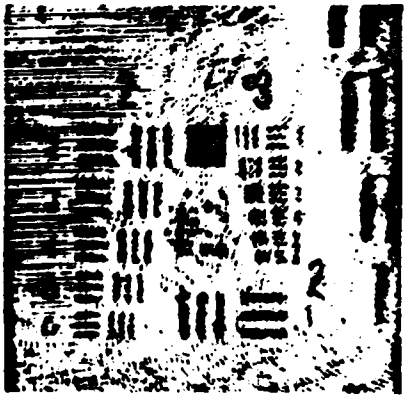

(b)

Fig. 2. Incoherent-to-coherent conversion utilizing phase conjugation in four-wave mixing: (a) spoke target; (b) USAF resolution target. The group 3.6, corresponding to a resolution of 14.3 lp/mm, is well resolved.

Fig. 3. Photorefractive incoherent-to-coherent conversion of a transparency with grey levels.

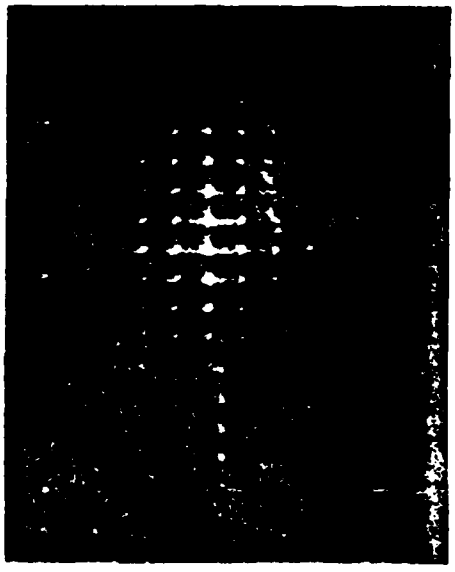

Fig. 4. Fourier transform of a grid pattern formed after a photorefractive incoherent-to-coherent conversion of the grid pattern pattern image.

grating can be recorded before, during, or after the crystal is exposed to the incoherent image. Therefore, a number of operating modes are possible. These include the Grating Erasure Mode (GEM), the Grating Inhibition Mode (GIM), and the Simultaneous Erasure Writing Mode (SEWM), among others.

In the Grating Erasure Mode, a uniform grating is recorded by interfering the two writing beams in the photorefractive crystal. This grating is then selectively erased by incoherent illumination of the crystal with an image-bearing beam. The incoherent image may be incident either on the same face of the crystal as the writing beams or on the opposite face. When the absorption coefficients of the writing and image-bearing beams give rise to significant depth nonuniformity within the crystal, these two cases will have distinct wavelength-matching conditions for response optimization.

In the Grating Inhibition Mode, the crystal is pre-illuminated with the incoherent image-bearing beam prior to grating formation. This serves to selectively decay (enhance) the applied transverse electric field in exposed (unexposed) regions of the crystal. After this pre-exposure, the writing beams are then allowed to interfere within the crystal, causing grating

formation with spatially varying efficiency due to vast differences in the local effective applied field. This technique will also work in the diffusion limit with no external applied field by means of a similar physical mechanism.

In the Simultaneous Erasure Writing Mode, the conventional degenerate four-wave mixing geometry is modified to include simultaneous exposure by an incoherent image-bearing beam, as shown schematically in Fig. 1. Diffraction by a phase grating in the four-wave mixing configuration has been modeled following two different approaches.[6,7] Common to both analyses, the diffracted intensity is proportional to both the readout intensity and the square of an effective modulation ratio, in the first-order approximation, and assuming no pump depletion. In addition, a uniform beam incident on the photosensitive medium at an arbitrary angle decreases the modulation ratio and hence the overall diffraction efficiency.[8] In the SEWM configuration, these effects can be combined with the diffraction of a conjugate beam in a four-wave mixing geometry to perform the incoherent-to-coherent image conversion. In particular, this conversion can be regarded as caused by selective spatial modulation of the grating by spatial encoding of the incoherent erasure beam. It should be noted here that a related image encoding process could be implemented in a nonholographic manner by premultiplication of the image with a grating.[9]

In our experiments, we have successfully produced incoherent-to-coherent conversions in all three operating mode configurations as well as in several modifications of the basic arrangements described above. We present here experimental results from our implementations of the Simultaneous Erasure Writing Mode.

The experimental arrangement in one implementation is as shown in Fig. 1. The two plane wave writing beams (labeled $I_1$ and $I_2$) are generated from an argon laser ($\lambda = 514$ nm) and interfere inside the photorefractive crystal to create a phase volume hologram. The readout beam $I_3$, collinear with $I_1$ to satisfy the Bragg condition, diffracts the phase conjugate beam $I_4$ at the same wavelength and with increased diffraction efficiency when a transverse electric field is applied to the electrooptic medium. An incoherently illuminated transparency $T(x,y)$ with intensity $I_s(x,y)$ (either quasi-monochromatic or white light) is imaged in the plane of the crystal. The beam splitter *BS* separates the diffracted signal from the writing beam; the Polaroid filter *P* in the output plane eliminates the unwanted scattered light to enhance the signal-to-noise ratio.[10] The photorefractive material utilized was a single crystal of bismuth silicon oxide (BSO), cut to expose polished (110) faces, and of dimensions $7.3 \times 6.9 \times 1.3$ mm$^3$.

A transverse electric field $E_0 = 4$ kV/cm was applied along the [$\bar{1}$10] axis perpendicular to the polished faces. The carrier frequency of the holographic grating, $f = 300$ lp/mm, was within the optimum range for the drift-aided charge transport process.[11] The vertically polarized coherent writing beam and signal intensities were $I_{1,2} = 0.4$ mW/cm$^2$ and $I_s = 8$ mW/cm$^2$, respectively. Figure 2 shows the converted images obtained from two binary transparencies (a spoke target and a USAF resolution target). The illumination was provided by a xenon arc lamp through a broadband filter centered at $\lambda = 545$ nm (FWHM = 100 nm). An approximate resolution of 15 lp/mm was achieved without optimizing factors such as the optical properties and quality of the crystal, the depth of focus in the bulk of the medium, the carrier frequency of the grating, and the relative intensities and wavelengths of the various beams. This spatial bandwidth is comparable with that obtained with a PROM[12] or a liquid crystal light valve.[13]

The image shown in Fig. 3 demonstrates the capability of the technique to reproduce many grey levels. To obtain this image, a negative transparency was illuminated with blue light ($\lambda = 488$ nm) derived from an argon laser and was focused on the BSO crystal. The holographic grating was recorded with green light ($\lambda = 514$ nm) and read out with an auxiliary red beam ($\lambda = 6328$ Å).

The 2-D Fourier transform formed by a lens after the incoherent-to-coherent conversion of a grid pattern is shown in Fig. 4. The fundamental spatial frequency of the grid was ~1 lp/mm. The existence of several diffracted orders and the well-focused diffraction pattern are positive indications that the device is suitable for coherent optical processing operations.

Although these results are preliminary, they clearly demonstrate the feasibility of real-time incoherent-to-coherent conversion utilizing phase conjugation in photorefractive BSO crystals. This device has potential for incoherent-to-coherent conversion with high resolution, which can be realized by optimizing the optical properties and quality of the crystal, the depth of focus in the bulk of the medium, the carrier frequency of the grating, and the relative intensities and wavelengths of the various beams. In addition, such a device is quite attractive from considerations of low cost, ease of fabrication, and broad availability. With such a device, numerous optical processing functions can be directly implemented that utilize the flexibility afforded by the simultaneous availability of incoherent-to-coherent conversion and volume holographic storage.

The authors would like to thank F. Lum for his technical assistance and Y. Owechko, J. Yu, and E. Paek for helpful discussions. This research was supported in part at USC by RADC under contract F19628-83-C-0031, the Defense Advanced Research Projects Agency, the Joint Services Electronics Program, and the Army Research Office and at Caltech by the Air Force Office of Scientific Research and the Army Research Office.

## References

1. P. Gunter, "Holography, coherent light amplification, and optical phase conjugation," Phys. Rep. 93,200 (1983).
2. D. M. Pepper, Opt. Eng. 21, 156 (1982).
3. J. O. White and A. Yariv, Appl. Phys. Lett. 37, 5 (1980).
4. A. R. Tanguay, Jr., in *Proceedings, ARO Workshop on Future Directions for Optical Information Processing, Lubbock, Tex., May, 1980* (1981), pp. 52–77.
5. D. L. Staebler and J. J. Amodei, J. Appl. Phys. 43, 1042 (1972).
6. J. Feinberg, D. Heiman, A. R. Tanguay Jr., and R. W. Hellwarth, J. Appl. Phys. 51, 1297 (1980).
7. N. V. Kukhtarev, V. B. Markov, S. G. Odulov, M. S. Soskin, and V. L. Vinetskii, Ferroelectrics 22, 961 (1979).
8. W. D. Cornish and L. Young, J. Appl. Phys. 46, 1252 (1975).
9. R. Grousson and S. Mallick, Appl. Opt. 19, 1762 (1980).
10. J. P. Herriau, J. P. Huignard, and P. Aubourg, Appl. Opt. 17, 1851 (1978).
11. J. P. Huignard, J. P. Herriau, G. Rivet, and P. Gunter, Opt. Lett. 5, 102 (1980).
12. Y. Owechko and A. R. Tanguay, Jr., Opt. Lett. 7, 587 (1982).
13. P. Aubourg, J. P. Huignard, M. Hareng, and R. A. Mullen, Appl. Opt. 21, 3706 (1982).

APPENDIX IX

465-01

# PHOTOREFRACTIVE INCOHERENT-TO-COHERENT OPTICAL CONVERSION

D. Psaltis and J. Yu
Department of Electrical Engineering
California Institute of Technology
Pasadena, California 91125

and

A. Marrakchi and A. R. Tanguay, Jr.
Optical Materials and Devices Laboratory
Departments of Electrical Engineering and Materials Science
University of Southern California, Los Angeles, California 90089-0483

## ABSTRACT

A method for performing incoherent-to-coherent conversion in photorefractive crystals is presented. The technique is experimentally demonstrated in $Bi_{12}SiO_{20}$ and a theoretical framework is established to analyze the performance of the device.

## INTRODUCTION

Two dimensional optical transparencies are used in the implementation of optical image processing systems as input incoherent-to-coherent transducers, and are also used for the recording of Fourier transform holograms. Most of the early optical image processors were implemented using photographic film for both purposes. The need for real time operation has prompted the development of devices with which it is possible to form reusable optical transparencies at high speed [1, 2]. In general, however, real time devices that are intended for use as input spatial light modulators (SLMs) are not suitable for holographic recording and vice-versa. This distinction exists partially due to the fact that a much higher spatial bandwidth is necessary for holographic recording, while at the same time the properties of high resolution holographic recording media (low sensitivity, response at low spatial frequencies) are not always compatible with the requirements of an efficient incoherent-to-coherent conversion process. Such a resolution-sensitivity tradeoff is familiar from the example of photographic (silver halide) films, for which high spatial bandwidth is in general accomplished at the expense of lower sensitivity.

The dichotomy between input SLMs and holographic elements is particularly evident in devices that are fabricated with photorefractive (PR) crystals. Photorefractive crystals are photosensitive as well as electrooptic. This feature makes it possible to record an optical image in such crystals, and subsequently modulate a separate optical beam with the recorded image. Real time SLMs, such as the PROM [3], have been fabricated with the photorefractive material $Bi_{12}SiO_{20}$, and this same crystal has also been used extensively in real-time holographic experiments [4]. The configuration and the properties of the holographic devices, however, are quite different from the PROM and other similar SLMs that are fabricated with $Bi_{12}SiO_{20}$.

In this paper we examine a method for performing incoherent-to-coherent conversion with a photorefractive device in the holographic configuration. There are two primary reasons that have motivated us to investigate this possibility: first, the construction of the holographic device is inexpensive and simple, and second, it is possible to record very high spatial frequencies in photorefractive crystals in the holographic configuration. This technique has been recently demonstrated experimentally by Kamshilin and Petrov [5] and independently by the authors [6]. In this paper the method is described, experimental results are presented, and an analytical model is employed to determine the electric fields induced in the photorefractive crystal by this recording mechanism.

465-01

## INCOHERENT-TO-COHERENT CONVERSION

The photorefractive incoherent-to-coherent optical converter is shown in Fig. 1. The photorefractive crystal is exposed to the interference pattern of two coherent plane waves, which induces the formation of a phase grating in the crystal. An electric field is externally applied in a direction parallel to the grating wavevector. The grating formation is attributed to photo-induced generation and subsequent retrapping of free carriers, resulting in a stored periodic space-charge field. The space-charge field introduces a proportional modulation of the index of refraction in the crystal through the electrooptic effect. In the configuration of Fig. 1, the crystal is also exposed to the incoherent image of an input object. The exposure to the incoherent intensity can take place during, after, or before the formation of the holographic grating. It is assumed that the depth of focus of the imaging system is sufficiently long so that the incoherent image is focused throughout the volume of the photorefractive crystal.

The incoherent illumination induces photogenerated carriers in the conduction band. As these carriers diffuse or drift and are retrapped, they partially cancel the holographically induced space-charge distribution, resulting in local erasure of the holographic grating in proportion to the incoherent intensity. The space-charge field that results from the combined exposure to the coherent and incoherent beams is a periodic grating whose amplitude is modulated approximately proportional to the negative of the incoherent image. A coherent reproduction of the incoherent image can be obtained by illuminating the crystal with an auxiliary laser beam at the appropriate Bragg angle and subsequently forming an image of the diffracted light.

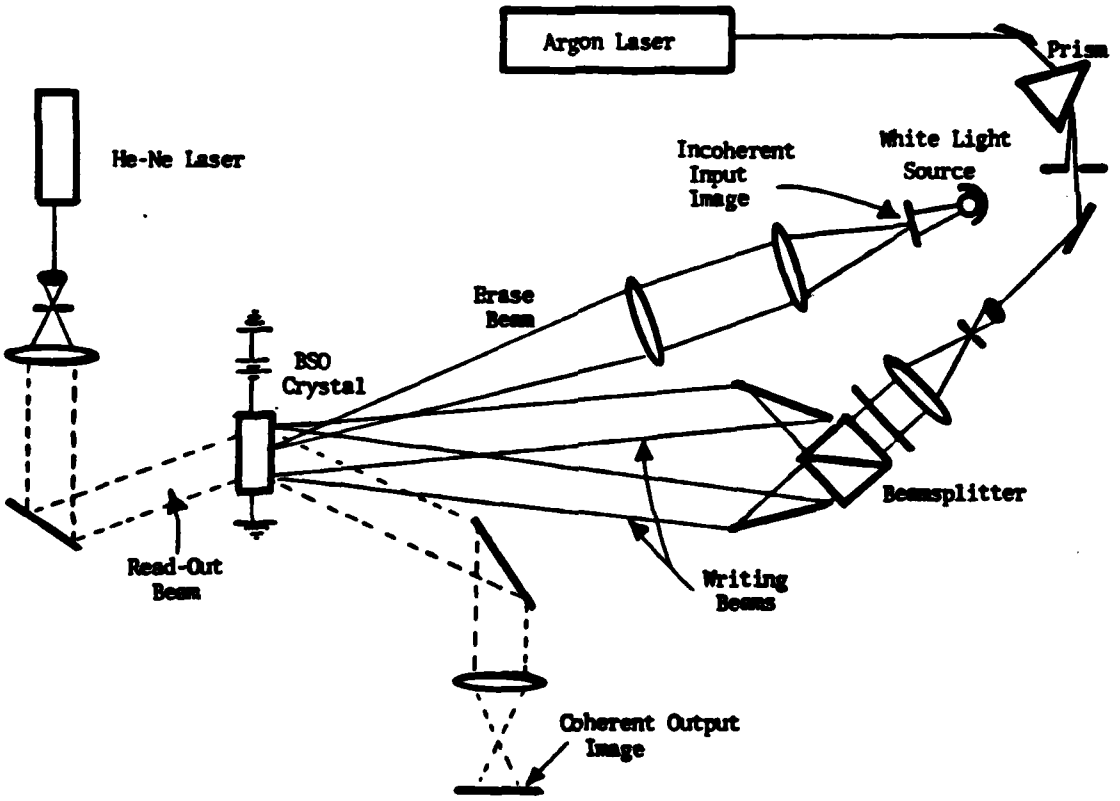


Fig. 1. Optical system for the implementation of incoherent-to-coherent conversion with a photorefractive crystal.

465-01

The system of Fig. 1 was assembled in the laboratory to demonstrate experimentally the feasibility of this technique. A (110) plate of single crystal $Bi_{12}SiO_{20}$ (BSO) with dimensions 10mm x 10mm x 2mm was used and an electric field equal to 6kV/cm was applied in the <001> direction. The holographic grating was formed with green light ($\lambda$ = 514 nm) derived from an Argon ion laser at a spatial frequency equal to 10 line pairs/mm. The average intensity of the coherent beam was 33 mW/cm$^2$. The $Bi_{12}SiO_{20}$ crystal was exposed simultaneously to an incoherent image with average intensity 1.7 mW/cm$^2$. The recorded image was read out with an expanded beam from a HeNe laser as shown in Fig. 4, and the coherent replica was obtained by imaging the plane of the $Bi_{12}SiO_{20}$ plate onto the output plane. Examples of images that were recorded after incoherent-to-coherent conversion are shown in Fig. 2.

A complete description of the performance that was observed in these initial experiments is presented in a separate paper in this volume [7]. We will briefly summarize some of the results here. Spatial frequencies in excess of 10 line pairs/mm were recorded and reconstructed, resulting in converted images with over 10 resolvable pixels with the 1 cm crystal used in the experiments. There is a direct trade-off between sensitivity and speed. Response times approximately equal to 30 msec were observed with relatively high incoherent intensity; at lower intensities ($\sim$ 1 mW/cm$^2$) the response time was approximately equal to 500 msec. It should be emphasized that these characteristics are simply preliminary observations at this stage. All of the performance characteristics depend strongly on materials and configuration parameters, and numerous trade-offs exist. The physical mechanisms that impose the fundamental limitations must be identified before the parameters can be chosen to yield optimum overall performance. To this end, a mathematical model is employed to analyze incoherent-to-coherent conversion in photorefractive crystals, as described in the following section.

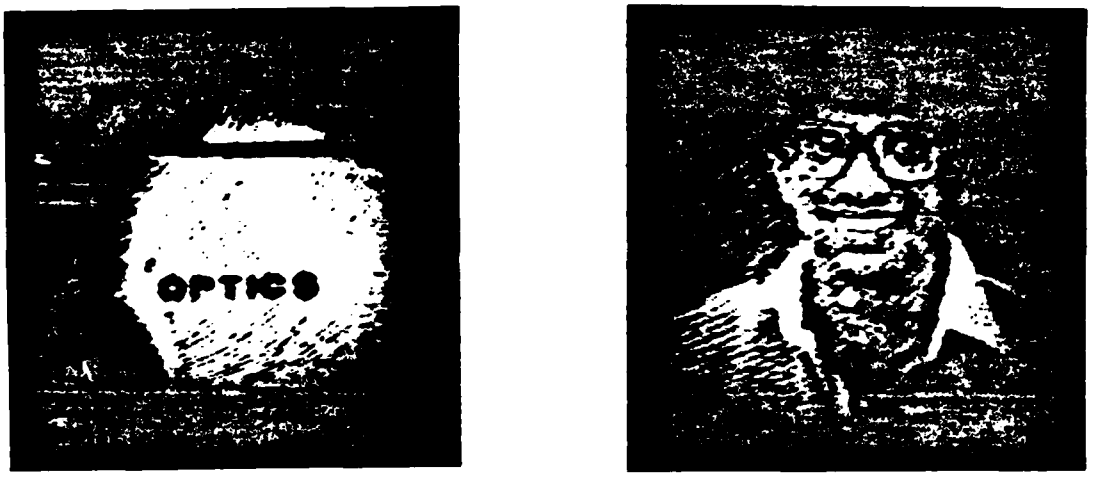


Fig. 2. Examples of photorefractive incoherent-to-coherent conversion.

## MATHEMATICAL MODEL

Holographic grating formation in photorefractive crystals has been extensively modeled [8]. The same basic formalism can also be used to analyze incoherent image recording in photorefractive crystals through erasure of a holographic grating. The analytical framework that has been proposed by Kukhtarev [8] is based on the following set of equations:

$$\frac{\partial n}{\partial t} = \frac{\partial N_D^i}{\partial t} + \frac{1}{e}\frac{\partial J}{\partial x} \tag{1}$$

$$\frac{\partial N_D^i}{\partial t} = sI(N_D - N_D^i) - \gamma n N_D^i \tag{2}$$

$$\frac{\partial E}{\partial x} = \frac{e}{\epsilon}\,(N_D^i - n - N_0) \tag{3}$$

$$J = en\mu E + k_B T \mu \frac{\partial n}{\partial x} \tag{4}$$

$$\nabla^2 \vec{E} + \omega^2 \mu \varepsilon (1 + \kappa^2 r E)\vec{E} = 0 \tag{5}$$

in which

| | |
|---|---|
| $n$ | is the density of electrons in the conduction band |
| $N_D^i$ | is the density of vacant donor sites |
| $e$ | is the electron charge |
| $J$ | is the current density |
| $x$ | is the coordinate along which the external voltage is applied |
| $s$ | is the absorption cross section |
| $I$ | is the intensity of the incident optical wave |
| $N_D$ | is the total density of donor sites |
| $\gamma$ | is the recombination coefficient |
| $E$ | is the electric field in the crystal |
| $\epsilon$ | is the dielectric constant |
| $N_0$ | is the density of vacant acceptor sites in the dark |
| $\mu$ | is the mobility |
| $K_B$ | is Boltzmann's constant |
| $T$ | is the temperature |
| $\mathcal{E}$ | is the amplitude of the electric field of the read-out light |
| $\omega/2\pi$ | is the optical frequency |
| $r$ | is the electrooptic coefficient |
| $n$ | is the index of refraction |

Equations (1)-(4) can be solved to determine the electric field E that is induced in the crystal by exposure to the input optical intensity I. Equation (5) is the wave equation, including the polarization field that is induced by the electric field in the crystal through the electrooptic effect. Once the electric field E is determined from Eqs. (1)-(4), Eq. (5) can be solved using coupled mode analysis [10] to determine the optical field diffracted by the photorefractive crystal. In this paper we concentrate on determining only the induced field E. We consider the simultaneous exposure of the crystal to the coherent grating and an incoherent image. The total light intensity incident on the crystal is the sum of the coherent and incoherent intensities:

$$I(x,t) = I_c\,[1 + m_c \cos(K_0 x)] + I_i(x,t) \tag{6}$$

where $I_c$ is the average intensity of the coherent light, $m_c$ is the modulation depth and $K_c/2\pi$ is the spatial frequency of the coherent grating. The intensity of the incoherent image is given by $I_i(x, t)$.

The set of Eqs. (1)-(4) describe a system with input intensity $I(x, t)$, the state of which is described by the four variables $N_D^i$, n, J and E. The solution of the four equations yields the electric field E. The fidelity with which the incoherent image $I_i$ is recorded can be investigated by studying the relationship between E and $I_i$. The solution of Eqs. (1)-(4) is in general difficult because they are nonlinear. Often these equations are solved by making simplifying assumptions that lead to full or partial linearization. The effect that we are investigating, however, is based on the nonlinearities, and we are therefore primarily interested in characterizing the nonlinear part of the response of the system. For this reason, we have included in the analysis all of the nonlinear terms. The strongest nonlinearity typically occurs in Eq. (4) where the current density J is proportional to the product of E and n, the number density of electrons in the conduction band. The product $nN_D^i$ that appears in Eq. (1) can also be a significant source of nonlinearity.

The critical role that the nonlinearities play in this device can be appreciated by considering the electric field distributions E that are induced by exposure to the coherent and incoherent beams independently. The coherent beams alone record a uniform grating; the incoherent beam alone induces a field distribution that is not an accurate reproduction of the incoherent intensity distribution (more on this later). If the system were linear, the combined exposure would simply induce the sum of these two field distributions. However, the nonlinearities give rise to additional, intermodulation terms in E and these are responsible for the accurate reproduction of the incoherent image upon reconstruction of the holographic grating that is observed experimentally.

The steady state behavior of the system is analyzed by setting all the time derivatives equal to zero in Eqs. (1)-(4) and choosing an incoherent illumination of the following form:

$$I_i(x,t) = I_i\,[1 + m_i \cos(K_i x)]. \tag{7}$$

in which $m_i$ is the modulation depth and $K_i/2\pi$ the spatial frequency of the incoherent grating. In this case the solution for the electric field E is in the form

$$E(x) = \sum_{m=-M}^{M} \sum_{n=-N}^{N} E_{mn} \exp[j(mK_c + nK_i)x], \tag{8}$$

and similarly for the other three variables, n, $N_D^i$, and J. Equations (1)-(4) can now be solved numerically, using the method of successive approximations, to obtain the coefficients of the expansion in Eq. (8). The calculation was performed for $m_c = m_i = 1$, $K_c/2\pi = 10$ c/mm, $K_i/2\pi = 10$ c/mm, and material parameters that were given by Peltier and Micheron [9] for $Bi_{12}SiO_{20}$.

The coefficients $E_{11}$, $E_{01}$ and $E_{10}$ are plotted in Fig. 3 as a function of the ratio $R = I_i/I_c$. The quantity $E_{11}$ is the coefficient of the intermodulation term of interest, $\cos(K_i x)\cos(K_c x)$. It is evident in Fig. 3 that $E_{11}$ attains a maximum at $R = 1$. It is interesting to note that in the experiments reported in the previous section, the much higher value of $R \sim 52$ was used. The reason for this choice can be appreciated by observing the behavior of $E_{10}$. The quantity $E_{10}$ is the coefficient of the $\cos(K_i x)$ term, and upon reconstruction it results in a uniform plane wave diffracted in the same general direction as the signal beam that is diffracted due to the $E_{11}$ grating. As a result it acts as a constant background bias that reduces the contrast of the coherent image. As shown in Fig. 3, the ratio $E_{11}/E_{10}$ increases (and hence the contrast improves) as R is increased. In a coherent optical system, a constant bias can be easily removed by spatial filtering and

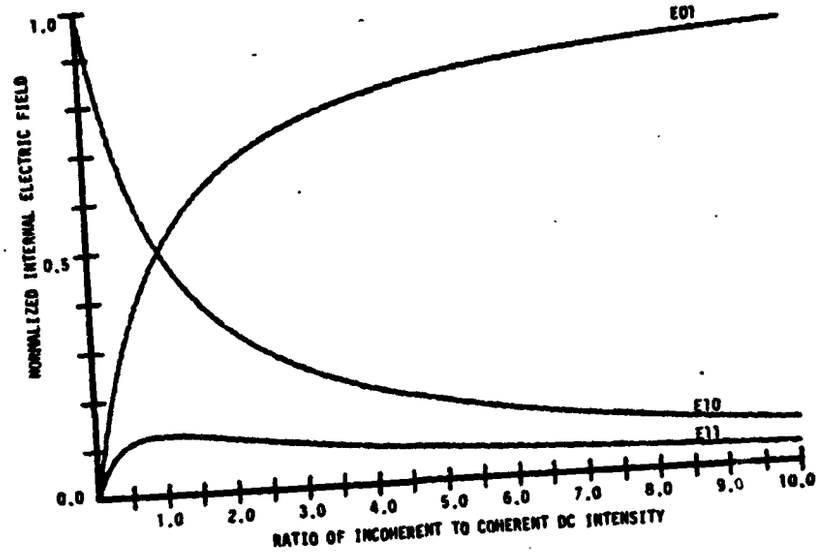


Fig. 3. Peak amplitude of three Fourier components of the electric field induced in the photorefractive crystal, as a function of the ratio of incoherent-to-coherent intensity.

therefore it is not necessary to use high incoherent intensity to obtain good contrast. A very significant conclusion that can be drawn is that the sensitivity for incoherent recording in this mode is equal to the sensitivity for holographic recording. Furthermore, a better approximation to linear incoherent recording is obtained in the range $0 \leq R \leq 1$ than at higher values of R.

The $E_{01}$ coefficient is also plotted in Fig. 3. This term is due to the direct recording of the incoherent grating in the photorefractive crystal. As can be seen from Fig. 3, $E_{01}$ is stronger than $E_{11}$ and thus the question may arise as to whether or not direct incoherent image recording in photorefractive crystals is feasible in the holographic configuration. Unfortunately direct recording is only possible for one dimensional

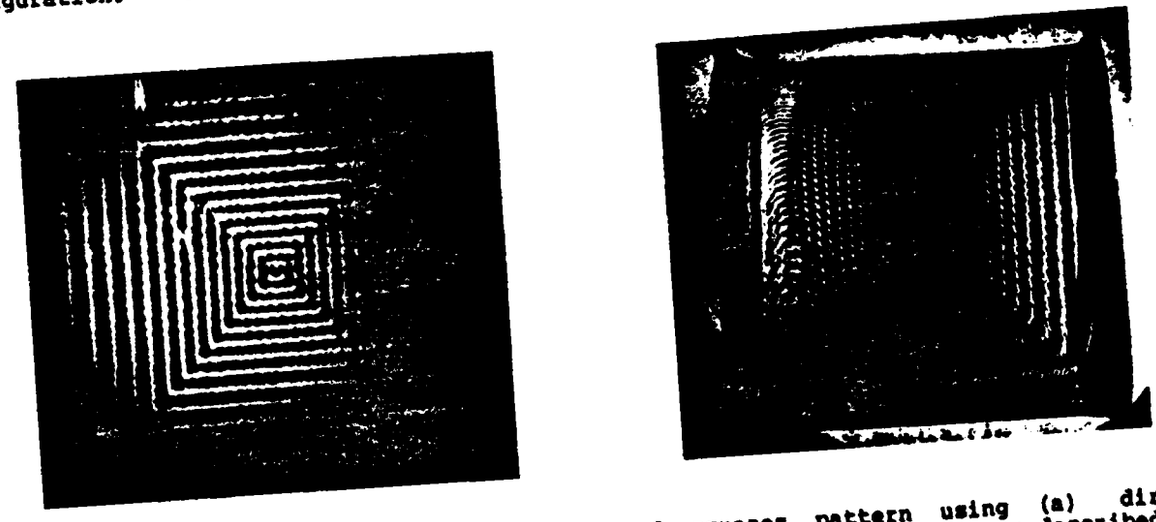

Fig. 4. Optical reconstruction of a nested squares pattern using (a) direct recording, and (b) holographic grating erasure techniques, as described in the text.

465-01

incoherent images in crystals such as $Bi_{12}SiO_{20}$, where an external field is required for efficient grating recording. A simple experiment was performed to demonstrate this. A transparency of a nested-squares pattern was used as the incoherent input in the experimental set-up described in the previous section. Coherent reproductions of this object were obtained from the $E_{\mu}$ and $E_{\phi i}$ gratings and they are shown in Figs. 4a and 4b, respectively. The external field was applied in the horizontal direction of Figs. 4. It is evident that information is recorded only in the direction parallel to the external field with direct exposure, whereas two dimensional recording is possible through erasure of the holographic grating.

## CONCLUSION

A novel recording method in photorefractive crystals has been presented. Our preliminary experimental and theoretical observations indicate that incoherent-to-coherent conversion can be implemented with this mechanism. Further experimental and theoretical work is needed to assess the full capabilities of this device.

## ACKNOWLEDGMENTS

The research reported in this paper is supported at Caltech by the Army Research Office and the Air Force Office of Scientific Research; at USC by the Air Force Systems Command (RADC) under contract F19628-83-C-0031, the Defense Advanced Research Projects Agency, the Joint Services Electronics Program, and the Army Research Office.

The authors would like to thank Y. Shi for performing some of the experiments described in this paper.

## REFERENCES

[1] A. R. Tanguay, Jr., in Proceedings of ARO Workshop on Future Directions for Optical Information Processing, Texax Tech University, Lubbock, Texas, 52-77, (1981).

[2] D. Casasent, Proc. IEEE., 67(5), 813 (1979).

[3] B. A. Horwitz and F. J. Corbett, Opt. Eng., 17, 353, (1978).

[4] R. A. Fisher, ed., Optical Phase Conjugation, Academic Press, New York, (1983).

[5] A. A. Kamshilin and M. P. Petrov, Sov. Tech. Phys. Lett., 6(3), 144, (1980).

[6] Y. Shi, D. Psaltis, A. Marrakchi and A. R. Tanguay, Jr., Appl. Opt., 22, 3665 (1983).

[7] A. Marrakchi, A. R. Tanguay, Jr., D. Psaltis and J. Yu, this volume.

[8] N. V. Kukhtarev, et. al., Ferroelec., 22, 2414, (1975).

[9] M. Peltier and F. Micheron, J. Appl. Phys., 45, 3683, (1977).

[10] H. Kogelnik, Bell Syst. Tech., 48, 2909, (1969).

APPENDIX X

465-12

# PHOTOREFRACTIVE INCOHERENT-TO-COHERENT OPTICAL CONVERTER: PHYSICAL AND MATERIALS CONSIDERATIONS

A. Marrakchi and A. R. Tanguay, Jr.
Optical Materials and Devices Laboratory
Departments of Electrical Engineering and Materials Science
University of Southern California, Los Angeles, California 90089-0483

and

J. Yu and D. Psaltis
Department of Electrical Engineering
California Institute of Technology, Pasadena, California 91125

## ABSTRACT

Volume holographic storage in photorefractive $Bi_{12}SiO_{20}$ (BSO) crystals is utilized to perform dynamic incoherent-to-coherent image conversion by means of selective spatial erasure of a uniform grating with white (or quasi-monochromatic) light. Preliminary results with binary and grey level transparencies are presented, and the conversion process is described in terms of a simple model which relates the diffracted intensity to the space-variant effective modulation ratio.

## INTRODUCTION

Real-time holography in photorefractive materials has been utilized for many applications in the areas of optical processing [1], non-destructive testing of vibrating structures [2], and image propagation through aberrating media [3]. In addition, the development of high performance spatial light modulators has received much recent attention, primarily for incoherent-to-coherent conversion functions in optical information processing and computing applications [4, 5]. We have reported in a previous paper [6] the successful application of volume phase holography to the real-time conversion of an incoherent image (quasi-monochromatic or white light illumination) into a coherent replica. Several possible configurations for the performance of this image transduction in photorefractive materials were discussed therein. Such a conversion process has been investigated independently, as reported in reference [7].

In this paper, we present a simple model that describes the incoherent-to-coherent conversion process in terms of the space-variant effective modulation ratio. The model is shown to satisfactorily explain the principal features of the device sensitometry behavior. The limiting resolution of the process is discussed, and geometric, systemic, and materials-related constraints are identified. Experimental measurements of the device temporal response characteristics are presented.

The high sensitivity of photoconductive and electrooptic crystals such as Bismuth Silicon Oxide ($Bi_{12}SiO_{20}$ or BSO) in the visible spectrum has allowed the simultaneous recording and reading of volume holograms to be achieved with time constants amenable to real-time operation. The holographic recording process in photorefractive materials involves photoexcitation, charge transport, and trapping mechanisms [8, 9]. When two coherent writing beams are allowed to interfere within the volume of such a crystal, free carriers are nonuniformly generated by absorption, and are redistributed by diffusion and/or drift under the influence of an externally applied electric field. Subsequent trapping of these charges generates a stored space-charge field, which in turn modulates the refractive index through the linear electrooptic (Pockels) effect and thus records a volume phase hologram. If both coherent writing beams are plane waves, the induced hologram will consist of a uniform grating.

In the Photorefractive Incoherent-to-Coherent Optical Conversion (PICOC) process, in addition to the holographically-induced charge distribution stored in the crystal, an incoherent image is focused in the volume of the photorefractive material, and creates a spatial modulation that can be transferred onto a coherent beam by reconstructing the holographic grating. The spatial modulation of the coherent reconstructed beam will then be a negative replica of the input incoherent image. The holographic grating can be recorded before, during or after the crystal is exposed to the incoherent image. Therefore, a number of distinct operating modes are possible. These include the Grating Erasure Mode (GEM), the Grating Inhibition Mode (GIM), and the Simultaneous Erasure/Writing Mode (SEWM), among others.

In the Grating Erasure Mode, a uniform grating is first recorded by interfering the two coherent writing beams in the photorefractive crystal. This grating is then selectively erased by incoherent illumination of the crystal with an image-bearing beam. The incoherent image may be incident either on the same face of the crystal as the writing beams, or on the opposite face. When the absorption coefficients of the writing and image-bearing beams give rise to significant depth nonuniformity within the crystal, these two cases will have distinct wavelength-matching conditions for response optimization.

In the Grating Inhibition Mode, the crystal is pre-illuminated with the incoherent image-bearing beam prior to grating formation. This serves to selectively decay (enhance) the applied transverse electric field in exposed (unexposed) regions of the crystal. After this pre-exposure, the coherent writing beams are then allowed to interfere within the crystal, causing grating formation with spatially varying efficiency due to significant differences in the local effective applied field.

In the Simultaneous Erasure/Writing Mode, the incoherent image modulation, the coherent grating formation process, and the readout function are performed simultaneously. In one possible implementation of this mode, the conventional degenerate four-wave mixing geometry can be modified to include simultaneous exposure by an incoherent image-bearing illumination, as shown schematically in Fig. 1. In this configuration, the coherent replica of the incoherently-exposed image appears in the conjugate diffracted beam.

The PICOC process can thus be regarded as caused by selective spatial modulation of a grating by spatial encoding of an incoherent erasure beam. It should be noted here that a related image encoding process could be implemented in a non-holographic manner by pre-multiplication of the image with a grating [10].

## PHOTOREFRACTIVE INCOHERENT-TO-COHERENT OPTICAL CONVERSION

In the remainder of this paper, we examine the Simultaneous Erasure/Writing Mode in more detail. As a specific example, we will discuss the configuration in which the coherent writing beams and the incoherent image-bearing beam illuminate the same face of a BSO photorefractive crystal, with a transverse electric field applied along the <110> axis as shown in Fig. 2. Consider an incident intensity distribution of the form

$$\begin{aligned} I_T(x) &= I_G(x) + I_S(x) \\ &= I_G(1 + m_G \cos K_G x) + I_S(1 + m_S \cos K_S x) \end{aligned} \tag{1}$$

with $I_G = I_1 + I_2$ and $m_G = 2(I_1 I_2)^{1/2}/I_G$, in which $K_G$ and $K_S$ are the wavevectors of the coherent grating (G) and a particular harmonic component of the incoherent image (S), and $m_G$ and $m_S$ are the respective modulation ratios. Due to the nonlinear dependence of the induced space-charge field on the incident intensity, such a distribution will generate a refractive index modulation which can be written in the form

$$\begin{aligned} \Delta n(x) &= C_1 \cos K_G x + C_2 \cos K_S x \\ &+ C_3 \cos [(K_G - K_S)x] \\ &+ C_4 \cos [(K_G + K_S)x] \\ &+ \text{Other Terms.} \end{aligned} \tag{2}$$

465-12

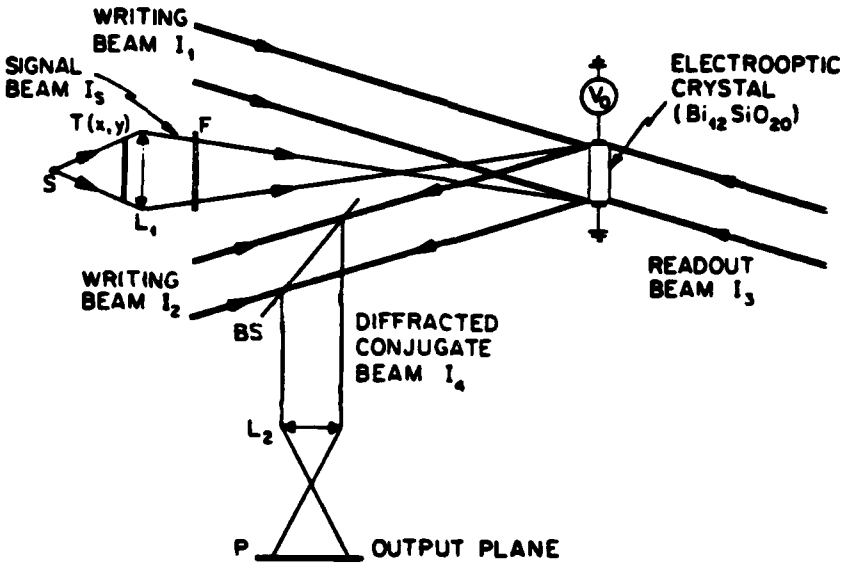


Fig. 1 Experimental configuration for photorefractive incoherent-to-coherent optical conversion (PICOC) in the Simultaneous Erasure/Writing Mode (SEWM). The writing beams $I_1$ and $I_2$, and the reading beam $I_3$, are generated from an argon laser ($\lambda$ = 514 nm). The phase conjugate beam $I_4$ is diffracted at the same wavelength. The transparency T(x, y) is illuminated with a xenon arc lamp S and imaged onto the $Bi_{12}SiO_{20}$ crystal with the optical system $L_1$ through a filter F($\lambda$ = 545 nm). A coherent replica is formed in the output plane by utilizing beamsplitter BS in conjunction with lens $L_2$ to image the surface of the crystal onto the output plane through polarizer P.

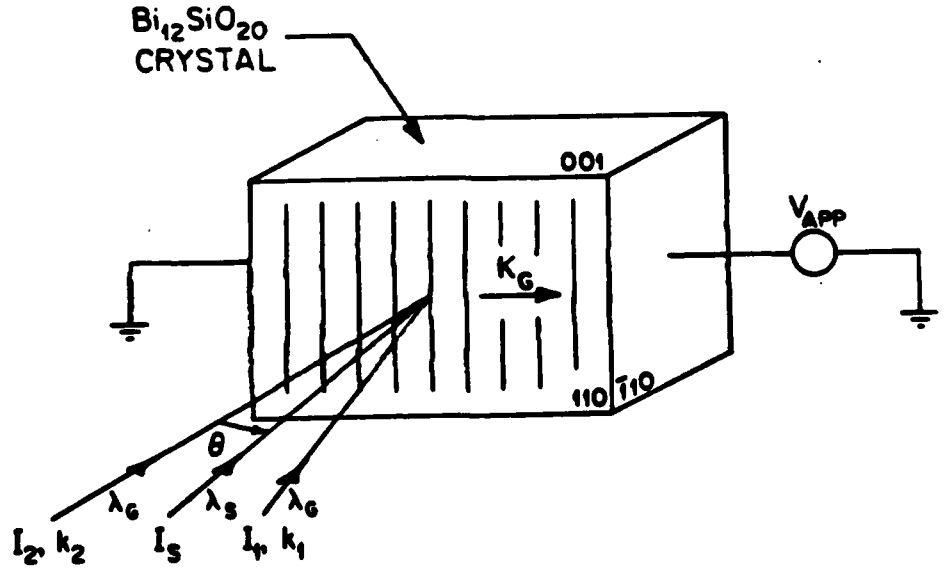


Fig. 2 PICOC transverse electrooptic configuration and recording geometry. The volume holographic grating with wavevector $K_G$ is formed by the coherent writing beams $I_1$ and $I_2$, and the incoherent information is encoded on the beam $I_S$.

Note in particular that n(x) contains the sum and difference spatial frequencies as well as the fundamental harmonics. The constants $C_i$ (i = 1 to 4) represent the amplitudes of each frequency component. Thus, the far-field diffraction pattern shown in Fig. 3 will comprise several beams, each corresponding to a specific term in the refractive index modulation.

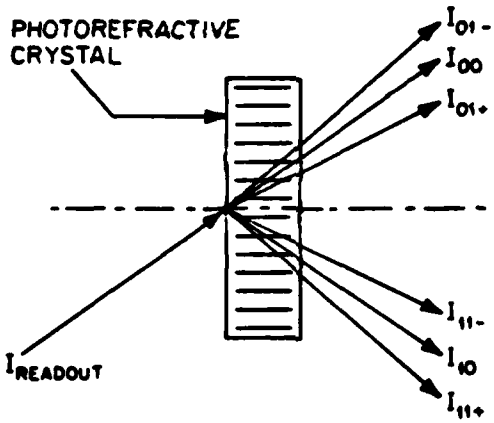


Fig. 3 Far-field diffraction pattern resulting from the nonlinear interaction of two gratings in a photorefractive crystal.

To demonstrate incoherent-to-coherent conversion in the four-wave mixing configuration, the experimental arrangement of Fig. 1 was utilized with a 1.3 mm thick (110)-cut BSO crystal. A transverse electric field ($E_0$ = 4 kV/cm) was applied along the <110> axis, and the carrier frequency of the holographic grating (f = 300 line pairs/mm) was chosen to lie within the optimum range for drift-aided charge transport in BSO [11].

In this implementation, the two plane wave writing beams (labeled $I_1$ and $I_2$) are generated from an argon laser ($\lambda_G$ = 514 nm) and interfere inside the (110)-cut BSO crystal to create a volume phase hologram. The readout beam $I_3$, collinear with $I_1$ to satisfy the Bragg condition, is diffracted to form the phase conjugate beam $I_4$ at the same wavelength. Increased diffraction efficiency results when a transverse electric field is applied to the electrooptic medium. An incoherently illuminated transparency T(x, y), with intensity $I_s$(x, y) (either quasi-monochromatic or white light), is imaged in the plane of the crystal. The beam-splitter BS separates the diffracted signal from the writing beam, and the polarizing filter P in the output plane eliminates the unwanted scattered light to enhance the signal-to-noise ratio [12]. The vertically polarized coherent writing beam and signal intensities were $I_{1,2}$ = 0.4 mW/cm$^2$ and $I_s$ = 8 mW/cm$^2$, respectively. The incoherent illumination was provided by a xenon arc lamp through a broadband filter centered at $\lambda_s$ = 545 nm (FWHM = 100 nm).

The converted images obtained from two binary transparencies (a spoke target and a USAF resolution target), and from a black and white slide with grey levels are shown in Figs. 4 and 5, respectively. The original transparency and its converted image have reversed contrast. An approximate resolution of 15 line pairs/mm (as derived from the resolution target image) was achieved without optimizing factors such as the optical properties and quality of the crystal, the depth of focus in the bulk of the medium, the carrier frequency of the grating, the relative intensities and wavelengths of the various beams, or the Bragg diffraction condition (discussed below). This spatial bandwidth is comparable to that obtained with a PROM [13] or a liquid crystal light valve [14].

A number of distinct factors influence the ultimate resolution achievable with the PICOC spatial light modulator. These factors can be classified as geometric, systemic, and materials-related in nature. Each of these resolution limitations are described in detail below.

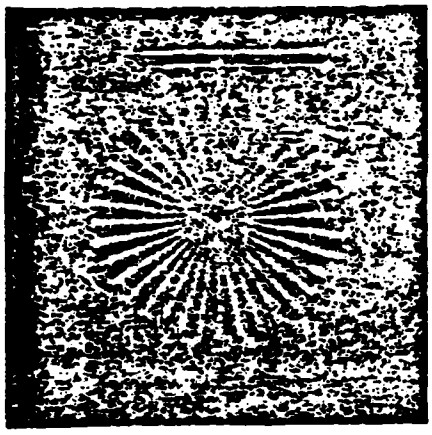

(a)

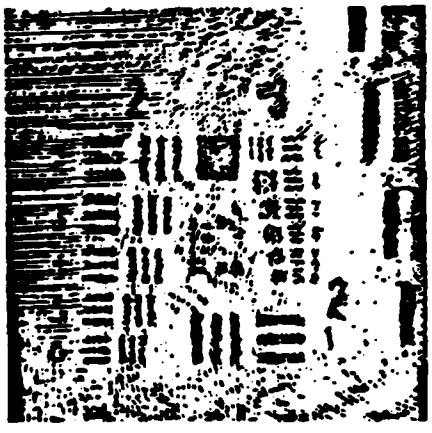

(b)

Fig. 4 Photorefractive incoherent-to-coherent optical conversion of two binary transparencies: (a) spoke target, and (b) USAF resolution target.

Fig. 5 Photorefractive incoherent-to-coherent optical conversion of a grey-level transparency.

Geometric resolution limitations derive principally from the incorporation of an incoherent imaging system in the four-wave mixing geometry, and from the finite crystal thickness required to create a volume holographic grating. These effects are illustrated in Figs. 6 and 7. Figure 6 describes the case for which $\alpha_g d<1$, such that the induced holographic grating has finite amplitude throughout the volume of the crystal. As can be seen from the Figure, the optimum focal point occurs in the volume of the crystal (in the center when $\alpha_g d<<1$), and is not localized on the front surface of the crystal. The resolution will then be proportional to $(W/2)^{-1}$, which is in turn equal to $4n F\#/d$. In this expression, n is the refractive index of the electrooptic crystal, F# is the F-number of the input incoherent imaging system (assumed 1:1), and d is the crystal thickness. For example, for $n = 2.5$, $d = 1mm$, and an F-number of 5, the resolution limit is approximately 50 line pairs/mm. Figure 7 describes the case for which $\alpha_g d>>1$, such that the induced holographic grating has significant amplitude only within a thin layer of thickness $d_{eff} = \alpha_g^{-1}$. In this case, the resolution will be given by $4n F\#\alpha_g$. For $n = 2.5$, $d = 1mm$, $\alpha_g = 100cm^{-1}$, and an F-number of 5, the resolution limit is approximately 500 line pairs/mm.

Several systemic resolution constraints derive from the utilization of a volume hologram in the image conversion process. One such constraint is that the coherent grating spatial frequency must be significantly larger than the signal (incoherent image) bandwidth

in order to effect separation of the 0th and 1st order diffracted beam components. In addition, the range of spatial frequencies distributed about the coherent grating spatial frequency should be in an optimum region of the modulation transfer characteristic of the device.

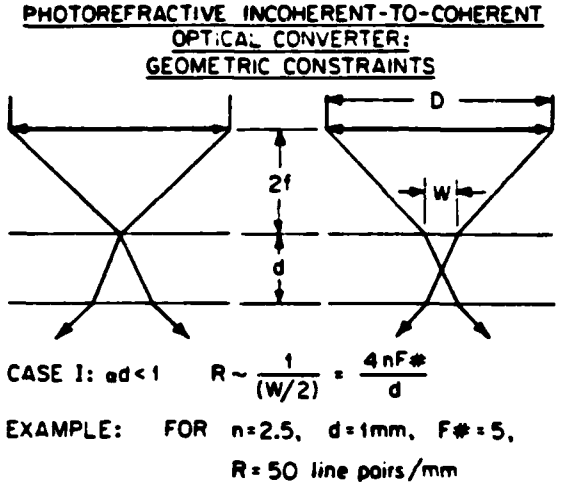


Fig. 6 Geometric constraints imposed on PICOC resolution by the finite F-number of the input optics, for the case $ad < 1$.

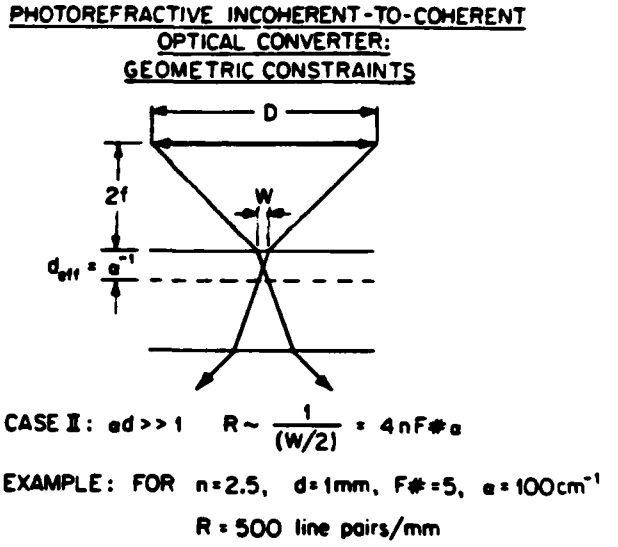


Fig. 7 Geometric constraints imposed on PICOC resolution by the finite F-number of the input optics, for the case $ad >> 1$.

A third fundamental systemic constraint on the PICOC device resolution derives from Bragg detuning effects associated directly with the use of a volume hologram. This effect is strikingly illustrated in Figure 8, which is comprised of converted images of a 5 line pair/mm Ronchi ruling and their related coherent Fourier transforms, for two orthogonal orientations of the incoherent grating wavevector relative to the coherent grating wavevector. As can be seen from the Figure, a significant difference in resolution exists between cases in which the wavevector of the ruling (incoherent grating) is parallel or perpendicular to the coherently-written (holographic) grating. This difference derives principally from a wavevector matching condition, as shown in Figs. 9 and 10. In Fig. 9, the incoherent grating wavevector is parallel to the coherent grating wavevector, a condition achieved by *symmetrically disposing the incident coherent* beams about the *normal* to the crystal, while simultaneously arranging the incoherent imaging system such that its optical axis is parallel to the crystal normal. In this case, significant Bragg detuning occurs for even small incoherent grating wavevectors (resulting in angular deviations of the diffracted beam). In Fig. 10, the incoherent grating wavevector is arranged to lie tangent to the circle defined by the incident coherent grating wavevectors, such that a significantly increased angular deviation of the diffracted beam is allowed before significant Bragg detuning effects occur. Such a wavevector tangency condition is automatically satisfied when the incoherent grating wavevector is normal to the coherent grating wavevector (as it is in the orientation normal to the plane of incidence). For the arrangement described in Fig. 10, wavevector tangency is assured for both orientations, so that the horizontal and vertical resolutions become degenerate for this case. An equivalent condition is described in Ref. [7] for the case of distinct reading and writing beam wavelengths.

A fourth related systemic constraint involves the tradeoff between saturation diffraction efficiency and achievable resolution due to grating thickness. Within limits, increases in grating thickness increase the diffraction efficiency, but at the same time increase the Bragg detuning per unit angle. This condition creates a familiar resolution/sensitivity tradeoff situation in which one can be optimized at the expense of the other.

Additional resolution limitations derive from material parameter constraints that influence the physics of grating formation. This limitation is essentially described by the behavior of the diffraction efficiency as a function of the spatial frequency with the applied transverse electric field as a parameter [11]. The amplitude modulation transfer function of the grating itself depends on the spatial frequency dependence of the maximum space-charge field, which in turn depends on carrier mobilities and lifetimes, the applied field, the nature and distribution of traps in the crystal, and the trap occupancy (Fermi) level.

Optimization of the PICOC device resolution necessarily involves simultaneous satisfaction of all three types of constraints, and must be undertaken also in compromise with factors that directly affect the device sensitivity. In succeeding paragraphs, we

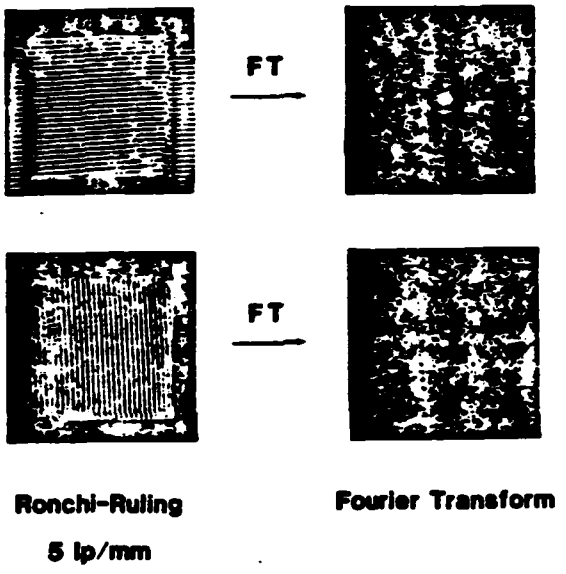


Fig. 8 Coherent replica images and corresponding Fourier transforms of a 5 line pair per mm Ronchi ruling after photorefractive incoherent-to-coherent conversion.

present a model that allows the device sensitivity to be understood and optimized. It should be noted here that amplification via energy transfer has been observed in the four-wave mixing configuration in $BaTiO_3$ [15], and in the two-wave mixing configuration in a BSO crystal [16, 17]. By utilizing this effect in the PICOC geometry described in this paper, incoherent-to-coherent conversion could be performed with improved energy sensitivity without sacrifice of resolution.

The following simple model describes the encoding of the incoherent information onto the coherent diffracted beam, by taking into account only the effective modulation ratio of the exposure in the bulk of the photorefractive material. The different intensities incident on the crystal are as shown in Fig. 2. The intensity pattern resulting from simultaneous illumination with the coherent writing beams and the incoherent image-bearing beam is given by Eqn. (1), which describes the case of a one-dimensional incoherent sinusoidal grating with a fundamental component at wavevector $K_s$. The space-charge field $E_{sc}$ is related to the current density $J(x, t)$ and the free-carrier concentration $n(x, t)$ through the following system of equations [18]:

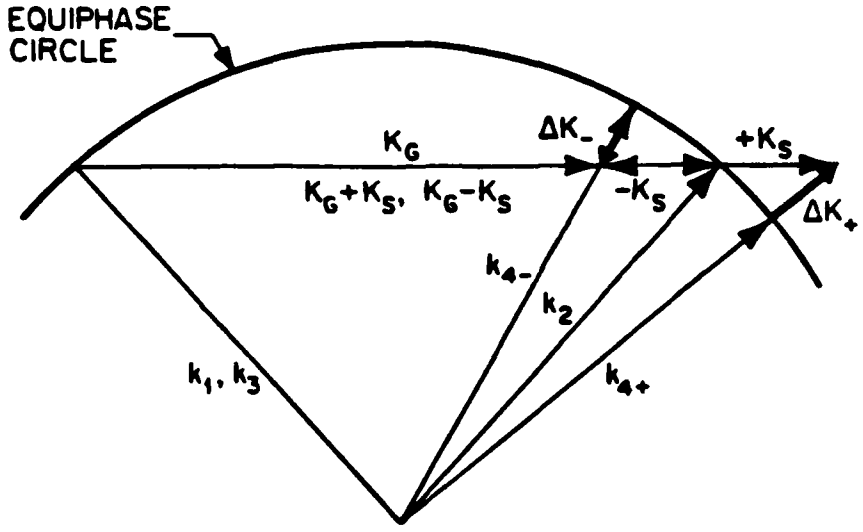


Fig. 9 Wavevector diagram of the photorefractive incoherent-to-coherent conversion process, for the case of collinear signal ($K_S$) and grating ($K_G$) wavevectors. Readout with a beam incident at wavevector $k_3$ results in diffracted beams at $k_{4+}$ and $k_{4-}$, with corresponding Bragg mismatches $\Delta K_+$ and $\Delta K_-$.

**Current density equation**

$$J(x,t) = eD \frac{\partial n(x,t)}{\partial x} + e\mu n(x,t) \left[E_{sc}(x,t) + E_0\right] \tag{3}$$

**Continuity equation**

$$\frac{\partial n(x,t)}{\partial t} = g(x) - \frac{n(x,t) - n_d}{\tau} + \frac{1}{e} \frac{\partial J(x,t)}{\partial x} \tag{4}$$

**Maxwell's equation (integral form)**

$$E_{sc}(x,t) = -\frac{1}{\epsilon} \int_0^t J(x,t)dt + G(t) \tag{5}$$

$$\int_0^L E_{sc}(x,t)dx = 0 \tag{6}$$

in which $g(x)$ is the generation rate, $n_d$ is the free-carrier concentration in the dark, $E_0$ is the applied transverse field, and $G(t)$ is a boundary condition-dependent constant of integration. If one assumes that the quantum efficiency $\xi$, which is the probability of creating a free electron by an absorbed photon of energy $\hbar\omega$, is not wavelength-dependent in the range of interest, the intensity distribution $I_T(x)$ gives rise to the free-carrier generation rate

$$g(x) = \frac{\alpha_G \xi}{\hbar\omega_G} I_G(1 + m_G \cos K_G x) \exp(-\alpha_G d) + \frac{\alpha_S \xi}{\hbar\omega_S} I_S(1 + m_S \cos K_S x) \exp(-\alpha_S d) \tag{7}$$

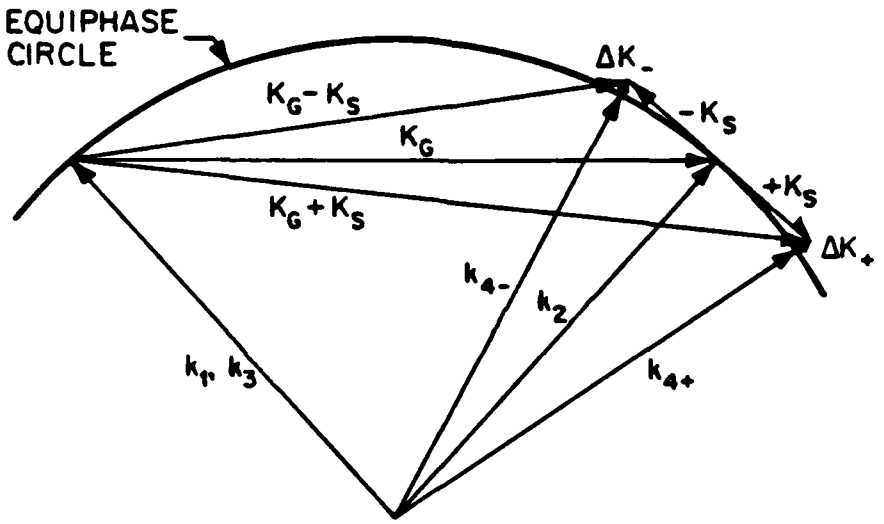


Fig. 10 Wavevector diagram of the photorefractive incoherent-to-coherent optical conversion process, for the case wherein the signal wavevector is tangent to the equiphase circle. Readout with a beam incident at wavevector $k_3$ results in diffracted beams at $k_{4+}$ and $k_{4-}$, with significantly reduced Bragg mismatches $\Delta K_+$ and $\Delta K_-$.

in which d is the crystal thickness, and the intensity absorption coefficients are $\alpha_S$ at $\lambda_S$ and $\alpha_G$ at $\lambda_G$. Since free-carrier redistribution will occur both by drift and diffusion, the resultant space-charge field will depend on both the carrier concentration n(x) and its spatial gradient $\partial n/\partial x$. Solution of this system of equations is extremely complicated in general, and must be accomplished in the context of boundary conditions applicable to a given experimental situation. In the development that follows, several simplifying assumptions are made that are appropriate for the SEWM configuration in the steady state, and in the large transverse applied field limit (to enhance the saturation diffraction efficiency).

In the saturation regime (steady state), the current density is constant and the carrier concentration is given by

$$n(x) = n_d + \tau g(x) \tag{8}$$

in which the free-carrier lifetime $\tau$ is assumed to be the same for the writing and the erasure beams, and unaffected by the presence or absence of illumination. In the strong drift regime for which the applied field is much larger than the diffusion field ($E_0 >> E_D$; $E_D = Kk_BT/e$), solution of the system of Eqns. (3-6) subject to the additional constraints expressed in Eqns. (7) and (8) yields the following expression for the space-charge field

$$E_{sc} = \frac{m_G^{eff} E_{DG} \sin K_G x + m_S^{eff} E_{DS} \sin K_S x}{1 + m_G^{eff} \cos K_G x + m_S^{eff} \cos K_S x} \tag{9}$$

$$+ E_0 \left[ \frac{(1 - (m_G^{eff})^2)^{1/2}}{1 + m_G^{eff} \cos K_G x + m_S^{eff} \cos K_S x} - 1 \right]$$

with

$$m_G^{eff} = \frac{m_G}{1 + \frac{\alpha_S \lambda_S}{\alpha_G \lambda_G} \frac{I_S}{I_G} \exp\left[(\alpha_G - \alpha_S)d\right]} \tag{10}$$

and

$$m_S^{eff} = \frac{m_S}{1 + \frac{\alpha_S \lambda_S}{\alpha_G \lambda_G} \frac{I_S}{I_G} \exp\left[(\alpha_G - \alpha_S)d\right]} \tag{11}$$

Assuming further that the effective fringe modulation ratios ($m_G^{eff}$, $m_S^{eff}$) are small and that $E_{DS} << E_{DG} << E_0$, the space-charge field amplitudes at each harmonic component of interest are given by:

$$E_{sc}(K_G) = - m_G^{eff} E_0 \tag{12}$$

$$E_{sc}(K_G + K_S) = m_G^{eff} m_S^{eff} E_0 \tag{13}$$

$$E_{sc}(K_G - K_S) = m_G^{eff} m_S^{eff} E_0 \tag{14}$$

The refractive index modulation induced along a principal axis by the electrooptic effect is then given by

$$\Delta n(x) = \frac{1}{2} n_0^3 r_{41} E_{sc}(x) \tag{15}$$

$$= - \frac{1}{2} n_0^3 r_{41} m_G^{eff} E_0 \left[\cos K_G x - m_S^{eff} \cos(K_G + K_S)x - m_S^{eff} \cos(K_G - K_S)x\right]$$

or, by combining terms,

$$\Delta n(x) = - \frac{1}{2} n_0^3 r_{41} m_G^{eff} E_0 \left[1 - 2m_S^{eff} \cos K_S x\right] \cos K_G x. \tag{16}$$

For small diffraction efficiencies and low spatial frequencies $K_S$, the diffracted intensity pattern in the first order of the carrier grating can be expressed by the relation

$$I_4(x) = I_3 \left(\frac{\pi d\, n_0^3\, r_{41}\, m_G^{eff}\, E_0}{\lambda_G \cos\theta}\right)^2 \left(1 - 4m_S^{eff} \cos K_S x\right) \tag{17}$$

in the Kogelnik formulation [19]. This expression demonstrates that the information contained in the incoherent incident intensity distribution $I_S(x)$ (see Eqn. (1)) is transferred onto the coherent diffracted beam, performing an incoherent-to-coherent conversion in which the original contrast is reversed.

465-12

For the case of uniform erasure ($K_S = 0$), the diffracted beams $I_{11}$ and $I_{10}$ are degenerate (see Fig. 3). For the case of modulated erasure ($K_S \neq 0$), this degeneracy is broken and separate beams are observed. The diffraction efficiencies in these two cases are given by:

$$\eta(I_{10}) \propto [m_G^{eff}(R)]^2 E_0^2 \tag{18}$$

$$\eta(I_{11}) \propto [m_G^{eff}(R) m_S^{eff}(R)]^2 E_0^2 \tag{19}$$

where R is the ratio of the incoherent to the coherent beam intensities ($R = I_S/I_G$). Figures 11 and 12 illustrate the normalized diffraction efficiency of the $I_{10}$ beam for three typical erasure wavelengths ($\lambda_S$). The parameter $A_S$ is the ratio of the erasure beam to the writing beam intensity absorption coefficients ($A_S = \alpha_S/\alpha_G$). It is interesting to note that the maximum energy sensitivity does not generally occur for wavelength-matching ($\lambda_G = \lambda_S$). In fact, two limiting situations can be recognized. For a thin crystal (Fig. 11), the optimum sensitivity is obtained with a strongly absorbed erasure beam because the generation rate increases with the ratio $A_S$, while the attenuation factor $[\exp(\alpha_G - \alpha_S)d]$ has almost no effect on the effective modulation $m_G^{eff}$. Conversely, for a thick crystal (Fig. 12), the exponential term dominates and the optimum sensitivity is achieved when the incoherent source has the same wavelength as the laser with which the carrier grating is recorded. This is intuitively appealing since the phase grating is most effectively erased throughout the volume of the crystal for the case of wavelength matching.

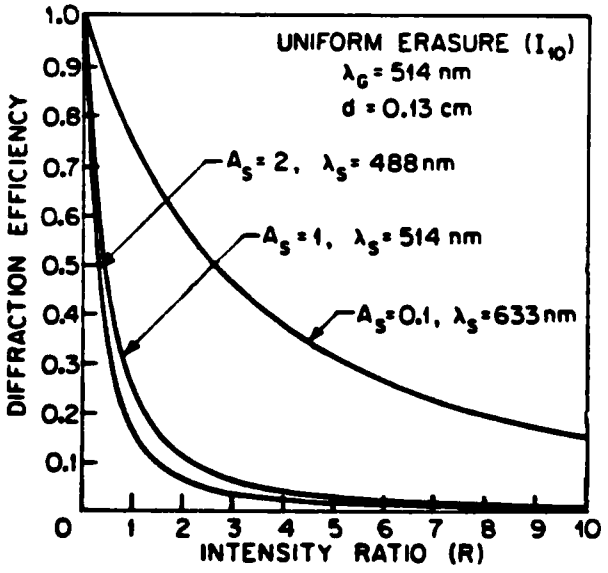


Fig. 11 Normalized diffraction efficiency of the $I_{10}$ beam (Uniform Erasure) as a function of the intensity ratio (R) for a 0.13 cm thick crystal. Three signal beam (S) wavelengths ($\lambda_S$) with corresponding absorption coefficients ($A_S$) are used to erase the coherent grating written at wavelength $\lambda_G$.

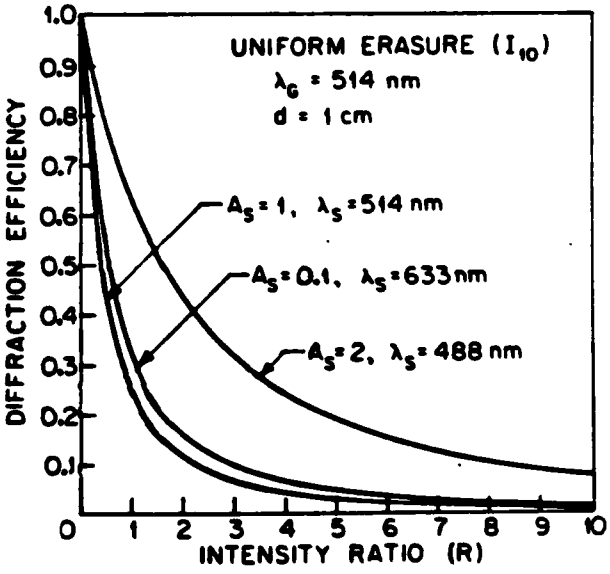


Fig. 12 Normalized diffraction efficiency of the $I_{10}$ beam (Uniform Erasure) as a function of the intensity ratio (R) for a 1.0 cm thick crystal. Three signal beam (S) wavelengths ($\lambda_S$) with corresponding absorption coefficients ($A_S$) are used to erase the coherent grating written at wavelength $\lambda_G$.

The normalized diffraction efficiency for the beam $I_{11}$ in the case of modulated erasure is shown in Fig. 13. As predicted by Eqn. (19), a maximum exists for $R_{eff} = 1$ where:

$$R_{eff} = R \frac{\alpha_S \lambda_S}{\alpha_G \lambda_G} \exp(\alpha_G - \lambda_S)d \qquad (20)$$

The existence of such a maximum is explained by the following. It is clear that when $R_{eff} = 0$, there is no diffraction in the $I_{11}$ direction. In addition, when $R_{eff}$ is large, the uniform component of the incoherent exposure almost completely erases the carrier grating and the diffracted intensity vanishes. Furthermore, a small intensity ratio ($R_{eff} \sim 1$) generates the maximum signal ($I_{11}$), but the uniform erasure ($I_{10}$) is weak and as a result the overall contrast is low. Conversely, a large ratio ($R_{eff} >> 1$), decreases the modulation $m_S^{eff}$, but at the same time diffraction in the beam $I_{10}$ is minimized so that the overall contrast is enhanced at the expense of sensitivity. In Figs. 4 and 5, R was set equal to 10

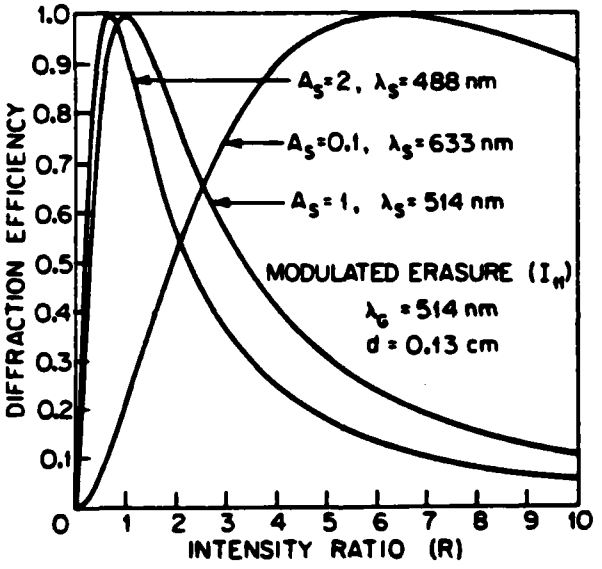


Fig. 13 Normalized diffraction efficiency of the $I_{11}$ beam (Modulated Erasure) as a function of the intensity ratio (R) for a 0.13 cm-thick crystal. Three signal beam (S) wavelengths ($\lambda_S$) with corresponding absorption coefficients ($A_S$) are used to erase the coherent grating written at wavelength $\lambda_G$.

in order to maximize the contrast in the negative imaging mode. However, a number of specialized readout techniques (e.g. Schlieren, phase contrast) could be employed to simultaneously optimize the signal intensity and the contrast ratio.

To verify the essential predictions of this simple model described above, the experimental arrangement shown in Fig. 14 has been utilized. The carrier grating is recorded in the BSO crystal at $\lambda_G$ = 514 nm and read out with a He-Ne laser at $\lambda_R$ = 633 nm incident at the Bragg angle. The incoherent grating is formed with a Michelson interferometer ($M_4$, $M_5$) using the blue line of the argon laser ($\lambda_S$ = 488 nm). The far-field diffraction pattern is located in the Fourier plane of the lens L. The results of theoretical calculations and experimental measurements of the normalized diffraction

465-12

PICOC: Experimental Set-up for Sensitometry and Transfer Function Measurements

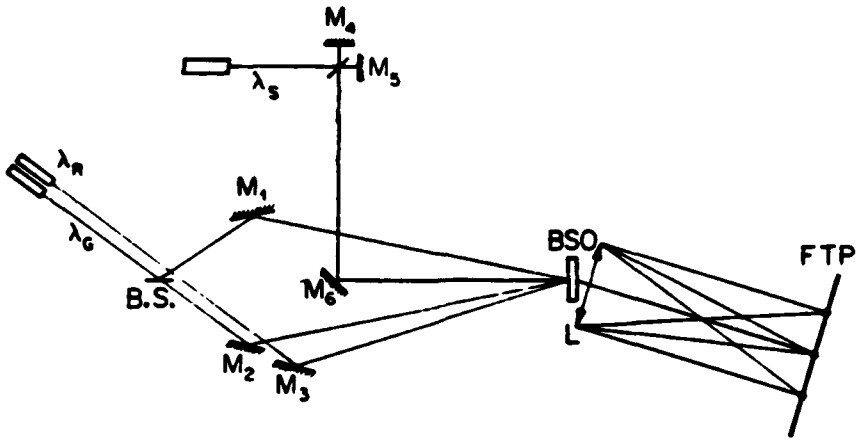


Fig. 14 Experimental arrangement for sensitivity and transfer function measurements, as described in detail in the text.

efficiency as a function of the intensity ratio R are presented in Fig. 15 for the case of uniform ($I_{10}$) erasure, and in Fig. 16 for the case of modulated ($I_{11}$) erasure. The general behavior of these curves is in agreement with the model. The discrepancy in the amplitude between the theoretical prediction and the experimental measurement likely derives from a large difference in grating modulation ratio between the two treatments. Experimentally, a large modulation ratio ($m_G \sim 1$) was employed in order to increase the diffracted intensity for the purpose of signal-to-noise ratio enhancement. In the theoretical development, however, the assumption of small modulation ratios ($m_G \ll 1$) was necessary to achieve analytic solution of the nonlinear coupled equations. An increase in the modulation ratio results in increased space charge field gradients that in turn enhance erasure sensitivity, as indicated by the experimental results shown in Fig. 15. This heightened sensitivity is strongly diminished at larger intensity ratios due to the reduced effective modulation ratio that results from uniform grating erasure. This explanation of the uniform erasure case also aids in understanding the behavior shown in Fig. 16 for the modulated case ($I_{11}$). At the larger (experimental) modulation ratio, the uniform component of the incoherent erasure beam is more effective in diminishing the carrier grating (represented by $I_{10}$ - see Fig. 15) than the (low modulation ratio) theory predicts, resulting in a decrease in sensitivity of $I_{11}$ at low values of R. On the other hand, for values of R much greater than 1, the carrier grating is erased more slowly than in the theoretical prediction. This results in a more gradual decline in the $I_{11}$ diffraction efficiency with increasing R than would occur at lower modulation ratios (see Fig. 16).

The general temporal response behavior of the $I_{11}$ (information-bearing) diffracted beam is shown in Fig. 17 for the two cases R = 1.5 and R = 5.0. In this experiment, the coherent grating is established and in the saturation regime at time t = 0, at which point the incoherent erasure beam is allowed to expose the crystal. For a small ratio R ($I_s$ = 0.6 mW/cm$^2$ in Fig. 17), the diffraction efficiency increases steadily with time until it reaches a maximum. However, for a strong incoherent beam ($I_s$ = 2 mW/cm$^2$ in Fig. 17), a transient effect appears. Initially, the beam $I_{10}$ is quite intense and diffracts from the composite grating at $K_G + K_s$ to generate a rapid rise in the amplitude of $I_{11}$, but the uniform part of the incoherent illumination simultaneously erases the coherent carrier grating and hence the diffraction efficiency decreases to a small steady-state value. The time constant for this particular set of experimental parameters is in the range 0.5-1.5 sec., although the device response time can be decreased by increasing the intensity of the carrier grating writing beams. In addition, the response time is strongly dependent on a number of intrinsic and extrinsic materials parameters. The full range of variation possible for the temporal behavior characteristic is not firmly established at this point.

465-12

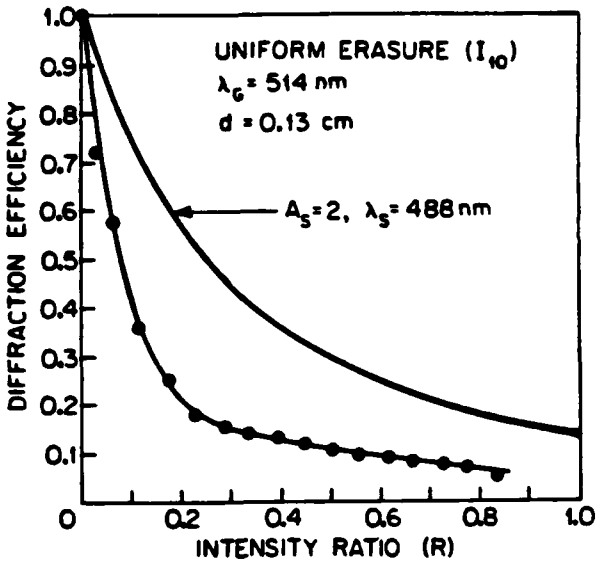


Fig. 15 Normalized experimental diffraction efficiency of the $I_{10}$ beam (Uniform Erasure) as a function of the intensity ratio (R). The corresponding theoretical prediction is also shown for comparison.

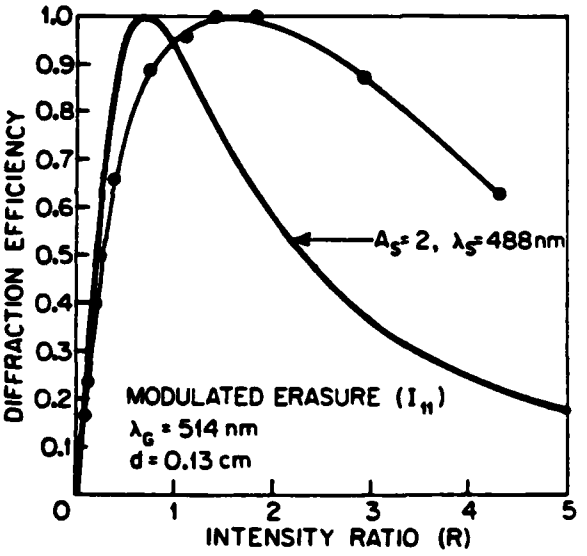


Fig. 16 Normalized experimental diffraction efficiency of the $I_{11}$ beam (Modulated Erasure) as a function of the intensity ratio (R). The corresponding theoretical prediction is also shown for comparison.

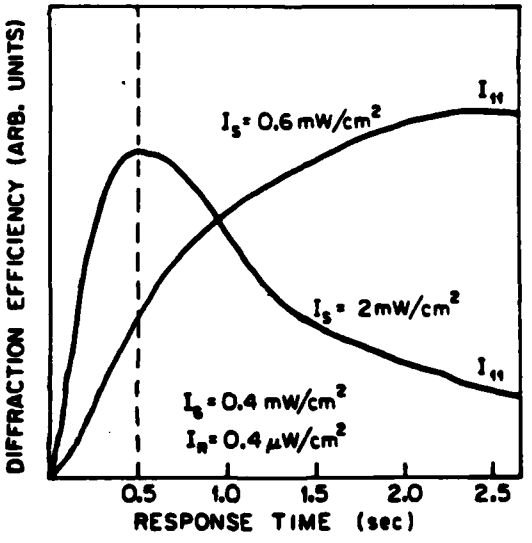


Fig. 17 Measured diffraction efficiency of the $I_{11}$ beam (Modulated Erasure) as a function of response time for two values of the signal intensity.

465-12

In conclusion, we have demonstrated the feasibility of real-time incoherent-to-coherent conversion utilizing phase conjugation in photorefractive BSO crystals. The physical basis of this effect is explained with a simple model which takes into account the influence of the effective modulation ratio on the diffraction efficiency of the different diffracted beams. Although the results are preliminary, the device which is proposed in this paper has potential for incoherent-to-coherent conversion with high resolution, which can be realized by optimizing the wavevector matching condition and the relative intensities and wavelengths of the various beams. In addition, the PICOC device is quite attractive from considerations of low cost, ease of fabrication, and broad availability. With such a device, numerous optical processing functions can be directly implemented that utilize the flexibility afforded by the simultaneous availability of incoherent-to-coherent conversion and volume holographic storage.

## ACKNOWLEDGEMENTS

The authors would like to thank F. Lum, D. Seery, and M. Garrett for their technical assistance. This research was supported in part at USC by the Air Force Systems Command (RADC) under Contract No. F19628-83-C-0031, the Defense Advanced Research Projects Agency, the Joint Services Electronics Program, and the Army Research Office; and at Caltech by the Air Force Office of Scientific Research and the Army Research Office.

## REFERENCES

[1] J. O. White and A. Yariv, Appl. Phys. Lett. 37, 5 (1980).

[2] A. Marrakchi, J. P. Huignard and J. P. Herriau, Opt. Comm. 34, 15 (1980).

[3] G. J. Dunning and R. C. Lind, Opt. Lett. 7, 558 (1982).

[4] A. R. Tanguay, Jr., Proc. ARO Workshop on Future Directions for Optical Information Processing, Texas Tech University, Lubbock, Texas, May, 1980, 52-77 (1981).

[5] D. Casasent, Proc. IEEE, 65, 143 (1977).

[6] Y. Shi, D. Psaltis, A. Marrakchi and A. R. Tanguay, Jr., Appl. Opt. 22, 3665 (1983).

[7] A. A. Kamshilin and M. P. Petrov, Sov. Tech. Phys. Lett. 6, 144 (1980).

[8] D. L. Staebler and J. J. Amodei, J. Appl. Phys. 43, 1042 (1972).

[9] M. Peltier and F. Micheron, J. Appl. Phys. 48, 3683 (1977).

[10] R. Grousson and S. Mallick, Appl. Opt. 19, 1762 (1980).

[11] J. P. Huignard, J. P. Herriau, G. Rivet and P. Gunter, Opt. Lett. 5, 102 (1980).

[12] J. P. Herriau, J. P. Huignard and P. Aubourg, Appl. Opt. 17, 1851 (1978).

[13] Y. Owechko and A. R. Tanguay, Jr., Opt. Lett. 7, 587 (1982).

[14] P. Aubourg, J. P. Huignard, M. Hareng and R. A. Mullen, Appl. Opt. 21, 3706 (1982).

[15] J. Feinberg and R. W. Hellwarth, Opt. Lett. 5, 519 (1980).

[16] J. P. Huignard and A. Marrakchi, Opt. Comm. 38, 249 (1981).

[17] H. Rajbenbach, J. P. Huignard and B. Loiseaux, Opt. Comm. 48, 247 (1983).

[18] M. G. Moharam, T. K. Gaylord and R. Magnusson, J. Appl. Phys. 50, 5642 (1979).

[19] H. Kogelnik, Bell Syst. Tech. J. 18, 2909 (1969).